PARTICLE NUMBER DENSITY DISTRIBUTION AND ITS TIME HISTORY FOR AN AUTOMOTIVE AIR FILTER

By

MANOJ KUMAR HALDHANI

Bachelor of Engineering

University of Rajasthan

Jaipur, India

1991

Submitted to the Faculty of the
Graduate College of the
Oklahoma State University
in partial fulfillment of
the requirements for
the Degree of
MASTER OF SCIENCE
December, 1993

OKLAHOMA STATE UNIVERSITY

PARTICLE NUMBER DENSITY DISTRIBUTION AND ITS TIME HISTORY FOR AN AUTOMOTIVE AIR FILTER

Thesis Approved :

Thesis Adviser

Dean of the Graduate College

ACKNOWLEDGMENTS

I want to express my deep regards for the almighty God without whose wish nothing is possible. I want to extend my deepest regards for my parents and brother whose love and encouragement has always shown me the right path.

My sincere gratitudes are due, to my major adviser Dr. R. L. Dougherty. His invaluable guidance and constant encouragement has always helped me. I am also highly indebted to my other committee members, Dr. F. W. Chambers and Dr. J. D. Spitler, for their valuable suggestions and guidance.

A sincere appreciation is extended to Purolator personnel, especially to Dr. G. Ferrel and J. Doty, for their keen interest in the project.

I am grateful to R. Taylor, D. Cooper and North Lab Workshop personnel for their help and cooperation. I would like to thank my colleagues F. Liang, R. Sabnis and Q. Cai for their understanding, help and cooperation.

I truly appreciate the financial support extended by Purolator Products, Inc. and Oklahoma Center for the Advancement of Science and Technology (OCAST).

I would like to thank all the persons who have helped me, directly or indirectly, in successfully completing this work.

TABLE OF CONTENTS

Chapter		Page
I.	INTRODUCTION	1
II.	LITERATURE REVIEW	4
III.	THEORY AND EXPERIMENTAL SETUP	26
IV.	RESULTS AND ANALYSIS	39
	Sensitivity Measurements	39
	Data Reproducibility Measurements	57
	Measurements at a Plane 6.625 In. Above the Filter Face	71
	Measurements at a Plane 3.625 In. Above the Filter Face	87
	Measurements at a Plane 2.125 In. Above the Filter Face	105
	Measurements at a Plane 0.625 In. Above the Filter Face	111
	Comparison at Different Heights Above the Filter Face	132
	Time History Measurements	156
V.	CONCLUSIONS AND RECOMMENDATIONS	195
REFERENCES		203
APPENDIXES		205
	APPENDIX A - LIST OF EQUIPMENT	206
	APPENDIX B - TRAVERSE AUTOMATION	208
	APPENDIX C - LISTING AND EXPLANATION OF SOURCE CODE FOR TRAVERSE	223
	APPENDIX D - DSA CONFIGURATION AND VARIABLE SETUP PAGES	229
	APPENDIX E - PARAMETER SETUPS EMPLOYED FOR MEASUREMENTS	235

LIST OF TABLES

Table		Page
1.	Water Consumption Rate of the Humidifier	62
2.	Estimation of Mist Intensity (Particles/Second) Generated by the Humidifier	63
3.	Theoretical Number Density at the Humidifier Outlet	64
4.	Test Information	69
5.	Tests Conducted at Various Planes	70
6.	Configuration Pages and the Accessing Keystrokes	230

LIST OF FIGURES

Figure		Page
1.	PMS ASAS-300X Laser Optical Particle Counter	6
2.	PMS LAS-X Laser Optical Counter [from: Liu, 1985]	7
3.	Climet 226 Optical Particle Counter	8
4.	HIAC Royco 1000A Laser Optical Particle Counter	9
5.	Optical Configuration Used by Farmer	11
6.	Example of Doppler Signal [from: Aerometrics, 1991]	13
7.	Optical Configuration Used by Tedjojuwono et al	15
8.	Optical Configuration Used by Wood et al.	19
9.	Block Diagram of Laser Imaging System	21
10.	A Particle Sampling Configuration Using Diffusion Battery	23
11.	Laser Probe Volume and Fringe Pattern	27
12.	Probe Volume and Fringe Patterns for the LDV System Employed	28
13.	Swept Volume	29
14.	Focusing and Probe Volume Geometries	30
15.	Experimental Setup	33
16.	Schematic of the Discrete Fourier Transform Method [from: Aerometrics, 1991]	36
17.	SAE Panel Filter Universal Test Housing [from: SAE, 1987]	37

Figure Page

18. A Typical Variable Setup Employed 40

19. Dependence of Number Density and Velocity on Low Pass Filter for Channel 2 42

20. Dependence of Number Density and Velocity on Low Pass Filter for Channel 1 42

21. Dependence of Number Density and Velocity on Burst Filter for Channel 2 43

22. Dependence of Number Density and Velocity on Burst Filter for Channel 1 43

23. Dependence of Number Density and Velocity on Threshold for Channel 2 45

24. Dependence of Number Density and Velocity on Threshold for Channel 1 45

25. Dependence of Number Density and Velocity on Envelope Filter for Channel 2 47

26. Dependence of Number Density and Velocity on Envelope Filter for Channel 1 47

27. Dependence of Number Density and Velocity on Sampling Frequency for Channel 2 49

28. Dependence of Number Density and Velocity on Sampling Frequency for Channel 1 49

29. Dependence of Velocity on Channels Enabled 51

30. Dependence of Number Density on Channels Enabled 51

31. A Sample Variable Page for Terminating Data Acquisition, and for Data Documentation and Storage 53

32. A Sample Output Page 54

33. Dependence of Velocity on Laser Power 56

34. Dependence of Particle Counts on Laser Power 58

35. Dependence of Number Density on Laser Power 58

Figure Page

36. Data Reproducibility 59

37. Variation of Number Density and Velocity with Different Filters 61

38. Schematic Diagram of the Humidifier Setup for Providing Seeding in a Jet (Not to Scale) 65

39. Filter Mounted in Plexiglas Housing 67

40. Measurement Grid for Automotive Air Filter AF 3192 68

41. Three-Dimensional Plot of Number Density Distribution for Test D, at a Plane 6.625 In. Above the Filter Face 73

42. Two-Dimensional Plot of Number Density Distribution at Different Grid Sections for Test D, at a Plane 6.625 In. Above the Filter Face 73

43. Three-Dimensional Plot of Velocity Profile for Test D, at a Plane 6.625 In. Above the Filter Face 75

44. Two-Dimensional Plot of Velocity Profiles at Different Grid Sections for Test D, at a Plane 6.625 In. Above the Filter Face 75

45. Three-Dimensional Plot of Number Density Distribution for Test E, at a Plane 6.625 In. Above the Filter Face 77

46. Two-Dimensional Plot of Number Density Distribution at Different Grid Sections for Test E, at a Plane 6.625 In. Above the Filter Face 78

47. Two-Dimensional Plot of Number Density Distribution at Different Grid Sections for Test E, at a Plane 6.625 In. Above the Filter Face 78

48. Two-Dimensional Plot of Number Density Distribution at Different Grid Sections for Test E, at a Plane 6.625 In. Above the Filter Face 79

49. Two-Dimensional Plot of Number Density Distribution at Different Grid Sections for Test E, at a Plane 6.625 In. Above the Filter Face 79

50. Comparison of Number Densities for Tests D and E, at Y=0 In. for a Plane 6.625 In. Above the Filter Face 81

51. Comparison of Number Densities for Tests D and E, at Y=1 In. for a Plane 6.625 In. Above the Filter Face 81

Figure Page

52. Comparison of Number Densities for Tests D and E, at Y=2 In. for a Plane 6.625 In. Above the Filter Face 82

53. Three-Dimensional Plot of Velocity Profile for Test E, at a Plane 6.625 In Above the Filter Face 83

54. Two-Dimensional Plot of Velocity Profiles at Different Grid Sections for Test E, at a Plane 6.625 In. Above the Filter Face 84

55. Two-Dimensional Plot of Velocity Profiles at Different Grid Sections for Test E, at a Plane 6.625 In. Above the Filter Face 84

56. Comparison of Velocitiy Profiles for Tests D and E, at Y=0 In. for a Plane 6.625 In. Above the Filter Face 85

57. Comparison of Velocitiy Profiles for Tests D and E, at Y=1 In. for a Plane 6.625 In. Above the Filter Face 85

58. Comparison of Velocitiy Profiles for Tests D and E, at Y=2 In. for a Plane 6.625 In. Above the Filter Face 86

59. Three-Dimensional Plot of Number Density Distribution for Test C, at a Plane 3.625 In. Above the Filter Face 89

60. Two-Dimensional Plot of Number Density Distribution at Different Grid Sections for Test C, at a Plane 3.625 In. Above the Filter Face 89

61. Three-Dimensional Plot of Velocity Profile for Test C, at a Plane 3.625 In. Above the Filter Face 90

62. Two-Dimensional Plot of Velocity Profiles at Different Grid Sections for Test C, at a Plane 3.625 In. Above the Filter Face 90

63. Three-Dimensional Plot of Number Density Distribution for Test K, at a Plane 3.625 In. Above the Filter Face 92

64. Two-Dimensional Plot of Number Density Distribution at Different Grid Sections for Test K, at a Plane 3.625 In. Above the Filter Face 92

65. Three-Dimensional Plot of Velocity Profile for Test K, at a Plane 3.625 In. Above the Filter Face 93

Figure Page

66. Two-Dimensional Plot of Velocity Profiles at Different Grid Sections for Test K, at a Plane 3.625 In. Above the Filter Face 93

67. Three-Dimensional Plot of Number Density Distribution for Test G, at a Plane 3.625 In. Above the Filter Face 95

68. Two-Dimensional Plot of Number Density Distribution at Different Grid Sections for Test G, at a Plane 3.625 In. Above the Filter Face 96

69. Two-Dimensional Plot of Number Density Distribution at Different Grid Sections for Test G, at a Plane 3.625 In. Above the Filter Face 96

70. Two-Dimensional Plot of Number Density Distribution at Different Grid Sections for Test G, at a Plane 3.625 In. Above the Filter Face 98

71. Two-Dimensional Plot of Number Density Distribution at Different Grid Sections for Test G, at a Plane 3.625 In. Above the Filter Face 98

72. Comparison of Number Densities for Tests C, K and G at Y=0 In. for a Plane 3.625 In. Above the Filter Face 99

73. Comparison of Number Densities for Tests C, K and G at Y=1 In. for a Plane 3.625 In. Above the Filter Face 99

74. Comparison of Number Densities for Tests C, K and G at Y=2 In. for a Plane 3.625 In. Above the Filter Face 100

75. Three-Dimensional Plot of Velocity Profile for Test G, at a Plane 3.625 In. Above the Filter Face 101

76. Two-Dimensional Plot of Velocity Profiles at Different Grid Sections for Test G, at a Plane 3.625 In. Above the Filter Face 102

77. Two-Dimensional Plot of Velocity Profiles at Different Grid Sections for Test G, at a Plane 3.625 In. Above the Filter Face 102

78. Comparison of Velocity Profiles for Tests C, K and G at Y=0 In. for a Plane 3.625 In. Above the Filter Face 103

79. Comparison of Velocity Profiles for Tests C, K and G at Y=1 In. for a Plane 3.625 In. Above the Filter Face 103

Figure Page

80. Comparison of Velocity Profiles for Tests C, K and G at Y=2 In. for a Plane 3.625 In. Above the Filter Face 104

81. Three-Dimensional Plot of Number Density Distribution for Test J, at a Plane 2.125 In. Above the Filter Face 106

82. Two-Dimensional Plot of Number Density Distribution at Different Grid Sections for Test J, at a Plane 2.125 In. Above the Filter Face 106

83. Three-Dimensional Plot of Velocity Profile for Test J, at a Plane 2.125 In. Above the Filter Face 107

84. Two-Dimensional Plot of Velocity Profiles at Different Grid Sections for Test J, at a Plane 2.125 In. Above the Filter Face 107

85. Three-Dimensional Plot of Number Density Distribution for Test L, at a Plane 2.125 In. Above the Filter Face 109

86. Two-Dimensional Plot of Number Density Distribution at Different Grid Sections for Test L, at a Plane 2.125 In. Above the Filter Face 109

87. Three-Dimensional Plot of Velocity Profile for Test L, at a Plane 2.125 In. Above the Filter Face 110

88. Two-Dimensional Plot of Velocity Profiles at Different Grid Sections for Test L, at a Plane 2.125 In. Above the Filter Face 110

89. Comparison of Number Densities for Tests J and L, for a Plane 2.125 In. Above the Filter Face 112

90. Comparison of Number Densities for Tests J and L, for a Plane 2.125 In. Above the Filter Face 112

91. Comparison of Number Densities for Tests J and L, for a Plane 2.125 In. Above the Filter Face 113

92. Comparison of Velocity Profiles for Tests J and L, for a Plane 2.125 In. Above the Filter Face 114

93. Comparison of Velocity Profiles for Tests J and L, for a Plane 2.125 In. Above the Filter Face 114

94. Comparison of Velocity Profiles for Tests J and L, for a Plane 2.125 In. Above the Filter Face 115

Figure Page

95. Three-Dimensional Plot of Number Density Distribution for Test B, at a Plane 0.625 In. Above the Filter Face 117

96. Two-Dimensional Plot of Number Density Distribution at Different Grid Sections for Test B, at a Plane 0.625 In. Above the Filter Face 117

97. Three-Dimensional Plot of Velocity Profile for Test B, at a Plane 0.625 In. Above the Filter Face 118

98. Two-Dimensional Plot of Velocity Profiles at Different Grid Sections for Test B, at a Plane 0.625 In. Above the Filter Face 118

99. Three-Dimensional Plot of Number Density Distribution for Test I, at a Plane 0.625 In. Above the Filter Face 120

100. Two-Dimensional Plot of Number Density Distribution at Different Grid Sections for Test I, at a Plane 0.625 In. Above the Filter Face 120

101. Three-Dimensional Plot of Velocity Profile for Test I, at a Plane 0.625 In. Above the Filter Face 121

102. Two-Dimensional Plot of Velocity Profiles at Different Grid Sections for Test I, at a Plane 0.625 In. Above the Filter Face 121

103. Three-Dimensional Plot of Number Density Distribution for Test M, at a Plane 0.625 In. Above the Filter Face 123

104. Two-Dimensional Plot of Number Density Distribution at Different Grid Sections for Test M, at a Plane 0.625 In. Above the Filter Face 123

105. Three-Dimensional Plot of Velocity Profile for Test M, at a Plane 0.625 In. Above the Filter Face 124

106. Two-Dimensional Plot of Velocity Profiles at Different Grid Sections for Test M, at a Plane 0.625 In. Above the Filter Face 124

107. Three-Dimensional Plot of Number Density Distribution for Test H, at a Plane 0.625 In. Above the Filter Face 126

108. Two-Dimensional Plot of Number Density Distribution at Different Grid Sections for Test H, at a Plane 0.625 In. Above the Filter Face 126

109. Three-Dimensional Plot of Velocity Profile for Test H, at a Plane 0.625 In. Above the Filter Face 127

Figure Page

110. Two-Dimensional Plot of Velocity Profiles at Different Grid Sections for Test H, at a Plane 0.625 In. Above the Filter Face 127

111. Three-Dimensional Plot of Number Density Distribution for Test F, at a Plane 0.625 In. Above the Filter Face 129

112. Two-Dimensional Plot of Number Density Distribution at Different Grid Sections for Test F, at a Plane 0.625 In. Above the Filter Face 129

113. Three-Dimensional Plot of Velocity Profile for Test F, at a Plane 0.625 In. Above the Filter Face 130

114. Two-Dimensional Plot of Velocity Profiles at Different Grid Sections for Test F, at a Plane 0.625 In. Above the Filter Face 130

115. Three-Dimensional Plot of Number Density Distribution for Test A, at a Plane 0.625 In. Above the Filter Face 131

116. Two-Dimensional Plot of Number Density Distribution at Different Grid Sections for Test A, at a Plane 0.625 In. Above the Filter Face 131

117. Three-Dimensional Plot of Velocity Profile for Test A, at a Plane 0.625 In. Above the Filter Face 133

118. Two-Dimensional Plot of Velocity Profiles at Different Grid Sections for Test A, at a Plane 0.625 In. Above the Filter Face 133

119. Comparison of Number Densities for Tests B, I, M, H, F and A for a Plane 0.625 In. Above the Filter Face 134

120. Comparison of Number Densities for Tests B, I, M, H, F and A for a Plane 0.625 In. Above the Filter Face 134

121. Comparison of Number Densities for Tests B, I, M, H and F for a Plane 0.625 In. Above the Filter Face 135

122. Comparison of Number Densities for Tests B, H and F for a Plane 0.625 In. Above the Filter Face 135

123. Comparison of Velocity Profiles for Tests B, I, M, H, F and A for a Plane 0.625 In. Above the Filter Face 136

124. Comparison of Velocity Profiles for Tests B, I, M, H, F and A for a Plane 0.625 In. Above the Filter Face 136

Figure Page

125. Comparison of Velocity Profiles for Tests B, I, M, H, F and A for a Plane 0.625 In. Above the Filter Face 137

126. Comparison of Velocity Profiles for Tests B, H and F for a Plane 0.625 In. Above the Filter Face 137

127. Three-Dimensional Plot of Number Density Distribution for Test D, at a Plane 6.625 In. Above the Filter Face 139

128. Three-Dimensional Plot of Number Density Distribution for Test C, at a Plane 3.625 In. Above the Filter Face 139

129. Three-Dimensional Plot of Number Density Distribution for Test B, at a Plane 0.625 In. Above the Filter Face 140

130. Comparison of Number Densities for Tests D, C and B at Y=0 In. 141

131. Comparison of Number Densities for Tests D, C and B at Y=1 In. 141

132. Comparison of Number Densities for Tests D, C and B at Y=2 In. 142

133. Three-Dimensional Plot of Velocity Profile for Test D, at a Plane 6.625 In. Above the Filter Face 143

134. Three-Dimensional Plot of Velocity Profile for Test C, at a Plane 3.625 In. Above the Filter Face 143

135. Three-Dimensional Plot of Velocity Profile for Test B, at a Plane 0.625 In. Above the Filter Face 144

136. Comparison of Velocity Profiles for Tests D, C and B at Y=0 In. 145

137. Comparison of Velocity Profiles for Tests D, C and B at Y=1 In. 145

138. Comparison of Velocity Profiles for Tests D, C and B at Y=2 In. 146

139. Three-Dimensional Plot of Number Density Distribution for Test K, at a Plane 3.625 In. Above the Filter Face 148

140. Three-Dimensional Plot of Number Density Distribution for Test J, at a Plane 2.125 In. Above the Filter Face 148

141. Three-Dimensional Plot of Number Density Distribution for Test I, at a Plane 0.625 In. Above the Filter Face 149

Figure Page

142. Comparison of Number Densities for Tests K, J and I 150

143. Comparison of Number Densities for Tests K, J and I 150

144. Comparison of Number Densities for Tests K, J and I 151

145. Three-Dimensional Plot of Velocity Profile for Test K, at a Plane 3.625 In. Above the Filter Face 152

146. Three-Dimensional Plot of Velocity Profile for Test J, at a Plane 2.125 In. Above the Filter Face 152

147. Three-Dimensional Plot of Velocity Profile for Test I, at a Plane 0.625 In. Above the Filter Face 153

148. Comparison of Velocity Profiles for Tests K, J and I 154

149. Comparison of Velocity Profiles for Tests K, J and I 154

150. Comparison of Velocity Profiles for Tests K, J and I 155

151. Three-Dimensional Plot of Number Density Distribution for Test F, at a Plane 0.625 In. Above the Filter Face (Time=0 min.) 158

152. Three-Dimensional Plot of Number Density Distribution for Test F, at a Plane 0.625 In. Above the Filter Face (Time=30 min.) 158

153. Three-Dimensional Plot of Number Density Distribution for Test F, at a Plane 0.625 In. Above the Filter Face (Time=60 min.) 159

154. Three-Dimensional Plot of Number Density Distribution for Test F, at a Plane 0.625 In. Above the Filter Face (Time=90 min.) 159

155. Three-Dimensional Plot of Number Density Distribution for Test F, at a Plane 0.625 In. Above the Filter Face (Time=150 min.) 160

156. Two-Dimensional Plot of Number Density Distribution for Test F, at Different Grid Sections for a Plane 0.625 In. Above the Filter Face (Time=0 min.) 161

157. Two-Dimensional Plot of Number Density Distribution for Test F, at Different Grid Sections for a Plane 0.625 In. Above the Filter Face (Time=30 min.) 161

158. Two-Dimensional Plot of Number Density Distribution for Test F, at Different Grid Sections for a Plane 0.625 In. Above the Filter Face (Time=60 min.) 162

Figure Page

159. Two-Dimensional Plot of Number Density Distribution for Test F, at Different Grid Sections for a Plane 0.625 In. Above the Filter Face (Time=90 min.) 162

160. Two-Dimensional Plot of Number Density Distribution for Test F, at Different Grid Sections for a Plane 0.625 In. Above the Filter Face (Time=150 min.) 163

161. Three-Dimensional Plot of Velocity Profile for Test F, at a Plane 0.625 In. Above the Filter Face (Time=0 min.) 164

162. Three-Dimensional Plot of Velocity Profile for Test F, at a Plane 0.625 In. Above the Filter Face (Time=30 min.)..... 164

163. Three-Dimensional Plot of Velocity Profile for Test F, at a Plane 0.625 In. Above the Filter Face (Time=60 min.)..... 165

164. Three-Dimensional Plot of Velocity Profile for Test F, at a Plane 0.625 In. Above the Filter Face (Time=90 min.)..... 165

165. Three-Dimensional Plot of Velocity Profile for Test F, at a Plane 0.625 In. Above the Filter Face (Time=150 min.)..... 166

166. Two-Dimensional Plot of Velocity Profiles for Test F, at Different Grid Sections for a Plane 0.625 In. Above the Filter Face (Time=0 min.) 167

167. Two-Dimensional Plot of Velocity Profiles for Test F, at Different Grid Sections for a Plane 0.625 In. Above the Filter Face (Time=30 min.) 167

168. Two-Dimensional Plot of Velocity Profiles for Test F, at Different Grid Sections for a Plane 0.625 In. Above the Filter Face (Time=60 min.) 168

169. Two-Dimensional Plot of Velocity Profiles for Test F, at Different Grid Sections for a Plane 0.625 In. Above the Filter Face (Time=90 min.) 168

170. Two-Dimensional Plot of Velocity Profiles for Test F, at Different Grid Sections for a Plane 0.625 In. Above the Filter Face (Time=150 min.) 169

171. Three-Dimensional Plot of Number Density Distribution for Test H, at a Plane 0.625 In. Above the Filter Face (Time=0 min.)..... 170

172. Three-Dimensional Plot of Number Density Distribution for Test H, at a Plane 0.625 In. Above the Filter Face (Time=45 min.)..... 170

Figure Page

173. Three-Dimensional Plot of Number Density Distribution for Test H, at a Plane 0.625 In. Above the Filter Face (Time=90 min.) 171

174. Three-Dimensional Plot of Number Density Distribution for Test H, at a Plane 0.625 In. Above the Filter Face (Time=135 min.) 171

175. Three-Dimensional Plot of Number Density Distribution for Test H, at a Plane 0.625 In. Above the Filter Face (Time=280 min.) 172

176. Two-Dimensional Plot of Number Density Distribution for Test H, at Different Grid Sections for a Plane 0.625 In. Above the Filter Face (Time=0 min.) 173

177. Two-Dimensional Plot of Number Density Distribution for Test H, at Different Grid Sections for a Plane 0.625 In. Above the Filter Face (Time=45 min.) 173

178. Two-Dimensional Plot of Number Density Distribution for Test H, at Different Grid Sections for a Plane 0.625 In. Above the Filter Face (Time=90 min.) 174

179. Two-Dimensional Plot of Number Density Distribution for Test H, at Different Grid Sections for a Plane 0.625 In. Above the Filter Face (Time=135 min.) 174

180. Two-Dimensional Plot of Number Density Distribution for Test H, at Different Grid Sections for a Plane 0.625 In. Above the Filter Face (Time=280 min.) 175

181. Three-Dimensional Plot of Velocity Profile for Test H, at a Plane 0.625 In. Above the Filter Face (Time=0 min.) 176

182. Three-Dimensional Plot of Velocity Profile for Test H, at a Plane 0.625 In. Above the Filter Face (Time=45 min.) 176

183. Three-Dimensional Plot of Velocity Profile for Test H, at a Plane 0.625 In. Above the Filter Face (Time=90 min.) 177

184. Three-Dimensional Plot of Velocity Profile for Test H, at a Plane 0.625 In. Above the Filter Face (Time=135 min.) 177

185. Three-Dimensional Plot of Velocity Profile for Test H, at a Plane 0.625 In. Above the Filter Face (Time=280 min.) 178

186. Two-Dimensional Plot of Velocity Profiles for Test H, at Different Grid Sections for a Plane 0.625 In. Above the Filter Face (Time=0 min.) 180

Figure Page

187. Two-Dimensional Plot of Velocity Profiles for Test H, at Different Grid Sections for a Plane 0.625 In. Above the Filter Face (Time=45 min.) 180

188. Two-Dimensional Plot of Velocity Profiles for Test H, at Different Grid Sections for a Plane 0.625 In. Above the Filter Face (Time=90 min.) 181

189. Two-Dimensional Plot of Velocity Profiles for Test H, at Different Grid Sections for a Plane 0.625 In. Above the Filter Face (Time=135 min.) 181

190. Two-Dimensional Plot of Velocity Profiles for Test H, at Different Grid Sections for a Plane 0.625 In. Above the Filter Face (Time=280 min.) 182

191. Three-Dimensional Plot of Number Density Distribution for Test L, at a Plane 0.625 In. Above the Filter Face (Time=0 min.)..... 183

192. Three-Dimensional Plot of Number Density Distribution for Test L, at a Plane 0.625 In. Above the Filter Face (Time=50 min.)..... 183

193. Three-Dimensional Plot of Number Density Distribution for Test L, at a Plane 0.625 In. Above the Filter Face (Time=100 min.)..... 184

194. Three-Dimensional Plot of Number Density Distribution for Test L, at a Plane 0.625 In. Above the Filter Face (Time=150 min.)..... 184

195. Three-Dimensional Plot of Number Density Distribution for Test L, at a Plane 0.625 In. Above the Filter Face (Time=300 min.)..... 185

196. Two-Dimensional Plot of Number Density Distribution for Test L, at Different Grid Sections for a Plane 0.625 In. Above the Filter Face (Time=0 min.) 186

197. Two-Dimensional Plot of Number Density Distribution for Test L, at Different Grid Sections for a Plane 0.625 In. Above the Filter Face (Time=50 min.) 186

198. Two-Dimensional Plot of Number Density Distribution for Test L, at Different Grid Sections for a Plane 0.625 In. Above the Filter Face (Time=100 min.) 187

199. Two-Dimensional Plot of Number Density Distribution for Test L, at Different Grid Sections for a Plane 0.625 In. Above the Filter Face (Time=150 min.) 187

200. Two-Dimensional Plot of Number Density Distribution for Test L, at Different Grid Sections for a Plane 0.625 In. Above the Filter Face (Time=300 min.) 188

Figure Page

201. Three-Dimensional Plot of Velocity Profile for Test L, at a Plane 0.625 In. Above the Filter Face (Time=0 min.) 189

202. Three-Dimensional Plot of Velocity Profile for Test L, at a Plane 0.625 In. Above the Filter Face (Time=50 min.) 189

203. Three-Dimensional Plot of Velocity Profile for Test L, at a Plane 0.625 In. Above the Filter Face (Time=100 min.) 190

204. Three-Dimensional Plot of Velocity Profile for Test L, at a Plane 0.625 In. Above the Filter Face (Time=150 min.) 190

205. Three-Dimensional Plot of Velocity Profile for Test L, at a Plane 0.625 In. Above the Filter Face (Time=300 min.) 191

206. Two-Dimensional Plot of Velocity Profiles for Test L, at Different Grid Sections for a Plane 0.625 In. Above the Filter Face (Time=0 min.) 192

207. Two-Dimensional Plot of Velocity Profiles for Test L, at Different Grid Sections for a Plane 0.625 In. Above the Filter Face (Time=50 min.) 192

208. Two-Dimensional Plot of Velocity Profiles for Test L, at Different Grid Sections for a Plane 0.625 In. Above the Filter Face (Time=100 min.) 193

209. Two-Dimensional Plot of Velocity Profiles for Test L, at Different Grid Sections for a Plane 0.625 In. Above the Filter Face (Time=150 min.) 193

210. Two-Dimensional Plot of Velocity Profiles for Test L, at Different Grid Sections for a Plane 0.625 In. Above the Filter Face (Time=300 min.) 194

211. Three-Dimensional View of Traverse Table Before Automation 209

212. Top View of Traverse Table 210

213. Eight Lead Bifilar Motor 212

214. Stepper Motor Mounted on the Traverse Table 214

215. Adapter Connected to Lead Screw and Lovejoy Coupling 215

216. Block Diagram of Traverse Automation 216

217. Face of a CMD-40 Showing Terminal Strips 217

Figure Page

218. Eight Lead Motor Connected in Parallel 218

219. Connections on Terminal Strip 1 219

220. Connector 3 Used for Digital Output 221

221. Instrument Configuration 230

222. Configuration Menu # 1 231

223. Configuration Menu # 2 231

224. Factory Configuration # 1 232

225. Factory Configuration # 2 232

226. Factory Configuration # 3 233

227. Factory Configuration # 4 233

228. Factory Configuration # 5 234

229. Parameter Setup I 235

230. Parameter Setup II 236

231. Parameter Setup III 236

234. Parameter Setup IV 237

235. Parameter Setup V 237

236. Parameter Setup VI 238

NOMENCLATURE

a	half of probe volume length (micrometer, μm)
b	half of probe volume thickness (μm)
c	radius at beam waist (μm)
d	diameter of collimating lens (millimeter, mm)
f	focal length of collimating lens (mm)
f_p	fractional value of the peak amplitude
f_s	fractional value of the peak amplitude, or sampling frequency
n	number of particles
t	transit time (sec)
t_p	time corresponding to f_p (nanosecond, ns)
t_s	time corresponding to f_s (ns)
A_h	probe volume cross-sectional area in horizontal plane (μm^2)
A_p	peak amplitude of a Gaussian scattering pulse
A_v	probe volume cross-sectional area in vertical plane (μm^2)
D	particle number density (m^{-3})
I_{smax}	maximum scattered intensity from a bright fringe (watts/m^2)
I_{smin}	minimum scattered intensity from a dark fringe (watts/m^2)
N	number of particles
N_s	number of samples obtained over a burst signal
$P_g{}^1$	d.c. signal power for a single scattering center (watts)

$P_S{}^1$	a.c. signal power for a single scattering center (watts)
$\overline{P_g^n}$	d.c. signal power for n scattering centers (watts)
$\overline{P_s^n}$	a.c. signal power for n scattering centers (watts)
T_S	sampling time (sec)
U	mean velocity (m/s)
V	swept volume (m^3)
$\overline{V_n}$	particle visibility function
V_S	signal visibility
W	distance between two specified fractional values of the peak intensity for a Gaussian beam (μm)
$\overline{V}$	ensemble average on particle visibility function
α	beam focusing angle (degree)
σ	standard deviation

CHAPTER I

INTRODUCTION

An air filter is an essential and significant component for an automobile. It filters out dust and other particle impurities and thus supplies clean air to the engine. While doing so, it must offer minimal resistance to the air flow to the engine. The performance of an engine with regard to power and efficiency greatly depends upon the quality of clean air supplied to it. Therefore, performance of an air filter is of critical importance and interest. Hence, it becomes imperative that better and better air filters with regard to design, material, workmanship and performance should be developed.

Although particle distribution is related to the air flow distribution for an air filter, it should be explored and researched independently. This is because it is not necessary that the particles should follow the flow pattern and, in fact, the presence of the particles actually changes the flow. Thus, the knowledge of particle and flow distribution for an air filter are complementary to each other.

It is anticipated that the most efficient filtration should occur when the filter is exposed to a flow that is uniformly distributed over its face with an optimal face velocity. In other words, for the most efficient filtration to occur, the flow should be evenly spread over the face of the filter. Further, there should not be any significant variation in the velocity as compared to an optimal velocity over the entire face of the filter. However, it is very difficult for this kind of ideal uniform flow to exist over a pleated filter. This is because of the complex geometry of a pleated filter. Also, certain operations during its manufacture may produce porosity variations over the filter media that may be further responsible for small scale variations in flow distribution over the filter. Besides these

small scale flow variations, large scale flow non-uniformities may result due to different filter housings. Then, the filter will not operate with an optimal face velocity over its entire surface, and its filtration will not match uniform velocity design calculations.

The panel filter universal test housing specified in the SAE Air Cleaner Test Code [SAE, 1987] is like a diffuser. The inlet of the housing is configured as a wide angle diffuser with wall divergence angles of approximately 60 and 37 degrees. The housing does not end in an open exit like a standard diffuser, and the flow through it exits through the reduced area of the tested filter. Thus, the tested filter forms the diffuser outlet and fixes its area ratio. The inlet flow distributions, therefore, may vary for different filter sizes and even for the same filter at different flow rates.

Particle distribution over a filter, like flow distribution, also depends upon a number of factors like the type of filter housing, type and location of flow inlet, flow rate, flow velocity, etc. Hence, it is typically not expected that particles will be uniformly distributed over the entire filter. Also as the filter gets old due to its constant usage, its performance changes. This may be because the filter does not collect particles evenly over its entire face; and thus, the flow resistance may change locally over time, changing the flow distribution and consequently the filter performance. The literature review reveals that currently, there is no detailed experimental analysis of filtration characteristics available. In fact, the most common and popular test for evaluating filter performance, the SAE test [SAE, 1987], also evaluates a filter in terms of an 'overall efficiency'. The SAE test simulates the entire life of a filter by passing an extremely large amount of dust through it, until a specified pressure drop is obtained across the filter. This specified pressure drop differs from one model of the filter to the other and is generally specified by the manufacturing company. A typical value for this pressure drop is 10 in. of water. The test takes approximately thirty minutes. The weight gained by the filter during the test, which is due to the dust trapped by it, is the 'dust capacity' of the filter. The ratio of the weight of the dust collected by the filter to the weight of the dust to which it was exposed,

gives the 'overall efficiency' of the filter. The 'overall efficiency', thus, is an average of filter performance over time and over the entire filter, without considering any time or location dependent variations.

The present work employed laser Doppler velocimetry, which is the state-of-the-art technique, to obtain knowledge of the filter performance variations with time and with location. All of the measurements involved in this work were conducted at a flow rate of 125 (±3%) cubic feet per minute (cfm) and using automotive air filters AF-3192. Measurements were taken at four different levels (6.625, 3.625, 2.125 and 0.625 in.) above the face of the filter.

The knowledge of particle number density distribution and how it changes with time is an indispensable tool for developing more accurate and reliable air filter performance testing techniques. Also it helps in understanding the complex and yet not adequately understood filtration principles. Above all, this knowledge leads directly to improved air filter designs. This work is novel, for it is one of a kind, where particle number density distribution and its time history for an air filter are researched and analyzed.

CHAPTER II

LITERATURE REVIEW

In order to obtain the particle number density distribution, a particle counting technique was needed. A thorough literature review was performed so as to have an idea about the various methods, techniques and instruments which have been used in the past for counting particles and determining particle number density. The literature review suggests that optical methods seem to be most popular for both counting and sizing of particles. Most of these methods provide information and data which can be analyzed relatively easily, so as to infer particle size without actually counting particles. However, it is difficult to deduce information pertaining to particle numbers just by the indirect analysis of the experimental data. Therefore, most of the research has been concentrated on particle sizing as opposed to particle counting, and not many methods or techniques are available to independently count particles without being concerned about their size.

As mentioned before, optical methods are the most popular methods for both counting and sizing of particles. Briefly, optical methods can be characterized as either imaging or light scattering. Imaging methods are generally limited to particle sizes above 5 to 10 micrometer (μm) in practice and require complex image analysis equipment for real-time output [Holve and Annen, 1984]. Light scattering methods can count and size particles as small as 0.1 μm but they require a complex and elaborate experimental set up with regard to 'collecting optics' for scattered light from particles. Both methods can be further subdivided into ensemble or single particle techniques. Single particle techniques measure parameters like velocity and size for every particle under observation as opposed to ensemble techniques which measure average values of the parameters for a number of

particles. The single particle methods, as opposed to ensemble methods, are capable of giving spatial resolution, absolute number densities and more detailed size distribution information.

Optical particle counters count and infer the size of a particle by measuring the light scattered by the particle. This is done by directing a dilute stream of particles through a small scattering volume illuminated by a light source, usually a laser. The light scattered by the particles into certain angular limits is sensed by a photodetector. The output from the detector, the instrument response, leads to the measurement of the particle count and size. The instrument response is affected by the refractive index and shape of the particles as well as by the optical design of the instrument. Optical counters are widely used for measuring the concentration and size distribution of airborne particles. Their ability to measure single, individual particles makes them particularly suitable for applications like monitoring particulate contaminants in clean rooms and measurement of particle sizes in clean gases used in semi-conductor and integrated circuit manufacturing [Liu et al., 1985].

Just to have an idea of the commercially available optical particle counters, a very brief outline of some of them is included. Figures 1 and 2 are the schematics of the two widely used commercially available laser optical particle counters [Liu et al., 1985]. The first is a narrow angle instrument in which the scattered light in the angular range of 4-22 degrees is collected by the light collecting optics for measurement. The second one is a wide angle instrument in which scattered light collected in the 35-130 degree range is used. Figure 3 shows another type of optical particle counter in which conventional white light from an incandescent light source is used [Liu et al., 1985]. The scattered light is collected by means of an elliptical mirror between the angles of 15 and 105 degrees. Figure 4 shows a high flow rate (28.3 liters/minute) laser optical particle counter [Liu et al., 1985]. A large angle elliptical mirror is used to collect the scattered laser light in a direction of 90 degrees from the incident beam.

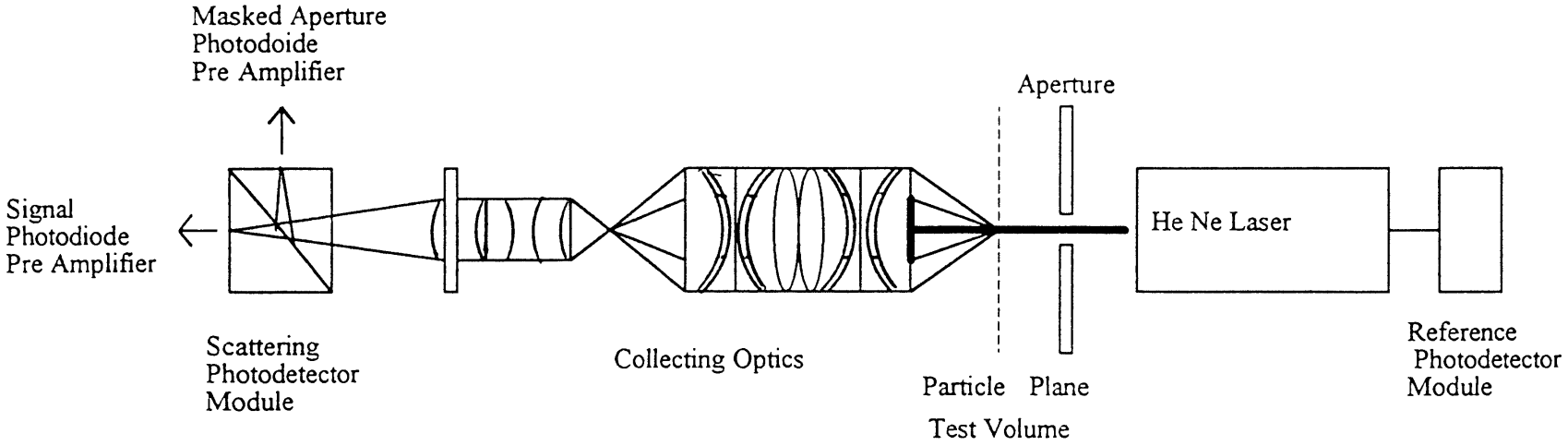

Figure 1. PMS ASAS-300X Laser Optical Particle Counter

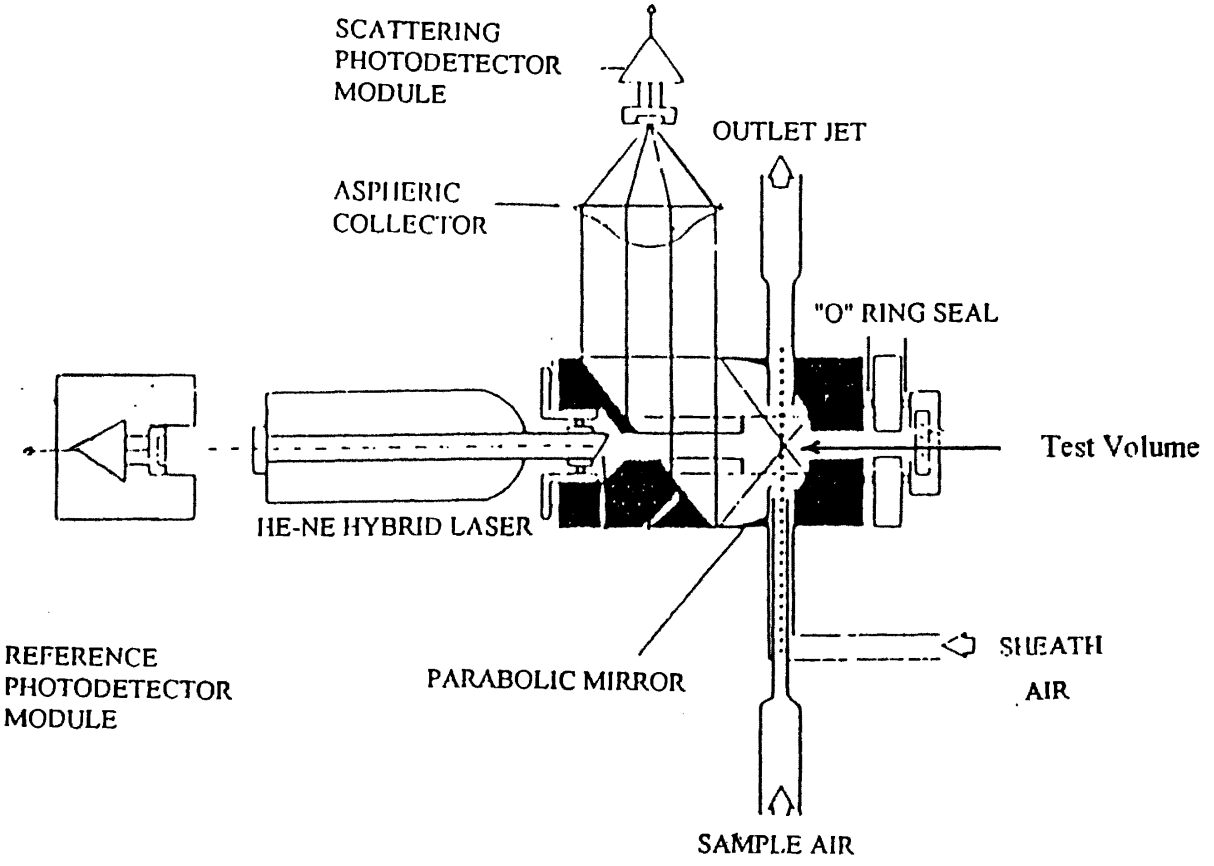

Figure 2. PMS LAS-X Laser Optical Counter [from: Liu, 1985]

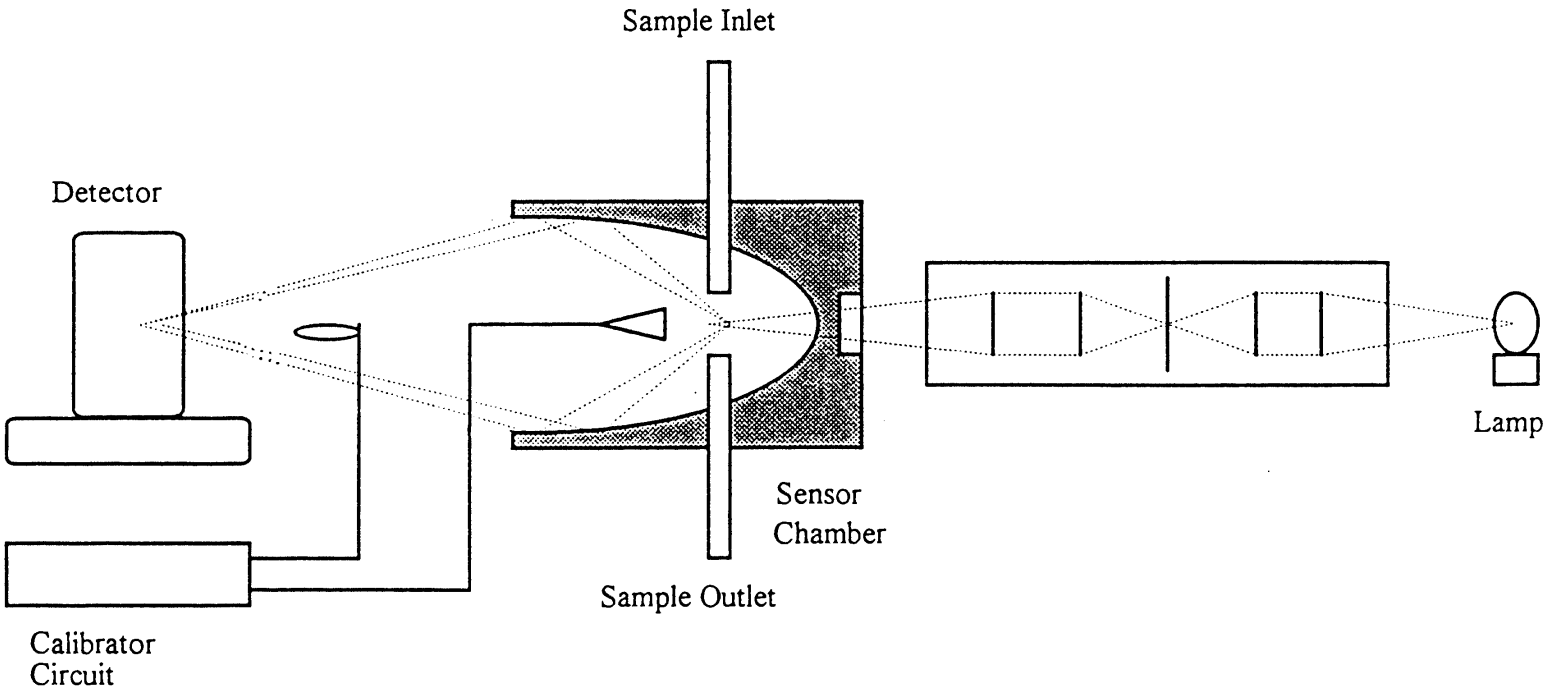

Figure 3. Climet 226 Optical Particle Counter

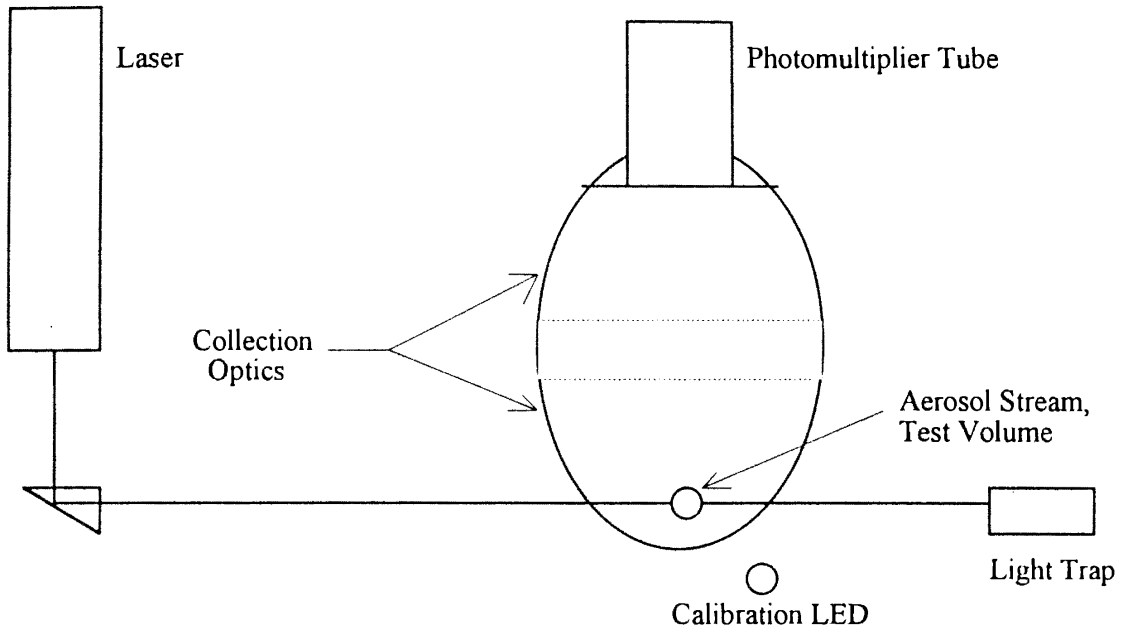

Figure 4. HIAC Royco 1000A Laser Optical Particle Counter

Generally, to determine the absolute number density of particles, their velocity should also be known. Holve [1982] described a simple single beam transit timing velocimetry (TTV) method for obtaining the velocity of the particles. He used the fact shown by an earlier researcher, Hirleman, that the distance W between two specified fractional values of the peak intensity for a Gaussian beam is a constant property of the beam focus only. Hence, for any particle size or trajectory, a Gaussian scattering pulse is generated with an arbitrary peak amplitude A_p. Two attenuated values, f_sA_p and f_pA_p, were electronically stored, where f_s and f_p were fractional values of the peak amplitude. These were compared to the rest of the trailing edge of the pulse. A comparator circuit was used to generate a clock start signal when the pulse amplitude equaled f_sA_p at time t_s and correspondingly, a stop signal was generated when the pulse amplitude equaled f_pA_p

at time t_p. The difference t_p- t_s was the particle transit time and was stored for each valid pulse. The velocity was determined then by $W/(t_p-t_s)$.

A single laser beam was used by Holve [1982] and the sample volume was defined by the intersection of the beam waist and 1 : 1 imaging of the detector pinhole. The lens system was oriented off-axis to the beam illumination axis to give the minimum sample volume. He believed that it was necessary to make the sample volume as small as possible so that only one Gaussian particle trajectory at a time was viewed in the sample volume. Holve et al. [1981] has discussed in detail the requirements for that condition to exist. In general, however, the number density (if measured in particles/cm^3) should be less than 0.4 of the sample volume (if measured in cm^3). The single beam technique for transit time velocimetry could handle flows with number densities around $10^6/cm^3$ [Holve, 1982]. A pulse analysis circuit along with two commercial nuclear instrumentation modules were used to obtain timing information from the trailing edges of the scattered pulses. A pulse shape analyzer tracked the amplified pulse and sent the start and stop clock pulses to a time-to-pulse height converter. That provided a standard width output pulse with an amplitude proportional to the time interval between a start and subsequent stop pulse input. A standard multichannel analyzer was used to record the amplitude pulses which gave the desired time interval. It is important to mention that for a single beam, this method is insensitive to direction and thus can measure only the speed of the scattering particles.

Farmer [1972] analyzed a method for determining particle size, number density and velocity utilizing a laser interferometer. This method, in principle, is similar to other modern methods which employ laser Doppler velocimetry for counting particles. The method took advantage of the non-uniform illumination of a particle by a set of spatially well defined interference fringes generated by two or more crossed laser beams. Figure 5 [Farmer, 1972] shows an experimental arrangement to generate such fringes. The laser beam was split into two beams of equal intensity that were brought to a simultaneous

cross-focus point or the probe volume by a lens. A Huygens diagram showed that the interference fringes existed as planes that were perpendicular to the plane of the beam center lines and parallel to the bisector of the beams [Farmer, 1972]. Farmer [1972] used a suggestion from Rudd [1969] that the Doppler frequency of light scattered from the probe volume could be interpreted in terms of the rate at which a scatter center crosses alternate dark and bright interference fringes. Precise knowledge of the fringe spacing and time period of the scattered light could allow calculation of the velocity of the particle.

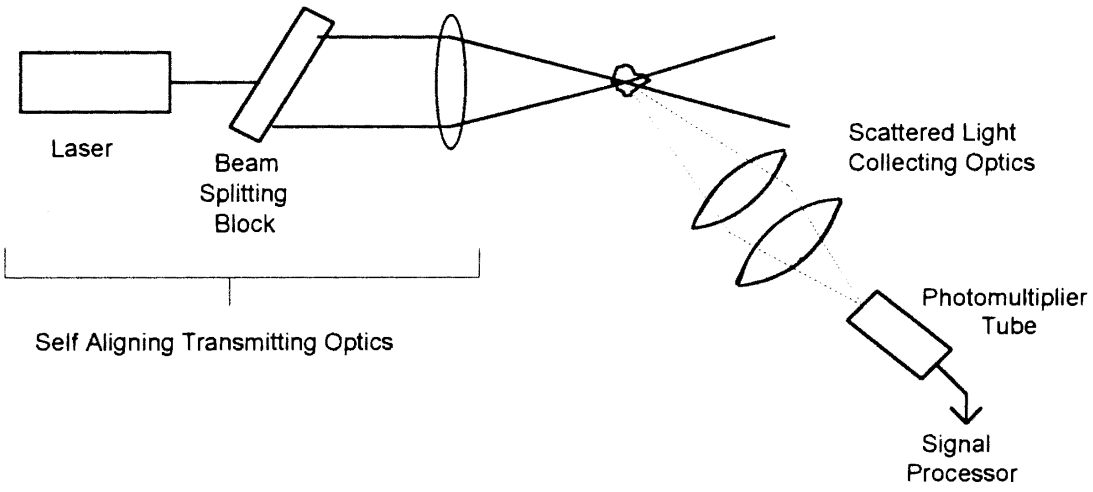

Figure 5. Optical Configuration Used by Farmer

Farmer [1972] observed the scattered signal from interference fringes and defined the ratio of ac to dc in the signal as the signal visibility V. V was fully equivalent to the Michelson visibility function [Farmer, 1972] and was defined as

$$V = (I_{smax} - I_{smin}) / (I_{smax} + I_{smin}), \quad (1)$$

where I_{smax} was the maximum scattered intensity from a bright fringe and I_{smin} was the corresponding minimum scattered intensity from the next consecutive dark fringe. V could be written as

$$V = (P_s^1) / (P_g^1), \tag{2}$$

where P_s^1 represented the ac signal power for a single scattering center as detected by the collection optics, and Pg^1 represented the dc signal power for a single scattering center. This process of obtaining the visibility for a particle is equivalent to centering a particle first on a bright fringe, then on the next consecutive dark fringe and calculating the respective amount of scattered intensity.

To determine the number density of particles in the probe volume, it was assumed that all scattering centers have the same velocity, although it had not been established that this was a necessary condition for the analysis. Farmer [1972] defined the n particle visibility function $\overline{V_n}$ as

$$\overline{V_n} = (\overline{P_s^n}) / (\overline{P_g^n}), \tag{3}$$

where $\overline{P_s^n}$ and $\overline{P_g^n}$ are the respective ac signal and dc signal powers for n particles. He further simplified the above equation so that it could be written as

$$\overline{V_n} = \overline{V} / \sqrt{n}, \tag{4}$$

where $\overline{V}$ is the ensemble averaged one particle visibility function for the size distribution of the n particles. Thus, n could be determined experimentally.

Tedjojuwono et al. [1984] proposed a dual beam, differential type laser Doppler velocimeter to measure the number density of homogeneous monodisperse particles. They used the variation in the visibility of the photodetector signal as a function of the crossing angle of the two beams to measure the particle number density.

In the two beam differential type laser Doppler velocimeter, a spatial fringe distribution is made by crossing two Gaussian laser beams of the same intensity. When a particle moves across this fringe distribution, light is scattered according to the rate of

dark-bright variations. When the scattered light is detected by a photodetector, the so called Doppler burst signal is obtained in its output as shown in Fig. 6 [Aerometrics, 1991]. From the photodetector signal, Tedjojuwono et al. [1984] obtained visibility of a particle as a function of the crossing angle of the two beams. They derived the particle separation information from measurements of the peak positions of photodetector signal visibility. Thus, the visibility function gave particle separation which is an inverse measure of the number density of particles.

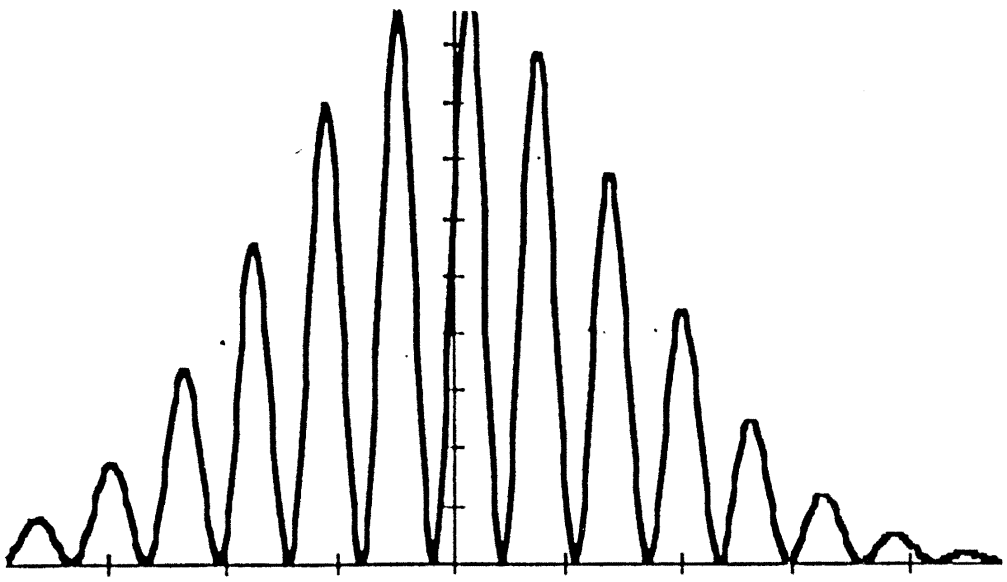

Figure 6. Example of a Doppler Signal [from: Aerometrics, 1991]

Initially, Tedjojuwono et al. [1984] attempted to use a half mirror and a pair of mirrors arrangement to vary the crossing angle of two beams. But that arrangement suffered from a lack of stability and was sensitive even to slightest vibration. Instead, they

used a stable arrangement with a Koster prism as shown in Fig. 7 [Tedjojuwono, 1984]. When the laser beam was passed through the Koster prism with an equilateral cross-section, it was divided into two parallel beams of equal intensity. After passing through the lens, the two parallel beams intersected at the focal point of the lens at an angle known as the crossing angle. Along the optical axis, the prism was precisely movable with a micrometer screw which automatically varied the separation of the two beams. A change in the separation resulted in varying the crossing angle of the two beams, and consequently, the fringe spacing.

Tedjojuwono et al. [1984] conducted a simple experiment by setting a large probe volume on a moving opaque screen with an equal separation pinhole array used as the sample object. Also they conducted an experiment using 1.1 micrometer (μm) diameter polystyrene particles as the microscopic objects. The particles were distributed uniformly in a transparent medium made of borax and polyvinyl alcohol, which was attached to a transparent glass disc. The glass disc was rotated by a motor. Measurements were made at a spot which gave a radial velocity of 0.24 m/sec.

Their method used the following two assumptions:

a) For microscopic particles under observation, the imaging system usually has a low depth of focus, so that the 3-D particle distribution was approximately treated as a 2-D distribution. In addition, the defocused image of particles becomes part of the background, so it could be neglected.

b) All of the particles were isotropic scatterers and had the same size, which was very small compared to the fringe spacing. Further, all of the particles were homogeneously distributed and were moving perpendicular to the fringes formed in the probe volume.

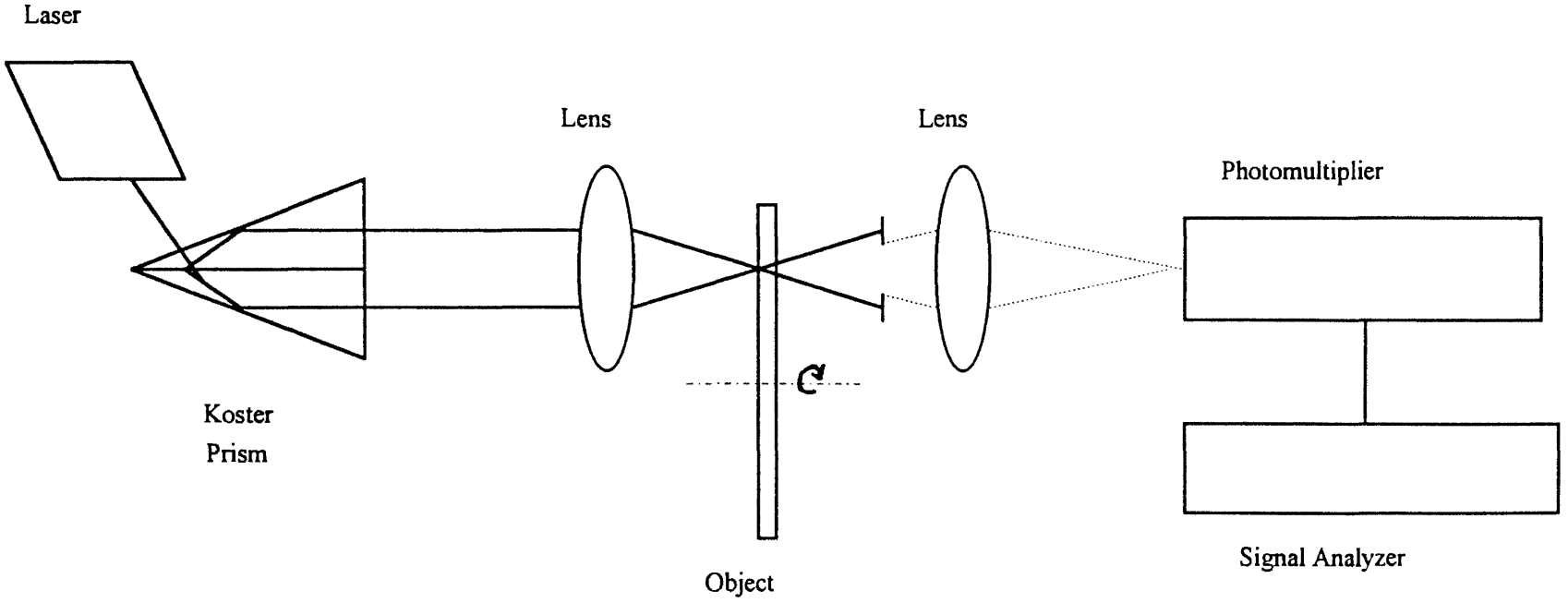

Figure 7. Optical Configuration Used by Tedjojuwono et al.

While using this method, care should be taken for the following two cases [Tedjojuwono, 1984]:

a) When the particle density is high, the second visibility peak may occur at a large crossing angle beyond the handling angle of the Koster prism. Then, the second peak of visibility cannot be seen.

b) For a large crossing angle, the condition that the particle size is small as compared to the fringe spacing may be violated. Then, the effect of particle size should be taken into consideration.

Spears and Robinson [1988] presented a method for experimentally determining the number density of particles which used fluctuations in the light scattering signal and an observation volume which could be varied experimentally. For a small number of particles in a laser focal volume ($N \leq 7$), they could simulate the effects of variable observation volume by direct calculations of scattered light intensity distributions. Both Gaussian and uniform laser intensities gave scattered light distributions which were sensitive to particle number. For narrow size distributions of particles (standard deviation $\sigma \leq 0.05$), the uniform laser intensity calculation gave structured light scattering distributions. Those could be used to infer particle number by simple comparison of distributions as a function of observation volume. For a large number of particles in the observation volume, they derived an equation to characterize the observed distribution of scattered light intensities. The equation included experimental fluctuations in detection as well as number density fluctuations. In that case, the experimental variation of observation volume and laser intensity gave a useful series of scattered light distributions. The scattered light distributions for each condition were characterized by a fluctuation factor, or normalized variance, and a simple polynomial equation related the series of observed fluctuation factors to the number density and experimental noise components. The method is independent of particle optical properties and shapes.

Spears and Robinson [1988] examined the distribution of the fluctuations for particle densities ranging from single particles to large numbers of particles in the laser excitation volume. It was observed that the shapes of the distributions were sensitive to the particle number for small numbers and small dispersions in size distribution. For large numbers of particles, a single parameter characterization of the distribution of detected signals sometimes could be used with a particular series of experimental measurements to define the number density in the presence of background noise fluctuations.

Spears and Robinson [1988] developed a complete expression for the observed signal, with reduction to predictions for large or small numbers of particles in the sample observation volume. The small number case could yield number densities by inspection of the light scattering distributions for various observation volumes. The case of large numbers of particles could be studied in the presence of background fluctuations by experimentally varying observation volume and laser power. They predicted a polynomial relation which could yield a good estimate of particle number density in optimum cases. The case of smaller particle numbers in the focal volume required a full analysis of each source of fluctuations to predict the final distributions. They could theoretically simulate experimental data for small numbers of particles in the observation volume with a mixture of analytical and Monte Carlo methods. They briefly compared the cases of uniform and Gaussian distributions of spatial laser intensities. Light scattering distributions observed with uniform laser intensity would have information on particle size distributions and particle number which could be analyzed by inspection when the size distribution was narrow ($\leq$5% standard deviation) and the particle number was small. Light scattering observed with Gaussian laser intensity would require simulation to derive size distribution data, and the distribution shape changes which signified number density changes would be less dramatic than for uniform laser intensity. For large numbers of particles, both types of laser intensity patterns could be used with experimental variations of laser observation volume and laser power to closely estimate the particle number density.

Wood and Samuelsen [1985] performed measurements on soot particulates in a turbulent, recirculating laboratory model combustor. They used a nonintrusive optical probe based on large angle intensity ratio scattering. Size range of the soot particulates were of 0.08 to 0.38 μm. Figure 8 [Wood and Samuelsen, 1985] shows the optical configuration which they employed. They used collection optics at 60 and 20 degrees off the optical axis. This enabled them to resolve particles as small as 0.08 μm. A 5-watt Argon-ion laser was used as the source of light. It was operated in the multiline mode. The laser lines were separated by a dispersion prism to resolve the blue line (488.0 nm). The beam was then focused to a 110 μm waist diameter using a focusing lens. The scattered intensity was detected at 60 and 20 degrees. The scattered light was focused to be detected by two photomultiplier tubes. The output signal from the photomultiplier tubes was passed into a logarithmic amplifier. The amplified signals were then fed to an intensity Ratio Processor (RP). The RP registered and processed the peaks of the two signals to binary numbers. The binary output was fed to a microcomputer which resolved that output into 62 bins. Each bin covered a definite size range, and hence, by knowing the counts in each bin, the size distribution was determined. The counts in each bin were divided by the time required to collect them, giving the count rate.

Count rate could be influenced by different parameters like the alignment and focusing of the two optical detectors and the signal processor thresholds. The interpretation of the measured intensity ratio was based on the analysis of the Mie scattering properties of a homogeneous, isotropic spherical particle. A special consideration therefore was given to soot particulates as they are nonspherical. Also, typically their index of refraction is not accurately measurable. Based on an earlier study by Hack et al. [1981], Wood and Samuelsen [1985] concluded that the combined error was 20-30% with some broadening of the distribution.

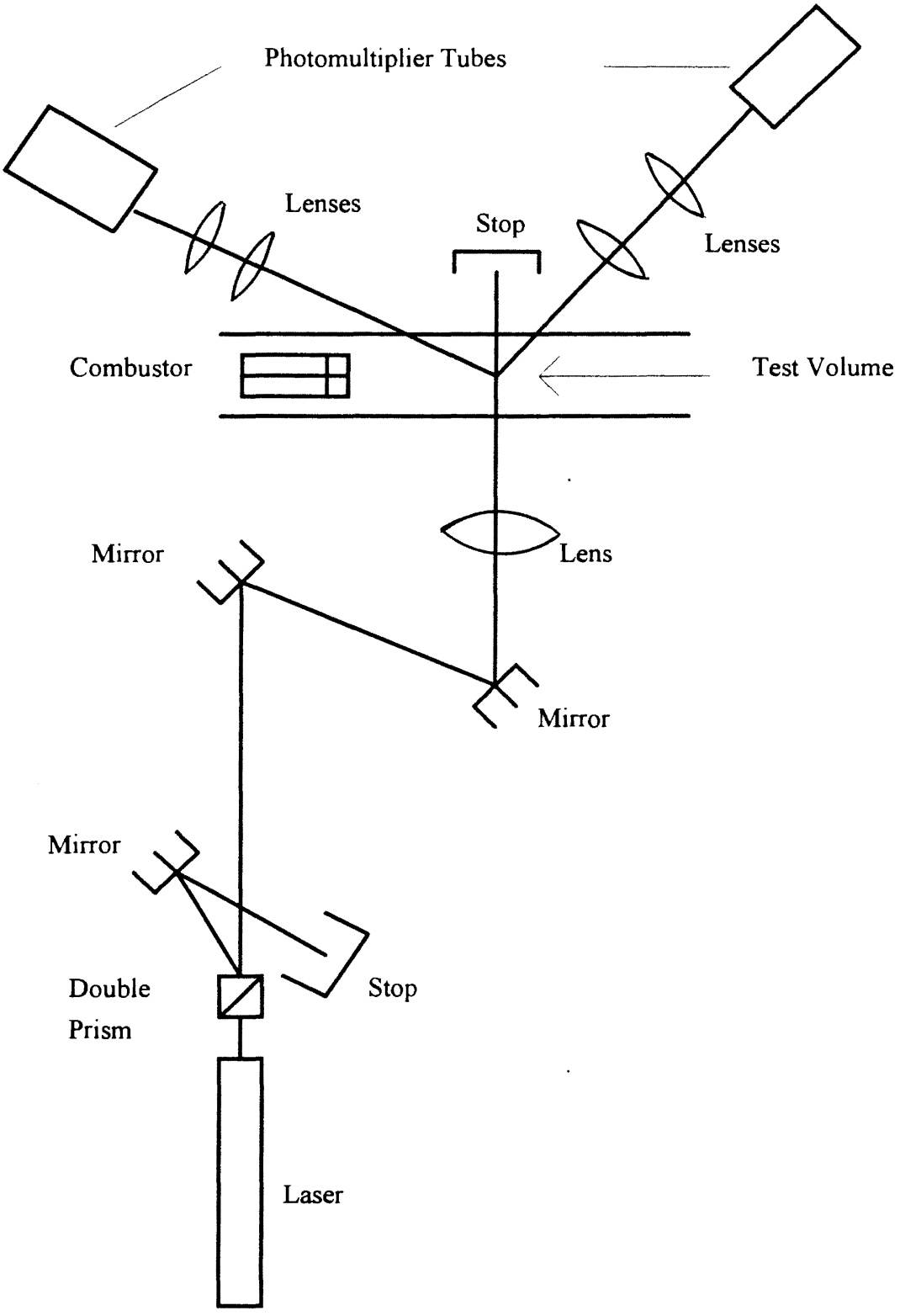

Figure 8. Optical Configuration Used by Wood and Samuelsen

Ahlers and Alexander [1985] developed a microcomputer based digital image processing system. That system could count and size small particle images generated by laser. They counted and sized particles in the range of 7 to 700 μm in the plane of focus and achieved processing rates of 5 to 600 frames per minute by using a real time image processor. They dealt with measuring static images in the plane of focus, for example, calibration reticles and particles placed between glass microscope slides.

Figure 9 [Ahlers and Alexander, 1985] shows a block diagram of the laser imaging system they used to generate the particle images. The test section that contained the particles was illuminated by a pulsed nitrogen laser. The beam was focused on an ultraviolet sensitive vidicon tube using a diffraction limited plano-convex lens. The camera and laser were synchronized, and the standard composite video was routed through a time/date generator before being passed to the image processing system. A real time image processor was used to digitize and store the video images, and a suitable host for the image processor was used. Ahlers and Alexander [1985] developed a pattern recognition scheme that was able to count and size images. It was based on the assumption that the video would consist of dark particle shadows on a light background. Further, the particles could be of any shape and could contain interior voids but should be continuous. They used a line segmentation technique to identify and measure the particle images. The particle diameters were then grouped into size ranges and summed over as many frames as needed. They carried out an extensive calibration process to make sure that results obtained were accurate and repeatable.

Ahlers and Alexander [1985] found that the best case calibration reticle data indicated less than 1% error for 25 to 100 μm particles and actual benchmark tests showed approximately a 3% error for 52.8 μm micro spheres. However, for sizes smaller than 25 μm, the accuracy was not found to be very good. In fact, below 10 μm, errors of ±10% could be expected. The limitation was due to system resolution and diffraction problems.

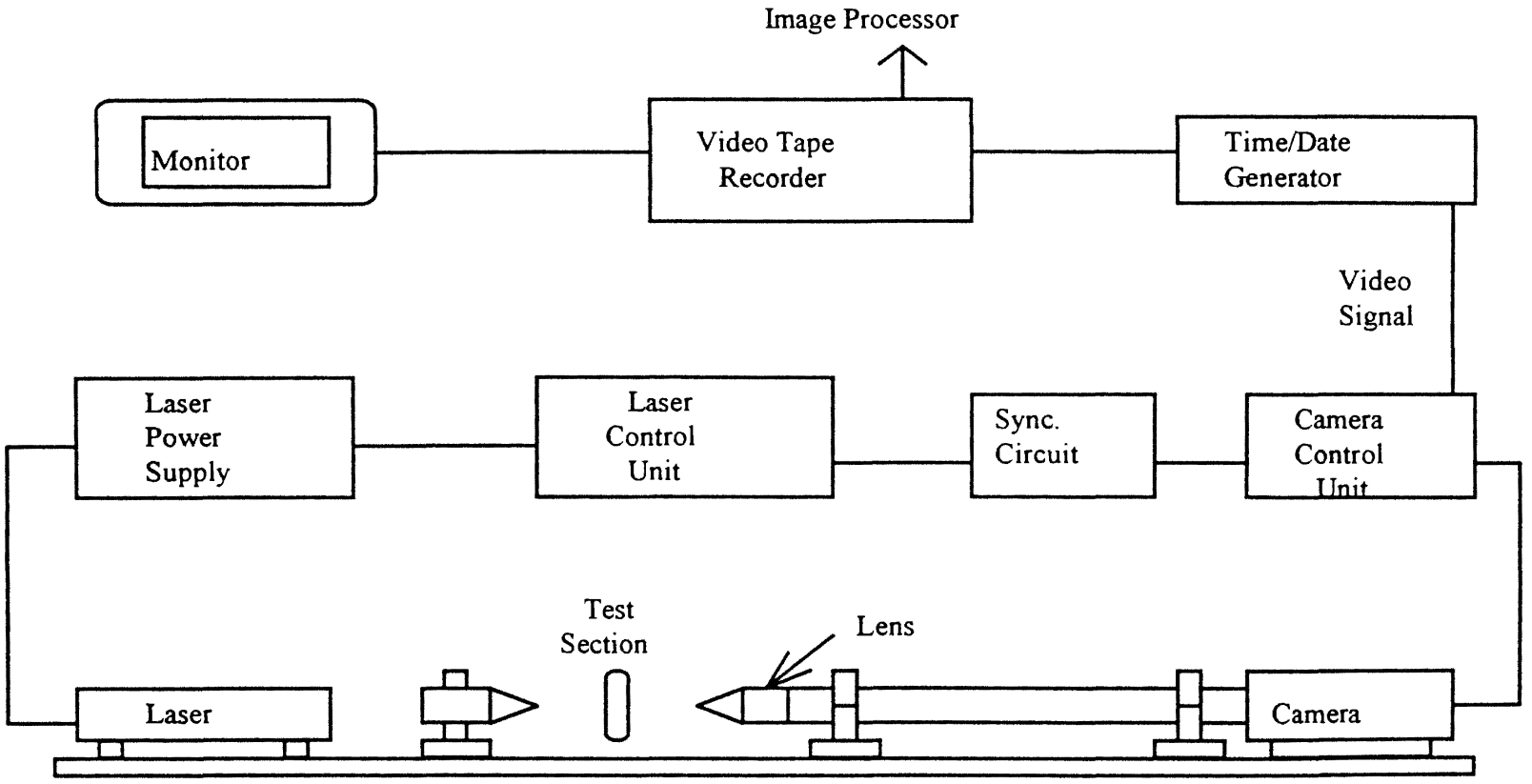

Figure 9. Block Diagram of Laser Imaging System

For sizing and counting particles larger than 0.1 μm, various optical particle counters are available. Particles smaller than 0.1 μm are generally counted with a condensation nucleus counter (CNC), and their sizing is done by combining the particle detection capabilities of a CNC with a particle size discrimination of a diffusion battery [Wu et al., 1989]. Such small submicron particles on wafers represent a major contamination problem in the microelectronics industry. A diffusion battery has an inlet for the sample air supply at one end and it is connected to a vacuum chamber at the other end. It has a number of parallel flow paths through a tiny channel. Brownian motion causes losses to the channel walls which are a function of particle diffusivity, channel dimensions and geometry and gas flow rate [Wu et al., 1989]. A diffusion battery can be used to determine diffusivity distributions which in turn are needed for particle size distributions. To determine diffusivity distributions, penetrated particle concentration is obtained first by using a CNC at distances along the flow paths. Figure 10 [Wu et al., 1989] shows a particle sampling configuration. A switching valve was used to connect the ports to the CNC. The concentrations at various ports were measured and converted to penetration values and then analyzed to obtain particle size distributions.

In this present work, a dual beam laser Doppler velocimeter was employed. The measurements obtained from the laser Doppler velocimeter were used in conjunction with the 'swept volume technique' to calculate particle number density. This is discussed in detail in Chapter III. This method is a single particle type optical method based on light scattering. It is similar to the methods of Farmer [1972] and Tedjojuwono et al. [1984] with regard to the employment of laser Doppler velocimetry. However, the technique is different. Whereas Farmer [1972] and Tedjojuwono et al. [1984] used visibility information, this method makes use of particle velocity information to obtain particle number density. This method, unlike those of Farmer [1972] and Tedjojuwono et al. [1984], does not assume that particles cross the interference fringes in the probe volume perpendicularly with a mean velocity. It does not have restrictions, such as, the particles

should be homogeneously distributed, of the same size, and smaller than the fringe spacing. These limitations greatly reduced the application of the method from Tedjojuwono et al. [1984].

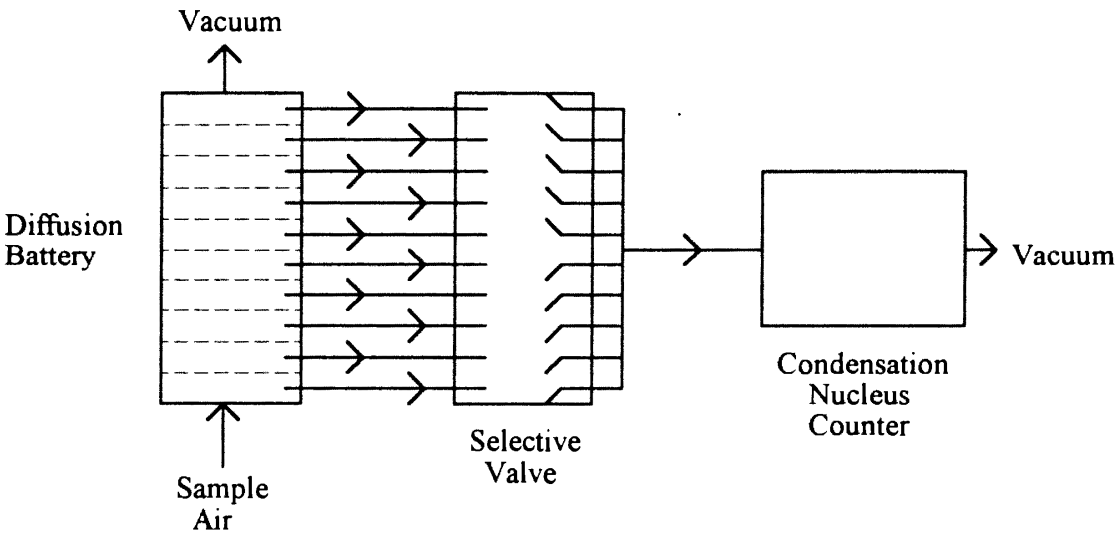

Figure 10. A Particle Sampling Configuration Using Diffusion Battery

However, the method employed in the present work has one inherent limitation. A very good signal is generated for a particle which is well within, or fully 'contained' in the probe volume. But for a particle which is partially in the probe volume, the signal generated may not be strong enough to be identified as a particle count. In that case, the only possibility left for the weak signal is to be considered as noise even though it was from a particle. This imposes a limitation on the size of particles that can be counted successfully by the present method. The particles should be sufficiently smaller than the probe volume so that, when detected, they are well within the probe volume. Further

research is required to know the exact allowable particle size. This kind of particle size limitation is associated with all of the methods discussed above. The present method does not allow the simultaneous presence of more than one particle in the probe volume as opposed to the method employed by Spears and Robinson [1988]. Therefore, this method is unsuitable for measurements involving very high particle concentrations. However, it is extremely simple and does not require complex analysis of the data. The dual beam laser Doppler velocimeter employed provided directional sensitivity to velocity measurements which was missing in the single beam method employed by Holve [1982].

The complete experimental setup and the laser Doppler velocimeter system employed for this present work is described in Chapter III. The laser Doppler velocimeter which was employed was not a completely automated system. It required a number of parameters and variables to be specified by the user through the controlling software. This is discussed in detail in Chapter III. In order to obtain accurate measurements, a thorough understanding of those governing parameters was required. A series of tests pertaining to 'sensitivity analysis' were performed, so as to enhance the understanding of those parameters with regard to their effect on the measurements. This is discussed in detail in Chapter IV. Also some other preliminary experiments were conducted to investigate the validity of the swept volume particle counting technique, to evaluate the laser Doppler velocimeter system with regard to data reproducibility, and to understand the effect of laser power on the measurements. This is explained in Chapter IV.

Initially, the traverse table for the transceiver of the laser Doppler velocimeter system employed was manually controlled. Later on, the traverse table was completely automated, with two-dimensional computer control, by this author. This is discussed in detail in Appendix B. Completely computer controlled automated traversing enabled movement of the probe volume conveniently, precisely and speedily to any desired location.

Once a fair degree of confidence was achieved, with regard to the swept volume counting technique, the laser Doppler velocimeter and the experimental setup, measurements were taken using several automotive air filters with model number AF 3192. All of the measurements involved in this work were conducted at a flow rate of 125 (±3%) cubic feet per minute (cfm). Measurements were taken in four different planes (6.625, 3.625, 2.125 and 0.625 in.) above the face of the filter. Particle number density distributions and their time history were obtained and analyzed. This is discussed in detail in Chapter IV.

CHAPTER III

THEORY AND EXPERIMENTAL SETUP

A laser Doppler velocimeter works on the principle of light scattering. A particle is illuminated by a coherent and monochromatic laser beam and the light scattered by it is detected by a photodetector. Two beams, almost of the same intensity, when crossed produce alternate dark and bright bands or fringes due to the phenomenon of interference as shown in Fig. 11. The volume where the two beams are crossed is called the probe volume. When a particle crosses the alternate dark and bright fringes and the light scattered by it is detected by a photodetector, a Doppler burst signal is produced as shown in Fig. 6. This signal is processed so as to obtain useful information about particle speed, flow, turbulence, etc. The Doppler burst signal, however, will not be produced if the particle is stationary. Therefore, the two beams used to produce interference fringes are made to differ slightly from each other in their frequencies. This is known as frequency shifting. Then they produce interference fringes which are not stationary but move, and hence, even a stationary particle produces the burst signal and is detected. Also the direction of the particle speed is obtained by employing frequency shifting. It is worthwhile to mention that laser Doppler velocimetry is non-intrusive, allowing measurements even in small and restricted flow passages without altering the flow. The only necessary prerequisite for applying laser Doppler velocimetry is that there should be optical access to the flow in the region where measurements are to be obtained.

The laser Doppler velocimeter which was employed uses two sets of beams. One of them operates in the horizontal plane while the other operates in the vertical plane. Therefore, the probe volume is actually obtained by simultaneously crossing four beams.

As shown in Fig. 12, the probe volume looks like an ellipsoid and has two different cross-sectional areas for measurement, one in the horizontal and one in the vertical plane. The advantage of using a dual beam laser Doppler velocimeter is that both of the velocity components, the horizontal and the vertical, of the particle can be obtained.

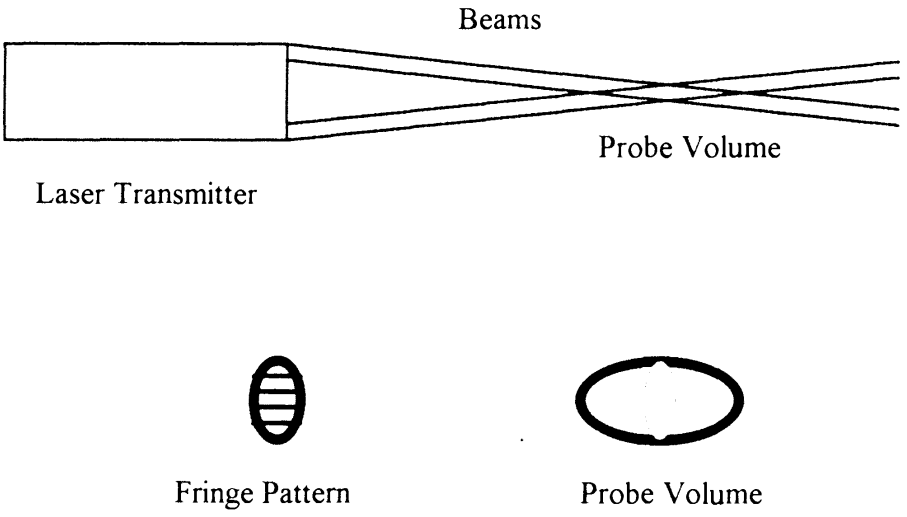

Figure 11. Laser Probe Volume and Fringe Pattern

The literature review revealed that, for particle counting, the easiest and in fact, the most convenient method was to somehow use particle velocity information in conjunction with other available information. My colleague, Mr. F. Liang [1993], suggested a possible method. We used a fairly simple and straightforward technique: the swept volume technique. As evident from the name, this technique was based on the volume effectively swept by the particles passing through the cross-sectional area of probe volume per unit time (Fig. 13). This swept volume was calculated by using the cross-

sectional area of the probe volume, the mean velocity of the particles and the time required to sweep this volume. The cross-sectional area of the probe volume was obtained by using the optical parameters of our system as explained below.

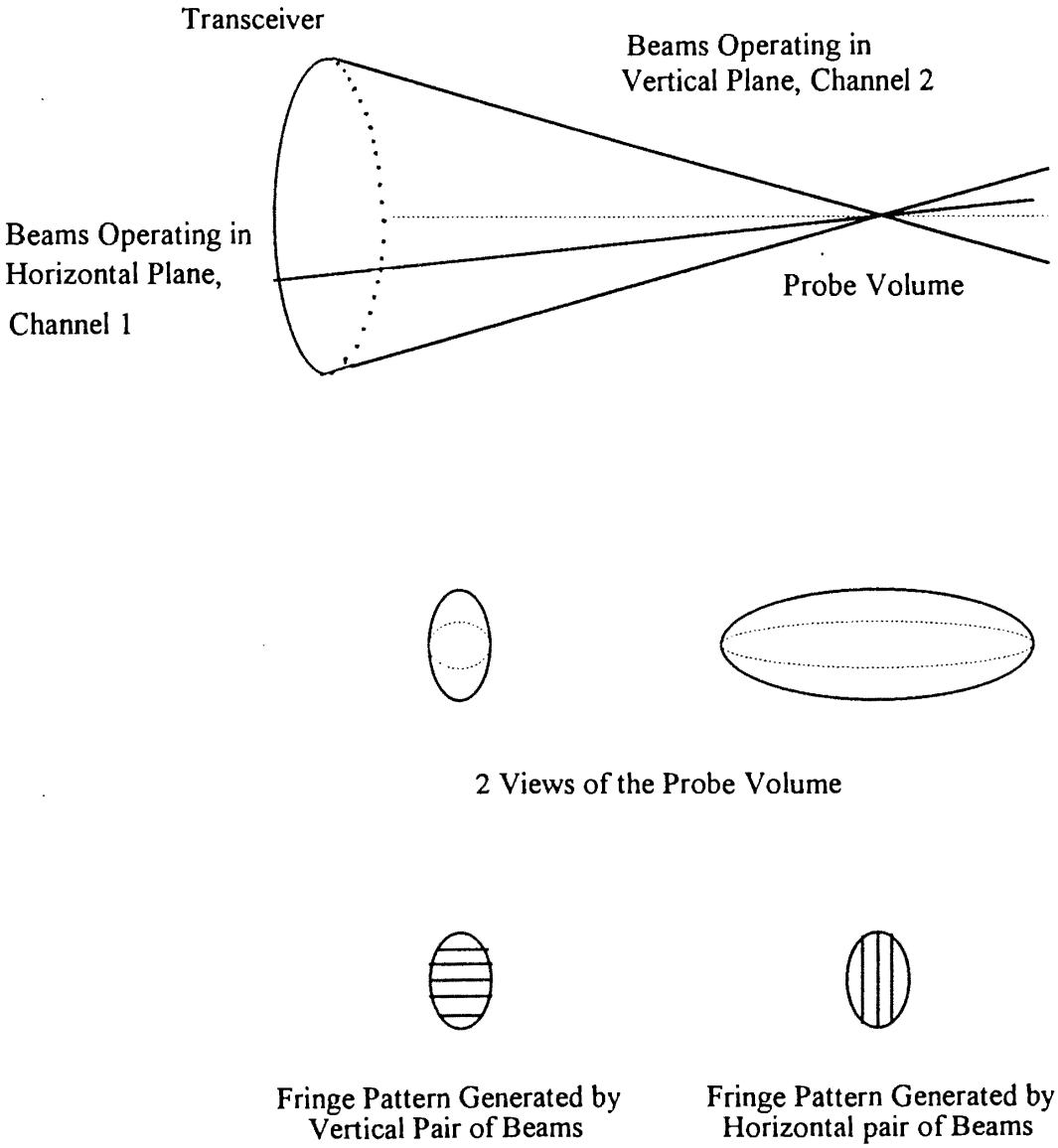

Figure 12. Probe Volume and Fringe Patterns for the LDV System Employed

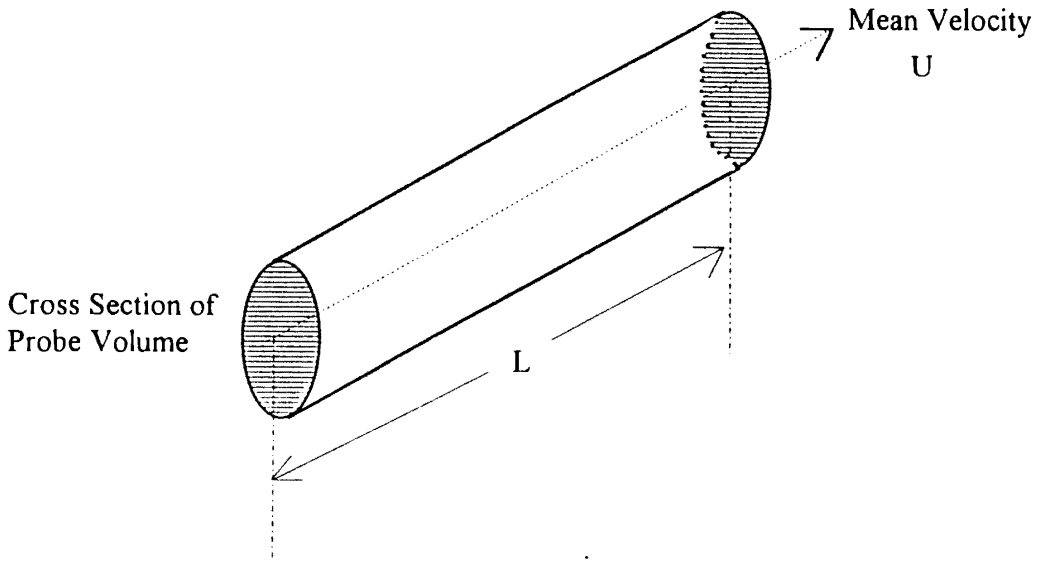

Figure 13. Swept Volume

Shown in Fig. 14 is the beam focusing angle α, which was obtained by simple trigonometry as

$$\alpha = 2 \tan^{-1}(d /2f) \quad (5)$$

where d and f are the diameter and focal length of the collimating lens respectively.

Figure 14 also shows a three-dimensional view of the probe volume. The radius at the beam waist is represented by c. Again, by using simple trigonometry, the other two dimensions, a and b, are obtained as

$$b = c / \cos (\alpha/2) \quad (6)$$

$$a = c / \sin (\alpha/2) \quad (7)$$

For our system, α is equal to 10.32 degrees, and c, b and a were 33.00, 33.13 and 367 μm, respectively.

Probe cross-sectional areas in the horizontal and vertical planes were obtained as

$$A_h = \pi ac \quad (8)$$

$$A_v = \pi ab \quad (9)$$

where A_h and A_v are the probe cross-sectional areas in the horizontal and vertical planes, respectively. Since c and b were approximately equal, these two cross-sectional areas were assumed to be the same.

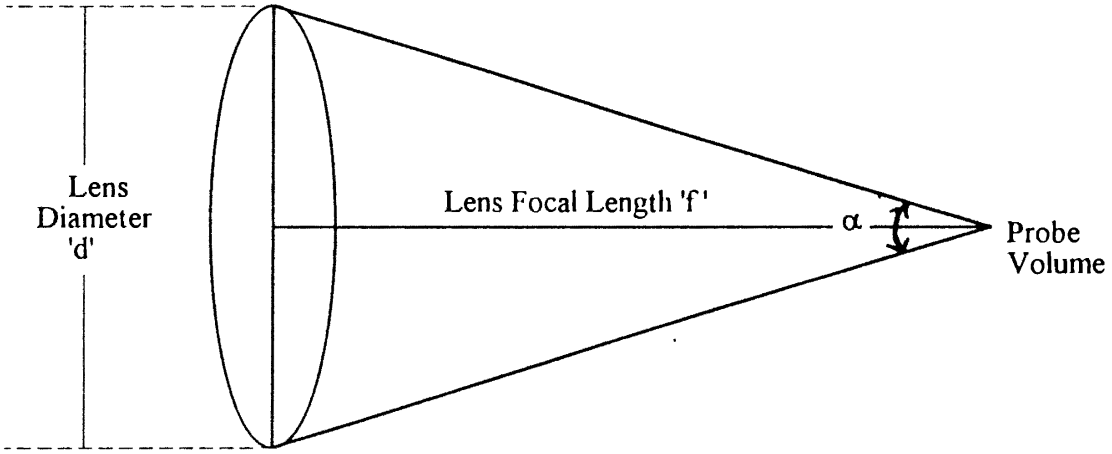

Focusing Geometry

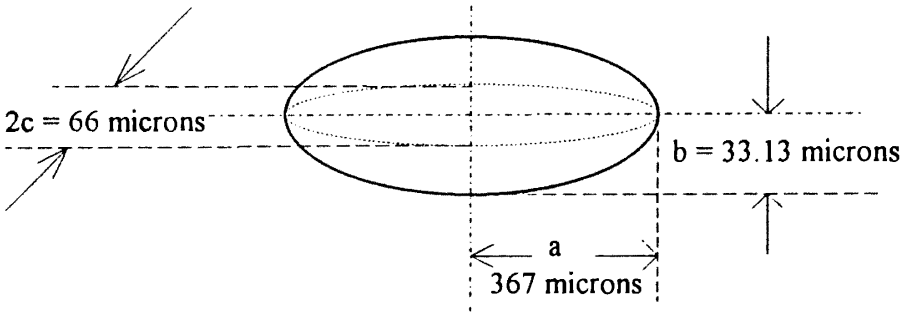

Probe Volume Geometry

Figure 14. Focusing and Probe Volume Geometries

The LDV system requires a number of parameters and variables to be specified through the software. This will be discussed later in this chapter. The system is customized only for velocity measurements, and it discriminates between a 'good' and a 'bad' signal depending upon the setting of these parameters and variables. No signal is obtained when there is no seeding. A 'good' signal is a signal which is validated by the operating parameter settings. Only the 'good' signals are processed and analyzed by the system for velocity, while the rest of the signals which are 'bad' are rejected. The rejected signals which are 'bad' for velocity measurements are nevertheless important as they may also be generated from particles in the probe volume. Therefore, for the calculation of particle number density, even the rejected signals are counted. Thus, besides the mean velocity and the sampling time, the number of signals or counts detected in the probe volume during that interval (sampling time) were obtained from LDV system measurements. Then, particle number density was calculated as follows:

$$V = L A = (U T_S) A \tag{10}$$

$$D = N / V \tag{11}$$

where V is the swept volume, A is the cross-sectional area of the probe volume, U is the mean velocity, T_S is the sampling time, N is the number of the signals detected or particle counts, and D is the particle number density.

The other possible method for obtaining number density was to obtain and analyze information pertaining to transit times of the particles. Transit time is the measured time for which a particle is within the probe volume. If the ratio of the 'sum of the time' that there is any particle detected in the probe volume to the total run time is obtained, then, this ratio divided by the probe volume is a measure of the number density. It is important to note that the term 'sum of the time' implicitly involves 'particle number' because this 'sum of time' is obtained by summing transit times of individual particles. This method requires complex analysis of the signal. However, the swept volume technique was much simpler to employ, and hence only that technique was explored and implemented.

Figure 15 [Liang, 1993] shows the experimental setup that was employed. A laser Doppler velocimeter system from Aerometrics, Inc. was used. The following is the list of the components of the system as labeled in Fig. 15. More information about the components with regard to the manufacturer and model number is given in Appendix A.

1. A 4 watt Argon ion laser from Coherent, Inc.
2. Remote control for the laser.
3. Fiber drive.
4. Bragg cell.
5. Photomultiplier tubes (two).
6. Doppler signal analyzer (DSA).
7. Oscilloscope.
8. IBM compatible 80486 computer and monitor.
9. Laser transceiver.
10. Automated traverse system.
11. Test housing.
12. Test filter.
13. Ultrasonic humidifier.
14. Blower.
15. TSI mass flow sensor.

The multi-line or non-monochromatic laser beam produced by the laser (1) was taken to the fiber drive (3) through successive reflection by the two mirrors. The laser could be fully controlled by the remote control (2).

The fiber drive provided beam splitting, frequency shifting and color separation. It incorporated a Bragg cell (4) which split the incoming beam into two beams of equal intensity. One beam was recognized as the zeroeth order beam and the other one as the first order beam. The Bragg cell also produced the frequency shift. The zeroeth order beam was not shifted in frequency, while the first order beam was shifted by 40 MHz.

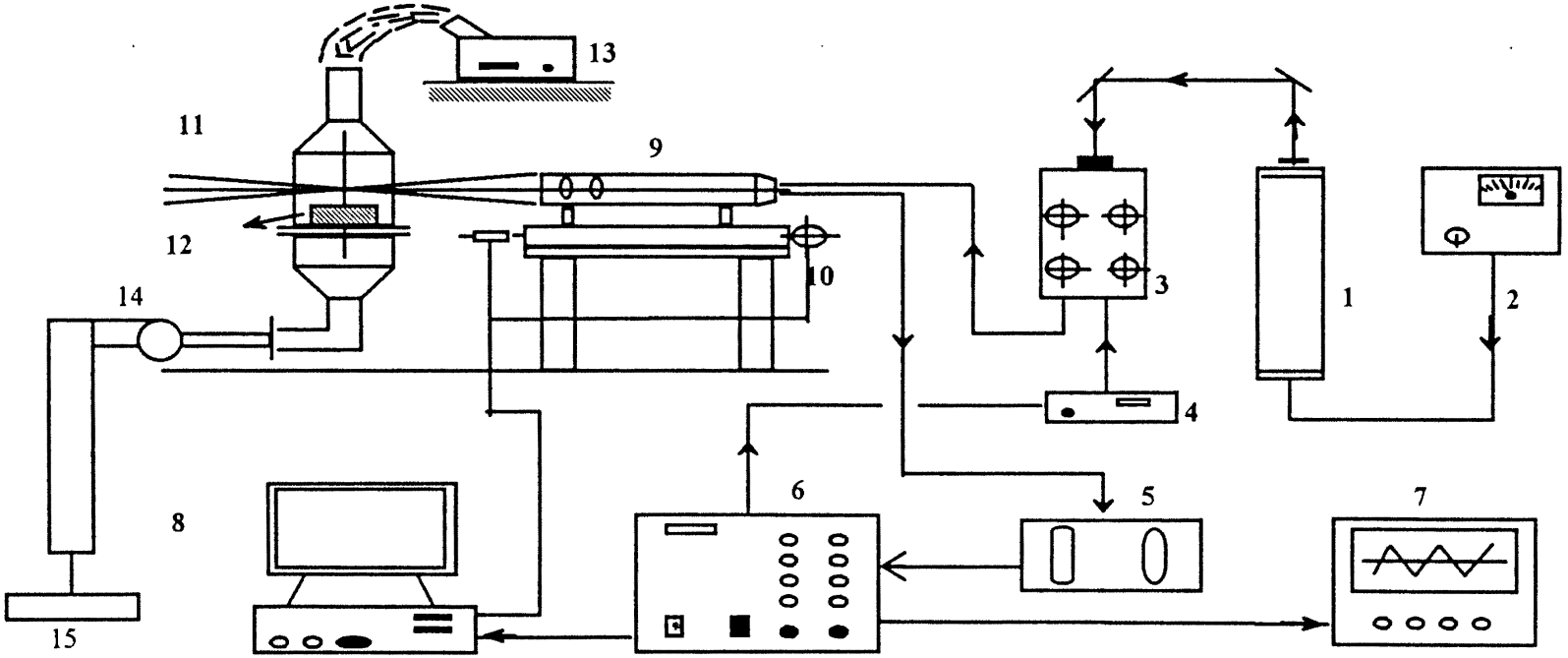

1. A 4 watt Argon ion laser from Coherent, Inc.
2. Remote control for the laser
3. Fiber drive
4. Bragg cell
5. Photomultiplier tubes (two)
6. Doppler signal analyzer
7. Oscilloscope
8. Computer and Monitor
9. Laser transceiver
10. Automated Traverse System
11. Test Housing
12. Test Filter
13. Ultrasonic Humidifier
14. Blower
15. TSI mass flow sensor

Figure 15. Experimental Setup

This 40 MHz modulating frequency was received by the Doppler Signal Analyzer (6). Two dispersion prisms were used to separate the beams into individual colors. Blue and green beams of the respective wavelengths, 0.4880 and 0.5145 μm, were thus produced. Therefore, from the fiber drive, four beams were obtained, two of each color. Out of the two beams of the same color, one was shifted and the other was unshifted in frequency. As explained earlier in this chapter, this was done to produce a moving fringe pattern.

The four beams from the fiber drive were taken to the transceiver (9) through optical cables. The transceiver performed two tasks, transmitting light and receiving the scattered light; and hence the name. It focused all of the four beams to generate the probe volume, and using the principle of back scattering, it received the scattered light from the particles in the probe volume.

The transceiver was supported on a completely automated, two-dimensional, computer controlled traverse table (10). As mentioned before, the traverse table was initially manually controlled, and it was automated later on by this author. This is discussed in detail in Appendix B.

The collected light from the transceiver was amplified by the photomultiplier tubes and was detected by the photodetector (5). The Doppler burst signal generated by the photodetector was taken to the Doppler signal analyzer which was the core of the entire system. It did all of the signal processing and controlled the system. The manual for the Doppler signal analyzer [Aerometrics, 1991] describes this in great detail. However, in this paragraph, I have tried to reiterate only the most relevant information. The Doppler Signal Analyzer uses high speed (maximum speed of 160 mega-Hertz) analog-to-digital converters with one bit resolution to record the signal. A Discrete Fourier Transform is used with the Fast Fourier Transform to determine the frequency of the signal. A Doppler burst signal consists of a sine wave or waves superimposed on a Gaussian envelope with a pedestal as shown in Fig. 6 [Aerometrics, 1991]. The signal is passed through a high pass filter to remove the pedestal component. This leaves a symmetric signal. A burst

detection scheme is then used to locate the burst signal which is recorded digitally and stored in memory. A square wave of the same frequency (or frequencies) as the original signal is generated by an analog-to-digital converter. Then the discrete Fourier transform is applied to determine the frequency (or frequencies) of the signal which in turn is inverted to yield the velocity. Applying the Discrete Fourier Transform is equivalent to multiplying the sampled wave by sine waves with N different frequencies. When the sampled data and sine wave have similar frequencies, the product will be large which appears as a maximum power in the frequency domain. Figure 16 [Aerometrics, 1991] shows the above method schematically.

The DSA was, in turn, controlled by the DSA software which was loaded on the 486-33 IBM compatible computer (item 8 of Fig. 15). The DSA also provided output for the oscilloscope (7). The oscilloscope was indispensable as it helped in observing the signal and setting of some software parameters.

The automotive test filter (12) was mounted in the plexiglas test housing (11). The plexiglas test housing is a full sized model of the SAE Panel Filter Universal Test Housing. Figure 17 shows details of the SAE Panel Filter Universal Test Housing [SAE, 1987]. The plexiglas model differs from the SAE test housing configuration in only one way. It does not have a 90 degree bend in its exit pipe. However, this difference was believed not to have any significant effect on the flowfield. The test housing was inverted so as to avoid increasing the height of the laser transceiver which would have been very inconvenient for taking the data. The plexiglas test housing was supported on a stand which provided manually adjustable vertical positioning of the housing with respect to the transceiver. Exact alignment of the test housing with respect to the transceiver was done by focusing all four colored laser beams on the centers of opposite sides of the housing. The centers were geometrically located and then marked with washable transparency pens.

A blower (item 14 of Fig. 15) was connected to the bottom of the test housing to pull air through the filter and hence to produce the flow. A TSI model 2012 mass flow

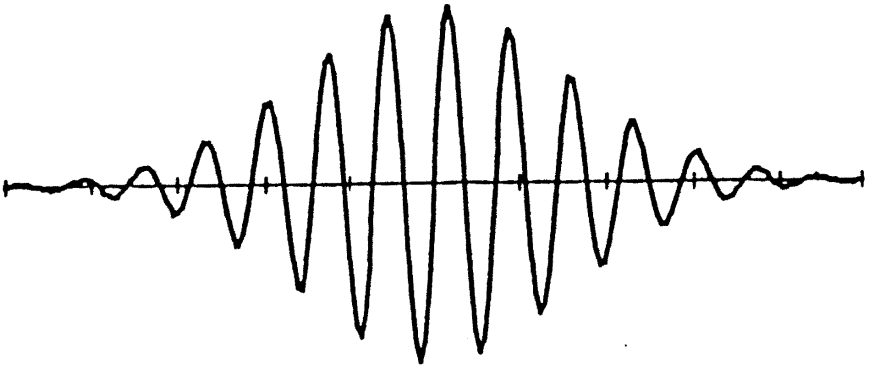

High Pass Filtered Signal

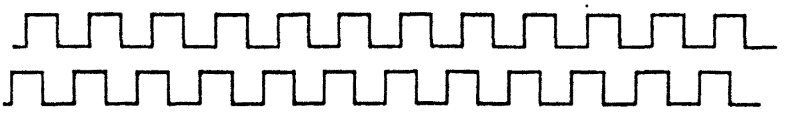

Square Wave Generated by Analog to Digital Converter

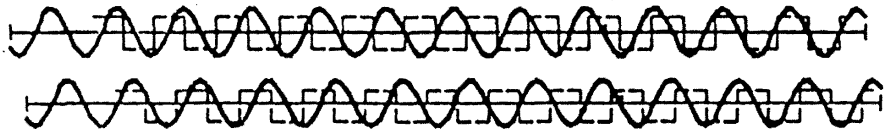

Applying Discrete Fourier Transform

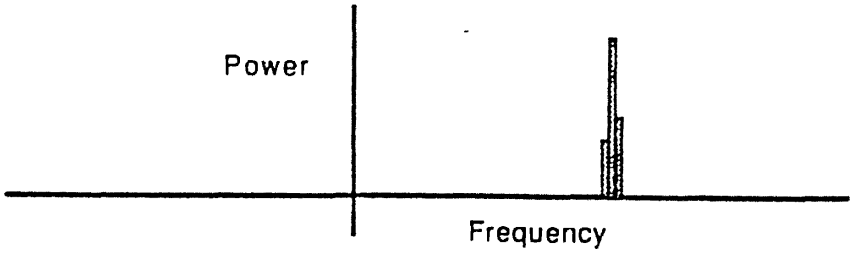

Power v/s Frequency Domain

Figure 16. Schematic of the Discrete Fourier Transform Method
[from: Aerometrics, 1991]

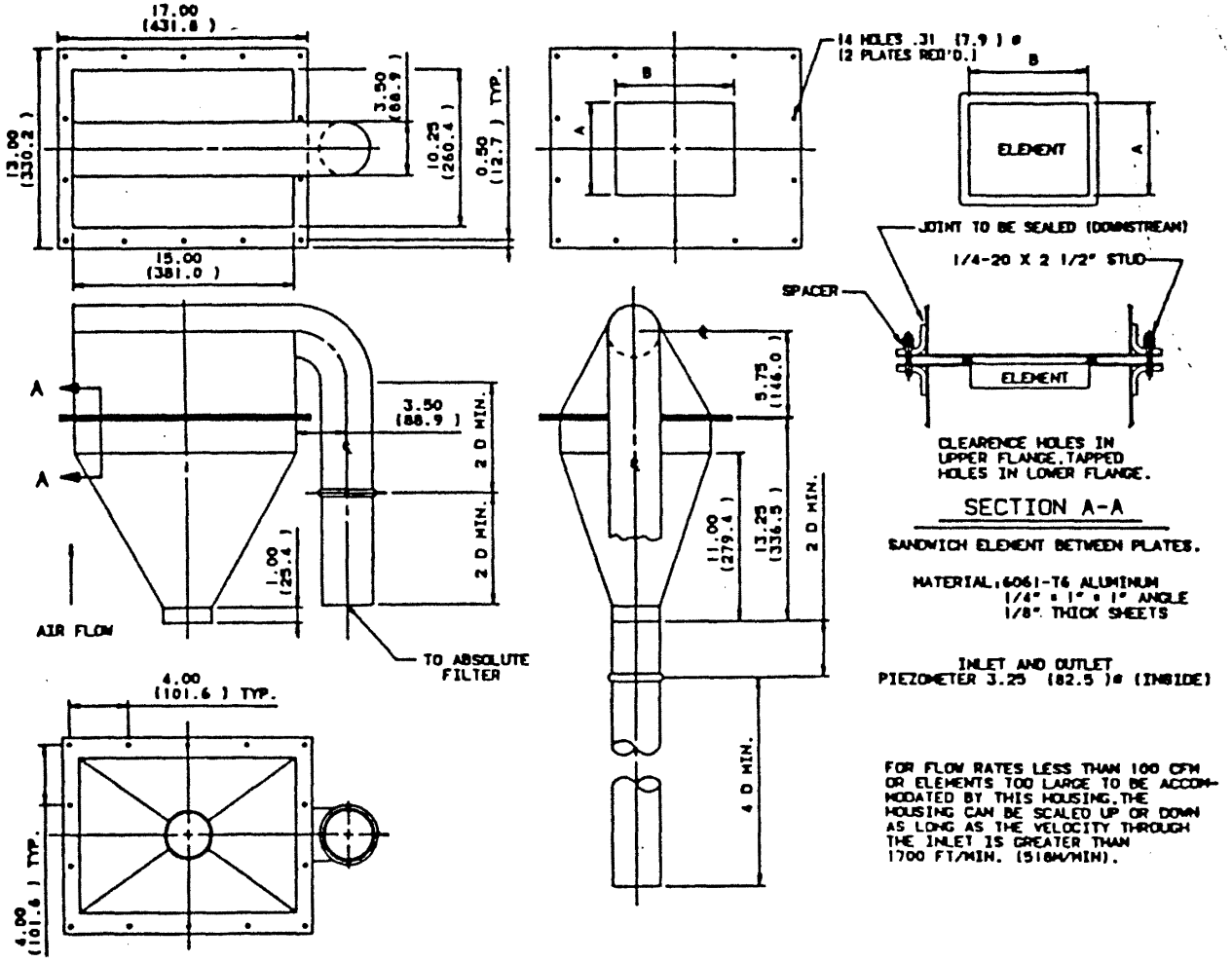

Figure 17. SAE Panel Filter Universal Test Housing [from SAE, 1987].

sensor (15) was used to measure volumetric air flow rate over the range from 0 to 500 scfm (±3%).

An ultrasonic humidifier (13) operating with distilled water was used to produce water particles which were used as seeding particles for the test. As will be explained in Chapter IV, observations were made so as to obtain an idea of the approximate sizes of the water particles generated by the humidifier. The humidifier produced water particles in a wide range, from 5 to 100 microns in diameter, with most of the particles of about 10 to 30 microns in diameter. The refractive index of water droplets is different from that of air, and hence, they reflect light well enough so that the light can be detected by the collecting optics and then processed. Moreover, water particles are safe for breathing as opposed to other seeding particles like latex particles which are deleterious if inhaled in large quantities.

The above described were the details of the swept volume counting technique and the experimental setup that were employed for this present work.

CHAPTER IV

RESULTS AND ANALYSIS

Sensitivity Measurements

As mentioned before, the laser Doppler velocimeter which was employed was not a completely automated system. There were a number of parameters and variables which were to be specified by the software so as to obtain accurate measurements. Those parameters, some of which were interrelated, required a suitable setting or assignment of values depending mainly upon the frequency of the Doppler burst, which in turn, depended upon the magnitude of the flow velocity. The setting of those governing parameters required a very good understanding of the manner in which the DSA worked. Detailed experiments were conducted to understand the effect of those parameters on the measurements obtained. The complete experimental setup has already been described in Chapter III. Measurements for the following sensitivity analysis were made at the center, and at a plane 0.625 in. above the face of the filter AF-3192, with a flow rate of 125 cfm and laser power of 3.5 watts. Repeatability of an individual measurement will be discussed later in this chapter under the section 'Data Reproducibility Measurements'.

Figure 18 shows an example of the variable setup for obtaining a typical measurement. As explained in Chapter III, the laser Doppler velocimeter system that was employed measured two components of the particle velocity, and therefore, variables were to be set for two channels. Channel 2 measured the major and the vertical component of the velocity, while channel 1 measured the minor and the horizontal component of the velocity (Fig. 12, Chapter III).

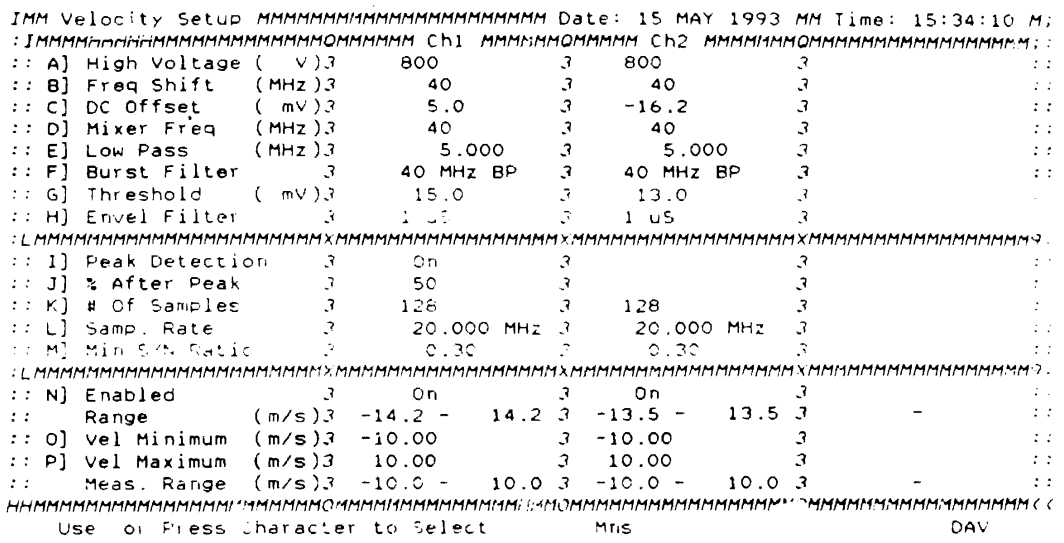

Figure 18. A Typical Variable Setup Employed

The variable 'high voltage' was used to set the photomultiplier tube operating voltage and was fixed at 800 Volts for all of the measurements. The variable 'frequency shift' was used to set shift frequency as explained in Chapter III, and was fixed at the frequency of the Brag cell (40 MHz). 'DC offset' was used to adjust the raw signal to a common ground level by monitoring the raw signal on the oscilloscope. 'Mixer frequency' was used for setting the frequency of the DSA mixer, and it was fixed at the Brag cell shift frequency (40 MHz).

'Low pass' was used to set low pass filter of the DSA so as to limit the high frequency noise band and to remove the upper side band of the mixed signal that was obtained from the mixer. Figure 19 shows the dependence of number density and velocity on the low pass filter setting for channel 2. From the figure, it is evident that the velocity does not vary much with the low pass filter setting. However, the number density may

vary by as much as 27 percent, from one low pass filter setting to another. For the present work, the low pass filter for channel 2 was mostly set at 5 MHz. Figure 20 shows the dependence of number density and velocity on the low pass filter setting for channel 1. From the figure, velocity and number density variations of about 7 and 15 percent, respectively, are observed. The low pass filter for channel 1 was also typically set at 5 MHz for the measurements involved in this present work.

The variable 'burst filter' was used to select a suitable burst filter that removed the high frequency noise before the signal reached the burst detector. Figure 21 shows the dependence of number density and velocity on the burst filter setting for channel 2. No data was obtained for 'all pass' and 10 MHz low pass settings. The velocity and number density showed variations as high as 26 and 81 percent, respectively, from one burst filter setting to another. Figure 22 shows the variation of number density and velocity on the burst filter setting for channel 1. The velocity is fairly constant with a maximum variation of 3 percent while the number density shows a variation as high as 900 percent. It was recommended by the DSA manual [Aerometrics, 1991], that for a velocity range of ±15 m/s, the 40 MHz band pass filter should be used. Since all of the velocities (3 to 8 m/s) involved in this work were well within this range, the 40 MHz band pass filter was used for all of the measurements.

The variable 'threshold' corresponds to the amplitude at which the burst signal would trigger. If set at a high value, only large particle bursts would be analyzed, and if set at a low value, it would allow the background noise to trigger the burst detector too often. It was adjusted by observing the raw and the burst detector signal on the oscilloscope, keeping the detector on (or up) for periods corresponding to the burst lengths.

Figure 23 shows the dependence of number density and velocity on the threshold setting for channel 2. A maximum variation of 25 percent is observed in the velocity. However, the velocities corresponding to the threshold settings of 0 and 5 mV are

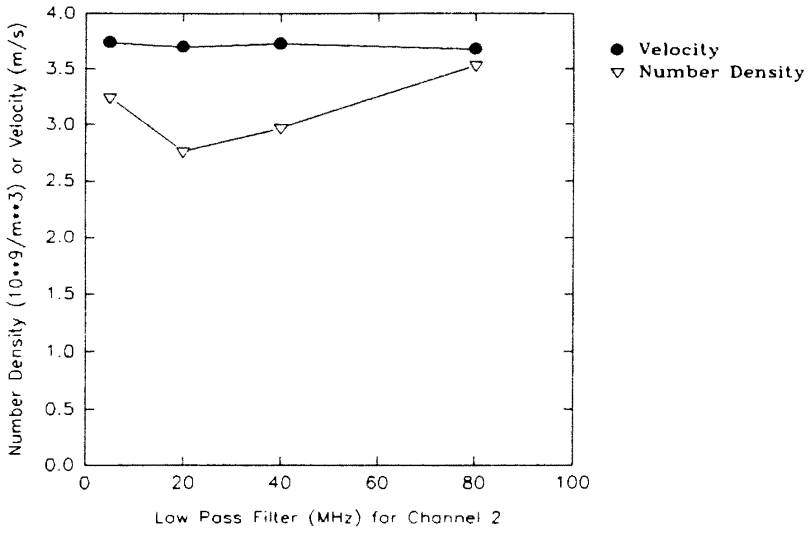

Figure 19. Dependence of Number Density and Velocity on Low Pass Filter for Channel 2

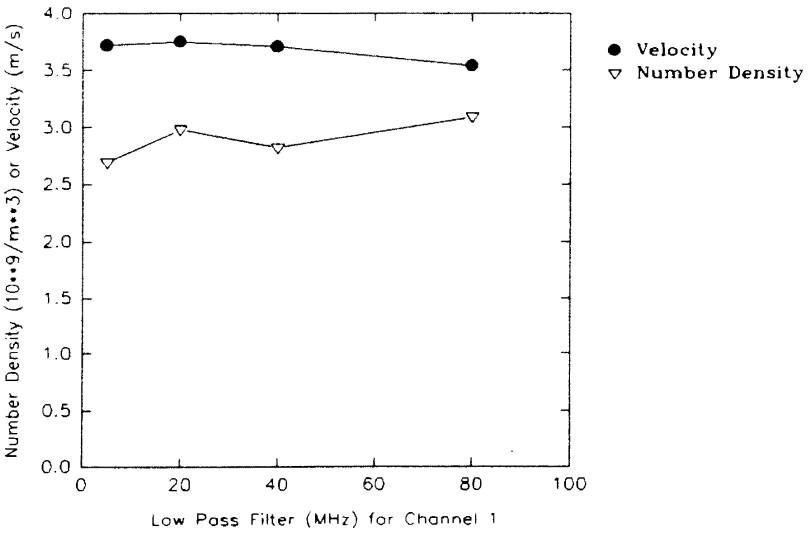

Figure 20. Dependence of Number Density and Velocity on Low Pass Filter for Channel 1

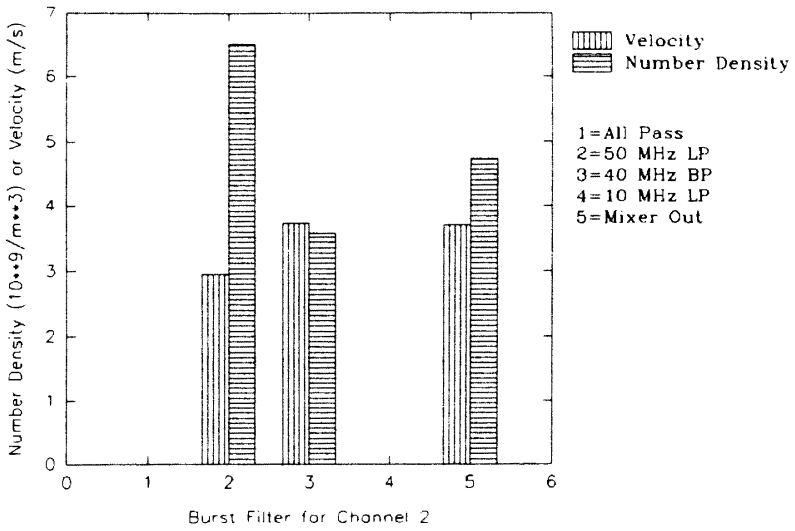

Figure 21. Dependence of Number Density and Velocity on Burst Filter for Channel 2

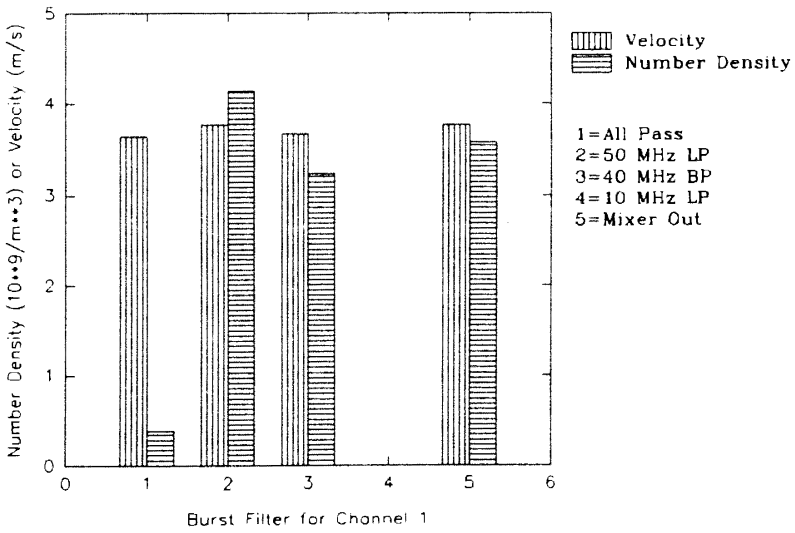

Figure 22. Dependence of Number Density and Velocity on Burst Filter for Channel 1

certainly erroneous and away from the mean velocity. It was thought that this might have been because, at such a low threshold level, the background noise instead of the particles, could trigger the burst detector. However, when the seeding was turned off, absolutely no signals and no counts were obtained, rejecting the above hypothesis. If a mean velocity value is assumed for these two points, as shown in the figure by a dotted line, then there is not much velocity variation and little number density variation below 10 mV. As expected, the number density decreases with an increase in the threshold setting as only bursts due to larger particles are analyzed. The decrease in the number density is sharp for the threshold bands of 0-15 mV and 25-35 mV. The number density is fairly constant for the threshold bands of 15-25 mV and 35-45 mV. Also, if a mean velocity from the threshold band of 10-50 mV is assumed for the threshold values of 0 and 5 mV, then the number density is fairly constant for the threshold band of 0-10 mV. The graph of number density variation with respect to threshold also indirectly indicates the relative size distribution of the particles present in the flow. Figure 24 shows the dependence of number density and velocity on the threshold setting for channel 1. A much lower variation in velocity and number density is observed.

Most of the measurements for this present work were taken at a threshold setting of 13 and 15 mV for channels 2 and 1, respectively. Some of the measurements were also taken at a low threshold setting of 4 and 8 mV for channels 2 and 1, respectively. However, as explained in the preceding paragraph, it might have been better to operate in the threshold band of 0-10 mV for all the measurements, and use the mean velocity from the threshold band of 10-50 mV for calculation of number density. That should have ensured detection of even the smallest particles.

The variable 'envelope filter' was used to select a suitable filter that smoothed the burst signal and removed the high frequency noise. It should be shorter than the shortest burst length. Figure 25 shows the dependence of number density and velocity on the envelope filter setting for channel 2. It is evident from the figure that the velocity is

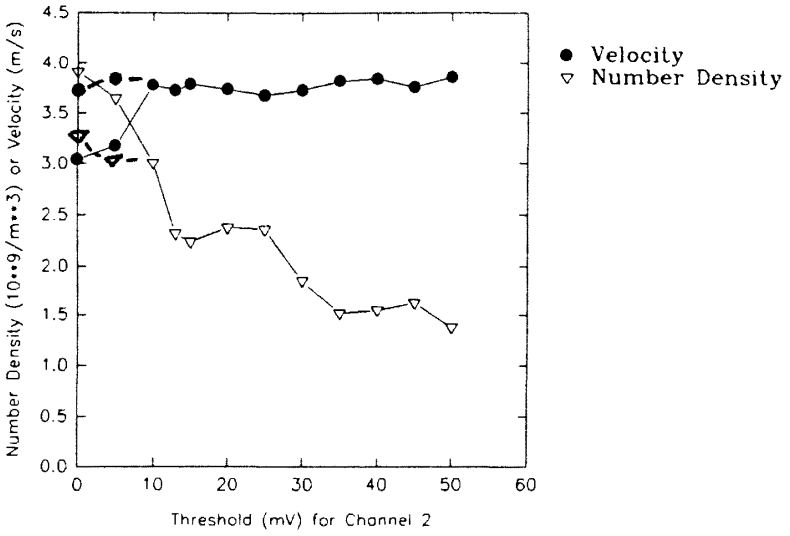

Figure 23. Dependence of Number Density and Velocity on Threshold for Channel 2

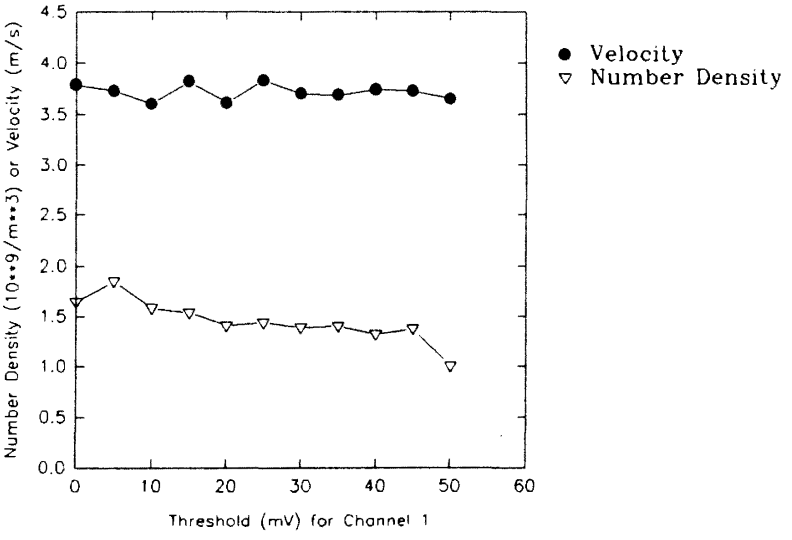

Figure 24. Dependence of Number Density and Velocity on Threshold for Channel 1

almost constant. However, the number density decreases steadily with increase in the size of the envelope filter. Figure 26 shows the dependence of number density and velocity on the envelope filter setting for channel 1. It is observed that the velocity shows a maximum variation of 6 percent while the number density shows a maximum variation of 35 percent among different envelope filter settings. The envelope filter was set at 100 nanoseconds (the minimum possible value) to begin with, and then was increased slowly, till it was just shorter than the shortest burst length observed on the oscilloscope. This procedure of setting the envelope filter was recommended by the DSA manual [Aerometrics, 1991]. Following this procedure, the envelope filters were typically set at 1 microsecond for both the channels for the measurements involved in this present work.

The parameter 'peak detector' was used to operate the peak detector that detected the center of the Gaussian pedestal. The peak detector should be switched 'off' when the input raw signal does not have a well defined peak. It was switched 'on' for all of the measurements involved in this work. The parameter '% after peak' determined the percent of the sampled signal taken after the peak. It was assigned a value of 50% for all of the measurements. Turning the peak detector 'off' or assigning values other than 50% to the parameter '% after peak' were never tried.

The parameter 'number of samples' determined the frequency and velocity resolution of the DSA. For both the channels, the number of samples in conjunction with the sampling frequency should be set so that the record length is shorter than the burst length. As recommended by the DSA manual [Aerometrics, 1991], the number of samples were fixed to be 128 for all the measurements. The number of samples N_S that could be acquired over the Doppler burst signal was limited by the sampling frequency, f_S, as shown by the equation given below [Aerometrics, 1991].

$$N_S = f_S * t \tag{12}$$

This is because the burst length or signal duration was limited by the transit time, t, of the particle. Transit time, as defined earlier, is the time for which a particle is in the probe

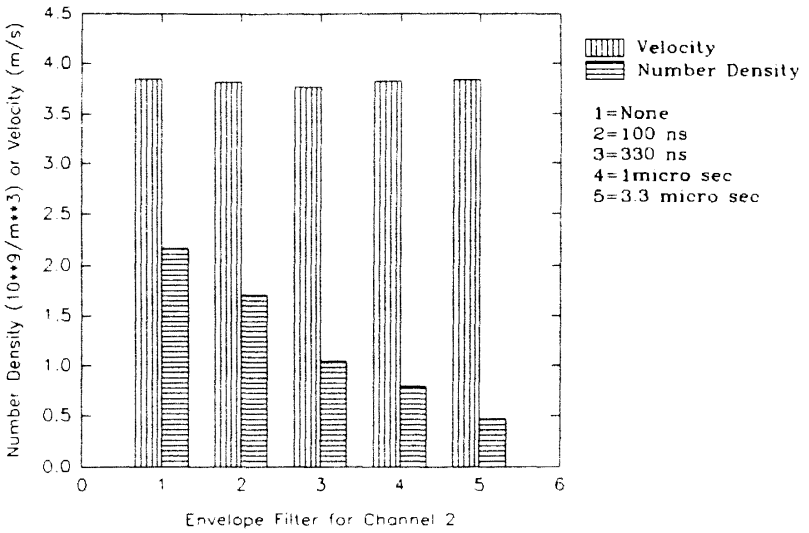

Figure 25. Dependence of Number Density and Velocity on Envelope Filter for Channel 2

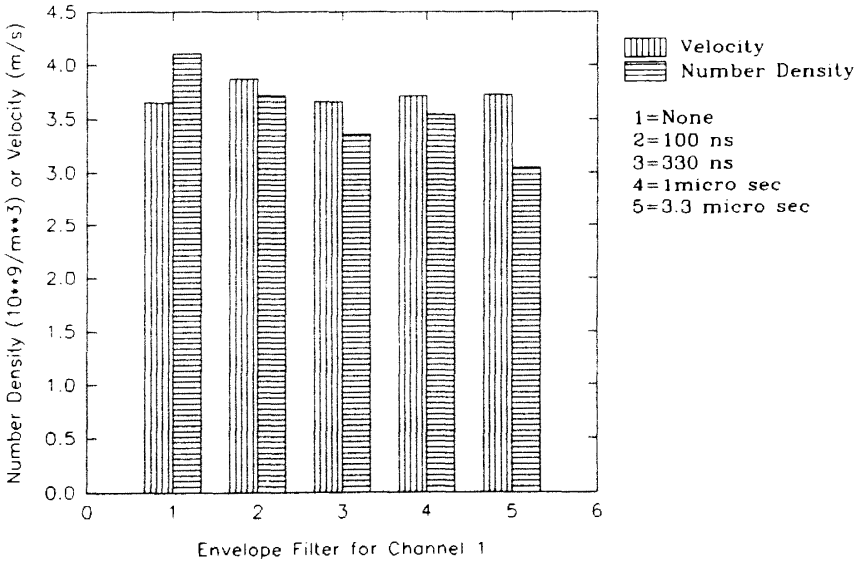

Figure 26. Dependence of Number Density and Velocity on Envelope Filter for Channel 1

volume. The accuracy of the frequency measurement improves with the number of samples acquired over the signal. It was tempting to assume that increasing the sampling frequency would result in improved accuracy. However, the frequency resolution is proportional to f_S/N_S, so little could be gained by increasing the sampling frequency [Aerometrics, 1991]. The other way to increase the number of samples acquired was to increase the transit time by enlarging the laser beam diameter. But this would result in loss of signal-to-noise ratio as the incident beam intensity on the particles would have been reduced. Therefore, it was best to sample at a high frequency through the software and keep the signal frequency at a value that was appropriate for that sampling frequency, using the mixer frequency selection in the software [Aerometrics, 1991].

The variable 'sampling frequency' was used to adjust the digitizing frequency for the sample points taken of the input signal. As mentioned before, this and the number of samples, should be set so that the record length is shorter than the burst length. Otherwise, very strange velocity measurements are obtained. Figure 27 shows the dependence of number density and velocity on the sampling frequency setting for channel 2. As expected, at a very low sampling frequency of 2.5 MHz., a strange and far from mean velocity of 1.5 m/s was observed. Disregarding this point, maximum variations of 14 and 36 percent were observed for velocity and number density, respectively. Figure 28 shows the dependence of number density and velocity on the sampling frequency setting for channel 1. Maximum variations of 5 and 40 percent are observed for velocity and number density, respectively. Generally, a sampling rate of 20 MHz was used for both of the channels for the measurements involved in this work.

The parameter 'minimum signal to noise ratio' was used to establish the minimum signal quality in an acceptable processed burst signal. For all of the measurements, it was fixed at 0.3, as recommended by the DSA manual [Aerometrics, 1991], to reject poor quality points while maintaining a high data rate.

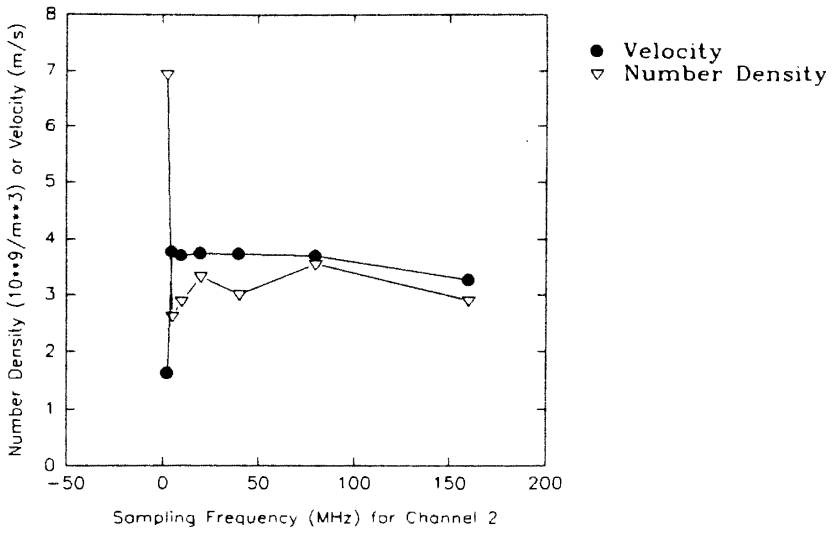

Figure 27. Dependence of Number Density and Velocity on Sampling Frequency for Channel 2

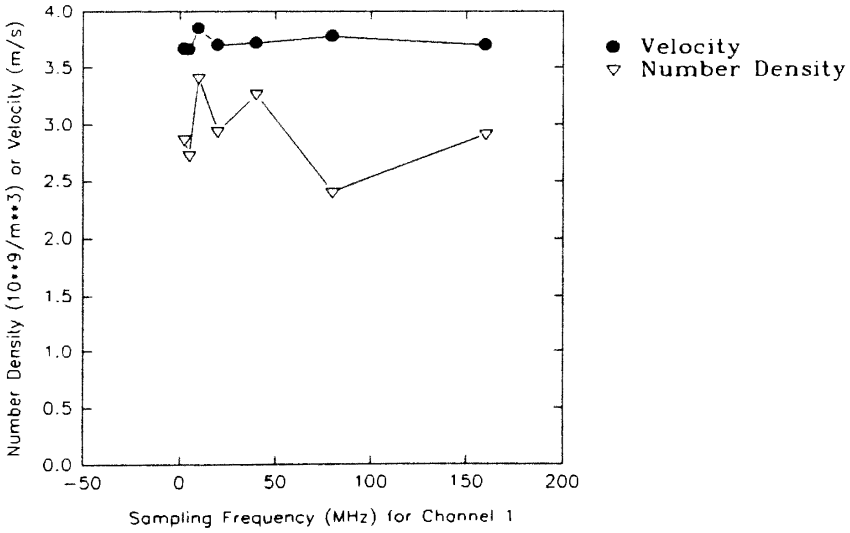

Figure 28. Dependence of Number Density and Velocity on Sampling Frequency for Channel 1

The option 'enabled' was used to toggle a particular channel on or off. As mentioned before, channel 2 measured the major (or vertical) component of the velocity, while channel 1 measured the minor (or horizontal) component of the velocity. If only one component of the velocity was of interest, then the other channel could be turned off. Both channels if kept on, gave the total velocity of the flow. Figure 29 shows velocity measurements keeping both of the channels on, and toggling off one channel at a time for six different runs. Also it shows the total velocity calculated from the component velocities obtained from channels 1 and 2. These runs were conducted within an interval of ten minutes. It is observed that since the minor component of the velocity is nominal, the total velocity (obtained by keeping both of the channels on) is almost identical to the major component of velocity. Also the total velocity (calculated from the component velocities obtained from channels 1 and 2) is identical (the data points overlap on graph) to the major component of velocity. Figure 30 shows the corresponding number density calculations. It is important to mention that always the total velocity (obtained by keeping both of the channels on) for the test was used for calculating the number density irrespective of the toggled channel (or channels). It is observed from the figure, that for each test, the number densities are identical for the cases when both of the channels are on and when only channel 2 is on. However, when only channel 1 is under operation, much higher particle counts, and consequently much higher number densities (two to three times of those when both channels are active) are obtained. It may be possible that since channel 1 alone measures very low velocities (minor component), other governing software parameters, such as the envelope filter, the sampling frequency and the number of samples, should have been suitably changed to obtain accurate measurements. For all of the measurements involved in this present work, both the channels were kept active.

The minimum and maximum measurable velocities, as per the governing signal processing parameters and the optical configuration, were displayed under 'velocity range'.

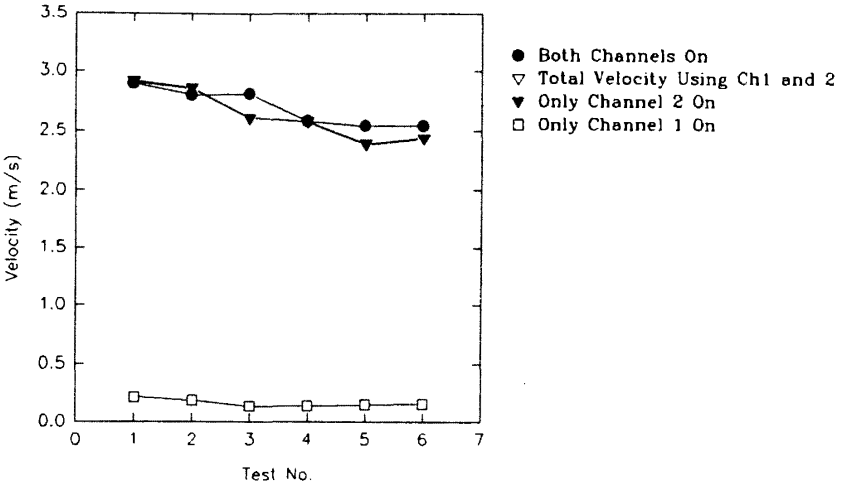

Figure 29. Dependence of Velocity on Channels Enabled

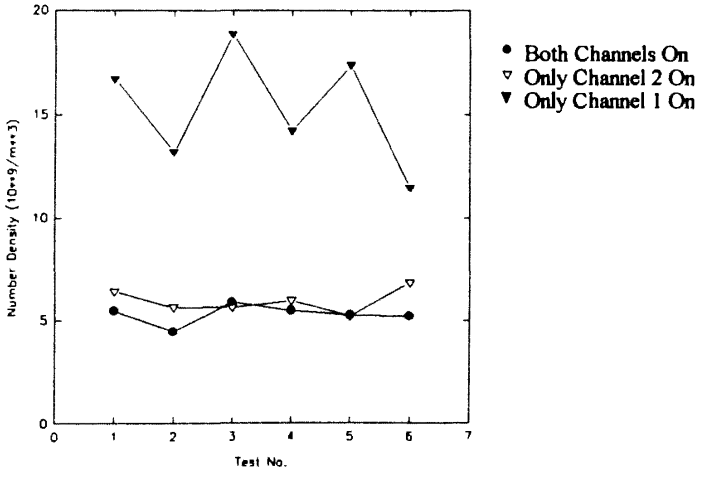

Figure 30. Dependence of Number Density on Channels Enabled

The portion of this range could be further restricted by setting 'velocity minimum' and 'velocity maximum'.

As already discussed in detail in Chapter III, the swept volume particle counting technique is primarily based on the velocity and the particle count measurements obtained by the laser Doppler velocimeter. As mentioned before in Chapter III, the laser Doppler velocimeter that was employed is customized only for velocity measurements. The sensitivity analysis also confirmed that the velocity measurements are far more constant than the number density measurements over a wide range of governing parameters and variable settings. The number density shows a comparatively wider range of variation because of the wide variation in the particle count measurements obtained by the laser Doppler velocimeter system. Further research is required to fully understand the relationship between the particle counts obtained by the system and the governing variables and parameters. The relatively wider variation in the particle count measurements may also be attributed to the unsteady seeding produced by the ultrasonic humidifier. This is discussed in detail, later in this Chapter. Therefore, it was considered best to set all of the governing parameters and variables so as to obtain accurate velocity measurements. An optimum and standard variable setup was used for most of the tests for one particular plane of the filter. This ruled out the possibility of biased results due to different variable setups being employed for different measurements.

Figure 31 shows the variable page from the DSA software that enabled one to terminate data acquisition and to properly document and store the data. The length or duration of data acquisition for a single measurement run by the system was governed by setting 'stop mode' and 'stop after' selections as desired. The data acquisition could be terminated either after a fixed interval of time or after the acquisition of a fixed number of valid samples. For the present work, 'time' was used as the limiting criterion for data acquisition and it was typically set for 10 or 30 seconds. The parameter 'time out' is critical when 'number of valid samples' is used as 'stop mode', and the rate of data

acquisition is low. 'Time out' setting governs the limiting time for which the DSA will wait and acquire data; and after this limiting time, the data acquisition will be terminated even though the required number of valid samples may not have been obtained. If 'time' is used as 'stop mode' then 'time out' should be set at a higher value than 'time' so that it does not terminate data acquisition before the set 'time' is elapsed. Setting 'time out' to 0 seconds disables this option. Since 'time' was used as the limiting criterion for all of the measurements involved in this work, the option 'time out' was disabled.

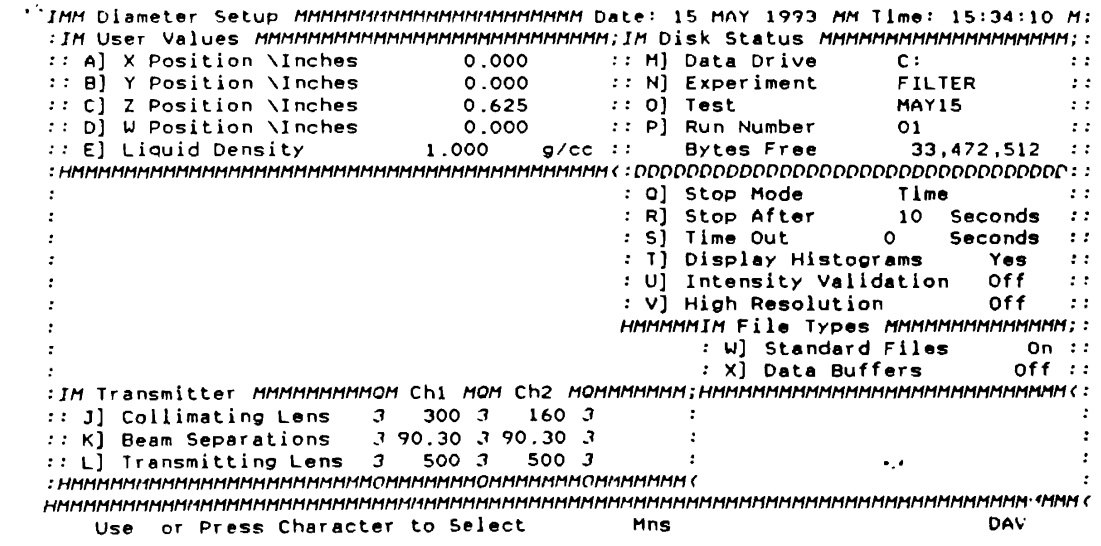

Figure 31. A Sample Variable Page for Terminating Data Acquisition, and for Data Documentation and Storage

Figure 32 shows an example output page resulting from the data acquisition and processing by the DSA. This output page gives information regarding the mean and rms velocities of the individual channels, the overall mean velocity of the flow, flow angle and

flow shear stress. It also gives information regarding 'coincidence' of both the channels tracking the same particle. Mean velocity for a particular channel is calculated as the arithematic mean of velocities obtained for that channel from all of the valid samples. Rms velocity for a particular channel is calculated as the square root of the mean of squared deviations from this mean velocity. The output page also gives information with regard to the number of signals attempted, the validated and percent of validated signals, and the run time. This has already been discussed in detail in Chapter III. It is worth mentioning that, due to some software error 'run time' is displayed as 'corrected run time', though it is not corrected in any manner. The output page also shows the velocity histograms for the individual channels.

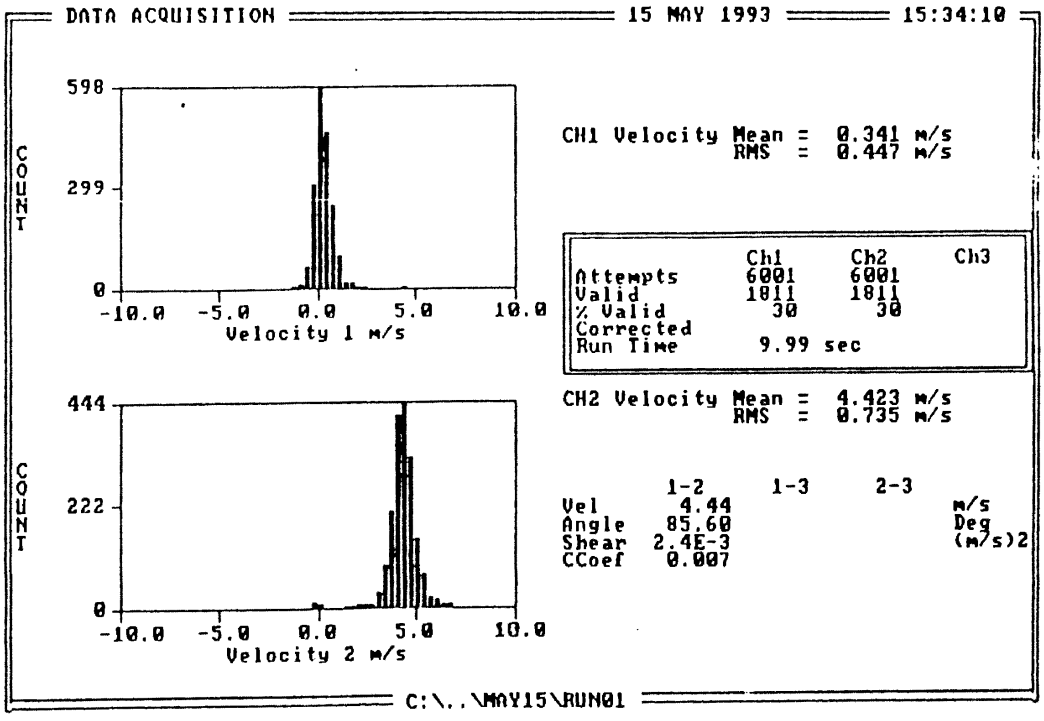

Figure 32. A Sample Output Page

Other variable setup pages pertaining to the optical parameters of the system, and DSA hardware configuration are attached in Appendix D. These pages show the factory settings of the variables and parameters, and once the system was successfully installed, these parameters and variables were never changed.

Laser power was an important experimental parameter. It was displayed on the remote control panel of the laser. It was measured before the laser beam was split into two pairs of beams (blue and green). Therefore, this measurement of laser power does not indicate that the two pairs of beams (blue and green) were of equal intensity. The blue beams operated in the vertical plane and were used to calculate the major component of the velocity, while the green beams operated in the horizontal plane and were used to calculate the minor component of the velocity.

Two independent tests on two different filters were conducted to understand the effect of laser power on the measurements. For both of the tests, the governing system parameters were the same, and measurements were taken at the center of the filter and at a plane 0.625 in. above the face of the filter. Figure 33 shows the dependence of velocity on laser power. It is evident from the graph that, for both of the tests, velocity is almost constant and does not vary much with laser power. Figure 34 shows dependence of number of particle counts obtained by the system, on laser power. The difference in the number of particle counts between the two tests can be attributed to dissimilar flow and dissimilar seeding. This is discussed later in this Chapter. From the figure, it is observed that for both of the tests, first the particle count increases slowly with laser power. Then, in an intermediate range of laser power, they show a steep increase and finally they tend to saturate. This could be attributed to the fact that particles of different size scatter different amounts of light. Thus, at low laser power, small particles were not detected. This was because, for that setup of the system parameters, they were not scattering enough light to be detected. As laser power was increased, more and more of those small particles were detected and counted. The particular range of laser power for which the increase in

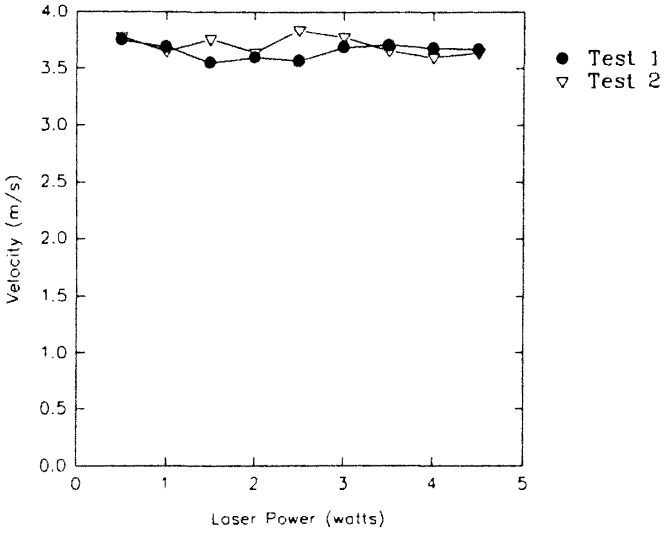

Figure 33. Dependence of Velocity on Laser Power

counts was steep indicates that a relatively large number of particles which were smaller existed but were not detected until the laser power was increased. The saturation indicates that all of the particles, even the very small ones, were detected. The curves suggest that measurements should therefore be taken with laser power high enough so that the system counts in the saturated region. The curves also indicate qualitatively, the relative size distribution of the particles present in the probe volume. For both of the tests, the saturation seemed to be at a laser power of 3.5 watts and beyond, irrespective of the different range of particle counts they were measuring. Therefore, a laser power of 3.5 watts was typically used for the measurements involved in this present work. Figure 35 shows the dependence of number density on laser power. For both of the tests, the number density curves exhibit a profile identical to their respective particle count profiles. This is in perfect accordance with the swept volume counting technique, since there is not much velocity variation for both of the tests.

Data Reproducibility Measurements

Experiments were conducted to check for the data reproducibility. Figure 36 shows results of two different tests using different filters. The experimental parameters, such as, laser power, flow rate, seeding and DSA software parameters were the same for both tests. Measurements were taken at the center and at a plane 0.625 inch above the face of the filter for both the tests. It is observed from the figure, that for test 1, the velocity is fairly constant with a maximum variation of 4 percent. The number density, however, shows a maximum variation of 40 percent. For test 2, the velocity is again fairly constant with a maximum variation of 25 percent, as opposed to the number density which shows a maximum variation of 96 percent. The variation in velocity measurements for one particular test, can only be attributed to the highly unpredictable, complex and rapidly changing flow within the housing. The variation in number density measurements for one

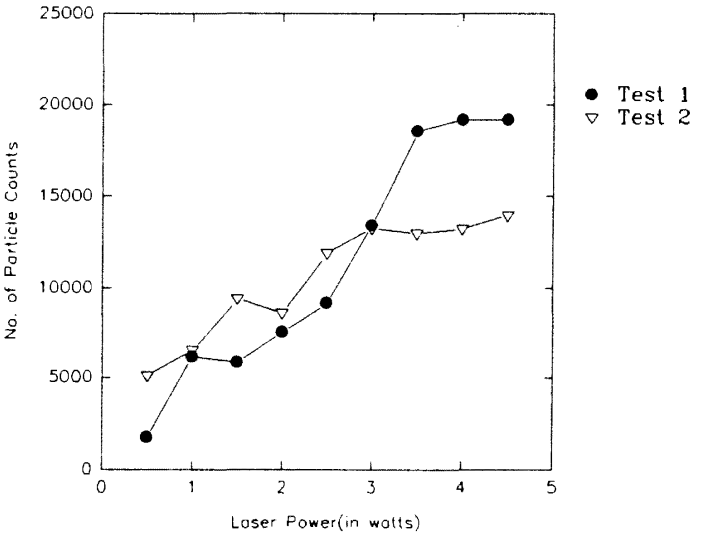

Figure 34. Dependence of Particle Counts on Laser Power

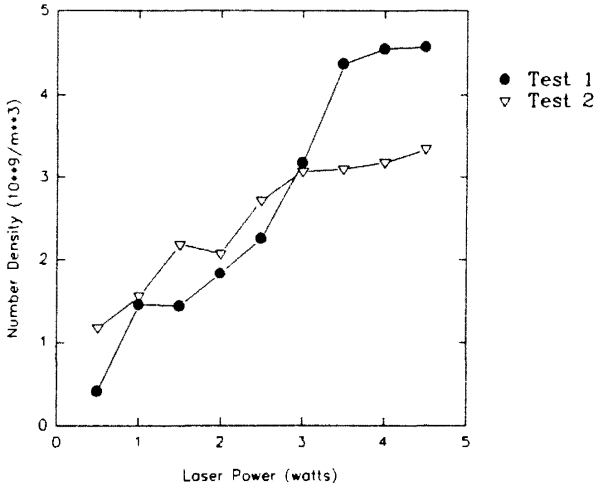

Figure 35. Dependence of Number Density on Laser Power

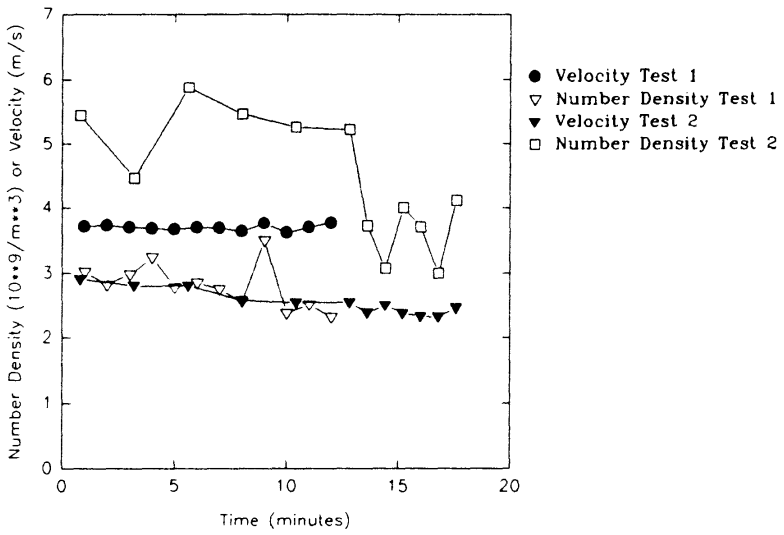

Figure 36. Data Reproducibility

particular test, can also be attributed to the unsteady seeding, in addition to the unsteady flow. The fact that velocity measurements varied by almost 70 percent on the two tests clearly suggests that the flow is different for different filters, even though the filters may be of the same type. This is reasonable, assuming that each filter is unique with regard to its material, workmanship, manufacture and handling. As described in detail in Chapter III, since the number density calculation is based on the velocity, the variation in velocity measurements from two different tests may result in variation in number density for the two tests if the number of counts remains constant. In the two tests discussed in this paragraph, it can be argued that the time-history effects may also be responsible for the variations observed in the measurements.

In order to avoid the undesirable time-history effects which might have come into existence in the two tests described in the preceding paragraph, several other tests were conducted. Figure 37 shows number density and velocity measurements for six different tests, all conducted with different filters. The experimental parameters, such as, laser power, flow rate, seeding and DSA software parameters were the same for all of these tests. The filters used were all new, dry and clean. Measurements were taken at the center and at a plane 0.625 in. above the face of the filter. It is evident from the figure that the velocity and the number density both show a wide variation from filter to filter, as discussed in the preceding paragraph. A maximum variation of 80 percent is observed in the velocity measurements. All of the above discussed tests with regard to data reproducibility emphatically suggested that the flow varied considerably from filter to filter. This was further confirmed when the number density distributions and velocity profiles were plotted for numerous filters. This is discussed later in this Chapter.

Once the proposed particle counting technique was carefully reviewed and analyzed, with regard to the information that could be obtained using the laser Doppler velocimeter system, some preliminary experiments were conducted to investigate the validity of the particle counting technique. Those experiments served the purpose of

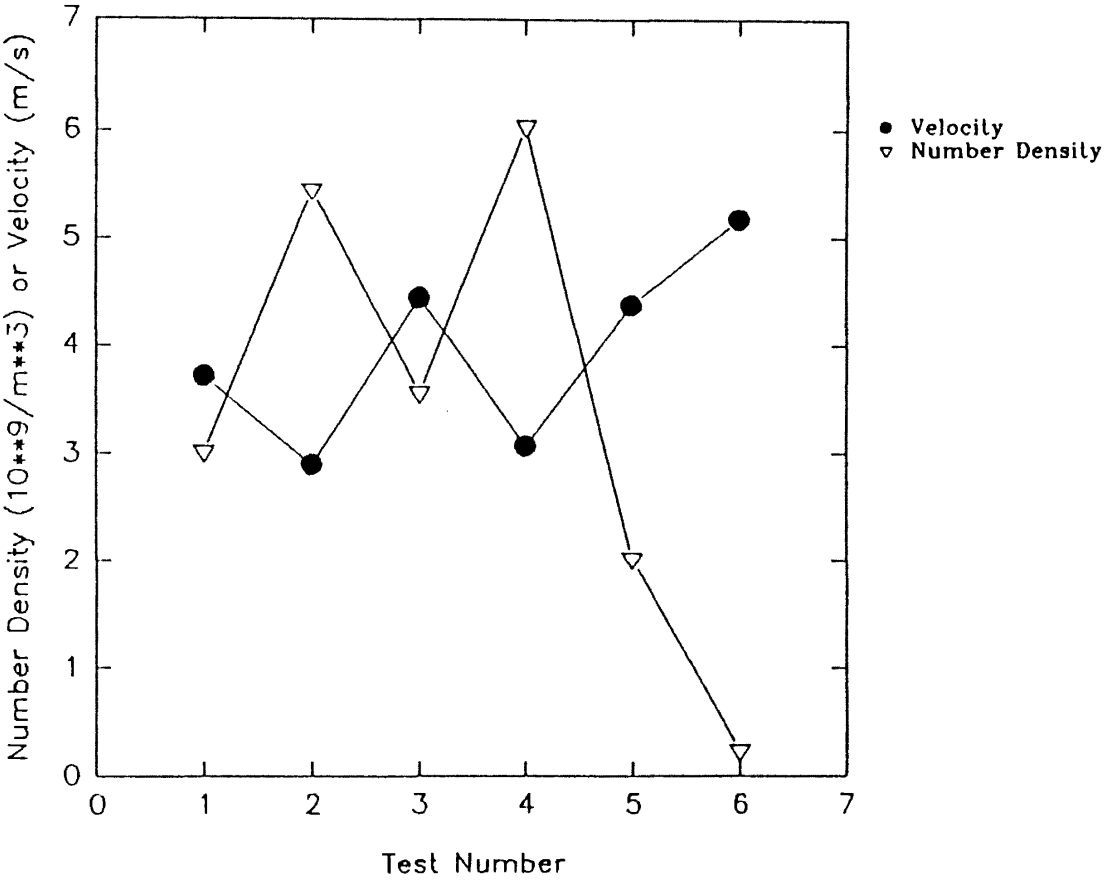

Figure 37. Variation of Number Density and Velocity with Different Filters

checking our counting technique and its compatibility with our laser Doppler velocimeter system.

As mentioned in Chapter III, an ultrasonic humidifier was used to generate seeding water particles for the laser Doppler velocimeter system. The rate at which those particles were generated (particles per unit time or mist intensity) could be varied using control switches over the humidifier. That rate of particles generated or mist intensity was estimated by experimentally determining the water consumption rate of the humidifier and the approximate size of particles generated by it. Table 1 shows the results of the experiment conducted to estimate the rate of water consumption by the humidifier. For the measurements shown in Table 1, the control switch for mist intensity on the humidifier was at the minimum level.

TABLE 1

WATER CONSUMPTION RATE OF THE HUMIDIFIER

Test No.	Time	Water Consumption Rate (gms/hr.)
1	1 st hour	85.6
2	2 nd hour	97.4
3	3 rd hour	110.2

Thus, the water consumption rate of the humidifier was found to increase with time. The reason may be that as the water level falls in the humidifier chamber, the

ultrasonic vibrations, which are responsible for generating water particles, are absorbed by a smaller amount of water, producing more atomized water particles.

The water particles generated by the humidifier were 'caught' on a glass slide and were carefully and repeatedly observed under a high magnification, high resolution microscope. It was observed that a wide range of water particles were generated from 5 to 100 microns in diameter. However, the majority of the particles (more than 50%) were observed to be in the range of 10 to 30 microns. In order to avoid any personal human error, independent observations were made by my colleague Mr. F. Liang, and those too confirmed my approximate estimate of the sizes of the water particles generated by the humidifier. Verbal communication with Mr. F. Liang pertaining to his preliminary visibility measurements using the laser Doppler velocimeter, confirms that the smallest particles generated by the humidifier are of the order of 3 microns in diameter. It is important to mention that these sizes were observed as soon as the particles were generated and came out of the humidifier nozzle. The sizes could also vary when the particles are used in the actual test flow. The exact mechanism for generating particle distribution by the humidifier was not explored.

Table 2 shows mist intensity (particles/second) calculations for various humidifier water consumption rates and different sizes of water particles. It was assumed that all of the particles were of the same size. Experimental characterization of the uniformity of the water droplets generated by the humidifier was not done.

Measurements were taken for the velocity at the center of the humidifier outlet using the laser Doppler velocimeter. The average velocity at the center was measured to be 1.55 m/s, and it was assumed that the velocity is constant over the cross-sectional area of the humidifier outlet. Also, the cross-sectional area of the humidifier outlet was measured and it was 6.558×10^{-04} m^2. By dividing the mist intensity of Table 2 by the above velocity and area, theoretical number density (particles/m^3) at the humidifier outlet was obtained and is tabulated in Table 3.

TABLE 2

ESTIMATION OF MIST INTENSITY
(PARTICLES/SECOND)
GENERATED BY THE
HUMIDIFIER

	1 micron	5 micron	10 micron	30 micron	50 micron
85.7(g/hr.)	4.547×10^{10}	3.637×10^{08}	4.547×10^{07}	1.684×10^{06}	3.637×10^{05}
97.4(g/hr.)	5.167×10^{10}	4.134×10^{08}	5.167×10^{07}	1.914×10^{06}	4.134×10^{05}
110.2(g/hr.)	5.846×10^{10}	4.677×10^{08}	5.846×10^{07}	2.165×10^{06}	4.677×10^{05}

The number density at the humidifier outlet was then obtained experimentally by the swept volume counting technique as explained in Chapter III. This measurement was also taken at the minimum possible mist intensity produced by the humidifier. This has already been discussed in detail in Chapter II. The average number density was determined to be 4.2×10^{10}. This was in fairly good agreement with the theoretical number density calculated for a size of 10 microns.

We intended to repeat this experiment with high mist intensity output from the humidifier, but no accurate measurements could be obtained by the laser Doppler velocimeter at the humidifier outlet at high mist intensity. This, as already discussed in Chapter II, was because of the high particle concentration.

Next, as shown in Figure 38, the humidifier was used to provide seeding in a jet flow. Jet flow has been studied very well by numerous researchers and the nature of the velocity profiles at different planes downstream the flow are well understood. Numerous tests were conducted to investigate the performance of the counting technique and the

laser Doppler velocimeter system. Also the understanding of the system parameters with regard to the system measurements was enhanced.

TABLE 3

THEORETICAL NUMBER DENSITY
AT THE HUMIDIFIER OUTLET

	1 micron	5 micron	10 micron	30 micron	50 micron
85.7(g/hr.)	4.473×10^{13}	3.578×10^{11}	4.473×10^{10}	1.657×10^{09}	3.578×10^{08}
97.4(g/hr.)	5.083×10^{13}	4.067×10^{11}	5.083×10^{10}	1.883×10^{09}	4.067×10^{08}
110.2(g/hr.)	5.751×10^{13}	4.591×10^{11}	5.751×10^{10}	2.130×10^{09}	4.601×10^{08}

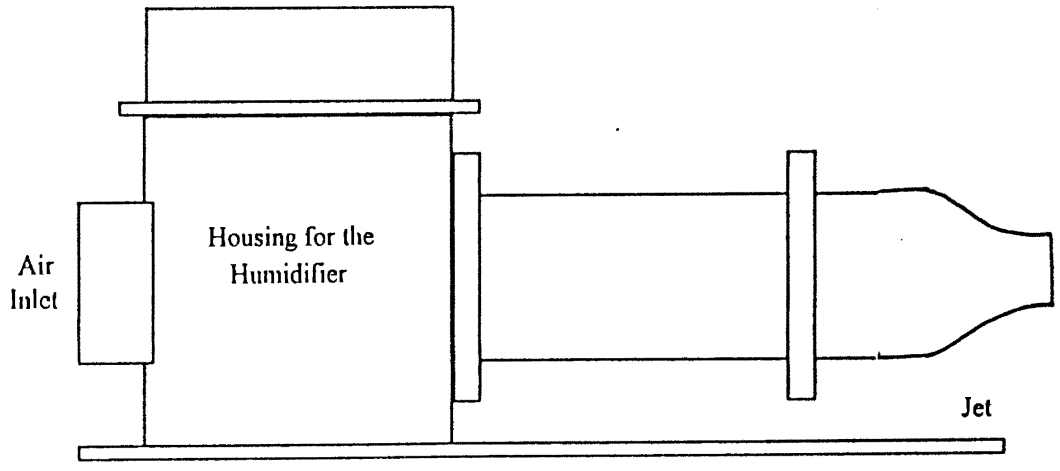

Figure 38. Schematic Diagram of the Humidifier Setup for Providing Seeding in a Jet (Not to Scale)

As mentioned before, once a fair degree of confidence was achieved due to all of the above described experiments, with regard to the swept volume counting technique and laser Doppler velocimeter system, measurements were taken for automotive air filter AF-3192, and particle number density distributions were calculated using those measurements. Figure 39 shows the filter mounted in a plexiglas test housing. The humidifier provided the required seeding. The water particles generated by the humidifier were pulled into the housing with the air flow. But this was not a very good method of providing seeding into the test housing, as it was not uniform. The input seeding was sensitive to even the slightest air current in the room. Also, the water particles were not distributed uniformly in the flow in the stabilizing inlet pipe of the housing. Instead, they may have taken a preferential path along any one side of the stabilizing pipe. The laser beams entered perpendicular to the plane of the paper. Henceforth, the front half of the filter refers to that half of the filter which is close to the side of the housing from where the beams enter, and the rear half is the other half of the filter which is further from the beam entering side. Figure 39 also shows the various planes at different heights above the filter at which measurements were taken. It is important to mention that the heights above the filter face were measured with a precision of 1/8 of an in. and they have been converted to the decimal form for convenience. As mentioned before, the measurements were taken over AF 3192 automotive air filters at a constant flow rate of 125 (±3%) cubic feet per minute (cfm).

Figure 40 shows the various positions for measurement over the filter. Those positions for measurement were in the form of a grid as shown in the figure. The size of the grid along the length or breadth of the filter refers to the distance between two consecutive positions of measurement along the length or breadth of the filter respectively. As mentioned earlier, complete computer controlled automated traversing enabled movement of the probe volume precisely and speedily to any location over the filter. As mentioned in Appendix B, precision that was obtained by the automated traversing was of

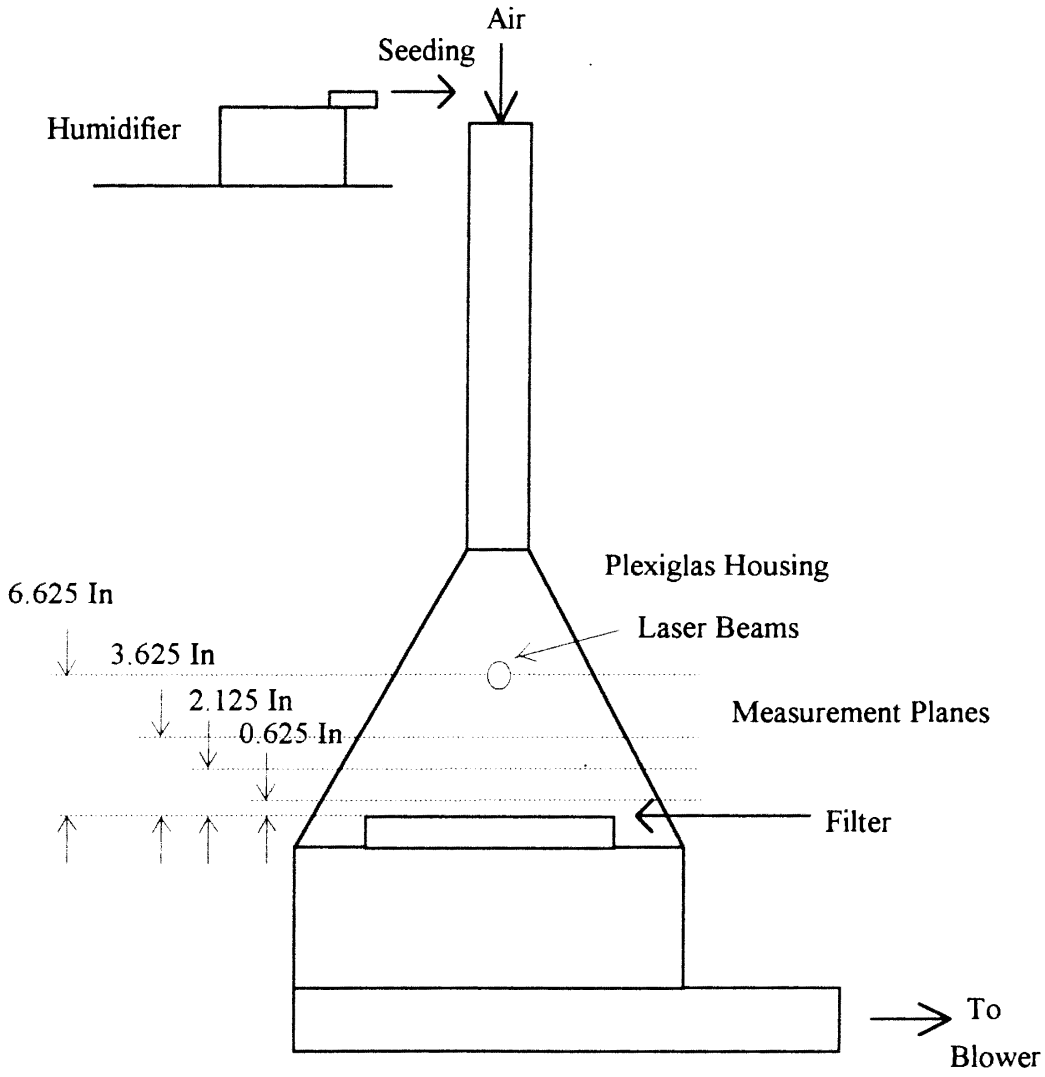

Figure 39. Filter Mounted in Plexiglas Housing

the order of ±0.001 of an in. per 10 in. of displacement. For most of the measurements involved in this work, a grid of 1±0.001 in. by 1±0.001 in. was used. However, this was not always the case, and exact measurement locations (and the grid) depended upon the degree of precision and closeness with which a filter was to be mapped. For example, for some tests at a plane close to the filter (0.625±0.125 in. above the filter face), a rather finer grid (0.938±0.001 in. by 0.792±0.001 in.) was chosen as compared to the grid (1± 0.001 in. by 1±0.001 in.) at a plane 3.625±0.125 in. above the filter. This obviously was because there was more interest in carefully investigating the number density distribution very close to the filter.

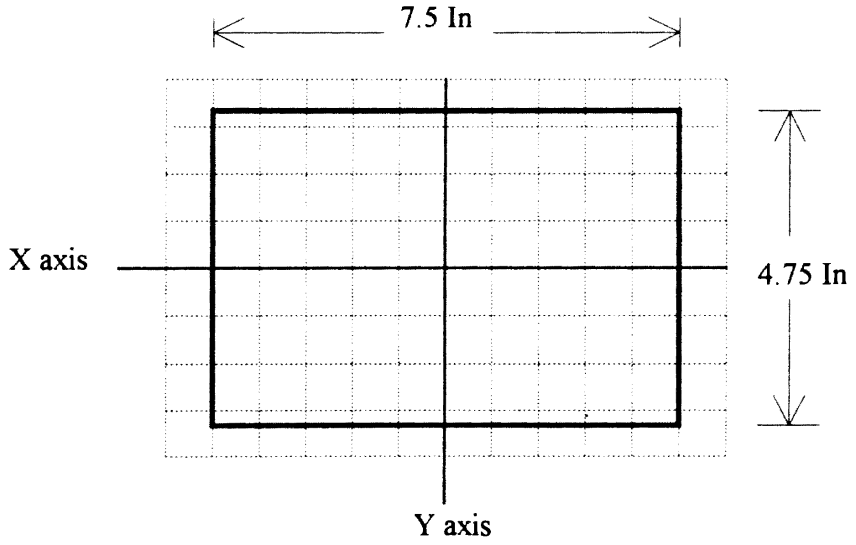

Figure 40. Measurement Grid for Automotive Air Filter AF 3192

It is worthwhile to mention that, for these measurements, it was assumed that a 'clean' filter would be a dry filter, as water particles were used for seeding the flow. Along

the same lines, a 'dirty' filter would be a wet filter; as both a 'dirty' filter and a wet filter are the result of 'usage'.

Thirteen different tests were conducted and each has been assigned an identification letter (from A through M) for convenience. Table 4 concisely presents the relevant information about these tests. The table shows the date when a particular test was conducted, whether a new or a used filter was employed, the grid used for taking the measurements, the humidifier setting with regard to the intensity of mist generation, and the specific software parameter setup employed. Six different parameter setups were employed for taking these measurements. These are attached in Appendix E. As mentioned before in Chapter III, a TSI mass flow sensor was used to monitor the volumetric air flow rate. This went out of calibration after the tests I through M were conducted. This may have been due to an accidental change in the gain or span of the instrument. Several tests were conducted by my colleagues with this out-of-calibration mass flow sensor. The flow measurements obtained by this were compared to those obtained using an air filter test stand, and a linear curve fit was obtained over the range of 0 to 500 cfm. Tests A through H were conducted using the out-of-calibration mass flow sensor in conjunction with this linear curve fit. Also, it is important to mention that for tests I through M, laser power was measured in terms of voltage (Vdc) across a specific resistance of the laser. This voltage was proportional to the laser power in watts. Saturation with regard to the number of particle counts and hence the number density was reached just below 8 Vdc.

As mentioned before, measurements were taken at four different levels above the face of the filter. Table 5 shows the total number of tests and the identifying names of the tests that were conducted at each level. Once again, it is worthwhile to mention that, the heights above the filter face were measured with a precision of 1/8 of an in., and they have been converted to the decimal form for convenience.

TABLE 4

TEST INFORMATION

Test Name	Date Performed	Filter Employed	Grid Used	Mist Intensity	Software Parameter Setup
A	04-08-93	New	0.5" by 0.5"	High	I
B	04-29-93	New	1" by 1"	High	II
C	04-30-93	Same as B	1" by 1"	High	III
D	05-01-93	Same as C &B	1" by 1"	High	III
E	05-07-93	Same as D, C & B	1" by 1"	High	III
F	05-09-93	New	1" by 1"	High	II
G	05-15-93	New	1" by 1"	High	III
H	05-15-93	New	1" by 1"	High	II
I	10-05-92	New	0.938" by 0.792"	Medium	IV
J	10-06-92	Same as I	1.875" by 1.188"	Medium	IV
K	10-06-92	Same as J & I	1.875" by 1.188"	Medium	IV
L	10-18-92	New	0.938" by 0.792"	High	V
M	10-27-92	New	0.938" by 0.792"	High	VI

TABLE 5

TESTS CONDUCTED AT VARIOUS PLANES

Level Above the Face of the Filter	No. of Tests Conducted	Test Names
6.625"	2	D and E
3.625"	3	C, G and K
2.125"	2	J and L
0.625"	6	A, B, F, H, I, M

Measurements at a Plane 6.625 In. Above the Filter Face

Figure 41 shows a three-dimensional plot of particle number density distribution for test D. From Table 5, it is clear that this test was conducted at a plane 6.625 inches above the face of the filter. As observed from Table 4, the filter used for this test was an old filter, and a grid of 1 in. by 1 in. was used for the test. It is also observed from Table 4, that the humidifier was operating at high mist intensity, and software parameter setup III was employed for taking measurements. A laser power of 3.5 watts was used. As mentioned before, measurements were taken at a flow rate of 125 cfm. Particle number density is represented by the z-axis. The length of the filter was along the x-axis while the breadth of the filter was along the y-axis. The coordinates (0 in., 0 in.) represent the center of the filter. The laser beams entered perpendicular to the plane of the paper, and in the direction of the y-axis. The exit duct of the test housing leading to the blower (as shown in Fig. 39) was located on the positive x-axis section of the filter (right side of Fig.

41). The above mentioned orientation has been strictly adhered to, in all of the three-dimensional plots which have been presented in this work.

From Fig. 41, it is observed that the number density is higher in and around the center of the filter, and it gradually decreases toward the edges of the filter. It is important to mention that the figure represents number density distribution only for the front half of the filter (positive y-axis direction). It is worthwhile to mention that this plane (6.625 in.) is the plane furthest from the face of the filter where measurements were obtained.

The three-dimensional plots of the particle number density distribution versus the filter dimensions, as in Fig. 41 present the overall distribution very well; but it is difficult to investigate detailed information from it. Therefore, two-dimensional plots were taken using the same data, which is equivalent to slicing the three-dimensional plot along the desired planes. The two-dimensional plots were taken at different planes along the grid lines.

Figure 42 is a two-dimensional plot of particle number density distribution at different grid planes parallel to the x-axis (along the length of the filter). The graph clearly shows that for grid planes closer to the center (y=0 in. and y=1 in.), the number density is highest at the centerline (x=0 in.) and decreases towards the edges of the filter (x=±3 in.). For the grid plane further from the center (y=2 in.), the number density is very low and the profile is almost flat with little variation with x-location. Also a fair degree of symmetry is exhibited by the number density profiles with respect to the plane x=0 in. In other words, the left and the right halves of the filter have a similar number density distribution. It was expected that, for any grid plane parallel to the y-axis (x=±3, ±2, ±1, 0 in.), the concentration would be highest at the centerline (y=0 in.) and would decrease toward the edge (y=2. In). This was true for all the grid planes parallel to the y-axis, except for one plane (x=0 in.). For this particular plane, x=0 in., number density was higher at y=1 in. rather than at y=0 in. This, as discussed later, was repeated for another test with this filter

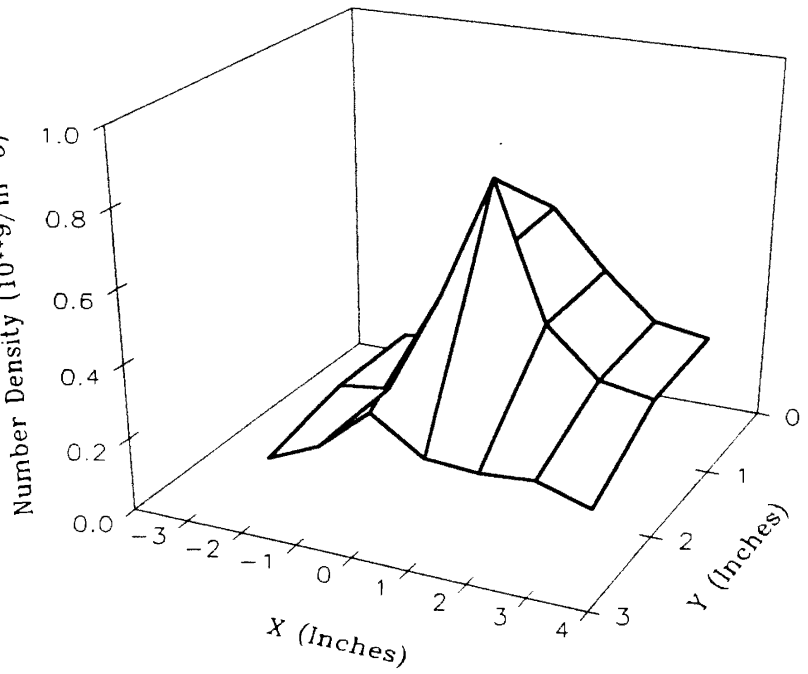

Figure 41. Three-Dimensional Plot of Number Density Distribution for Test D, at a Plane 6.625 In. Above the Filter Face

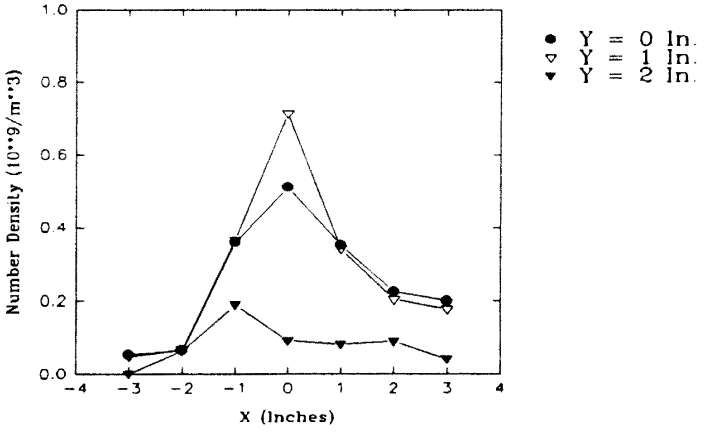

Figure 42. Two-Dimensional Plot of Number Density Distribution at Different Grid Sections for Test D, at a Plane 6.625 In. Above the Filter Face

at the same plane (test E) and was also observed for the measurements at a different plane with this filter (test C). Therefore, this deviation can be attributed to the typical filter used. Or else, it can well be argued that the number density need not necessarily be highest exactly at the center. The peak, instead, may exist at some other point close to the center. As discussed before, this may also be due to the preferential seeding along one of the walls of the stabilizing pipe.

As mentioned before, particle number density distribution should be investigated along with the flow distribution, so as to understand the relationship between the two. Therefore, for all of the measurements involved in this work, the corresponding velocity profiles were also investigated in conjunction with the particle number density distributions.

Figure 43 shows the corresponding three-dimensional plot of velocity profile at a plane 6.625 in. above the face of the filter for test D. The graph clearly shows that velocity is high at and around the center and decreases gradually toward the edges of the filter. Figure 44 is the corresponding two-dimensional plot obtained by slicing the three-dimensional plot of Fig. 43 as explained before for number density. The graph clearly shows that, for all the grid planes, the velocity is highest at the centerline (x=0 in.) and decreases toward the edges of the filter (x=±3 in.). However, for a grid plane further from the center (y=2 in.), the velocity is low and the profile shows relatively less variation with x-location. The graph clearly exhibits the symmetry for velocity profiles with respect to the central plane (x=0 in.). As expected, for grid planes parallel to the y-axis (x=±2, ±1, 0 in.), velocity is highest at the centerline (y=0 in.) and decreases toward the edge (y=2. in.). However, for grid planes at the edge (x=±3 in.), this may not necessarily be true because of the flow uncertainties and very low velocities involved.

Test D, therefore, suggests that at a plane far from the face of the filter, particles are concentrated toward the center of the filter as compared to the edges, and the number density distribution is fairly symmetrical for the left and right halves of the filter.

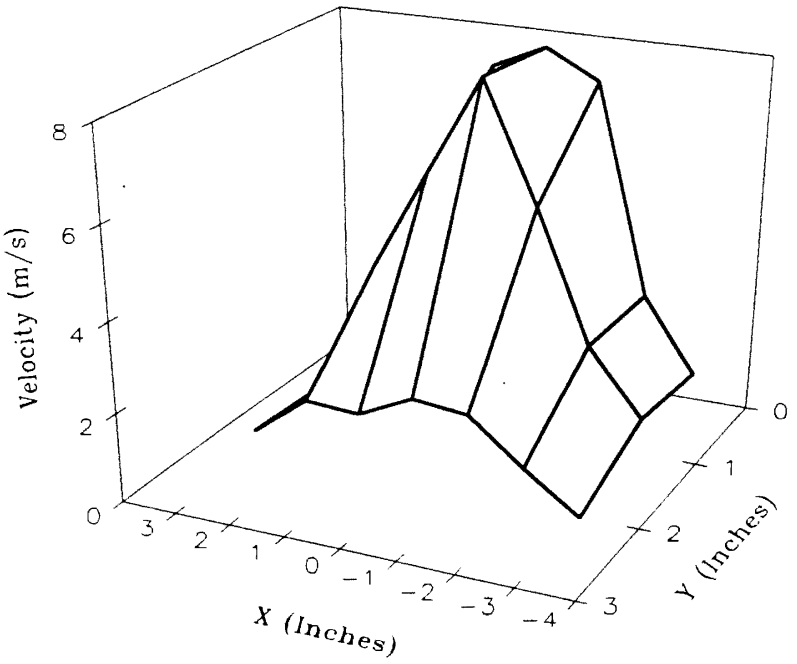

Figure 43. Three-Dimensional Plot of Velocity Profile for Test D, at a Plane 6.625 In. Above the Filter Face

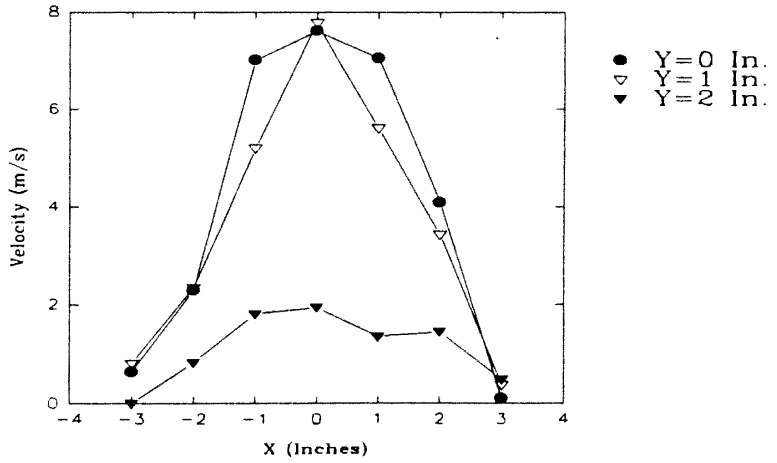

Figure 44. Two-Dimensional Plot of Velocity Profiles at Different Grid Sections for Test D, at a Plane 6.625 In. Above the Filter Face

However, the peak of the number density may not necessarily be at the exact center of the filter. The flow may have uncertainties at the edges.

Symmetry was expected between the front and the rear halves of the filter with regard to flow and particle number density distribution. To investigate this symmetry, another test (test E) was performed. As shown in Table 4, the same filter as for test D was used. Also the humidifier setting, the software parameter setup and the grid were same as for test D. A laser power of 3.5 watts was used as before. This time, however, measurements were taken also for the rear half of the filter.

Figure 45 shows the three-dimensional number density distribution over the face of the filter for test E. From the figure, it is observed that the number density is not highest at the center. Instead, it peaks at x=0 in. and y=±1 in. As mentioned before, two-dimensional plots were used to investigate the details of the number density distribution. Figures 46 and 47 are the two-dimensional plots of the number density distribution for the front (positive y-axis direction) and the rear (negative y-axis direction) halves of the filter, respectively. It is observed from Figs. 46 and 47 that the symmetry that was exhibited in the previous test with respect to the plane x=0 in. is missing. The number density is highest at the center (x=0 in.) and decreases toward the edges only for the planes y=±1 in. Also for all of the planes (y=±1, ±2, 0 in.), an unusually high number density was obtained at the x=-3 in. This could be due to some change in pleats of the filter at x=-3 in. location. As in the previous test (test D), for the plane x=0 in., the number density was higher at y=1 in. (and also y=-1 in.) rather than at y=0 in. To investigate the symmetry between the front and the rear halves of the filter, two-dimensional plots of number density were obtained at different grid planes parallel to the y-axis (along the breadth of the filter). These are shown in Figs. 48 and 49. These graphs suggest that symmetry does not exist with regard to number density between the front and the rear halves of the filter. But it can well be argued that, since the symmetry that was observed in the previous test (test D) between the left and right halves of the filter (along the x-axis) had also disappeared in this

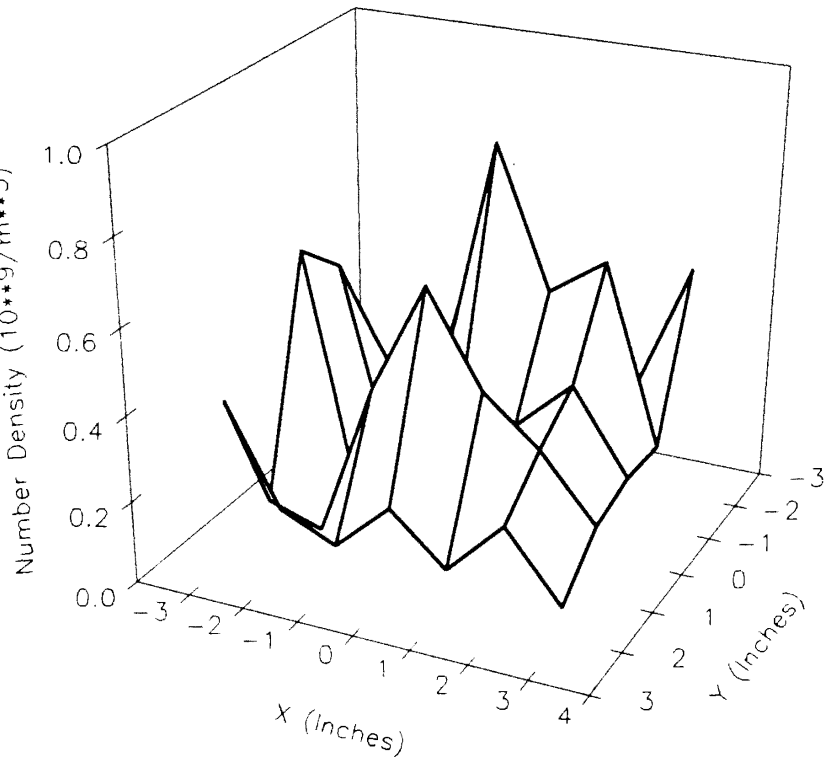

Figure 45. Three-Dimensional Plot of Number Density Distribution for Test E, at a Plane 6.625 In. Above the Filter Face

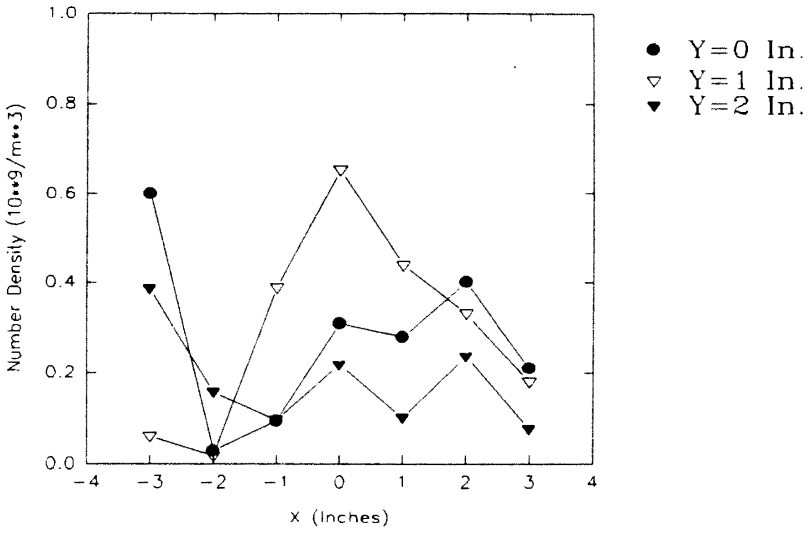

Figure 46. Two-Dimensional Plot of Number Density Distribution at Different Grid Sections for Test E, at a Plane 6.625 In. Above the Filter Face

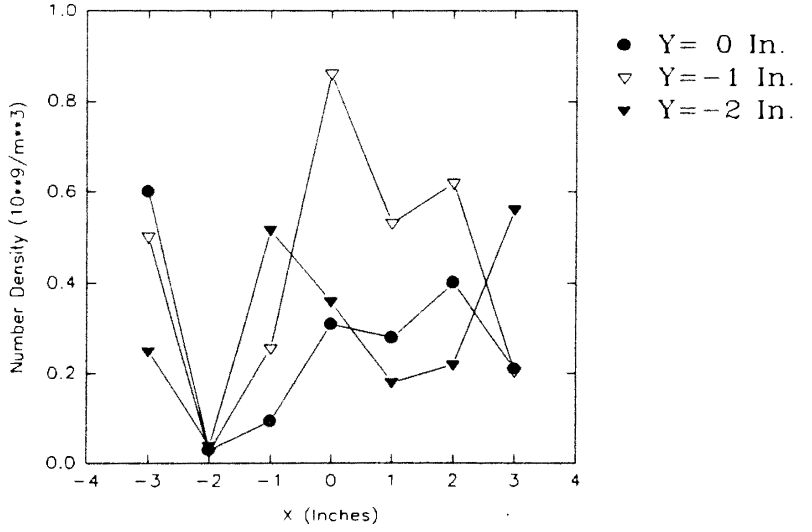

Figure 47. Two-Dimensional Plot of Number Density Distribution at Different Grid Sections for Test E, at a Plane 6.625 In. Above the Filter Face

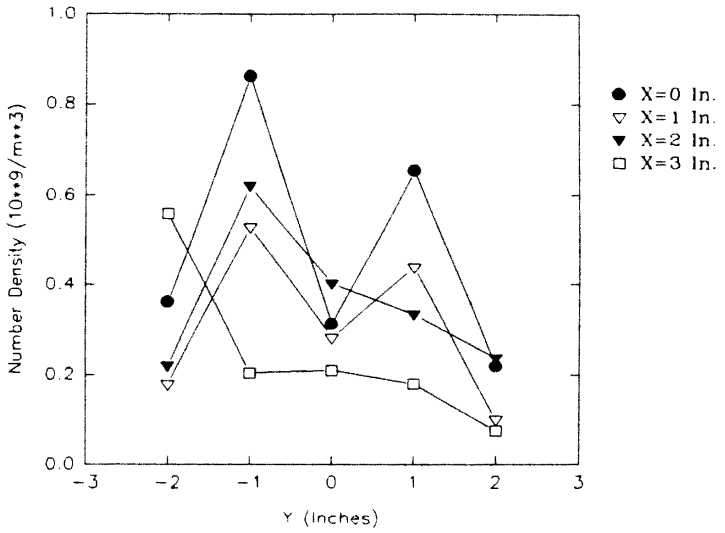

Figure 48. Two-Dimensional Plot of Number Density Distribution at Different Grid Sections for Test E, at a Plane 6.625 In. Above the Filter Face

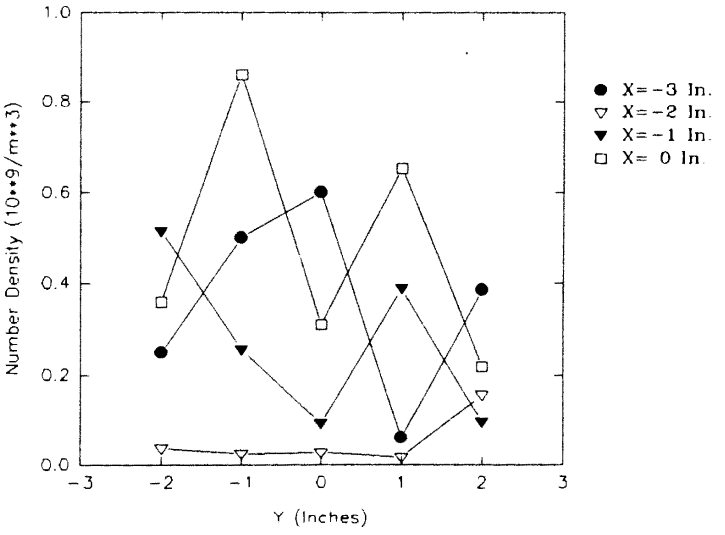

Figure 49. Two-Dimensional Plot of Number Density Distribution at Different Grid Sections for Test E, at a Plane 6.625 In. Above the Filter Face

test, it could be possible that symmetry existed in test D between the front and rear halves of the filter, and for this particular test, it was not exhibited.

Figures 50, 51, and 52 are comparisons of number densities for tests D and E at grid planes y=0 in., y=1 in., and y=2 in., respectively. These graphs clearly show that the number density varied considerably from one test to the other. Only for the plane y=1 in., the number densities were comparable for the two tests and showed the same profile.

To investigate any variation in the flow between the two tests, velocity profiles were plotted. Figure 53 shows the three-dimensional plot of velocity profile for test E. It is important to note that this figure shows measurements also for the rear half of the filter. The graph clearly shows that, as observed for test D, velocity is high at and around the center and decreases gradually toward the edges of the filter. Symmetry is observed between the front and rear halves of the filter. Figures 54 and 55 are the two-dimensional plots of velocity profiles at different grid planes parallel to the x-axis, for the front and rear halves of the filter, respectively. As observed for test D, these figures also show that for all of the grid planes, the velocity is highest at the centerline (x=0 in.) and decreases toward the edges of the filter (x=±3 in.). As before, the graphs clearly exhibit the symmetry for velocity profiles with respect to the central plane (x=0 in.). Also, as observed for test D, for grid planes parallel to the y-axis (x=±2, ±1, 0 in.), velocity is highest at the centerline (y=0 in.) and decreases toward the edges (y=±2 in.). However, for grid planes at the edge (x=±3 in.), this may not be necessarily true because of the flow uncertainties and very low velocities involved. These graphs also confirm the symmetry between the front and rear halves of the filter with regard to velocity profiles.

Figures 56, 57, and 58 are comparisons of the velocity profiles for the front half of the filter for tests D and E. It is observed that the velocity profiles for the two tests are almost identical. Only for the plane far off from the center (y=2 in.), velocities have increased at and around the center (x=0, ±1 in.) for test E.

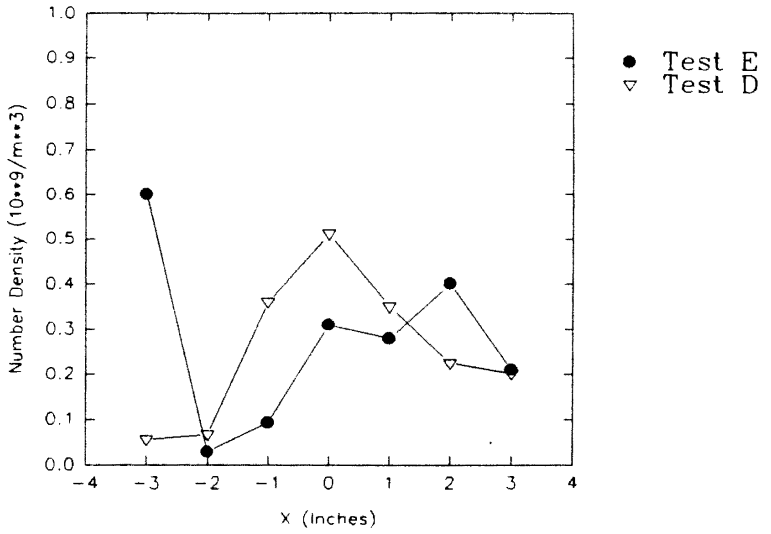

Figure 50. Comparison of Number Densities for Tests D and E, at Y=0 In. for a Plane 6.625 In. Above the Filter Face

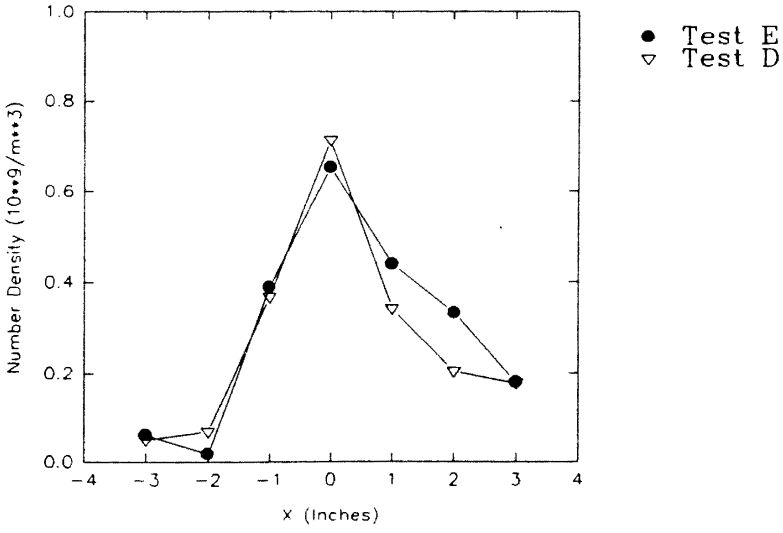

Figure 51. Comparison of Number Densities for Tests D and E, at Y=1 In. for a Plane 6.625 In. Above the Filter Face

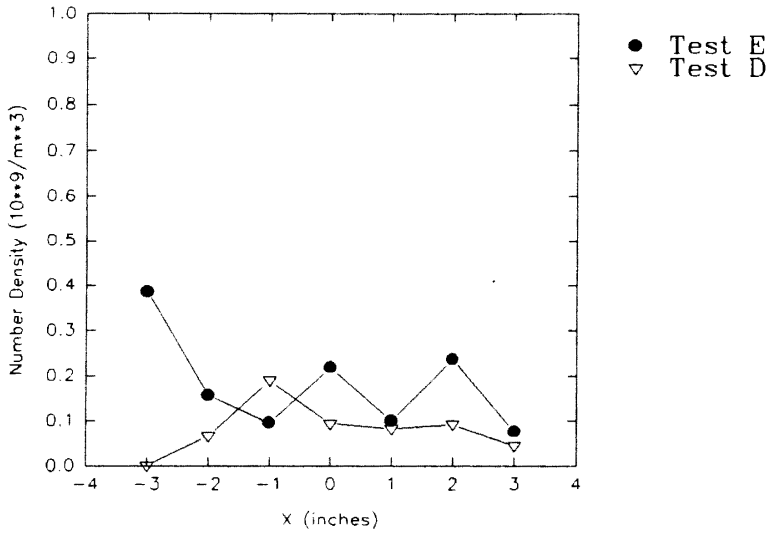

Figure 52. Comparison of Number Densities for Tests D and E, at Y=2 In. for a Plane 6.625 In. Above the Filter Face

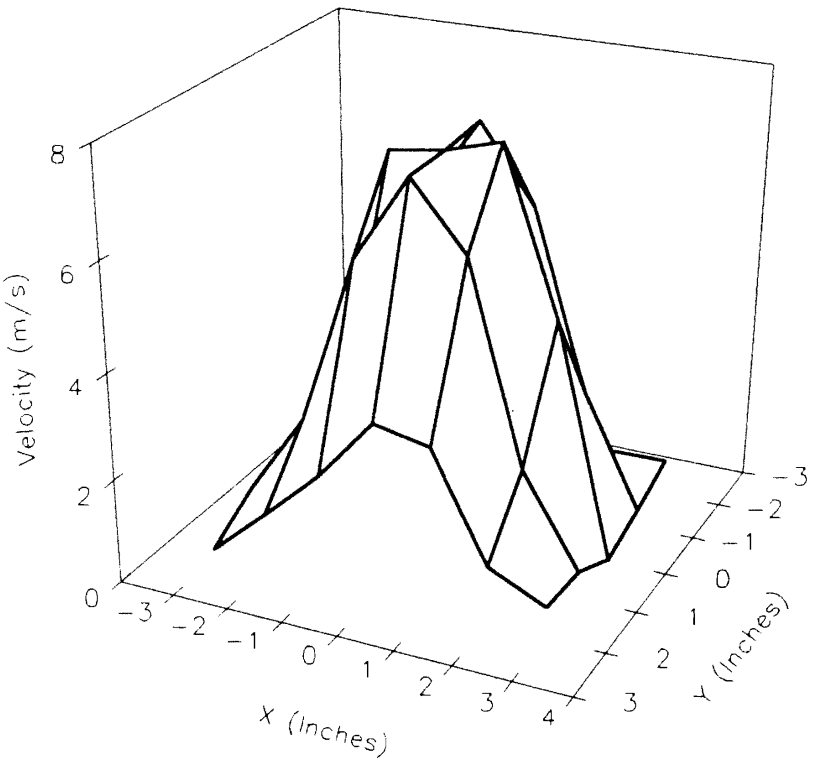

Figure 53. Three-Dimensional Plot of Velocity Profile for Test E, at a Plane 6.625 In. Above the Filter Face

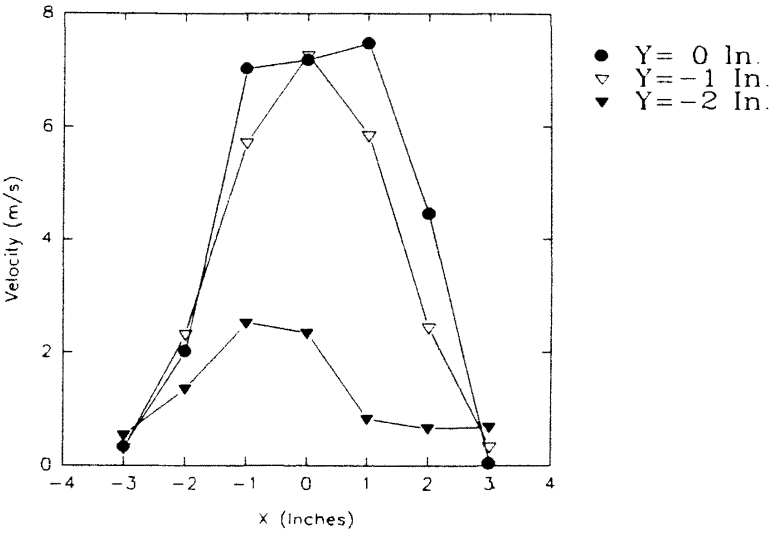

Figure 54. Two-Dimensional Plot of Velocity Profiles at Different Grid Sections for Test E, at a Plane 6.625 In. Above the Filter Face

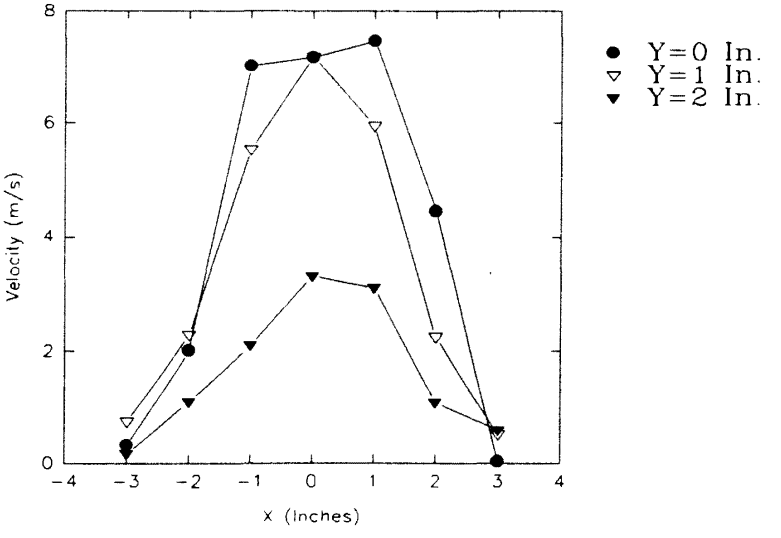

Figure 55. Two-Dimensional Plot of Velocity Profiles at Different Grid Sections for Test E, at a Plane 6.625 In. Above the Filter Face

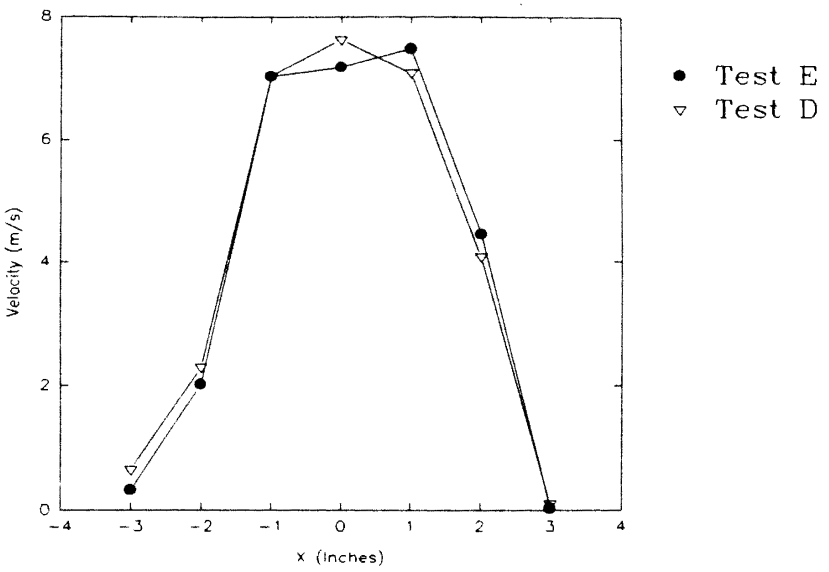

Figure 56. Comparison of Velocity Profiles for Tests D and E, at Y=0 In. for a Plane 6.625 In. Above the Filter Face

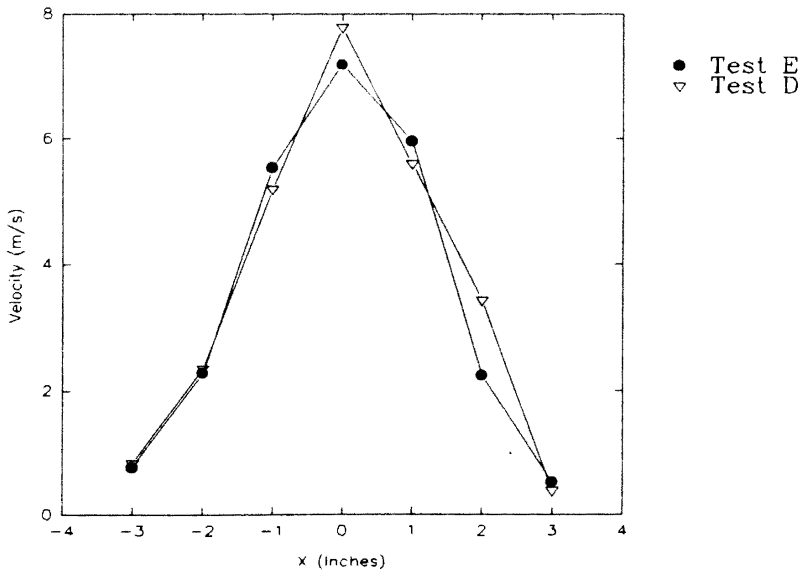

Figure 57. Comparison of Velocity Profiles for Tests D and E, at Y=1 In. for a Plane 6.625 In. Above the Filter Face

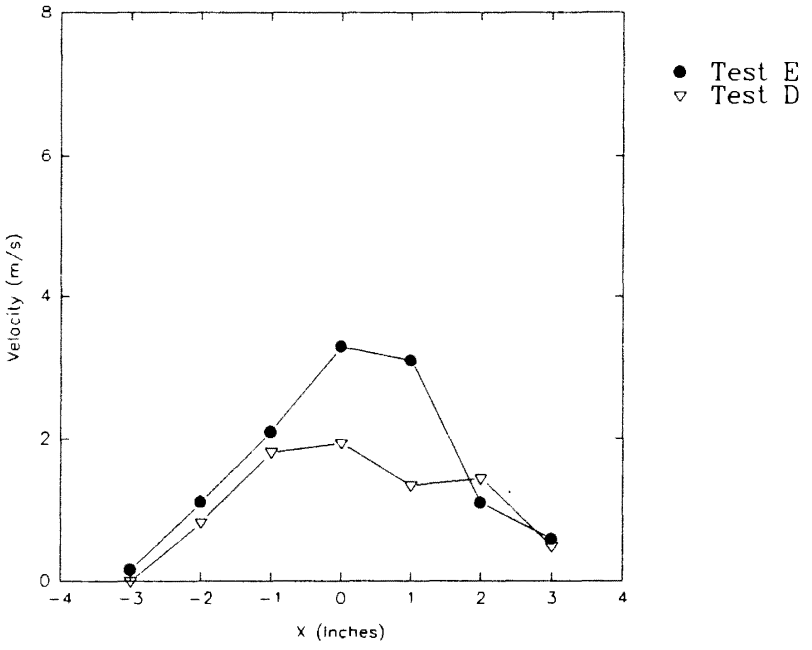

Figure 58. Comparison of Velocity Profiles for Tests D and E, at Y=2 In. for a Plane 6.625 In. Above the Filter Face

It is observed that the velocity profiles have not changed much for the two tests (tests D and E). However, the number density distribution seemed to be highly unpredictable. The various uncertainties involved with the seeding may have been responsible for this. The unsteady rate of water particle generation by the humidifier, the non-uniform and random manner in which the water particles are pulled into the stabilizing pipe of the housing, the absolute randomness with which seeding particles are mixed into the flow in the stabilizing pipe, and the possible flow uncertainties; all may have been responsible for the random number density distribution. It is worth mentioning that, evaporation of water droplets within the housing is believed to be highly improbable. Considering an approximate average velocity (from housing inlet to the filter face) of 5 ft./sec, and approximate height of 1 ft. of the housing, water droplets have only 0.2 sec to get evaporated. Moreover, the atmosphere within the housing was visually observed to be highly humid with water accumulating at the base plate, further ruling out the possibility of evaporation of water droplets.

Measurements at a Plane 3.625 In. Above the Filter Face

Figure 59 shows the three-dimensional number density distribution for test C. As shown in Table 5, test C was conducted at a plane 3.625 inches above the face of the filter. From Table 4, it is observed that tests D and E used the same filter as was used for test C. It is also observed that the grid used, the humidifier setting, and the parameter setup employed were also same for tests D, E and C. As mentioned before, a laser power of 3.5 watts was used. It is important to mention that measurements for test C were taken only for the front half of the filter. Hence, Fig. 59 represents number density distribution only for the front half of the filter (positive y-axis direction). From the figure it is observed that the number density is high around the center and it decreases toward the edges of the filter.

As mentioned before, two-dimensional plots were used to have a better insight into the number density distribution. Figure 60 shows a two-dimensional plot of particle number density distribution at different grid planes parallel to the x-axis (along the length of the filter). The graph clearly shows that, for all of the grid planes, the number density is highest at the centerline (x=0 in.) and decreases toward the edges of the filter (x=±3 in.). Also a very good symmetry is exhibited by the number density profiles with respect to the plane x=0 in. It was again expected that, for any grid plane parallel to the y-axis (x=±3, ± 2, ±1, 0 in.), concentration would be highest at the centerline (y=0 in.) and would decrease toward the edge (y=2 in.). As for tests D and E, this was true for all of the grid planes parallel to the y-axis, except for one plane (x=0 in.). For this particular plane, x=0 in., number density was higher at y=1 in. rather than at y=0 in.

Figure 61 shows the three-dimensional plot of velocity profile at the plane 3.625 in. above the face of the filter for test C. The graph clearly shows that velocity is high at and around the center and decreases gradually toward the edges of the filter. Figure 62 is the corresponding two-dimensional plot obtained by slicing the three-dimensional plot of Fig. 61. The graph clearly shows that, for all of the grid planes, the velocity is highest at the centerline (x=0 in.) and decreases toward the edges of the filter (x=±3 in.). The graph clearly exhibits symmetry for velocity profiles with respect to the central plane (x=0 in.). As expected, for grid planes parallel to y-axis (x=-3, 2, ±1, 0), velocity is highest at the centerline (y=0 in.) and decreases toward the edge (y=2 In). However, for the planes x=3 in. and x=-2 in., this was not true. This, as mentioned before, may be due to flow uncertainties.

Figure 63 shows the three-dimensional number density distribution for test K. As shown in Table 5, this test was also conducted at a plane 3.625 in. above the face of the filter. As shown in Table 4, an old filter was used for this test. A coarser grid of 1.875 in. by 1.188 inches was used for taking measurements, and the humidifier was operating at a medium level of mist intensity. Software parameter setup IV was employed for this test.

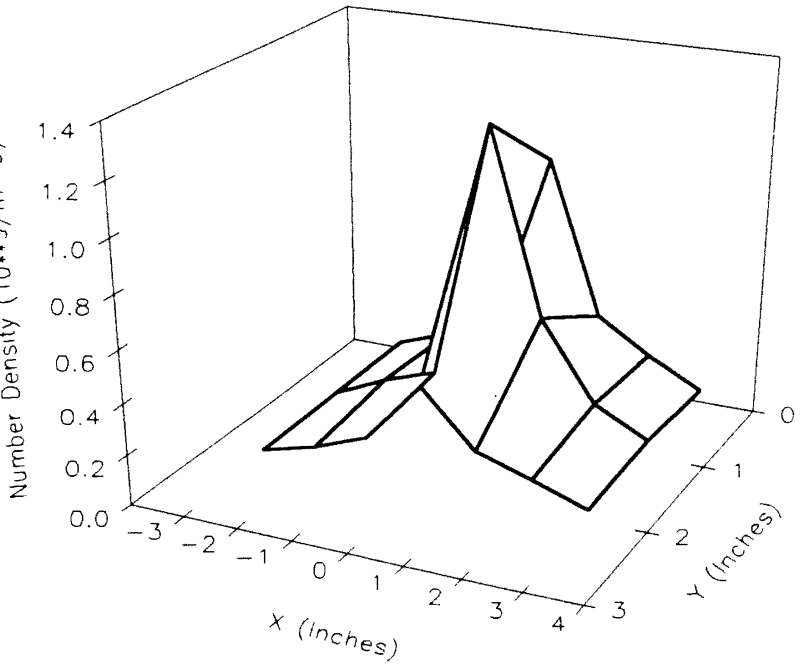

Figure 59. Three-Dimensional Plot of Number Density Distribution for Test C, at a Plane 3.625 In. Above the Filter Face

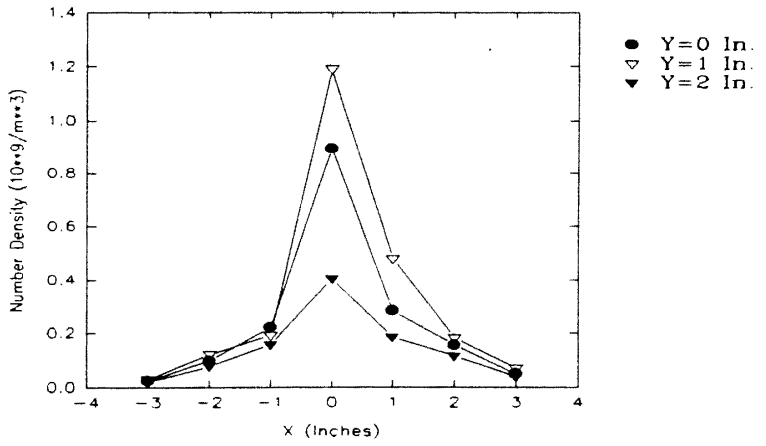

Figure 60. Two-Dimensional Plot of Number Density Distribution at Different Grid Sections for Test C, at a Plane 3.625 In. Above the Filter Face

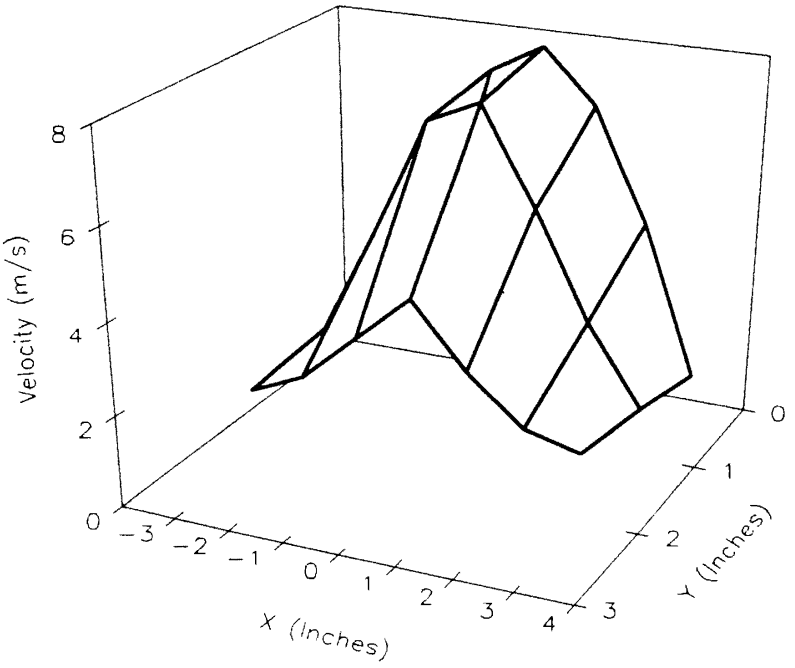

Figure 61. Three-Dimensional Plot of Velocity Profile for Test C, at a Plane 3.625 In. Above the Filter Face

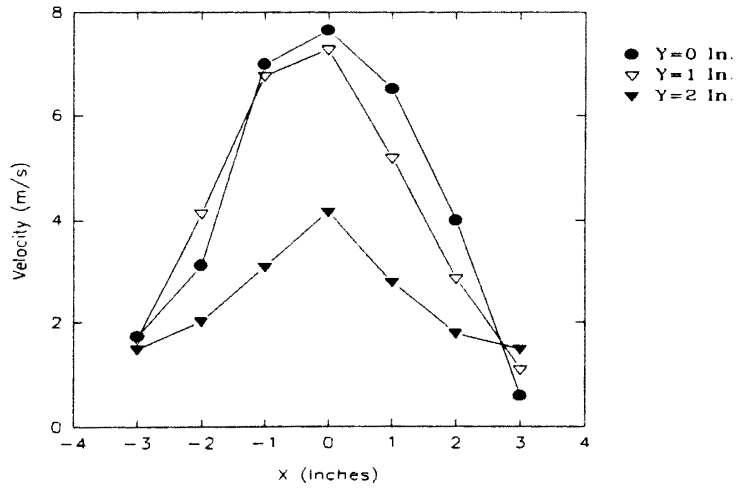

Figure 62. Two-Dimensional Plot of Velocity Profiles at Different Grid Sections for Test C, at a Plane 3.625 In. Above the Filter Face

It is important to mention that the laser was operating at 8 Vdc (which also corresponds to saturation). Measurements were taken only for the front half of the filter. From Fig. 63, it is evident that number density is high at and around the center and decreases toward the edges of the filter.

Figure 64 shows the corresponding two-dimensional plot of number density distribution at different planes parallel to the x-axis. The graph clearly shows that for all of the grid planes, the number density is highest at the centerline (x=0 in.) and decreases toward the edges of the filter (x=±3.75 in.). It is observed that, for the grid planes y=0 in. and y= 1.188 in., the number densities are almost the same for the right half of the filter. A very good symmetry is exhibited by the number density profile for the grid plane y=2.375 in., which is far from the center. However, for the grid planes y=0 in. and y=1.118 in., it is observed that, for the right half of the filter, the number density drop is steeper as compared to that for the left half of the filter. This may be due to the blower which was connected to the right side of the filter. This may also be attributed to the preferential seeding as discussed before. As expected, for any grid plane parallel to y-axis (x=±3.75, ±1.875, 0 in.) concentration is highest at centerline (y=0 in.) and decreases toward the edge (y=2.375 in.).

Figure 65 shows the three-dimensional plot of velocity profile for test K. The graph clearly shows that velocity is high at and around the center and decreases gradually toward the edges of the filter. Figure 66 is the corresponding two-dimensional plot obtained by slicing the three-dimensional plot of Fig. 65. The graph clearly shows that for all of the grid planes, the velocity is highest at the centerline (x=0 in.) and decreases toward the edges of the filter (x=±3.75 in.). As observed for the number density profiles, the velocity profiles for the grid planes y=1.188 in. and y=2.375 in. also show a steeper drop for the right half of the filter as compared to the left half. Also, as observed for the number density profiles, for the grid planes y=1.188 in. and y=2.375 in., the velocities are almost identical for the right half of the filter. As for number density, a very good

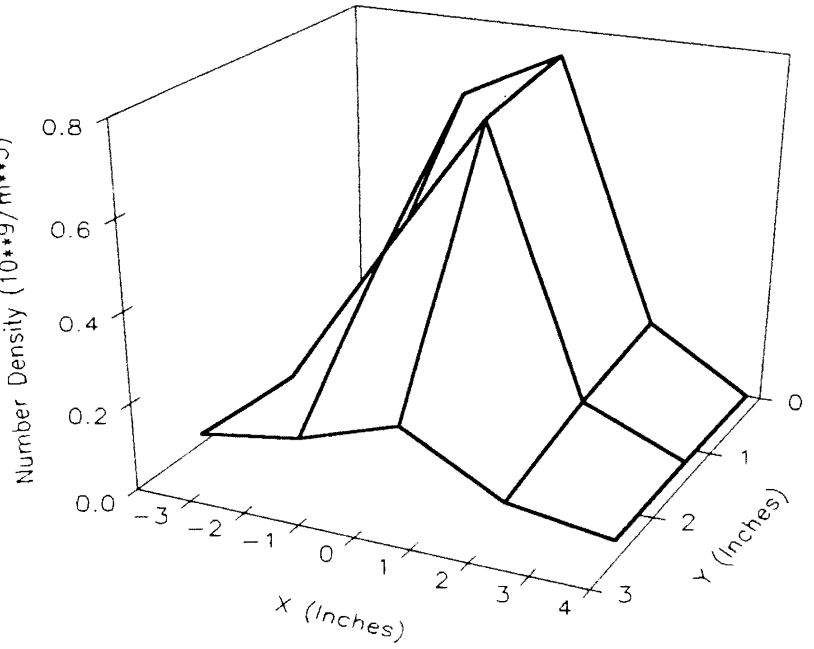

Figure 63. Three-Dimensional Plot of Number Density Distribution for Test K, at a Plane 3.625 In. Above the Filter Face

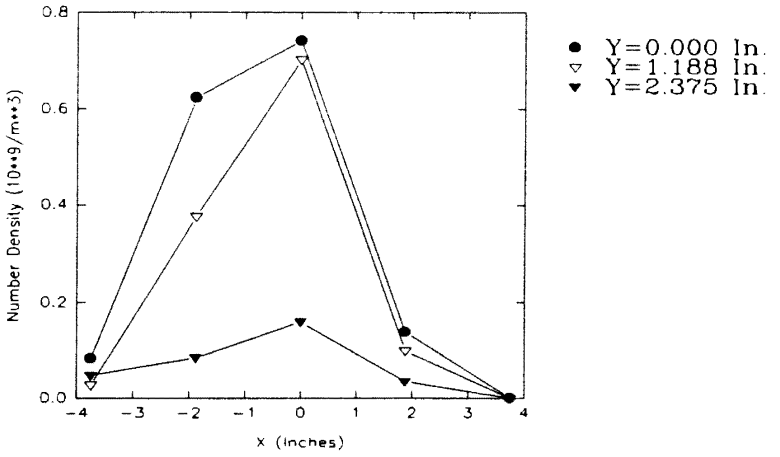

Figure 64. Two-Dimensional Plot of Number Density Distribution at Different Grid Sections for Test K, at a Plane 3.625 In. Above the Filter Face

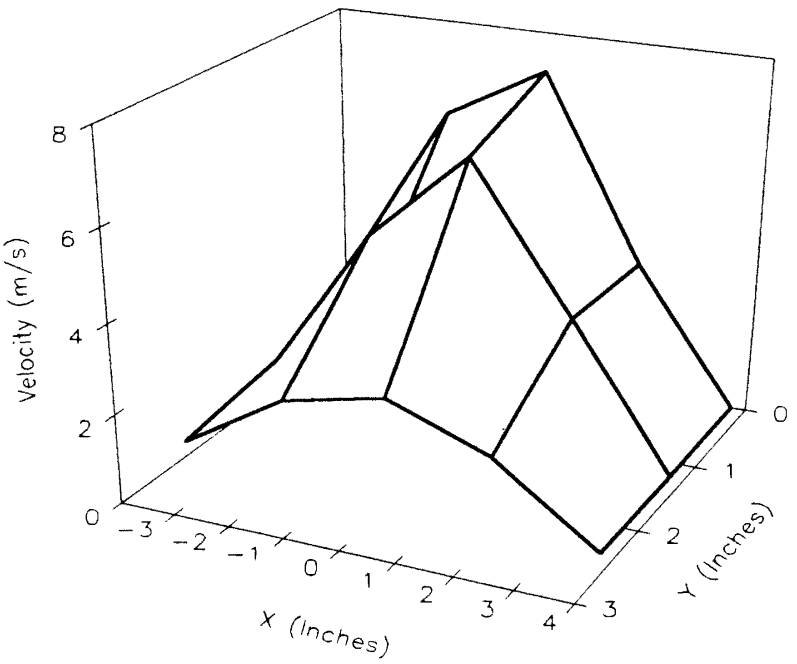

Figure 65. Three-Dimensional Plot of Velocity Profile for Test K, at a Plane 3.625 In. Above the Filter Face

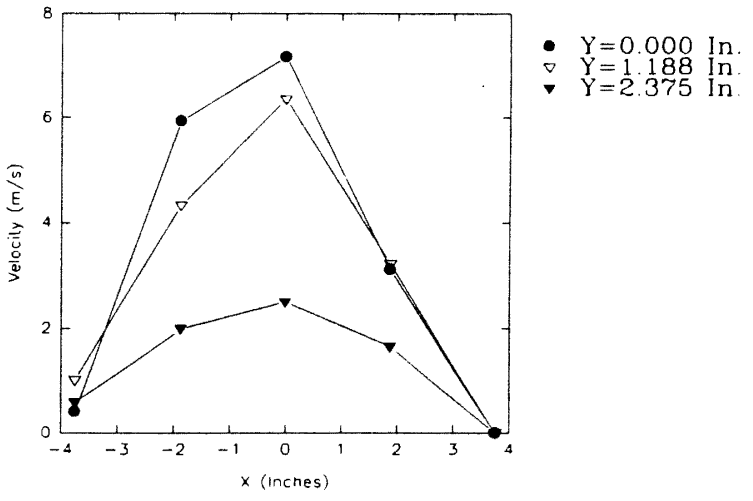

Figure 66. Two-Dimensional Plot of Velocity Profiles at Different Grid Sections for Test K, at a Plane 3.625 In. Above the Filter Face

symmetry is exhibited by the velocity profile for the grid plane y=2.375 in., which is far from the center. As expected, for the grid planes parallel to the y-axis (x=3.75, ±1.875, 0 in.), velocity is highest at the centerline (y=0 in.) and decreases toward the edge (y=2. in.). However, for the grid plane at the edge (x=-3 in.), this was not true because of the flow uncertainties and the very low velocities involved.

Tests C and K, therefore, suggest again that particles are concentrated toward the center of the filter as compared to the edges, and the number density distribution is fairly symmetrical for the left and right halves of the filter. The tests also suggest that the flow may have uncertainties, especially at the edges.

To explore the symmetry between the front and rear half of the filter at a plane 3.625 in. above the face of the filter, another test (test G) was performed with a new filter. As observed from Table 4, the humidifier setting, the grid and the governing software parameter setup were same as for test C. A laser power of 3.5 watts was used as before. Measurements were taken for the front half as well as for the rear half of the filter. Figure 67 shows the three-dimensional number density distribution over the face of the filter. Figures 68 and 69 are the two-dimensional plots of the number density distribution for the front (positive y-axis direction) and the rear (negative y-axis direction) halves of the filter, respectively. From the figures, it is observed that there is some degree of symmetry between the left and right halves of the filter for all of the grid planes parallel to the x-axis except for the central plane y=0 in. For this particular plane, the number density seems to gradually increase from the left extreme (x=-3 in.) of the filter to the point x=2 in., and then it drops down for the right extreme of the filter (x=3 in.). It is worth mentioning once again, that the blower to pull air was also connected to the right side of the housing at the plane y=0 in. The number density peaked slightly off-center at x=0 in. and y=1 in. It is observed that the number density is certainly low at the edges of the filter, though it can be low even at certain points on the filter which are not at the edges. The number density is highest at the center and decreases toward the edges only for the grid plane y=1

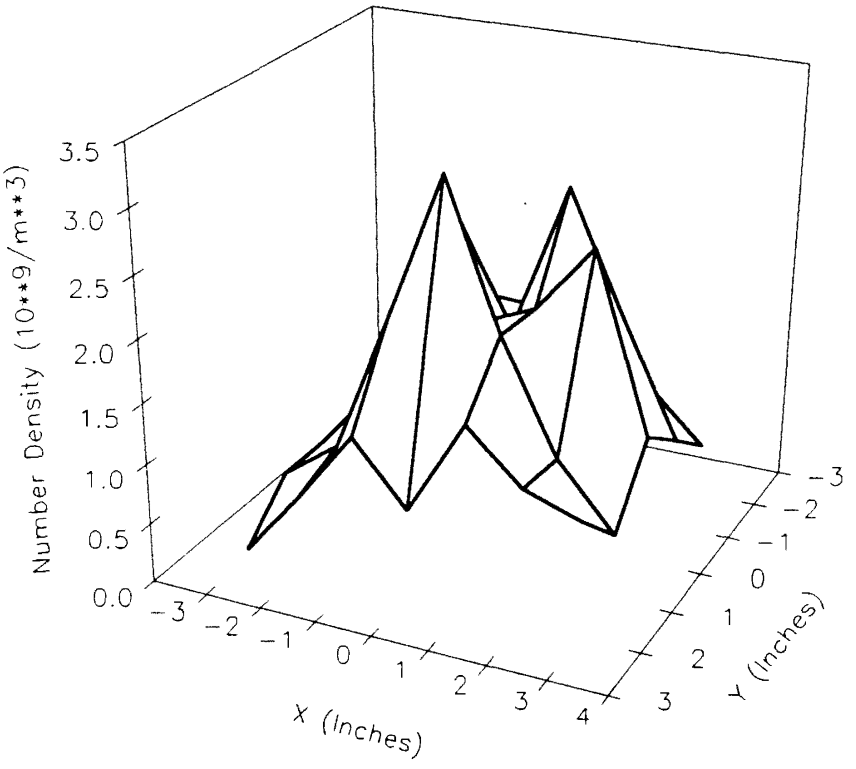

Figure 67. Three-Dimensional Plot of Number Density Distribution for Test G, at a Plane 3.625 In. Above the Filter Face

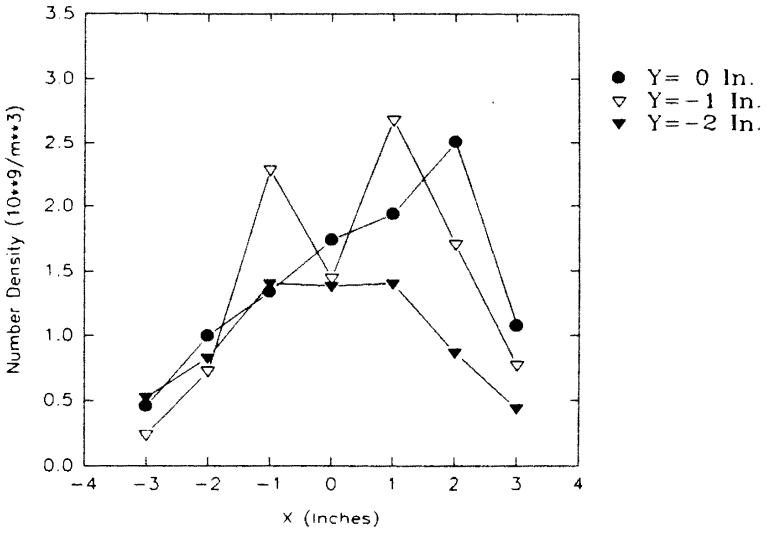

Figure 68. Two-Dimensional Plot of Number Density Distribution at Different Grid Sections for Test G, at a Plane 3.625 In. Above the Filter Face

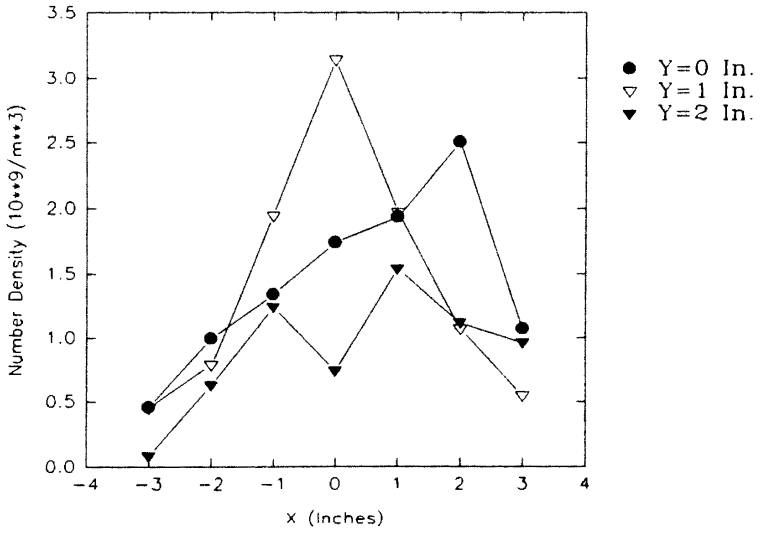

Figure 69. Two-Dimensional Plot of Number Density Distribution at Different Grid Sections for Test G, at a Plane 3.625 In. Above the Filter Face

in. The center (x=0 in.) shows a dip for the grid planes y=2 in. and y=-1 in. As mentioned before, symmetry between the front and the rear halves of the filter was investigated by plotting number density at different grid planes parallel to y-axis. These plots are shown in Figs. 70 and 71. It is observed that, for the central plane x=0 in., the density distribution is asymmetric. For other grid planes, a slight degree of symmetry is observed.

Figures 72, 73, and 74 are comparisons of number densities for tests C, K and G. It is observed that for test G, number densities are much higher than for tests C and K. This may be due to better seeding for test G. The profile of number density distribution is similar only for the grid plane y=1 in. For tests C and K, number densities are close.

Figure 75 shows the three-dimensional plot of velocity profile for test G. The graph clearly shows that, as observed for test C, velocity is high at and around the center and decreases gradually toward the edges of the filter. Symmetry is observed between the front and the rear halves of the filter. Figures 76 and 77 are the two-dimensional plots of velocity profiles at different grid planes parallel to the x-axis, for the front and rear halves of the filter, respectively. These figures show that the velocity is high at and around the centerline (x=0 in.) and decreases toward the edges of the filter (x=±3 in.). As before, the graphs clearly exhibit the symmetry for velocity profiles with respect to the central plane (x=0 in.). Only for the central plane (y=0 in.), the velocity profile is shifted to the right peaking at x=1 in. instead of x=0 in. These graphs also confirm the symmetry between the front and rear halves of the filter with regard to velocity profiles.

Figures 78, 79 and 80 are comparisons of the velocity profiles for the front half of the filter for tests C, K and G. It is observed that the velocity profiles for the three tests exhibit the same shape, though most of the velocities are not exactly identical.

Therefore, it can be concluded that the particles tend to concentrate around the center, and that the number density is low at the edges of the filter. The exact peak and distribution however may depend upon the specific filter being tested.

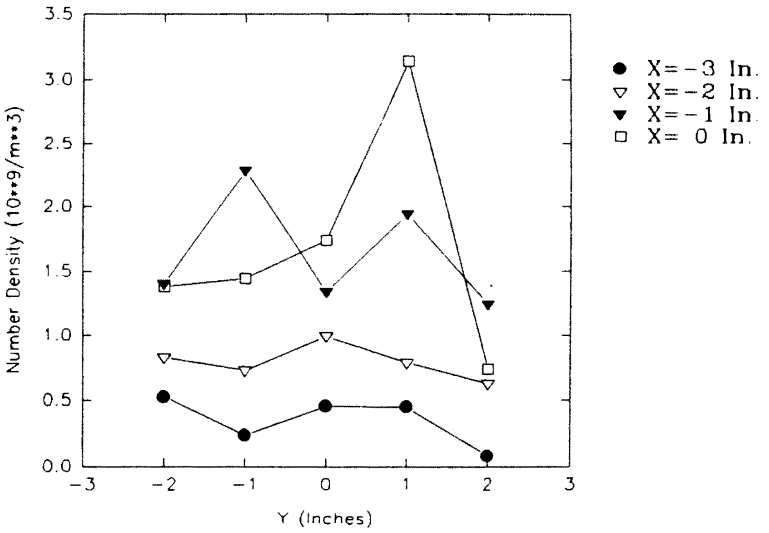

Figure 70. Two-Dimensional Plot of Number Density Distribution at Different Grid Sections for Test G, at a Plane 3.625 In. Above the Filter Face

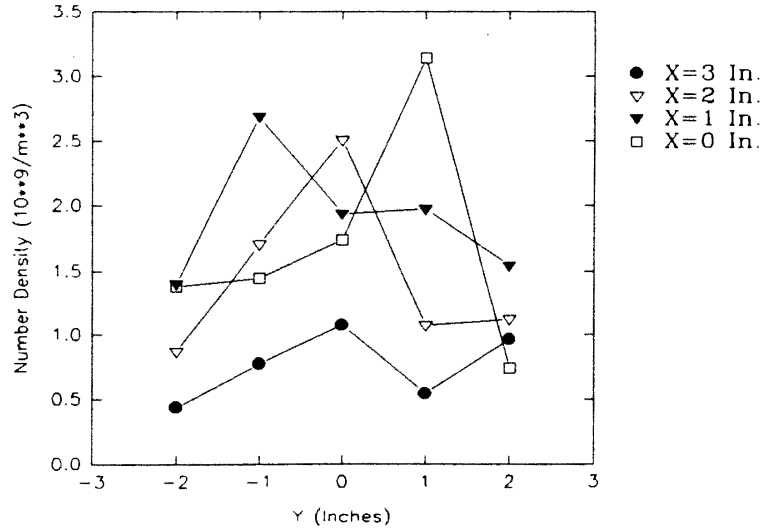

Figure 71. Two-Dimensional Plot of Number Density Distribution at Different Grid Sections for Test G, at a Plane 3.625 In. Above the Filter Face

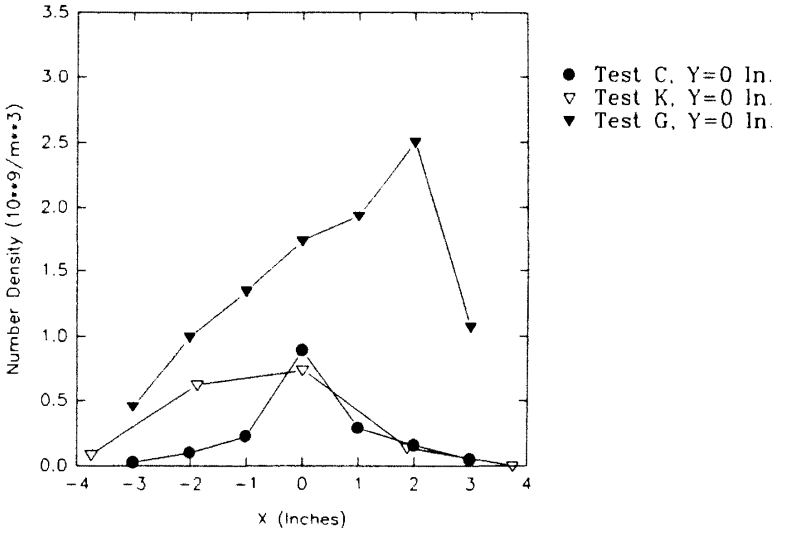

Figure 72. Comparison of Number Densities for Tests C, K and G at Y=0 In. for a Plane 3.625 In. Above the Filter Face

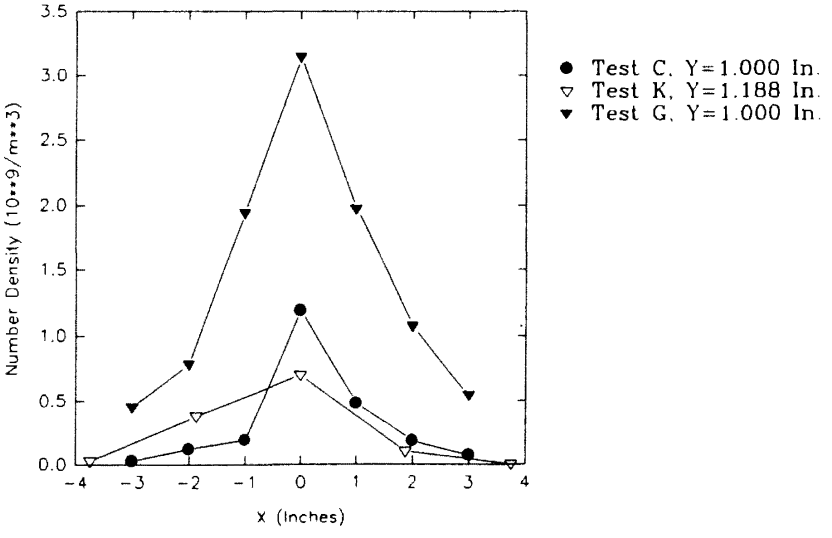

Figure 73. Comparison of Number Densities for Tests C, K and G at Y=1 In. for a Plane 3.625 In. Above the Filter Face

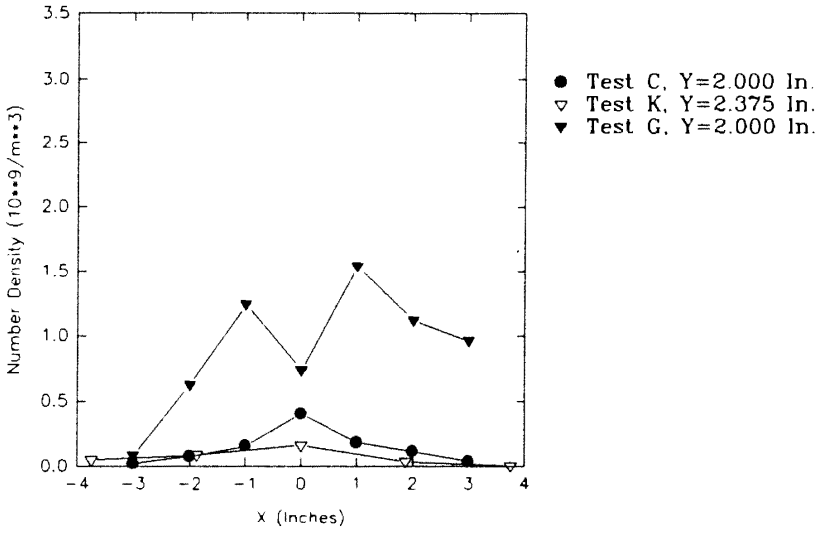

Figure 74. Comparison of Number Densities for Tests C, K and G at Y=2 In. for a Plane 3.625 In. Above the Filter Face

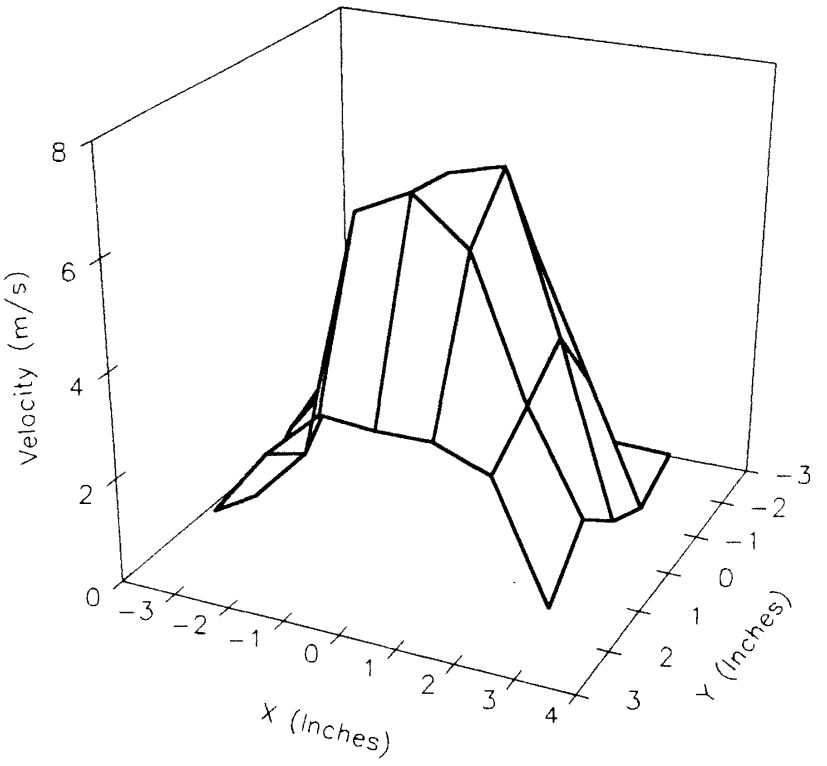

Figure 75. Three-Dimensional Plot of Velocity Profile for Test G, at a Plane 3.625 In. Above the Filter Face

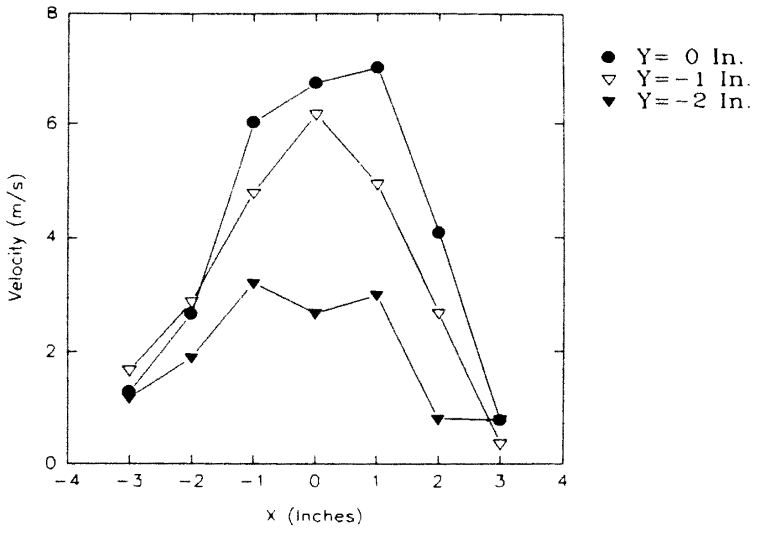

Figure 76. Two-Dimensional Plot of Velocity Profiles at Different Grid Sections for Test G, at a Plane 3.625 In. Above the Filter Face

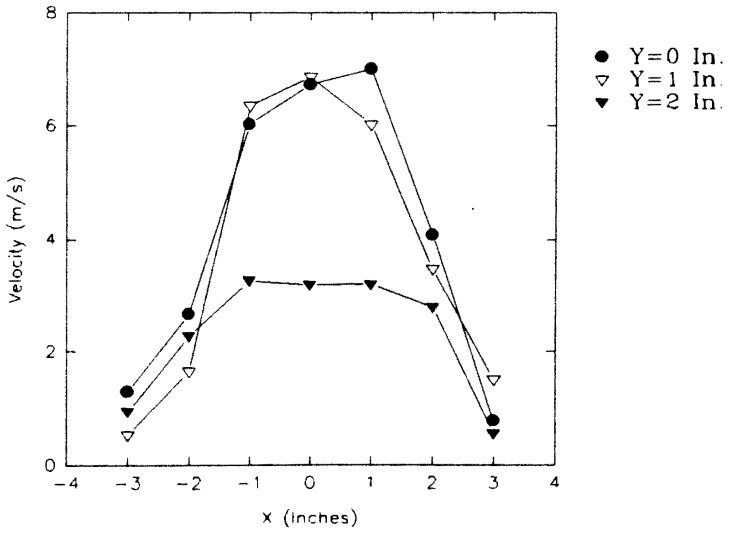

Figure 77. Two-Dimensional Plot of Velocity Profiles at Different Grid Sections for Test G, at a Plane 3.625 In. Above the Filter Face

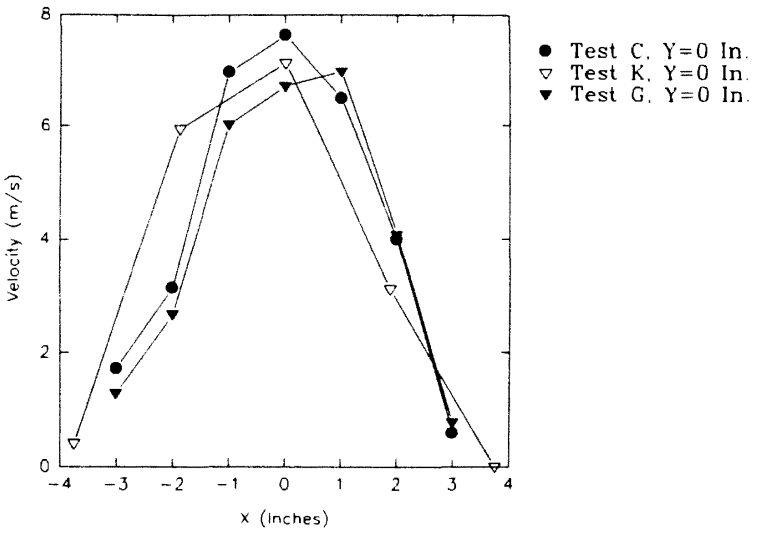

Figure 78. Comparison of Velocity Profiles for Tests C, K and G at Y=0 In. for a Plane 3.625 In. Above the Filter Face

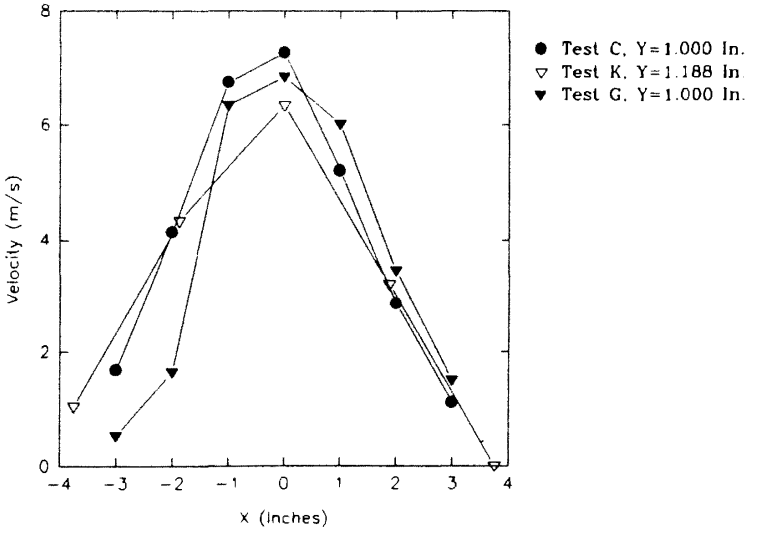

Figure 79. Comparison of Velocity Profiles for Tests C, K and G at Y=1 In. for a Plane 3.625 In. Above the Filter Face

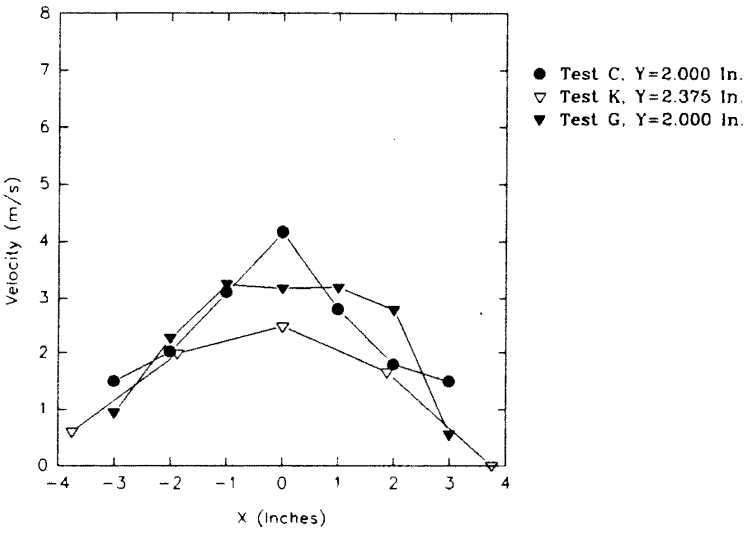

Figure 80. Comparison of Velocity Profiles for Tests C, K and G at Y=2 In. for a Plane 3.625 In. Above the Filter Face

Measurements at a Plane 2.125 In. Above the Filter Face

Test J, as shown in Table 5, was conducted at a plane 2.125 in. above the face of the filter. It is observed from Table 4 that test K also used the same filter as was used for test J. The humidifier setting, the grid and the software parameter setup were the same for tests K and J. The laser was operating at 8 Vdc. Measurements were taken only for the front half of the filter.

Figure 81 shows three-dimensional number density distribution for test J. From the figure, it is evident that number density is high at the center and decreases toward the edges of the filter. Figure 82 shows the corresponding two-dimensional plot of number density distribution at different planes parallel to the x-axis. The graph clearly shows that, for all of the grid planes, the number density is highest at the centerline (x=0 in.) and decreases toward the edges of the filter (x=±3.75 in.). A very good symmetry is exhibited by the number density profile for the grid plane y=2.375 in., which is far from the center. However, for the grid planes y=0 in. and y=1.118 in., it is observed that, for the right half of the filter, the number density drop is steeper as compared to that for the left half of the filter. This was observed for test K also. This may be due to the blower which was connected to the right side of the filter as suggested before, or it may be due to preferential seeding. This may also be attributed to the specific filter used. As expected, for the grid planes parallel to the y-axis (x=±3.75, ±1.875, 0 in.), concentration is highest at the centerline (y=0 in.) and decreases toward the edge (y=2.375 In).

Figure 83 shows the three-dimensional plot of velocity profile at a plane 2.125 in. above the face of the filter for test J. The graph clearly shows that velocity is high at and around the center and decreases gradually toward the edges of the filter. Figure 84 is the corresponding two-dimensional plot obtained by slicing the three-dimensional plot of Fig. 83. The graph clearly shows that, for all the grid planes, the velocity is highest at the centerline (x=0 in.) and decreases toward the edges of the filter (x= ±3.75 in.). As

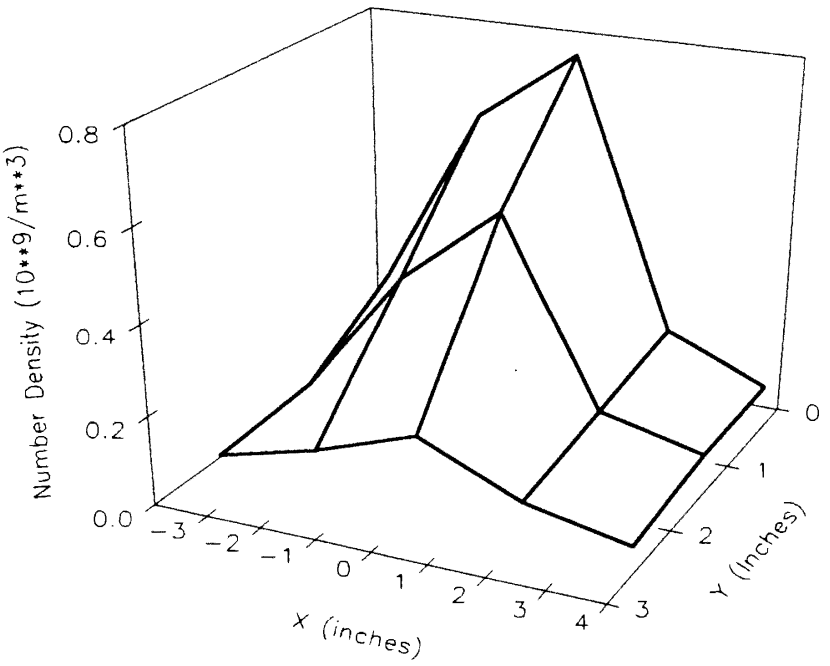

Figure 81. Three-Dimensional Plot of Number Density Distribution for Test J, at a Plane 2.125 In. Above the Filter Face

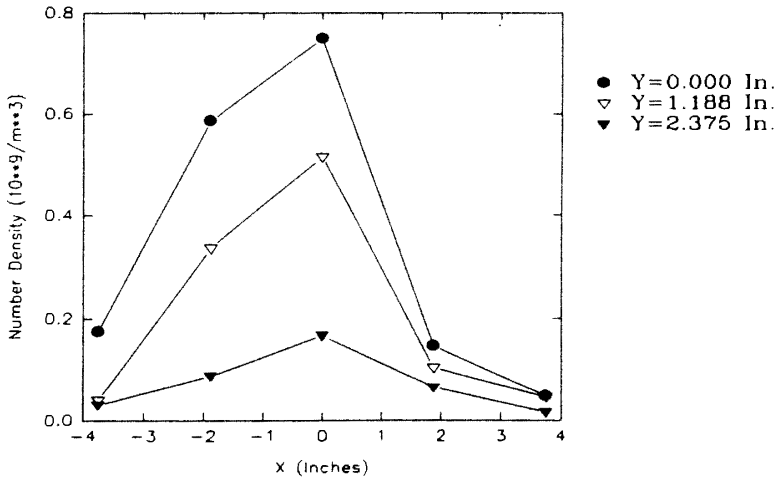

Figure 82. Two-Dimensional Plot of Number Density Distribution at Different Grid Sections for Test J, at a Plane 2.125 In. Above the Filter Face

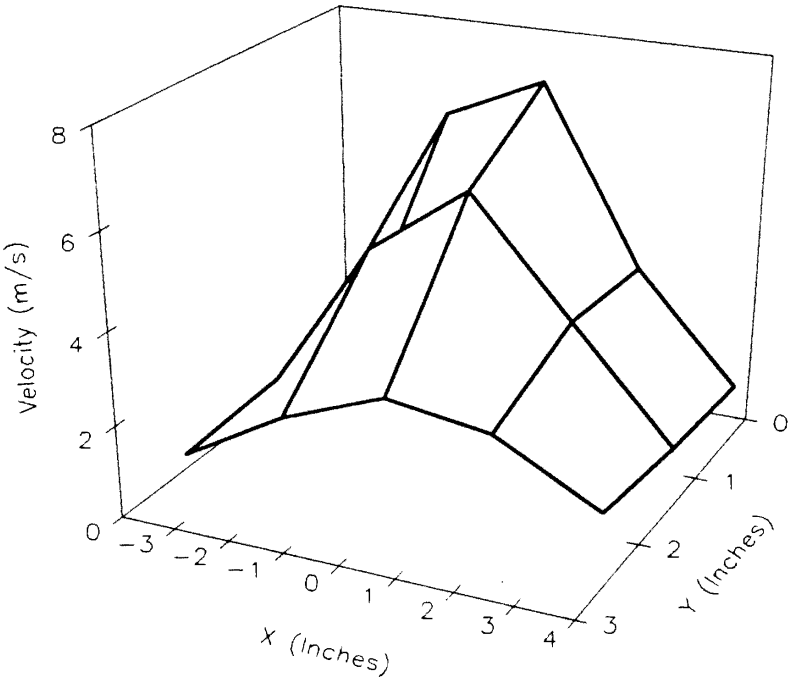

Figure 83. Three-Dimensional Plot of Velocity Profile for Test J, at a Plane 2.125 In. Above the Filter Face

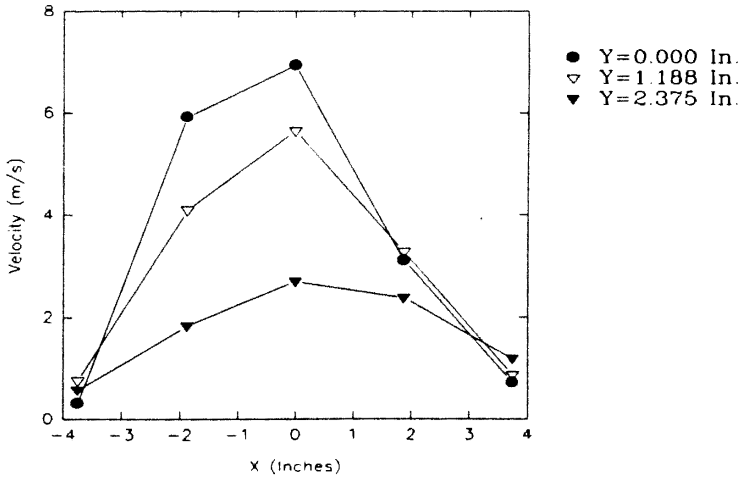

Figure 84. Two-Dimensional Plot of Velocity Profiles at Different Grid Sections for Test J, at a Plane 2.125 In. Above the Filter Face

observed for the number density profiles, the velocity profiles for the grid planes y=1.188 in. and y=2.375 in. also show a steeper drop for the right half of the filter as compared to the left half. This was also observed for test K. Also, as observed for the number density profiles and for test K, for the grid planes y=1.188 in. and y=2.375 in., the velocities are almost identical for the right half of the filter. A very good symmetry is exhibited by the velocity profiles for the grid planes y=1.188 in. and y=2.375 in. As expected, for the grid planes parallel to the y-axis (x=±1.875, 0 in.), velocity is highest at the centerline (y=0 in.) and decreases toward the edge (y=2. in.). For the grid planes at the edges (x=±3.75 in.) however, this was not true. Flow uncertainties, as mentioned before, may be responsible for this.

Test L, as shown in Table 5, was also performed at the same height of 2.125 in. above the face of the filter. As shown in Table 4, a new filter was used for the test. The humidifier was operating at high mist intensity. The grid used for this test was 0.938 in. by 0.792 in. Software parameter setup V was employed and the laser was operating at 8 Vdc. Measurements were taken only for a quarter of the filter.

Figure 85 shows three-dimensional number density distribution for test L. From the figure, it is evident that number density is high at the center and decreases toward the edges of the filter. Figure 86 shows the corresponding two-dimensional plot of number density distribution at different planes parallel to the x-axis. The graphs clearly show that, for all of the grid planes, the number density is highest at the centerline (x=0 in.) and decreases gradually toward the edge of the filter (x=3.75 in.). However, just at the corner of the filter, an unusually high number density is observed. It is important to note that number densities for all of the planes are very close to each other.

Figure 87 shows the three-dimensional plot of velocity profile at a plane 2.125 in. above the face of the filter for test L. The graph clearly shows that velocity is high at and around the center and decreases gradually toward the edge of the filter. Figure 88 is the corresponding two-dimensional plot obtained by slicing the three-dimensional plot of Fig.

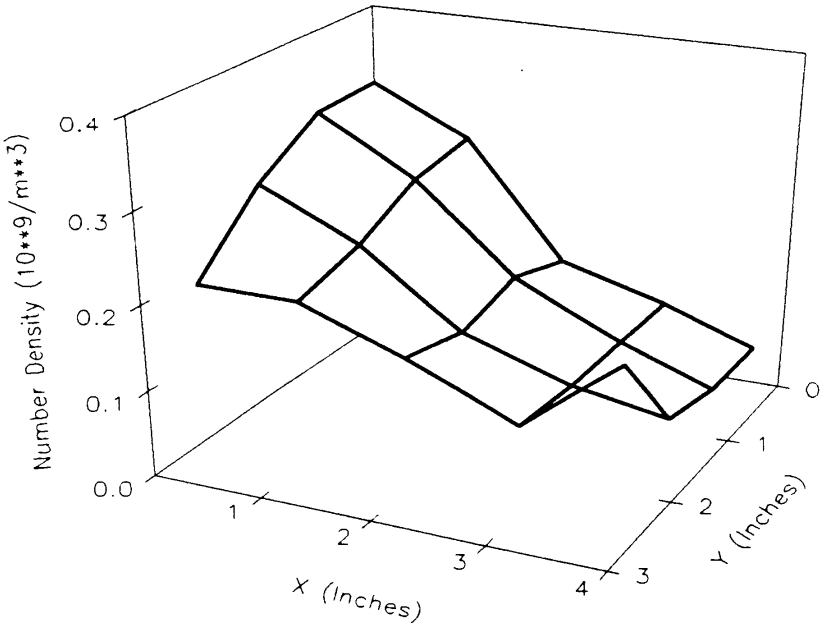

Figure 85. Three-Dimensional Plot of Number Density Distribution for Test L, at a Plane 2.125 In. Above the Filter Face

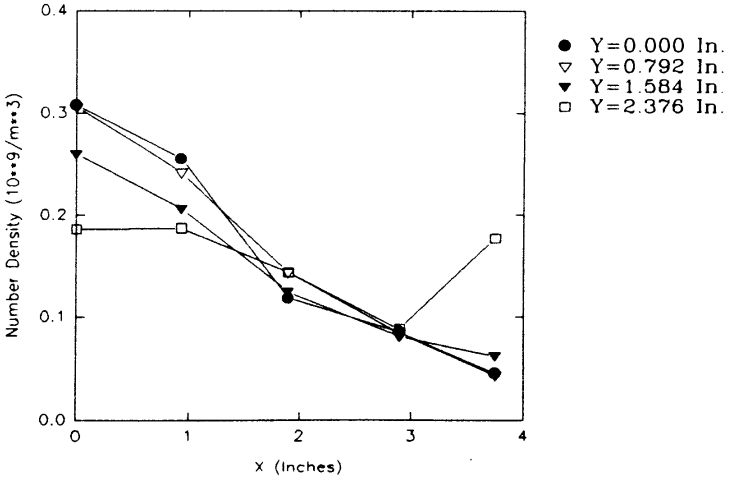

Figure 86. Two-Dimensional Plot of Number Density Distribution at Different Grid Sections for Test L, at a Plane 2.125 In. Above the Filter Face

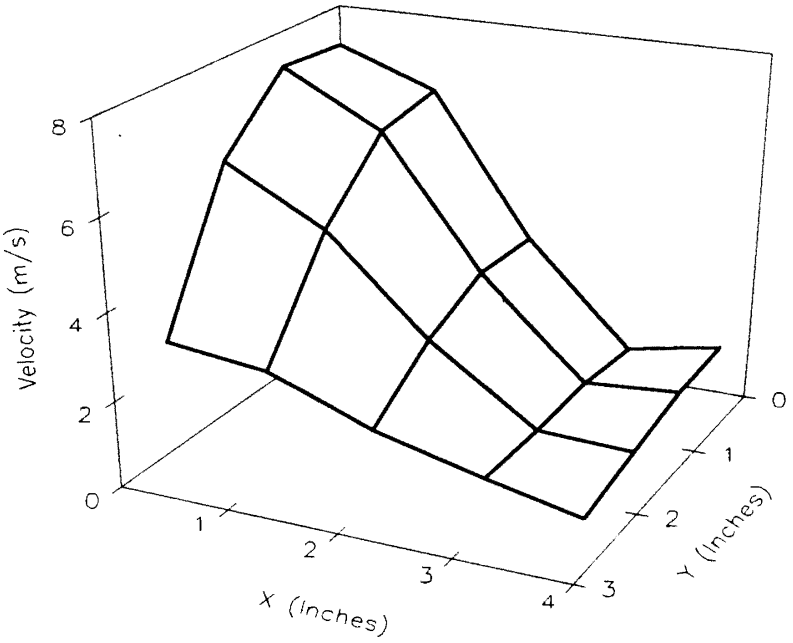

Figure 87. Three-Dimensional Plot of Velocity Profile for Test L, at a Plane 2.125 In. Above the Filter Face

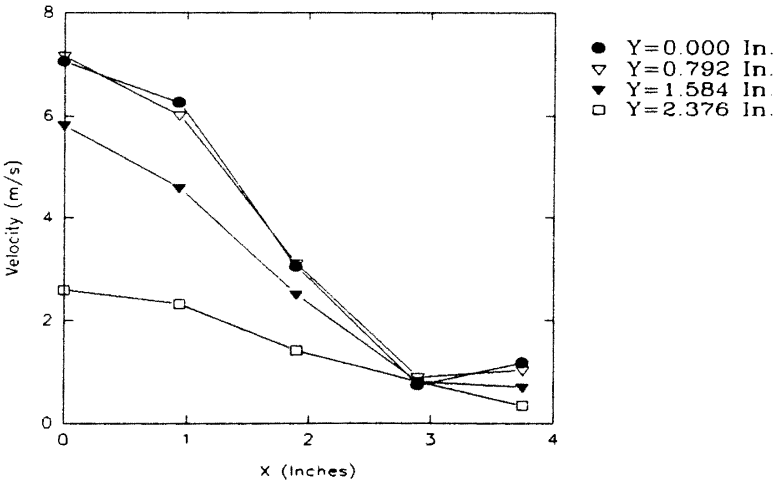

Figure 88. Two-Dimensional Plot of Velocity Profiles at Different Grid Sections for Test L, at a Plane 2.125 In. Above the Filter Face

87. The graph clearly shows that, for all of the grid planes, the velocity is highest at the centerline (x=0 in.) and decreases toward the edge of the filter (x=3.75 in.). For the central plane y=0 in., a slight and unusual increase in velocity is observed at the edge of the filter. As expected, for any grid plane parallel to the y-axis (x=±3.75, ±1.875, 0 in.) velocity is highest at the centerline (y=0 in.) and decreases toward the edge (y=2. in.). As observed for number density profiles, for the grid planes y=0 in. and y=0.792 in., velocities are almost identical. The number density and velocity trends are almost identical, suggesting that particles may follow the flow closely; and under ideal conditions, the number density distribution may replicate the velocity profile.

Figures 89 to 91 are comparisons of number densities for tests J and L at different grid planes. It is observed that, number density profiles for both the tests have the same trend though the profile is flatter for test L.

Figures 92 to 94 are comparisons of the velocity profiles for the above discussed two tests. Velocity profiles also exhibit the same trend though the velocities for the two tests are not identical.

Tests J and L, therefore, affirm that particles are concentrated at and around the center of the filter with number density decreasing gradually toward the edges of the filter. Flow uncertainty may exist at the edges and a high number density may be observed at the edges.

Measurements at a Plane 0.625 In. Above the Filter Face

Extensive measurements were taken for a plane 0.625 in. above the face of the filter. The difficulty with getting very close to the filter face, due to interference of the test housing's edge with the laser beams, limited the height above the filter at which measurements could be taken. This was the plane closest to the face of the filter where measurements were possible. Also, it is important to mention that, for this plane, the rear

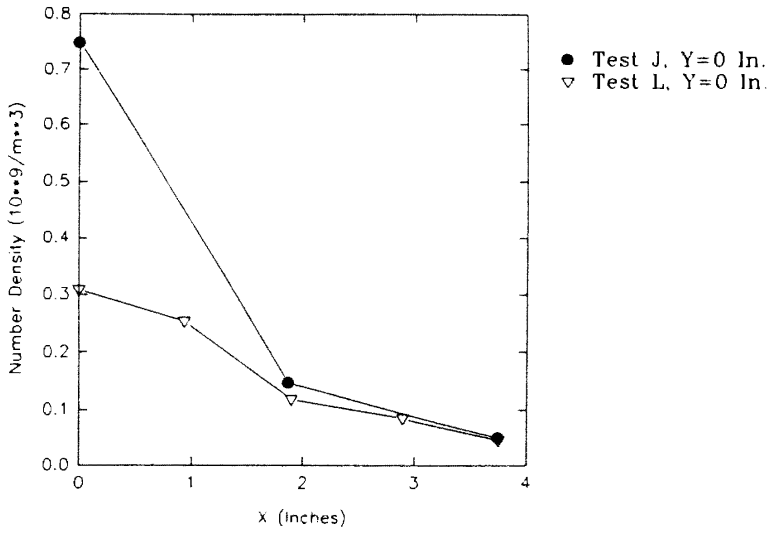

Figure 89. Comparison of Number Densities for Tests J and L, for a Plane 2.125 In. Above the Filter Face

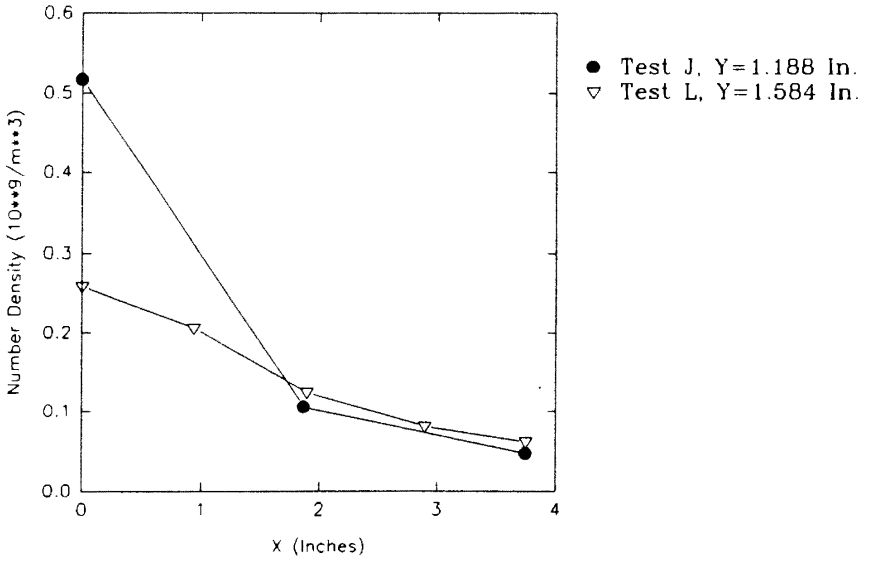

Figure 90. Comparison of Number Densities for Tests J and L, for a Plane 2.125 In. Above the Filter Face

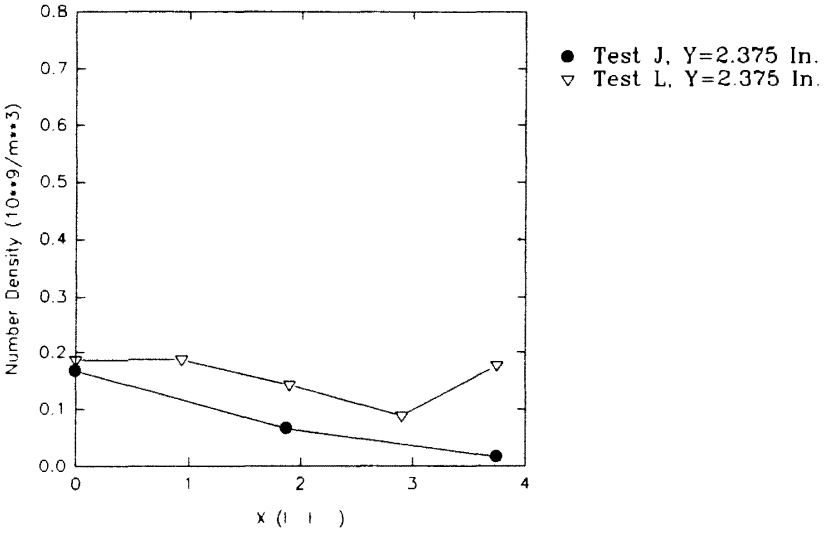

Figure 91. Comparison of Number Densities for Tests J and L, for a Plane 2.125 In. Above the Filter Face

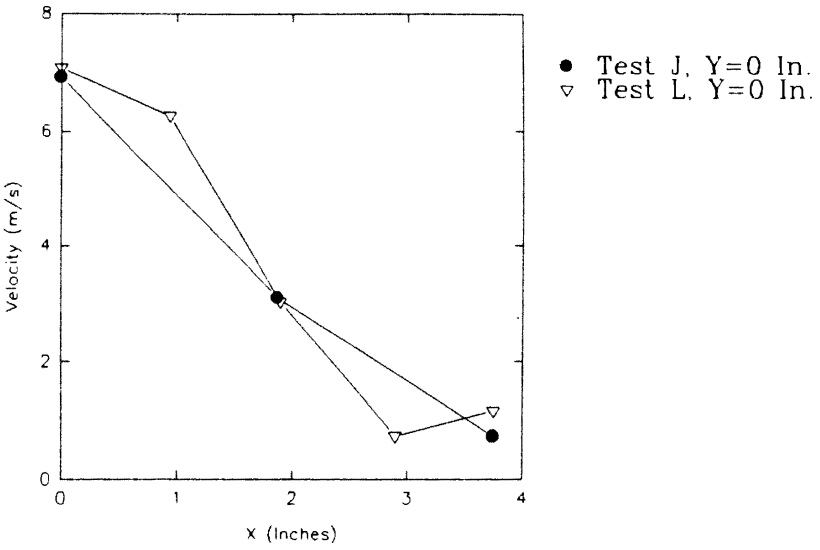

Figure 92. Comparison of Velocity Profiles for Tests J and L, for a Plane 2.125 In. Above the Filter Face

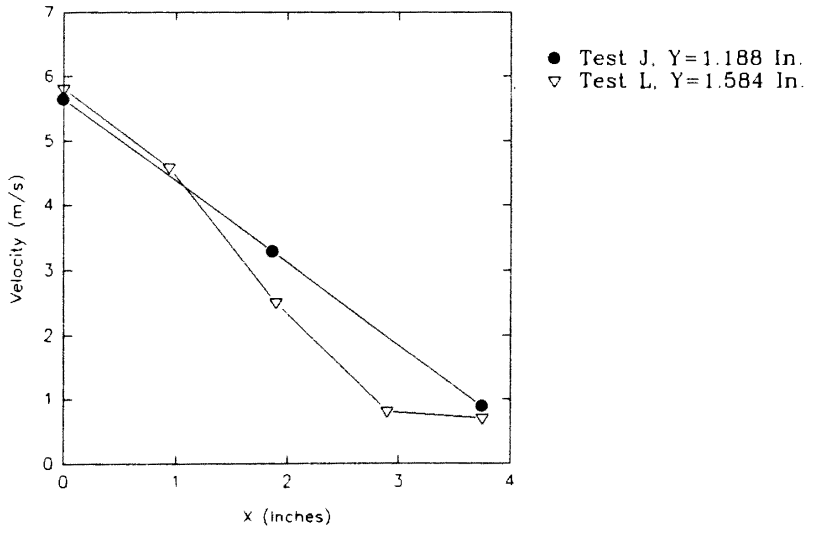

Figure 93. Comparison of Velocity Profiles for Tests J and L, for a Plane 2.125 In. Above the Filter Face

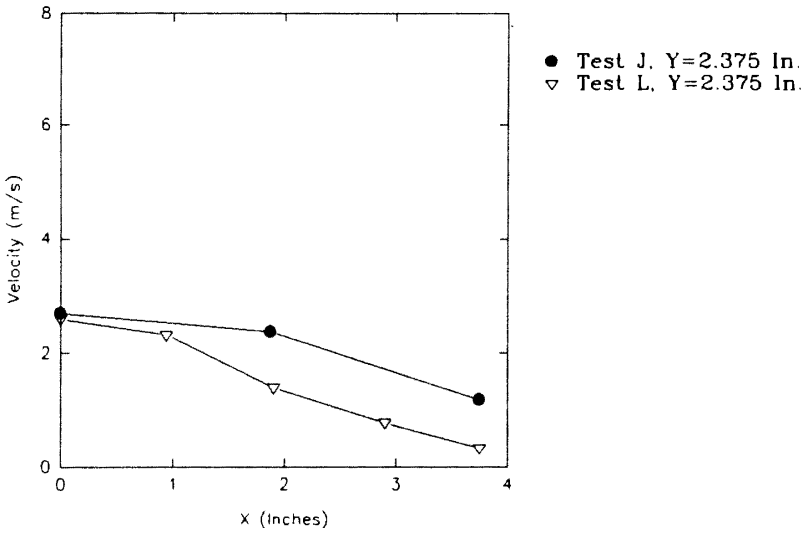

Figure 94. Comparison of Velocity Profiles for Tests J and L, for a Plane 2.125 In. Above the Filter Face

half of the filter could not be mapped due to the above mentioned difficulty. Being the plane closest to the filter, this was the plane of extreme interest and importance. The number density distribution at this plane would give the closest distribution to which the filter is actually exposed. Therefore, as shown in Table 5, six different tests (B, I, M, H, F and A) were conducted at this plane, all using different and new filters.

As observed from Table 4, the same filter was used for tests C, D and E as was used for test B. In other words, the filter was new and fresh for test B, and for the other tests (C, D and E), the same filter was used after it dried. The humidifier setting, the grid and the laser power (3.5 watts) were same for tests B, C, D and E. As shown in Table 4, test B employed software parameter setup II. Measurements were taken only for the front half of the filter. Figure 95 shows a three-dimensional plot of particle number density distribution for test B. From the figure, it is observed that the number density is highest at the center of the filter, and it gradually decreases toward the edges of the filter. Figure 96 shows a two-dimensional plot of particle number density distribution at different grid planes parallel to the x-axis (along the length of the filter). The graph clearly shows that, for all of the grid planes, the number density is highest at the centerline (x=0 in.) and decreases toward the edges of the filter (x=±4 in.). Also very good symmetry is exhibited by the number density profiles with respect to the plane x=0 in.

Figure 97 shows the three-dimensional plot of velocity profile for test B. The graph clearly shows that velocity is high at and around the center and decreases gradually toward the edges of the filter. Figure 98 is the corresponding two-dimensional plot obtained by slicing the three-dimensional plot of Fig. 97. The graph clearly shows that, for all of the grid planes, the velocity is highest at the centerline (x=0 in.) and decreases toward the edges of the filter (x=±4 in.). The graph clearly exhibits the symmetry for velocity profiles with respect to the central plane (x=0 in.). Also for grid planes parallel to the y-axis (x=3, ±2, ±1, 0 in.), velocity is highest at the centerline (y=0 in.) and decreases

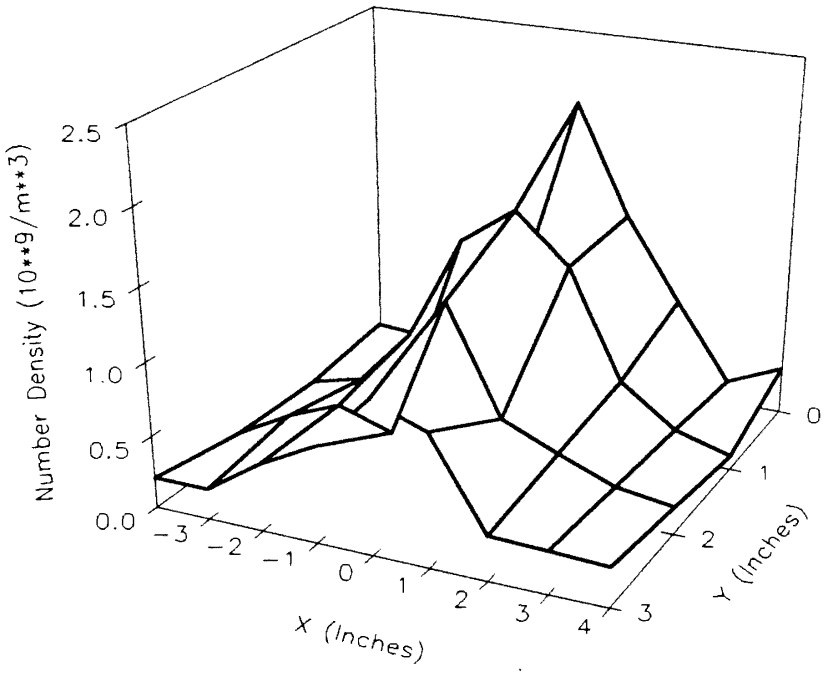

Figure 95. Three-Dimensional Plot of Number Density Distribution for Test B, at a Plane 0.625 In. Above the Filter Face

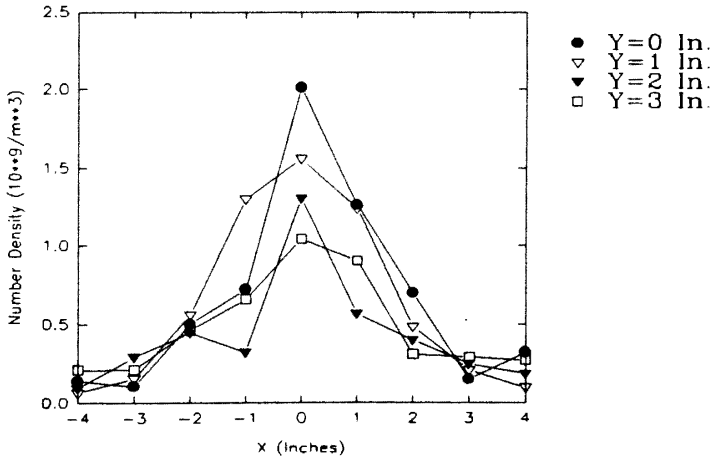

Figure 96. Two-Dimensional Plot of Number Density Distribution at Different Grid Sections for Test B, at a Plane 0.625 In. Above the Filter Face

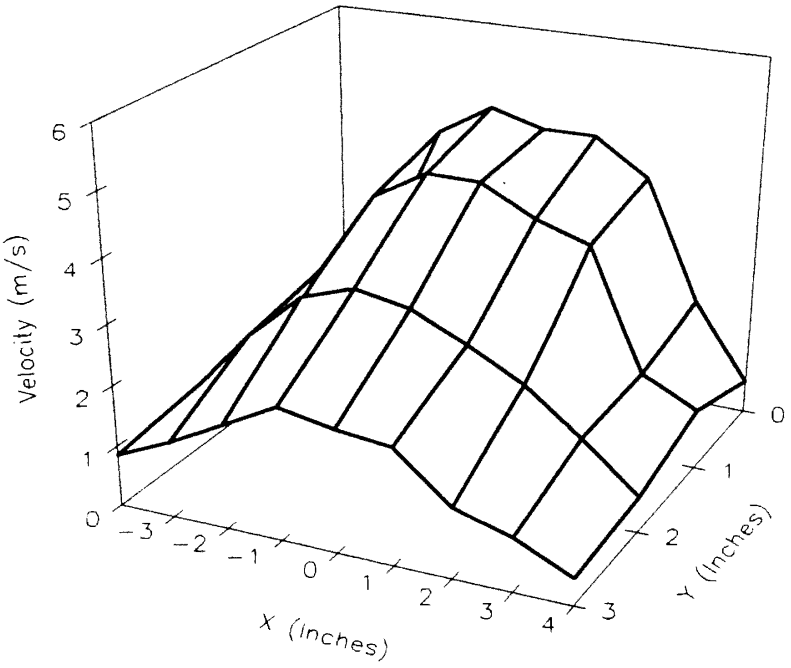

Figure 97. Three-Dimensional Plot of Velocity Profile for Test B, at a Plane 0.625 In. Above the Filter Face

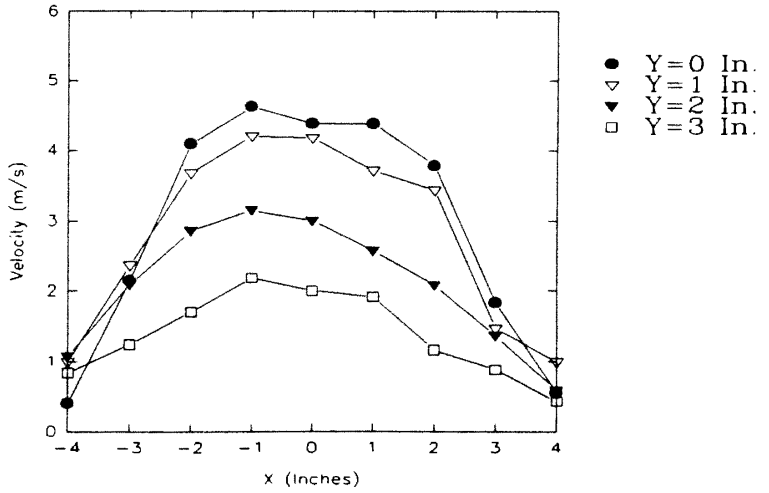

Figure 98. Two-Dimensional Plot of Velocity Profiles at Different Grid Sections for Test B, at a Plane 0.625 In. Above the Filter Face

toward the edge (y=3 in.). However, as observed before, for grid planes at the edges (x=-3, ±4 in.), this is not true.

Test I was also conducted at the same plane at 0.625 in. above the face of the filter. As observed from Table 4, the same filter was used for tests J and K as was used for test I. A grid of 0.938 in. by 0.792 in. was used. The humidifier setting and the software parameter setup (IV) were same for tests I, J and K, but a low laser power of 2.8 Vdc (which is far below the saturation limit, 8 Vdc) was used for test I.

Figure 99 shows a three-dimensional plot of particle number density distribution for test I. From the figure, it observed that the number density is high around the center and decreases gradually toward the edges of the filter. Figure 100 shows the corresponding two-dimensional plot of particle number density distribution at different grid planes parallel to the x-axis. The graph clearly shows that, for all of the grid planes except the y=0 in. grid plane, the number density is highest at the centerline (x=0 in.) and decreases toward the edges of the filter (x=±3.75 in.). For the plane y=0 in., an unusual dip is observed at the center. A very good symmetry is exhibited by the number density profiles with respect to the plane x=0 in. As expected, for the grid planes parallel to the y-axis (x=±3.75, ±2.814, ±1.875, ±0.938, 0 in.), number density is highest at the centerline (y=0 in.) and decreases toward the edge (y=2.375 in.). Toward the edges, this may not be true as number densities are very low and close to each other.

Figure 101 shows the three-dimensional plot of velocity profile for test I. The graph clearly shows that velocity is high at and around the center and decreases gradually toward the edges of the filter. Figure 102 is the corresponding two-dimensional plot obtained by slicing the three-dimensional plot of Fig. 101. The graph clearly shows that, for all of the grid planes, the velocity is highest at the centerline (x=0 in.) and decreases toward the edges of the filter (x=±4 in.). For every grid plane, the velocity profile is fairly flat around the center. The graph clearly exhibits symmetry for velocity profiles with respect to the central plane (x=0 in.). For the central grid plane y=0 in., higher velocities

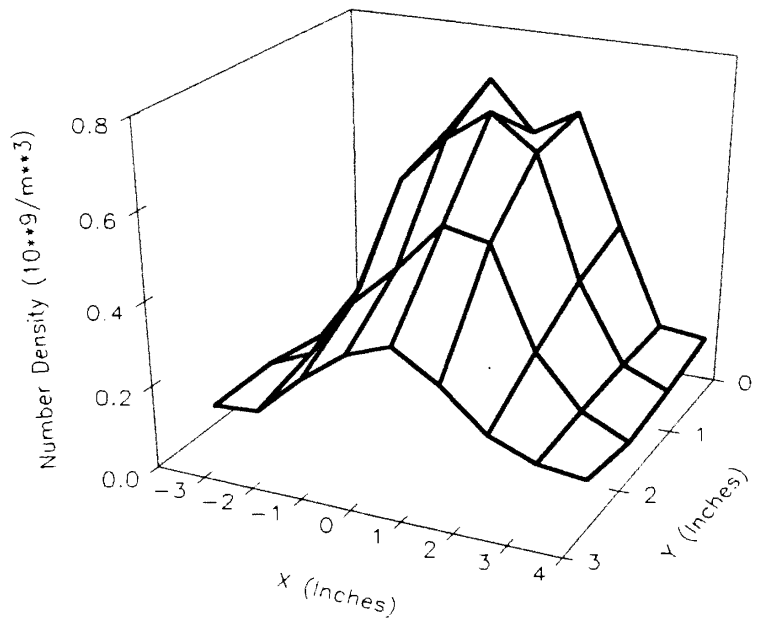

Figure 99. Three-Dimensional Plot of Number Density Distribution for Test I, at a Plane 0.625 In. Above the Filter Face

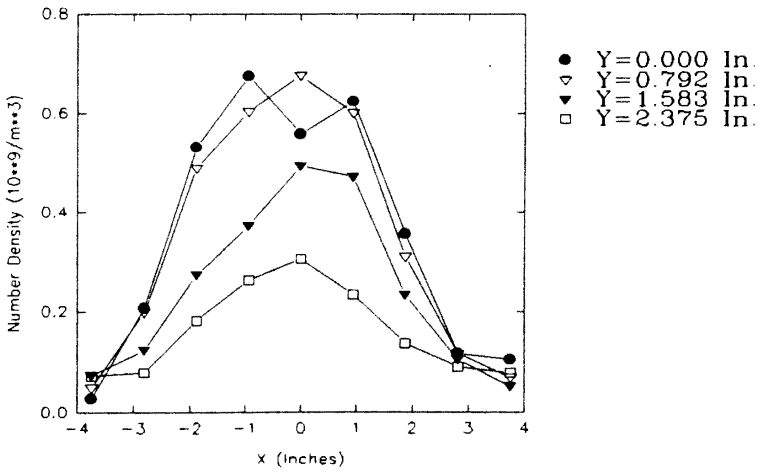

Figure 100. Two-Dimensional Plot of Number Density Distribution at Different Grid Sections for Test I, at a Plane 0.625 In. Above the Filter Face

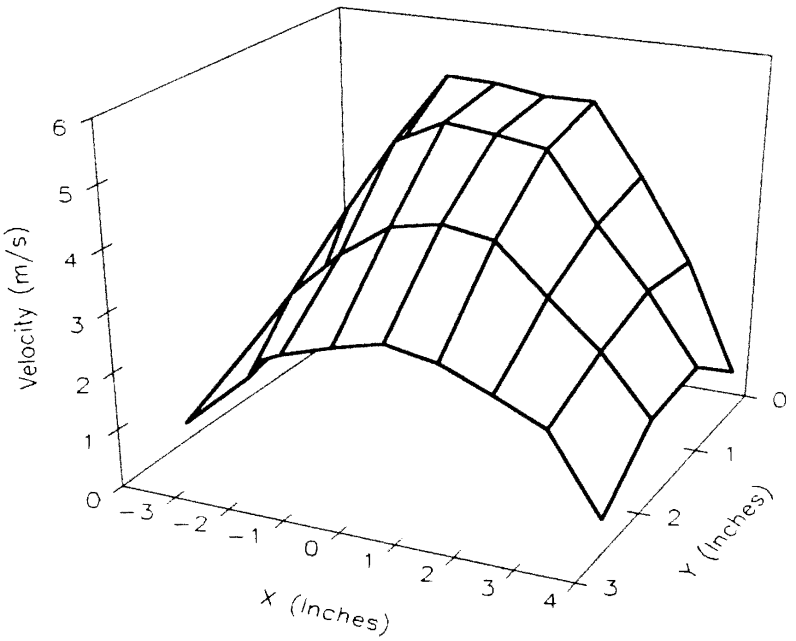

Figure 101. Three-Dimensional Plot of Velocity Profile for Test I, at a Plane 0.625 In. Above the Filter Face

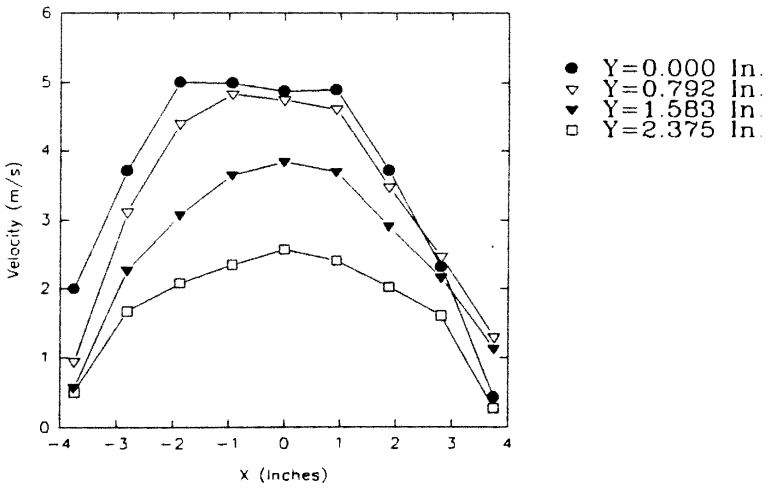

Figure 102. Two-Dimensional Plot of Velocity Profiles at Different Grid Sections for Test I, at a Plane 0.625 In. Above the Filter Face

are observed for the left half of the filter. It is observed that, for most of the grid planes parallel to the y-axis (x=-3.75, ±2.814, ±1.875, ±0.938, 0 in.), velocity is highest at the centerline (y=0 in.) and decreases toward the edge (y=2.375 in.). For the grid planes at the edge of the filter, such as for the plane x=3.75 in., this may not be necessarily true due to flow uncertainties.

Test M was also conducted at the same plane, 0.625 in. above the face of the filter. As observed from Table 4, a new filter was used for the test, and the humidifier was at high mist intensity. Parameter setup VI was used. A grid of 0.938 in. by 0.792 in. was used, and measurements were taken only for one quarter of the filter. Once again, a low laser power (2.8 Vdc) was used.

Figure 103 shows a three-dimensional plot of particle number density distribution for test M. Figure 104 shows the corresponding two-dimensional plot of particle number density distribution at different grid planes parallel to the x-axis. From the figures, it is observed that, for every grid plane, the number density peaks at x=-0.938 in. instead of x=0 in. and then it gradually decreases toward the edges. This may be due to preferential seeding or due to some specific filter characteristic. It is observed that number densities for the planes y=0 in. and y=0.792 in. are almost identical, as is the case for the planes y=1.584 in. and y=2.375 in. It is observed that the difference in the number densities for different grid planes parallel to x-axis really exist only for the region close to the center (x=0 in. to x=-2 in.).

Figure 105 shows the three-dimensional plot of velocity profile for test M. The graph clearly shows that velocity is high at and around the center and decreases gradually toward the edges of the filter. Figure 106 is the corresponding two-dimensional plot obtained by slicing the three-dimensional plot of Fig. 105. The graph clearly shows that for all of the grid planes, the velocity is highest at the centerline (x=0 in.) and decreases toward the edges of the filter (x=-4 in.). It is observed that, for all of the grid planes

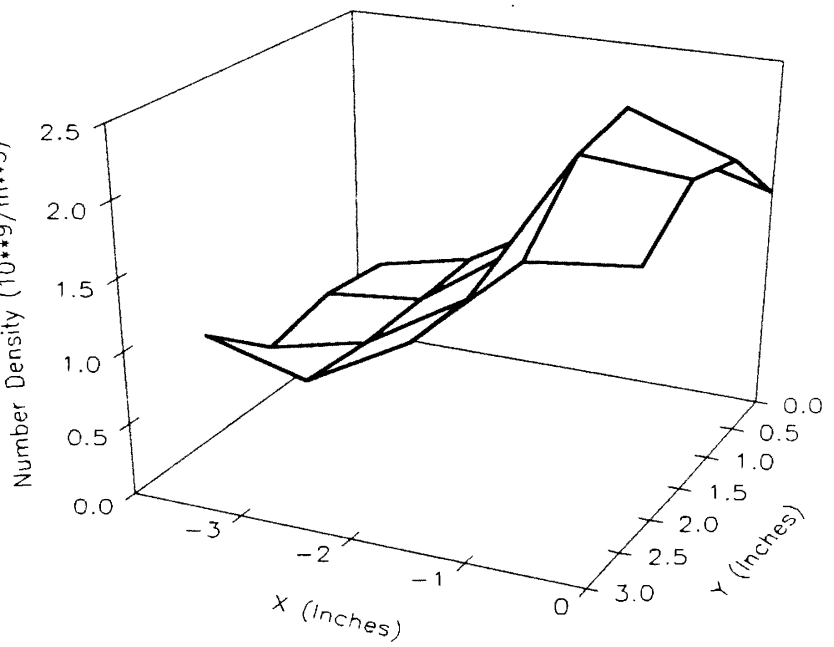

Figure 103. Three-Dimensional Plot of Number Density Distribution for Test M, at a Plane 0.625 In. Above the Filter Face

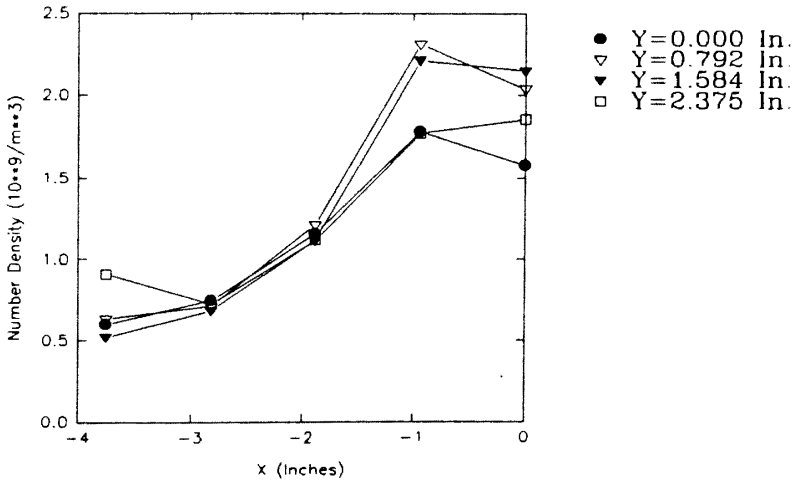

Figure 104. Two-Dimensional Plot of Number Density Distribution at Different Grid Sections for Test M, at a Plane 0.625 In. Above the Filter Face

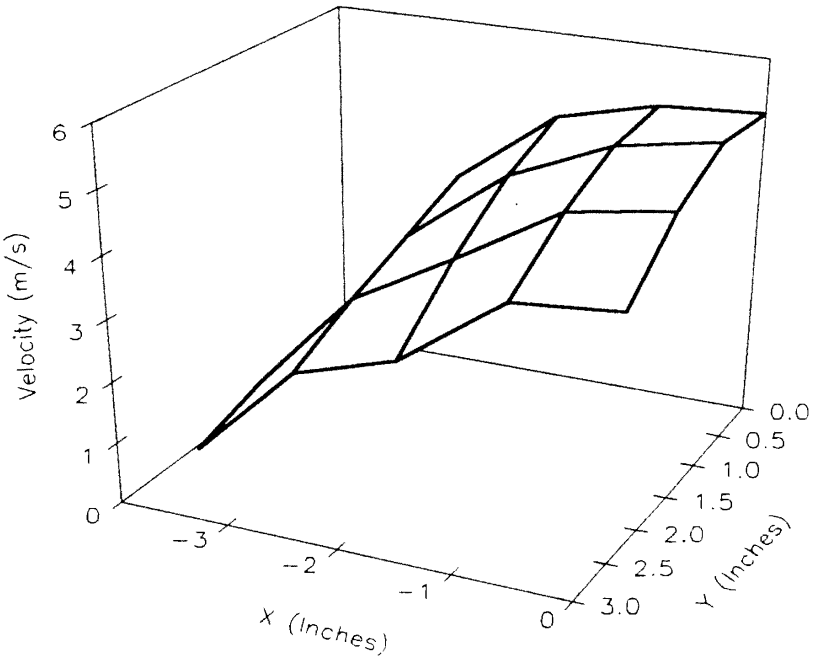

Figure 105. Three-Dimensional Plot of Velocity Profile for Test M, at a Plane 0.625 In. Above the Filter Face

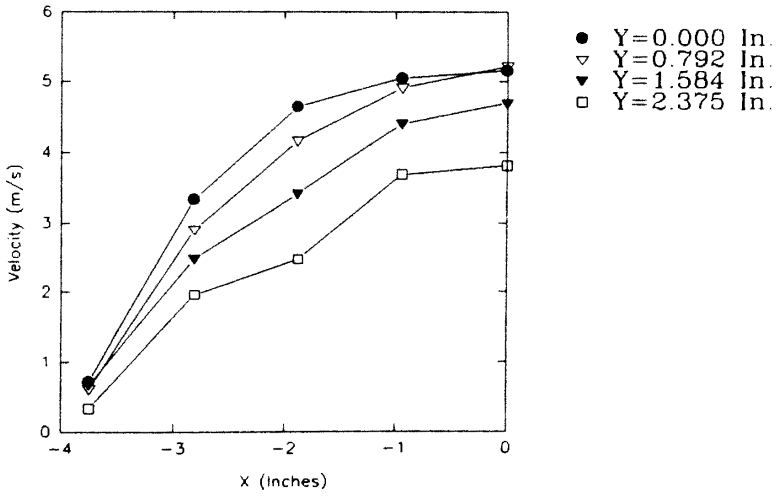

Figure 106. Two-Dimensional Plot of Velocity Profiles at Different Grid Sections for Test M, at a Plane 0.625 In. Above the Filter Face

parallel to the y-axis (x=-3.75, -2.814, -1.875, -0.938, 0 in.), velocity is highest at the centerline (y=0 in.) and decreases toward the edge (y=2.375 in.).

Tests B, I and M, therefore, confirm that particles are concentrated at and around the center of the filter with number density decreasing gradually toward the edges of the filter.

Figure 107 shows a three-dimensional plot of particle number density distribution for test H. As evident from Table 4, a new filter was used for this test. The grid used, the humidifier setting and the software parameter setup were same as for test B. A laser power of 3.5 watts was used. Figure 108 shows the corresponding two-dimensional plot of particle number density distribution at different grid planes parallel to the x-axis (along the length of the filter). It is observed from the figures that the number density for every grid plane is highest at and around the center and decreases toward the edges (x=±4 in.) of the filter. The peak of the number density distribution is observed at x=1 in. and y=1 in. Also a fair degree of symmetry is observed with respect to the central plane (x=0 in.). The number density seems to be slightly high outside the filter regime, as shown in Fig. 108 for points (x=4 in., y=3 in.) and (x=-4 in., y=0 in.).

Figure 109 shows the three-dimensional plot of velocity profile for test H. The graph clearly shows that velocity is high at and around the center and decreases gradually toward the edges of the filter. Figure 110 is the corresponding two-dimensional plot. The graph shows that, for all of the grid planes except for the central plane y=0 in., the peak of the velocity profile is shifted toward the left side of the filter at x=-1 in. The velocities decrease toward the edges of the filter (x=±4 in.). For the central plane y= 0 in., a slight dip is observed at the center. Also for grid planes parallel to the y-axis (x=3, ±2, ±1, 0 in.), velocity is highest at the centerline (y=0 in.) and decreases towards the edge (y=3 In). However, as observed before, for grid planes at the edges (x=-3, ±4 in.), this is not true.

Test H again suggests that, at a plane very near to the face of the filter, particles are concentrated toward the center of the filter as compared to the edges. The peak,

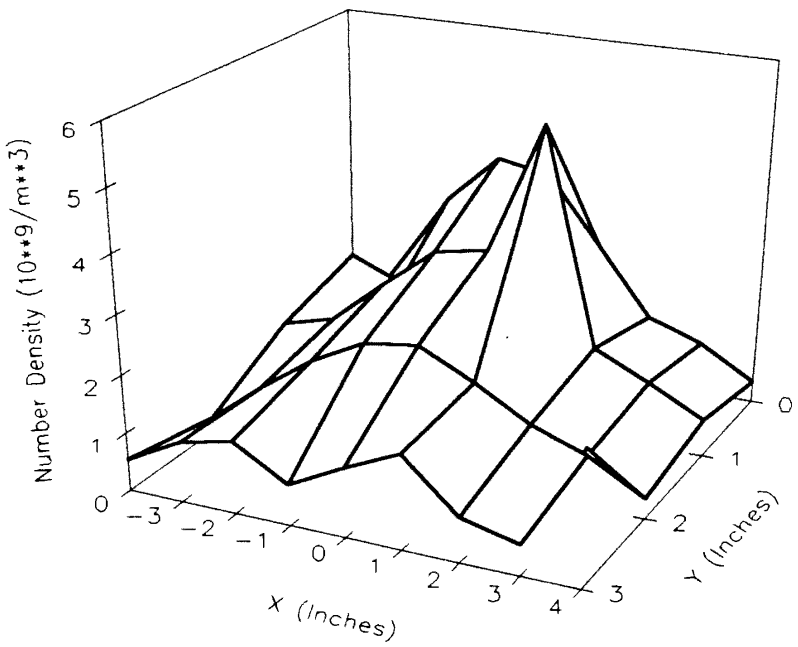

Figure 107. Three-Dimensional Plot of Number Density Distribution for Test H, at a Plane 0.625 In. Above the Filter Face

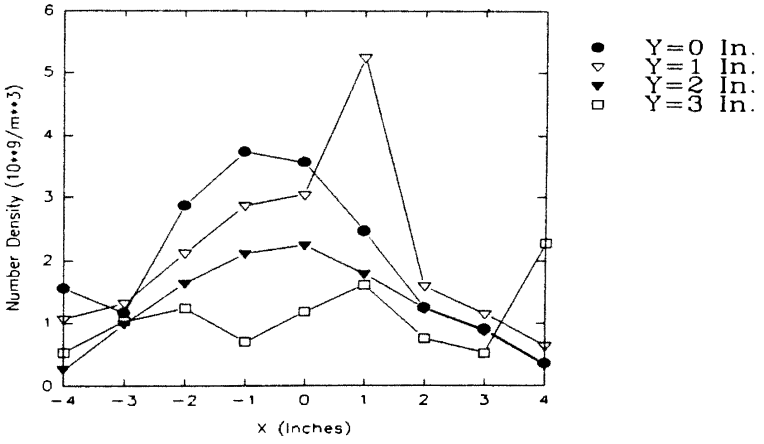

Figure 108. Two-Dimensional Plot of Number Density Distribution at Different Grid Sections for Test H, at a Plane 0.625 In. Above the Filter Face

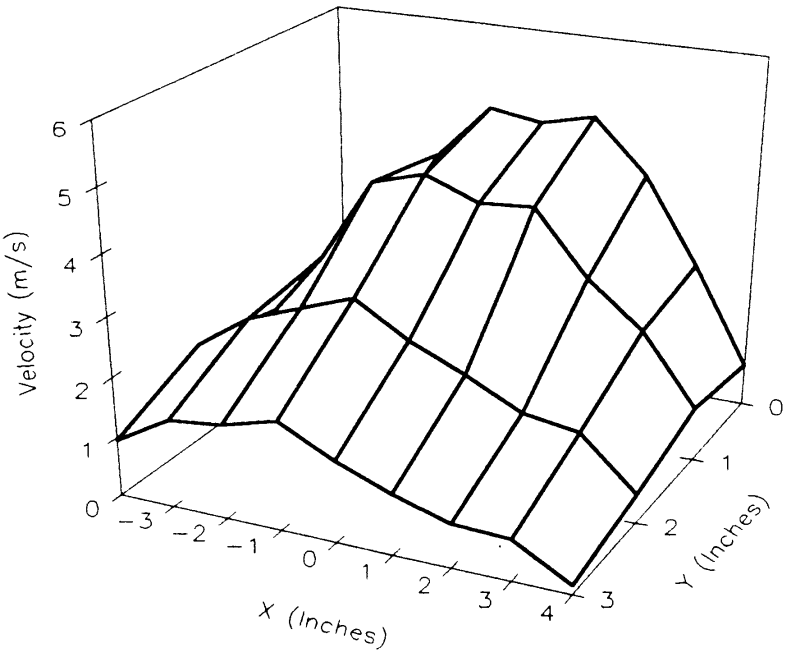

Figure 109. Three-Dimensional Plot of Velocity Profile for Test H, at a Plane 0.625 In. Above the Filter Face

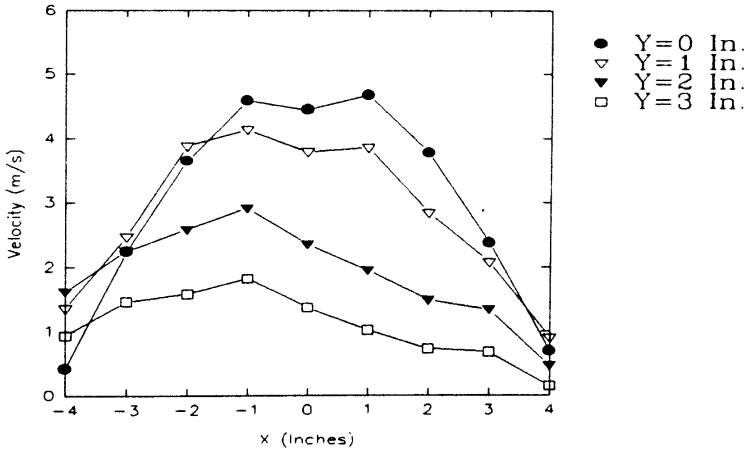

Figure 110. Two-Dimensional Plot of Velocity Profiles at Different Grid Sections for Test H, at a Plane 0.625 In. Above the Filter Face

however, may not necessarily be at the exact center. Also toward the edges of the filter, unusually high number densities may be observed.

Figure 111 shows a three-dimensional plot of particle number density distribution for test F. As observed from Table 4, a new filter was used for this test. The grid used, the humidifier setting, and the software parameter setup were the same as for tests F and B. A laser power of 3.5 watts was used. Figure 112 shows the corresponding two-dimensional plot of particle number density distribution at different grid planes parallel to the x-axis. Once again, it is observed that the number density is high for the planes $x=\pm 4$ in., which are outside the filter regime. In fact, peaks are observed at the points (x=4 in., y=0 in.) and (x=-4 in., y=2 in.). Disregarding the points of measurements outside the filter regime, a relatively flat number density profile is observed.

Figure 113 shows the three-dimensional plot of velocity profile for test F. Figure 114 is the corresponding two-dimensional plot. The graphs clearly show that velocity is high at and around the center and decreases gradually toward the edges of the filter. A slight dip is observed at the center x=0 in. for the grid plane y=0 in. A fair degree of symmetry is observed for all of the grid planes except for the plane y=3 in. But this plane is outside the filter regime, and therefore it had slightly odd velocities.

Test F suggests that the number density distribution can be fairly uniform and flat over the filter except for a couple of peaks around the center.

Figure 115 shows the three-dimensional plot of the velocity profile for test A. As shown in Table 4, a new filter was used for this test. Software parameter setup I was employed. Also a relatively finer grid of 0.5 in. by 0.5 in. was used for the measurements. High mist intensity was used, and the laser was operating at 3.5 watts. Figure 116 is the corresponding two-dimensional plot. It is observed that the number density is high and off-center at the grid plane x=-2 in. It is worthwhile to mention that measurements for the left half of the filter were taken after the right half. Since a finer grid was employed, time history effects may be responsible for shifting the peaks toward the left side of the filter.

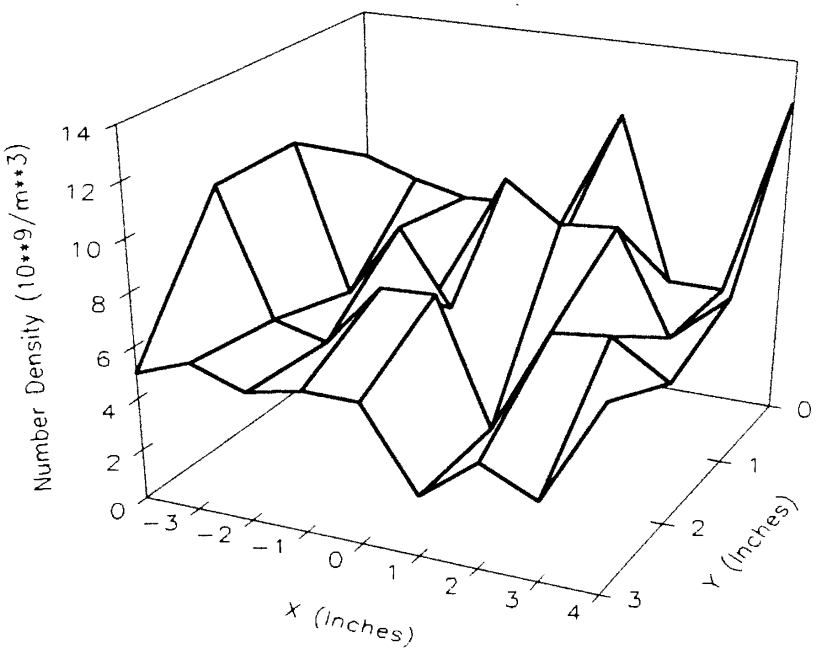

Figure 111. Three-Dimensional Plot of Number Density Distribution for Test F, at a Plane 0.625 In. Above the Filter Face

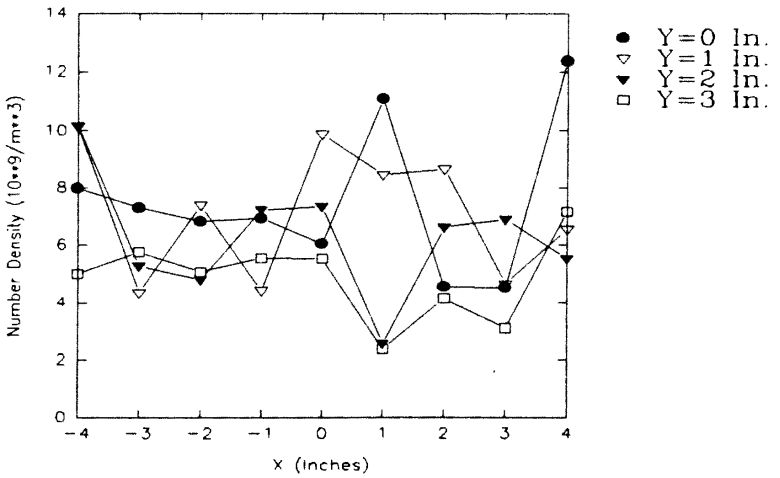

Figure 112. Two-Dimensional Plot of Number Density Distribution at Different Grid Sections for Test F, at a Plane 0.625 In. Above the Filter Face

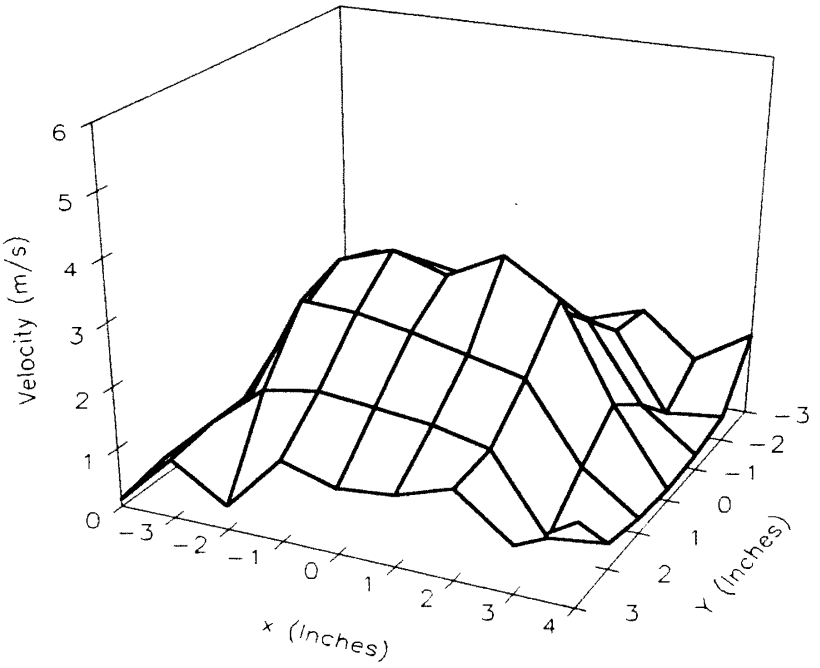

Figure 113. Three-Dimensional Plot of Velocity Profile for Test F, at a Plane 0.625 In. Above the Filter Face

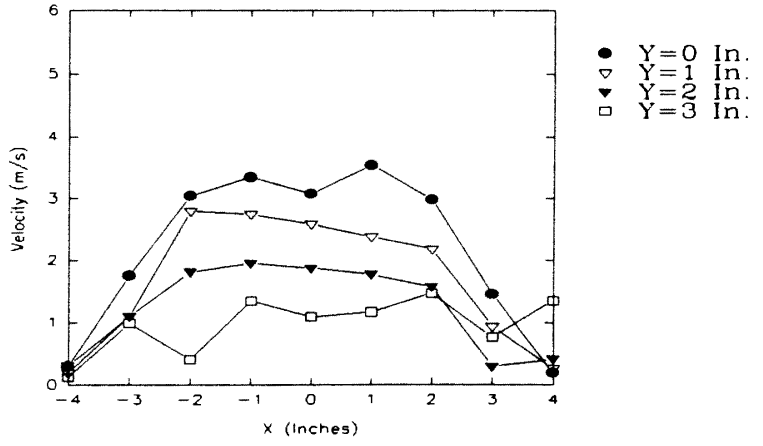

Figure 114. Two-Dimensional Plot of Velocity Profiles at Different Grid Sections for Test F, at a Plane 0.625 In. Above the Filter Face

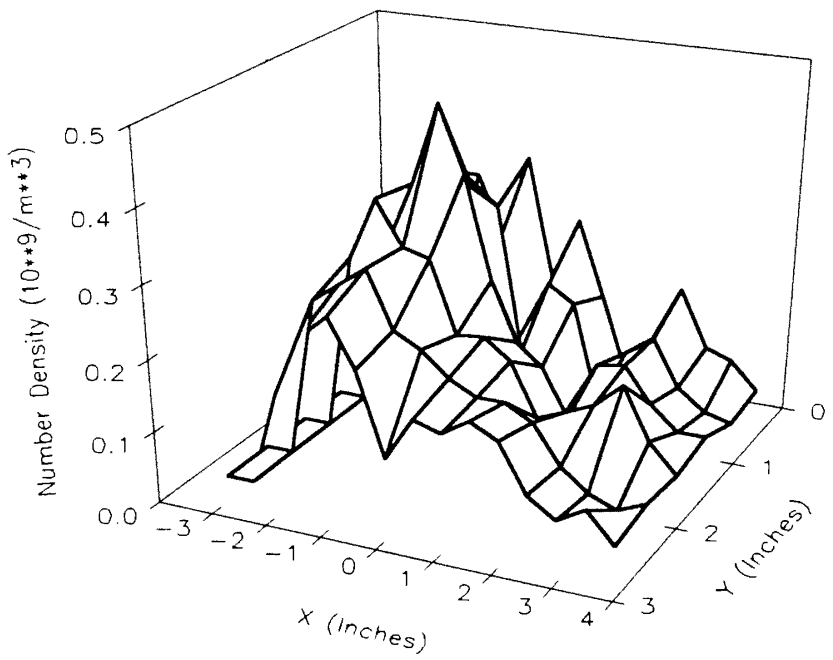

Figure 115. Three-Dimensional Plot of Number Density Distribution for Test A, at a Plane 0.625 In. Above the Filter Face

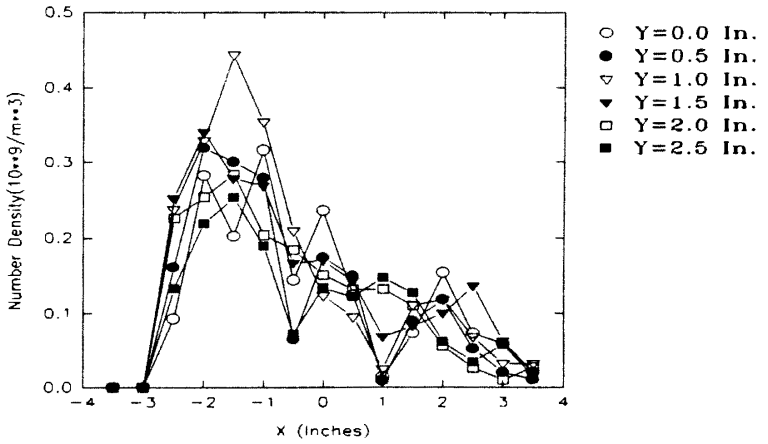

Figure 116. Two-Dimensional Plot of Number Density Distribution at Different Grid Sections for Test A, at a Plane 0.625 In. Above the Filter Face

Figure 117 shows the three-dimensional plot of the velocity profile for test A. Figure 118 is the corresponding two-dimensional plot. The graph shows that velocity profiles are high and flat at and around the center and decrease toward the edges of the filter.

Figures 119 to 122 are comparisons of number densities for tests B, I, M, H, F and A at different grid planes parallel to the x-axis. It is important to mention that the mist intensity generated by the humidifier, the grid used and the software parameters setup employed for these tests were different (Table 4). Laser power of 3.5 watts was used for tests B, H, F and A. Laser power of 2.8 Vdc was used for tests I and M. It is observed that, except for the test F, number densities for all of the other tests are close to each other and exhibit the same trend. Number density seems to be high at and around the center and drops toward the edges of the filter.

Figures 123 to 126 are comparisons of velocity profiles for tests B, I, M, H, F and A at different grid planes. As observed before, though the velocity profiles exhibit the same trend but velocities are not identical for different tests. This, as mentioned before, suggests that although the flow pattern over different filters may be similar, but the exact distribution depends upon the specific filter being tested.

Comparison at Different Heights Above the Filter Face

It is important to explore the behavior of number density distribution as a function of height above the face of the filter. It is evident from Table 4, that tests D, C and B were performed using the same filter and the same experimental conditions at planes 6.625, 3.625 and 0.625 in. above the face of the filter, respectively. Therefore, a comparison of number density and velocity profiles for these planes should reveal fairly the behavior of flow and particle distribution as the flow approaches the face of the filter.

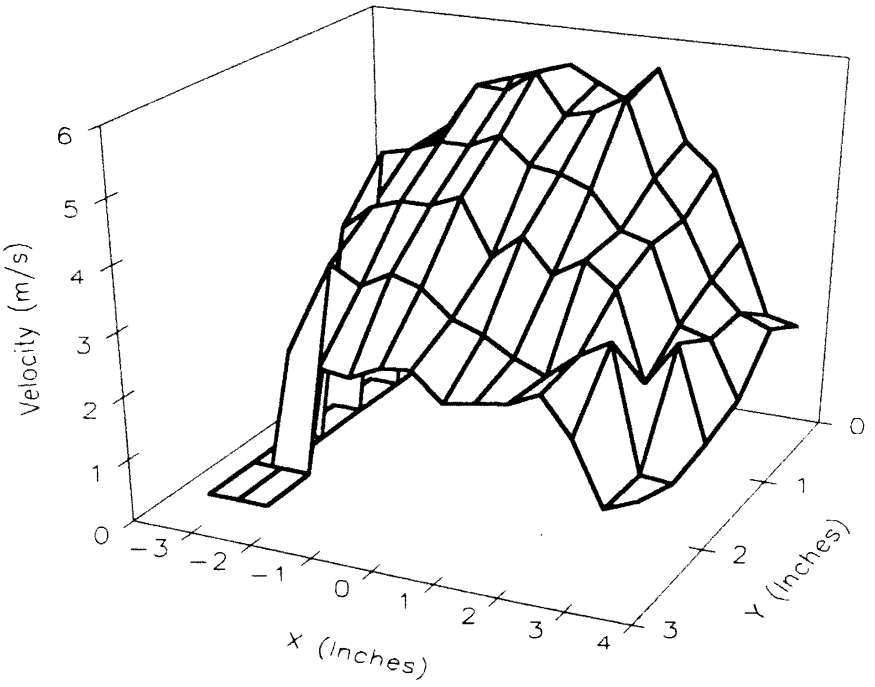

Figure 117. Three-Dimensional Plot of Velocity Profile for Test A, at a Plane 0.625 In. Above the Filter Face

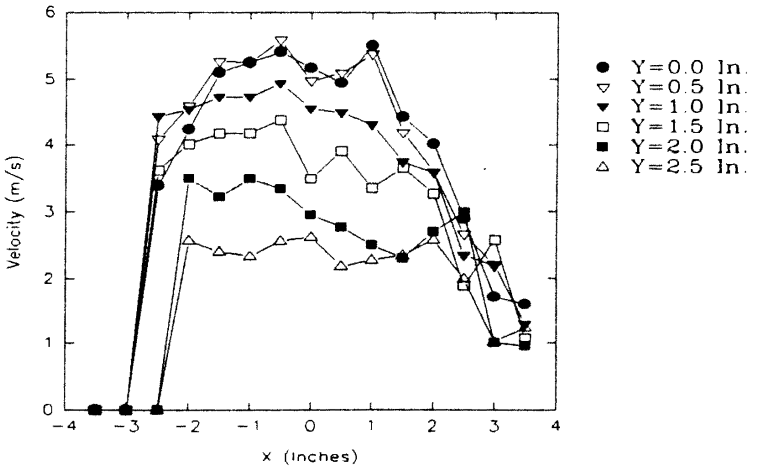

Figure 118. Two-Dimensional Plot of Velocity Profiles at Different Grid Sections for Test A, at a Plane 0.625 In. Above the Filter Face

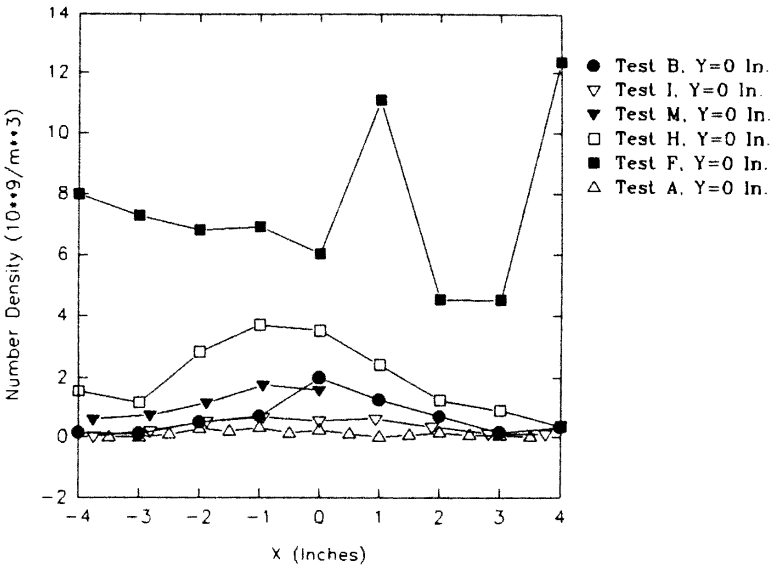

Figure 119. Comparison of Number Densities for Tests B, I, M, H, F and A for a Plane 0.625 In. Above the Filter Face

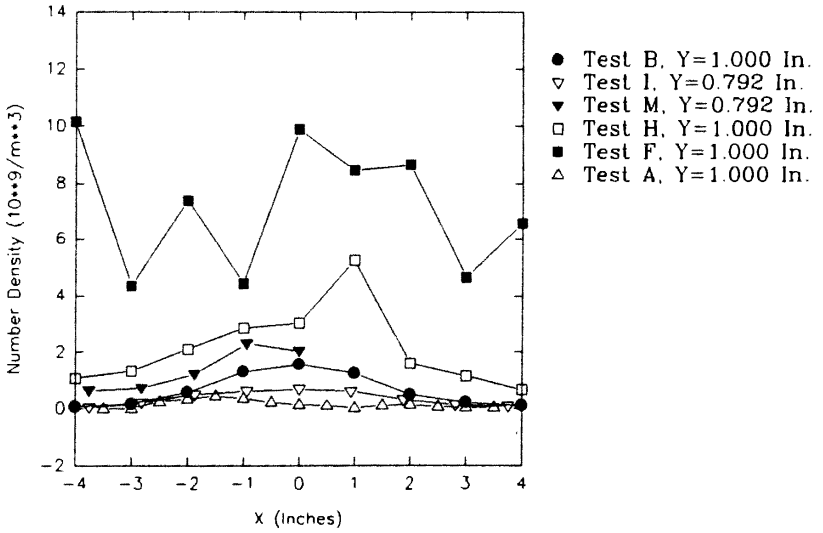

Figure 120. Comparison of Number Densities for Tests B, I, M, H, F and A for a Plane 0.625 In. Above the Filter Face

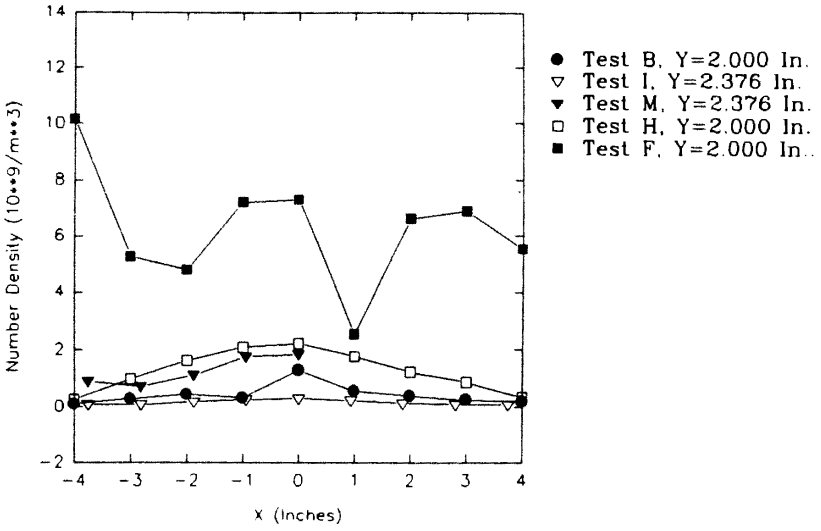

Figure 121. Comparison of Number Densities for Tests B, I, M, H and F for a Plane 0.625 In. Above the Filter Face

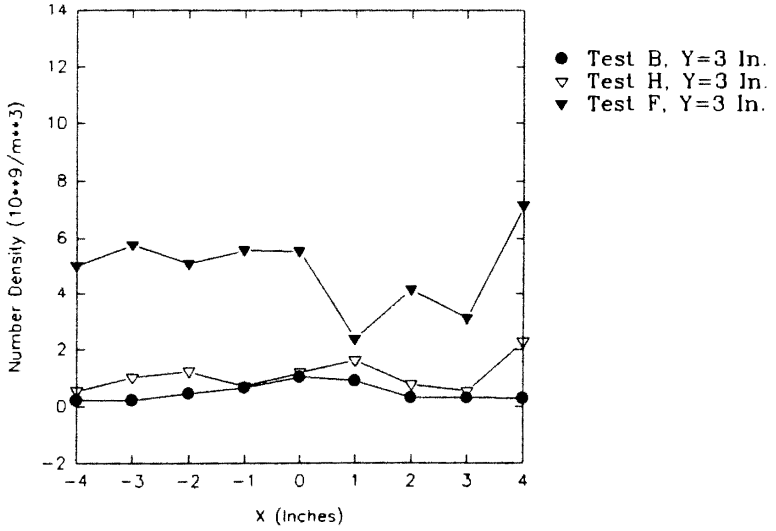

Figure 122. Comparison of Number Densities for Tests B, H and F for a Plane 0.625 In. Above the Filter Face

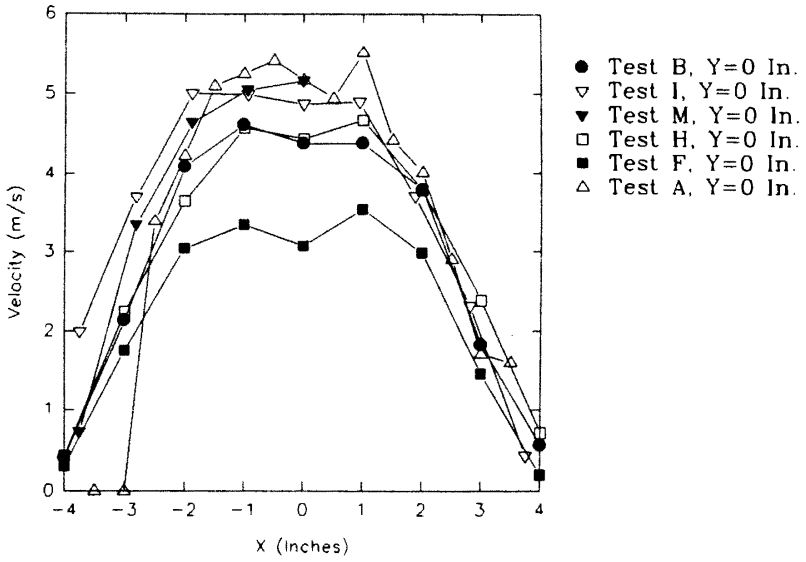

Figure 123. Comparison of Velocity Profiles for Tests B, I, M, H, F and A for a Plane 0.625 In. Above the Filter Face

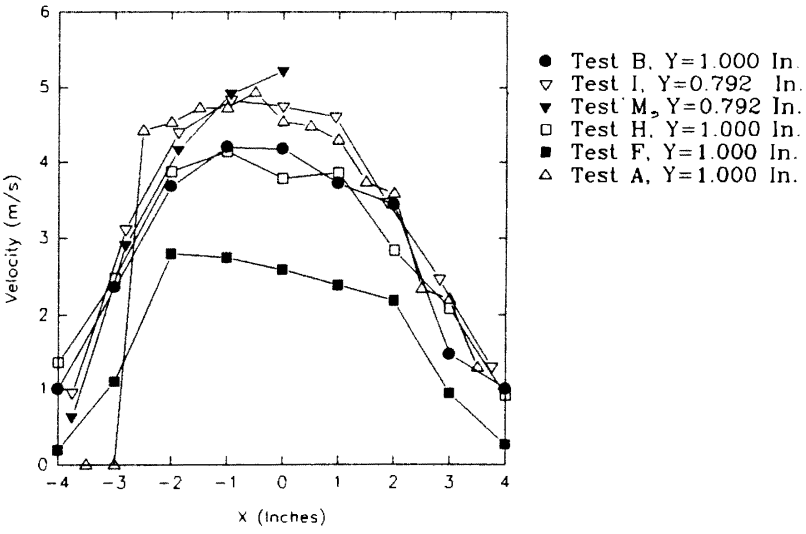

Figure 124. Comparison of Velocity Profiles for Tests B, I, M, H, F and A for a Plane 0.625 In. Above the Filter Face

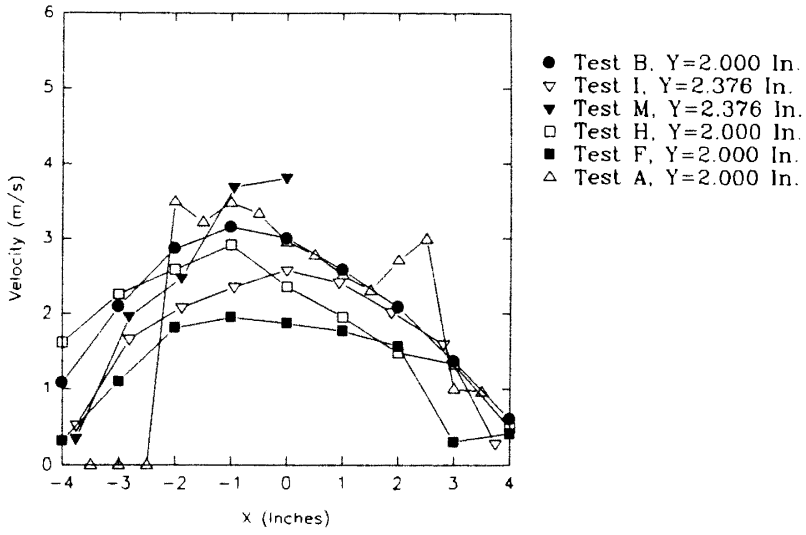

Figure 125. Comparison of Velocity Profiles for Tests B, I, M, H, F and A for a Plane 0.625 In. Above the Filter Face

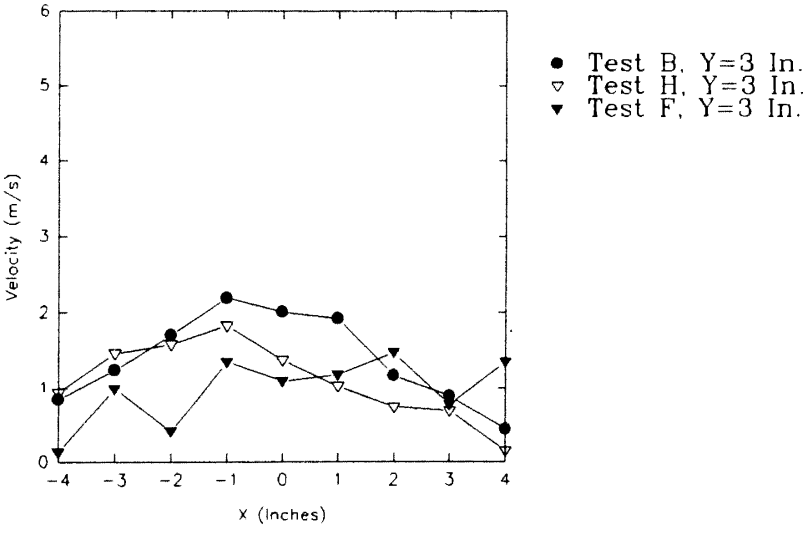

Figure 126. Comparison of Velocity Profiles for Tests B, H and F for a Plane 0.625 In. Above the Filter Face

Figures 127, 128 and 129 are the three-dimensional plots of number density distribution for the tests D, C and B, respectively. These have been presented and discussed before. It is worthwhile to reiterate that measurements for these tests were taken only for the front half of the filter. It is clear from these figures that the number density distribution maintains the same symmetrical profile, with concentration being highest at and around the center and gradually decreasing towards the edges of the filter, as the flow progresses toward the face of the filter. However, the number density increases as the flow progresses toward the face of the filter. Figures 130, 131 and 132 are the two-dimensional plots of number density at grid planes y=0 in., y=1 in. and y=2 in., respectively for tests D, C and B. It is clear from these figures that number density increases for each grid plane with the flow progressing toward the face of the filter. This may be due to the presence of water particles bounced from the filter face and staying close to the filter. Improved seeding, due to the stabilizing pipe getting closer to the humidifier outlet as the test housing is raised (Fig. 39), may also be responsible for this.

Figures 133, 134 and 135 are the three-dimensional plots of velocity profile for the tests D, C and B, respectively. Figures 136, 137 and 138 are the two-dimensional plots of velocity profiles at grid planes y=0 in., y=1 in. and y=2 in., respectively for tests D, C and B. As expected, the velocity profile falls in magnitude and tends to flatten as the flow progresses toward the filter face. For the grid planes y=0 and y=1 in., the velocity profiles for tests D and C are almost identical, showing that flow does not change much from 6.625 in. to 3.625 in., at least around the center of the filter. For grid plane y=3 in., the velocity profile for test C is higher than that of test D, indicating the expansion of the flow.

From Table 4, it is observed that tests K, J and I were performed using the same filter and with the same experimental conditions, at planes 3.625, 2.125 and 0.625 in. above the face of the filter, respectively. However, as mentioned before, test I was conducted using low laser power (2.8 Vdc) as compared to tests K and J which were

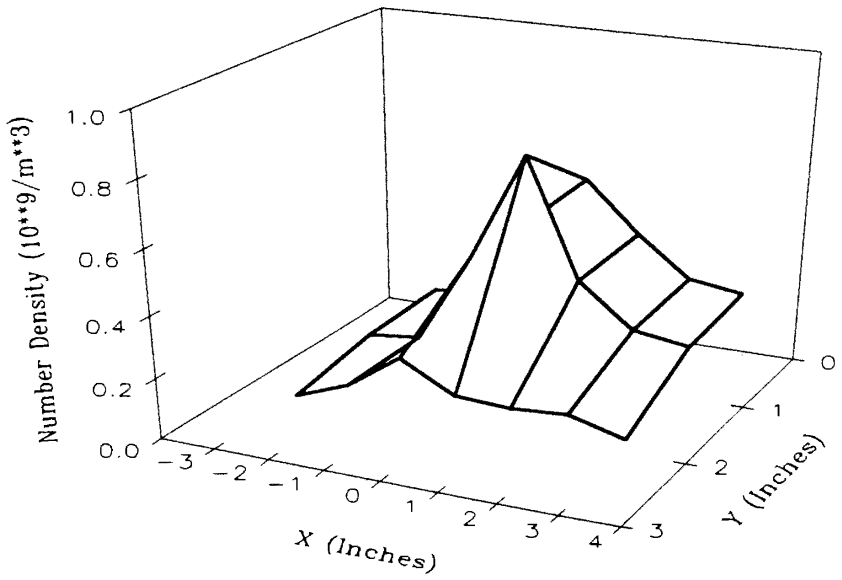

Figure 127. Three-Dimensional Plot of Number Density Distribution for Test D, at a Plane 6.625 In. Above the Filter Face

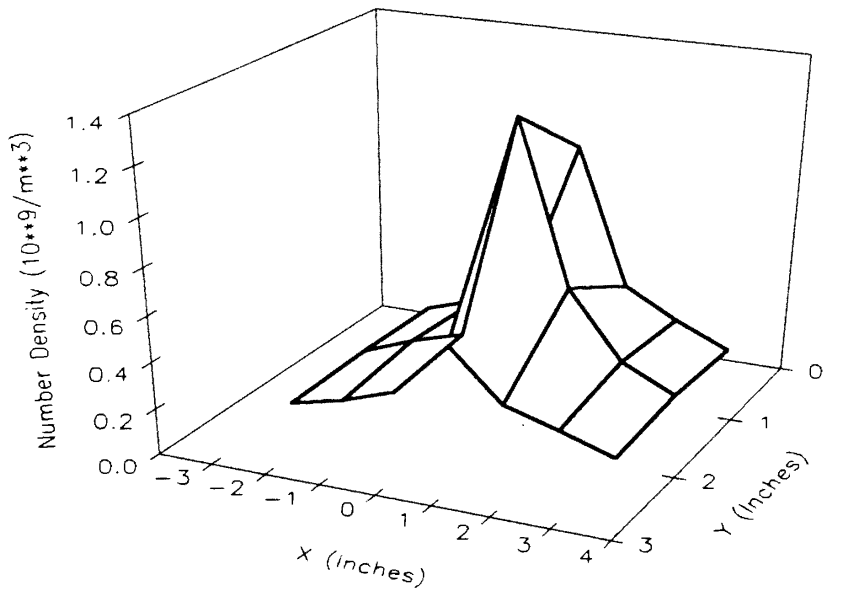

Figure 128. Three-Dimensional Plot of Number Density Distribution for Test C, at a Plane 3.625 In. Above the Filter Face

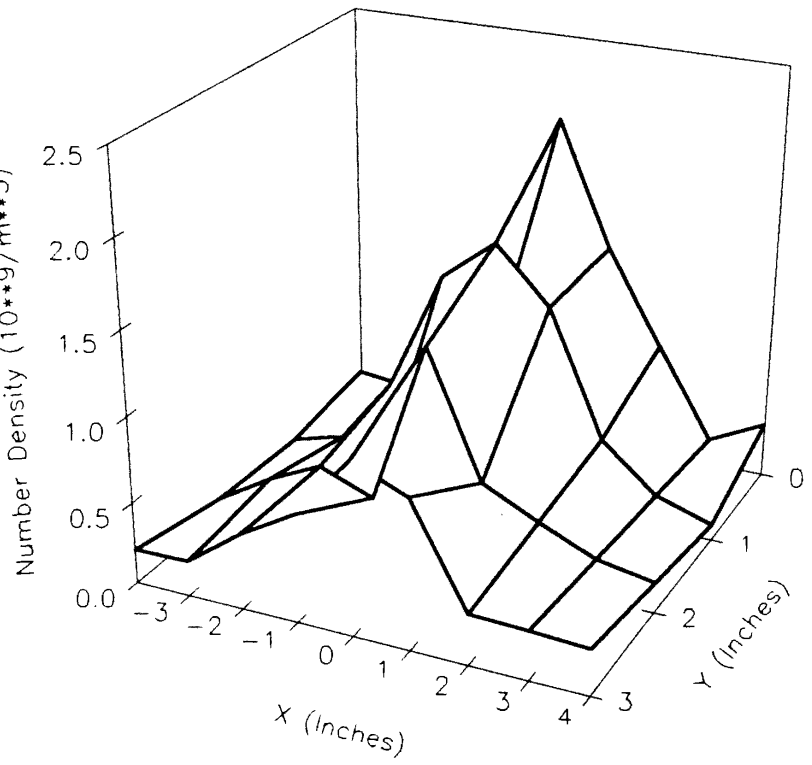

Figure 129. Three-Dimensional Plot of Number Density Distribution for Test B, at a Plane 0.625 In. Above the Filter Face

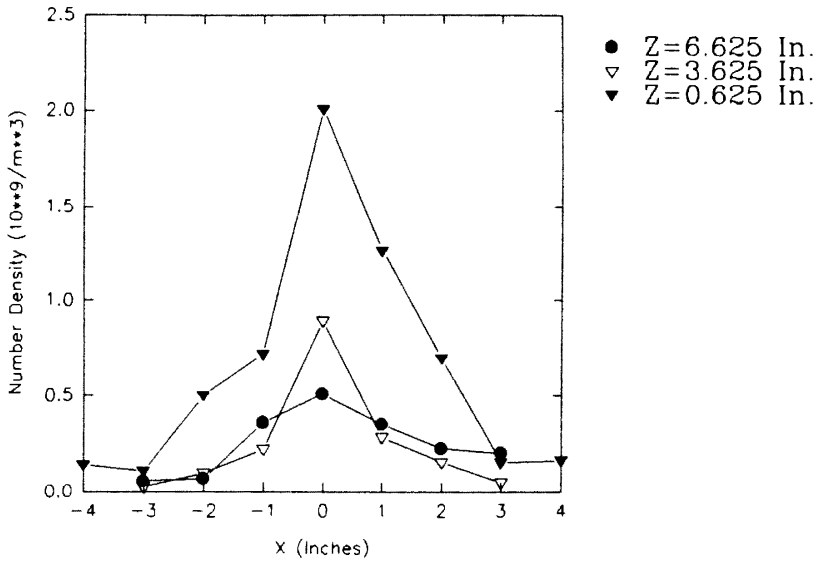

Figure 130. Comparison of Number Densities for Tests D, C and B at Y=0 In.

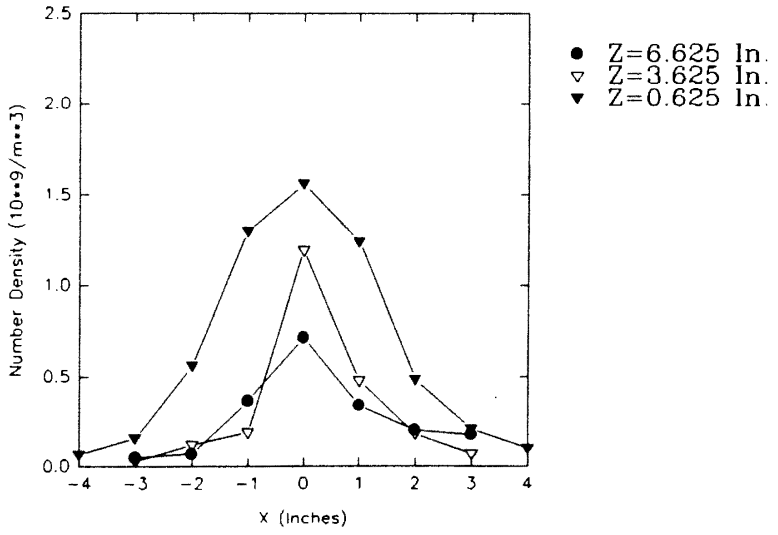

Figure 131. Comparison of Number Densities for Tests D, C and B at Y=1 In.

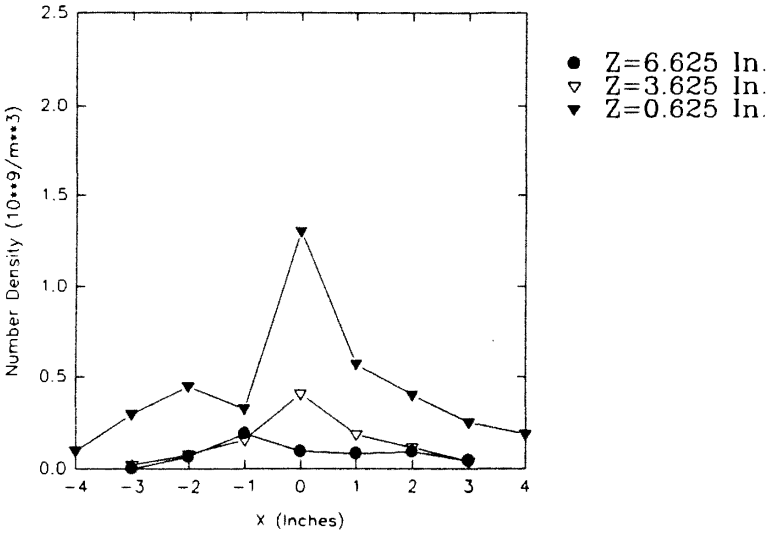

Figure 132. Comparison of Number Densities for Tests D, C and B at Y=2 In.

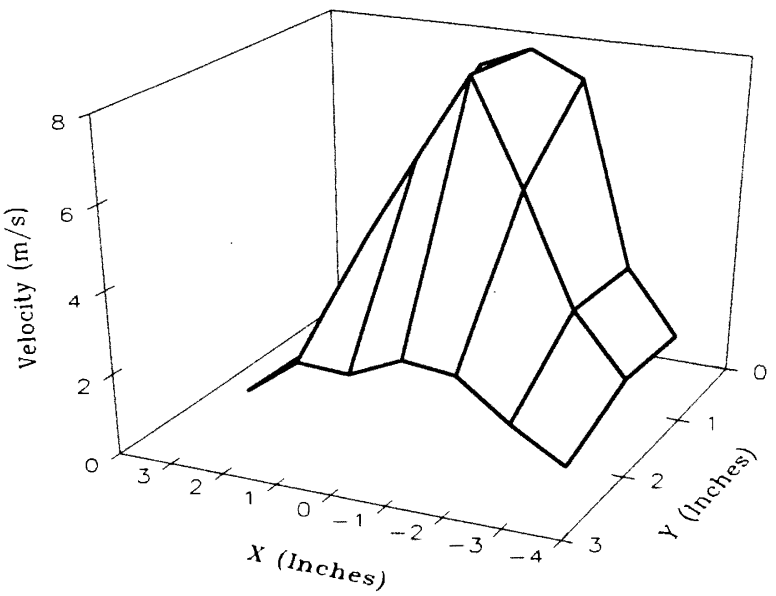

Figure 133. Three-Dimensional Plot of Velocity Profile for Test D, at a Plane 6.625 In. Above the Filter Face

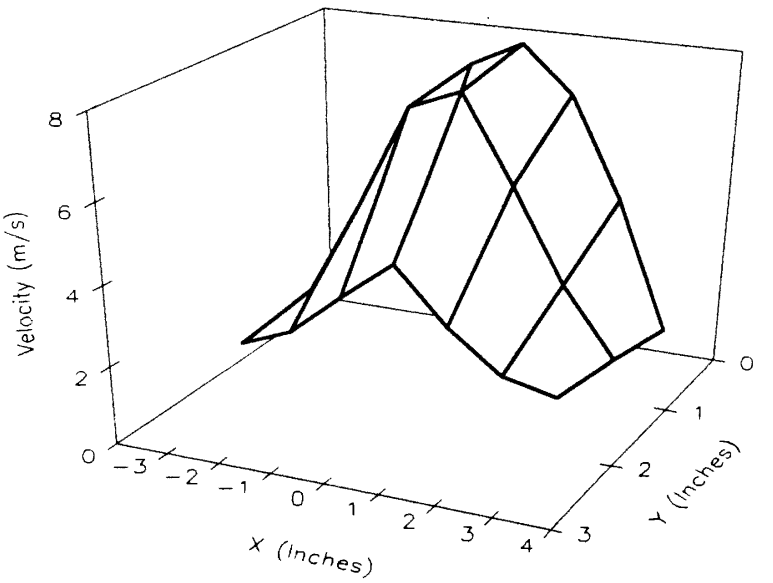

Figure 134. Three-Dimensional Plot of Velocity Profile for Test C, at a Plane 3.625 In. Above the Filter Face

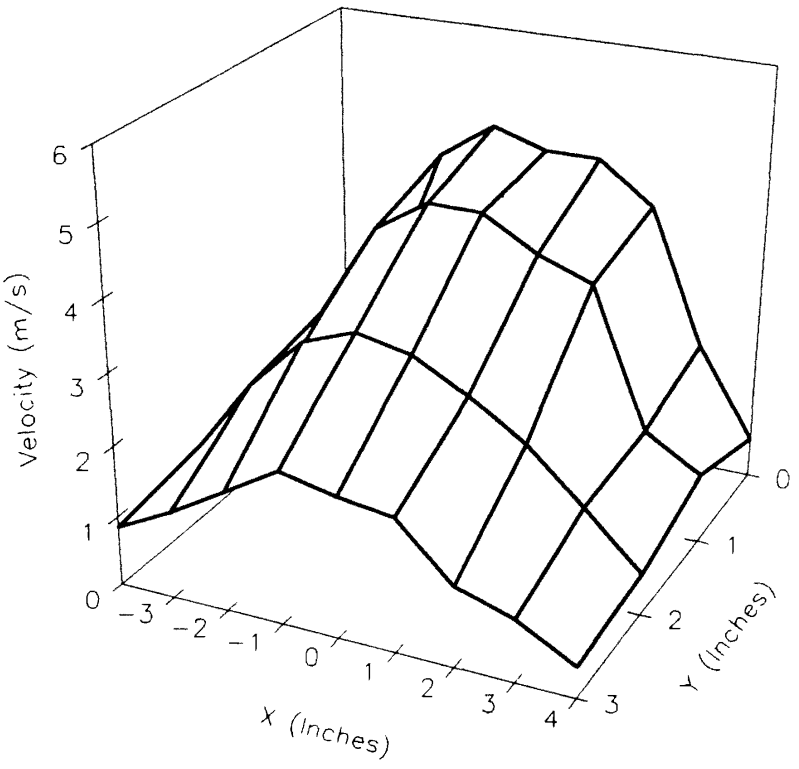

Figure 135. Three-Dimensional Plot of Velocity Profile for Test B, at a Plane 0.625 In. Above the Filter Face

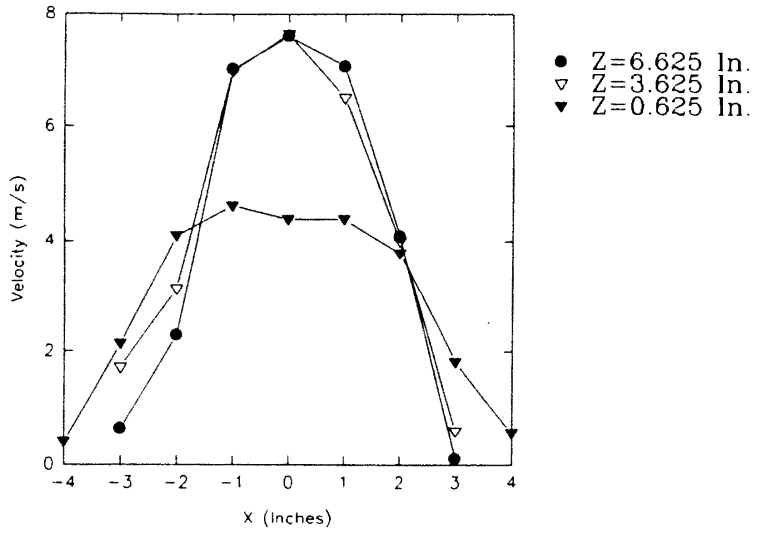

Figure 136. Comparison of Velocity Profiles for Tests D, C and B at Y=0 In.

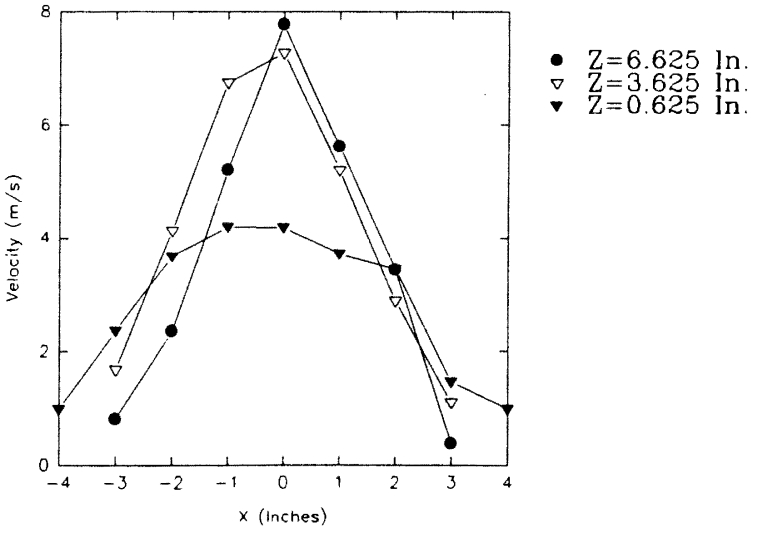

Figure 137. Comparison of Velocity Profiles for Tests D, C and B at Y=1 In.

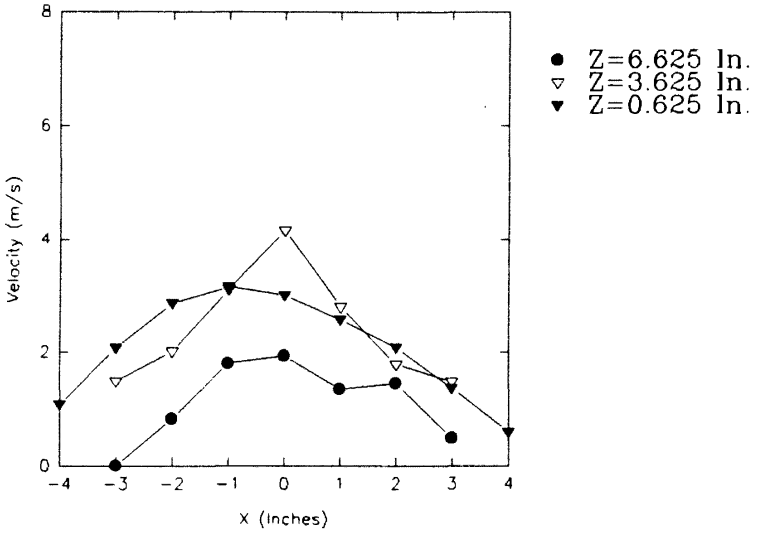

Figure 138. Comparison of Velocity Profiles for Tests D, C and B at Y=2 In.

conducted using high laser power (8 Vdc). Therefore, as discussed before in this chapter under the section 'Sensitivity Measurements', the actual number density profile for test I should have been higher than that measured. Figures 139, 140 and 141 are the three-dimensional plots of number density distribution for tests K, J and I, respectively. These also have been presented and discussed before. These figures also suggest that the number density distribution maintains the same symmetrical profile, with concentration being highest at and around the center and gradually decreasing toward the edges of the filter, with the flow getting closer to the filter face.

Figure 142 is a two-dimensional plot of number density distribution at grid plane y=0 in. for tests K, J and I. It is observed that the number density profile is almost identical for tests K and J. This is reasonable, considering that tests K and J were conducted at planes which differed just by 1.5 in. Even the profile for test I is comparable to those of K and J; and assuming a higher actual profile due to laser power difference for test I, the trend shown by this figure is the same as observed before - an increase in number density as the flow gets closer to the face of the filter. Figure 143 is a two-dimensional plot of number density distribution at grid plane y=1 in. for tests K and J and at y=0.792 in. for test I. Figure 144 is a two-dimensional plot of number density distribution at grid plane y=2 in. for tests K and J and at y=2.375 in. for test I. From Figs. 143 and 144, it is observed that the number density for test I is higher as compared to that for tests K and J, indicating the expansion of the flow as it progresses toward the filter face. An overall higher number density close to the filter face also affirms that rebounded particles from the filter face stay close to the filter.

Figures 145, 146 and 147 are the three-dimensional plots of velocity profiles for the tests K, J and I, respectively. Figure 148 is a two-dimensional plot of number density distribution at grid plane y=0 in. for tests K, J and I. Figure 149 is a two-dimensional plot of velocity profiles at grid plane y=1 in. for tests K and J and at y=0.792 in. for test I. Figure 150 is a two-dimensional plot of velocity profiles at grid plane y=2 in. for tests K

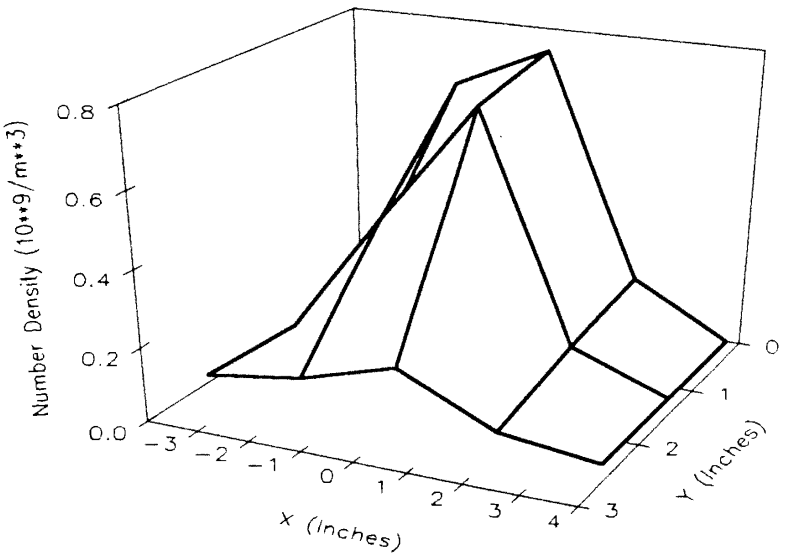

Figure 139. Three-Dimensional Plot of Number Density Distribution for Test K, at a Plane 3.625 In. Above the Filter Face

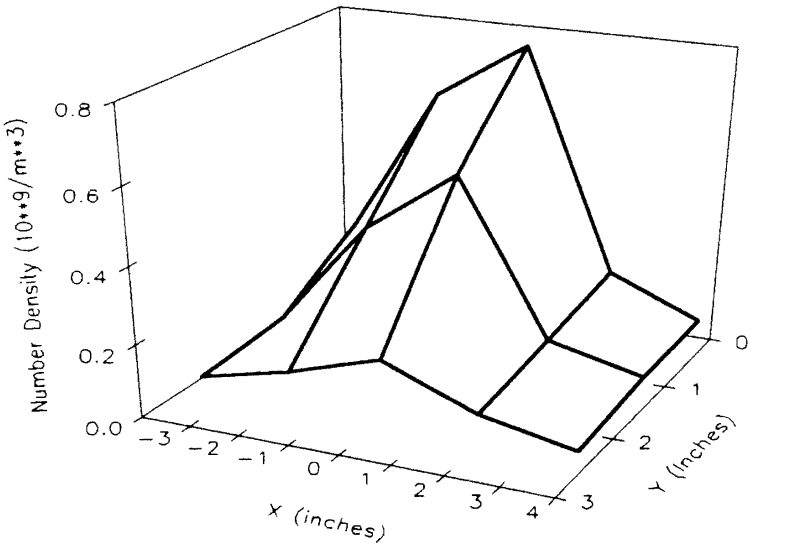

Figure 140. Three-Dimensional Plot of Number Density Distribution for Test J, at a Plane 2.125 In. Above the Filter Face

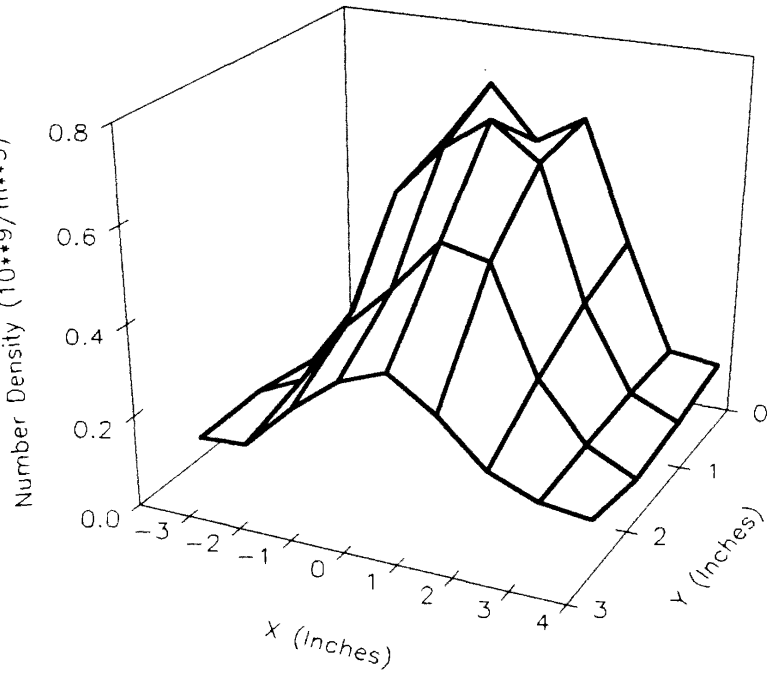

Figure 141. Three-Dimensional Plot of Number Density Distribution for Test I, at a Plane 0.625 In. Above the Filter Face

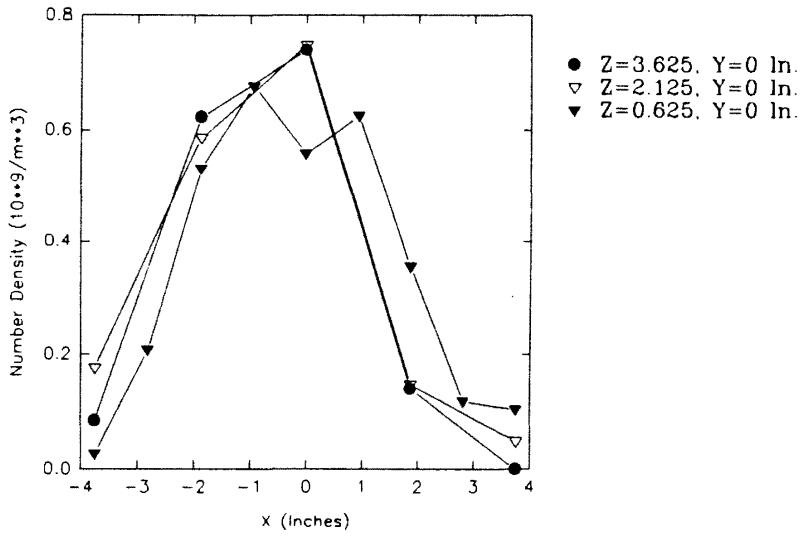

Figure 142. Comparison of Number Densities for Tests K, J and I

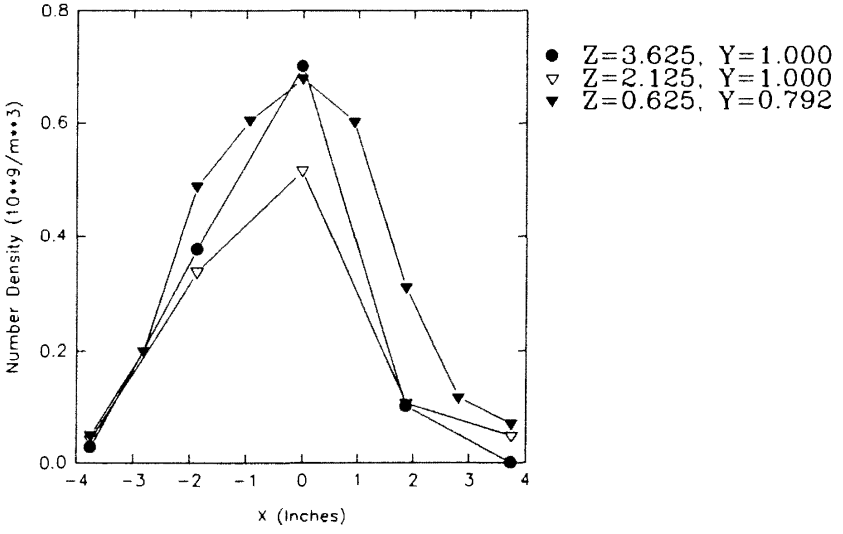

Figure 143. Comparison of Number Densities for Tests K, J and I

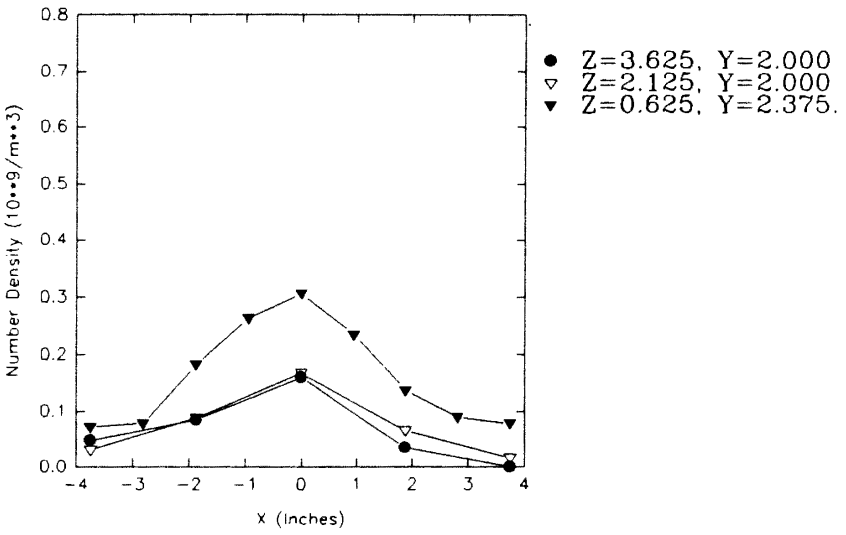

Figure 144. Comparison of Number Densities for Tests K, J and I

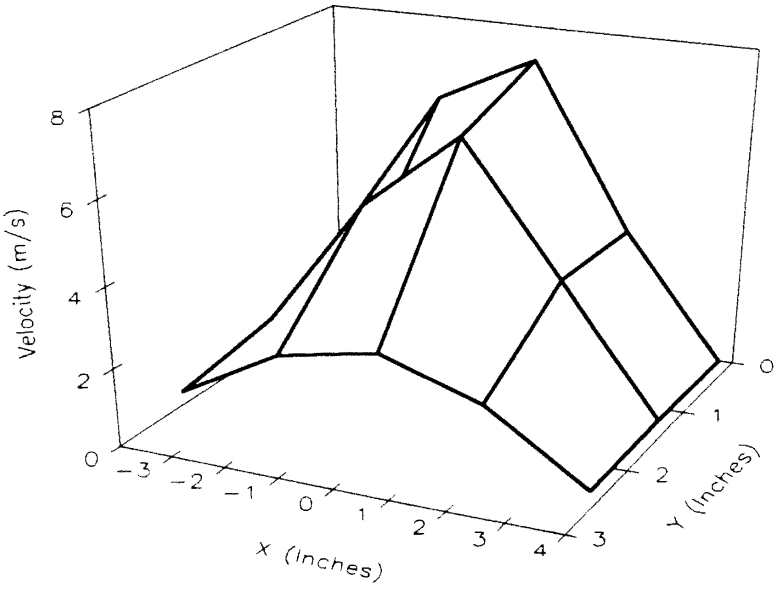

Figure 145. Three-Dimensional Plot of Velocity Profile for Test K, at a Plane 3.625 In. Above the Filter Face

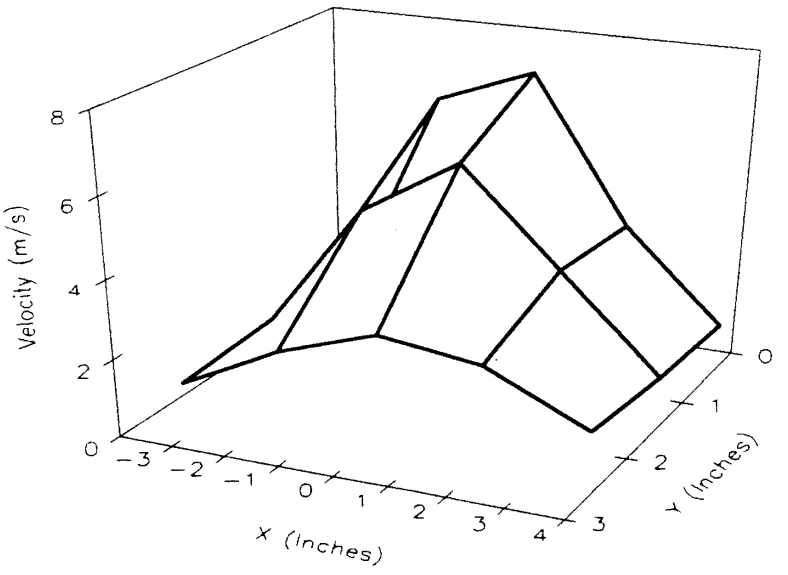

Figure 146. Three-Dimensional Plot of Velocity Profile for Test J, at a Plane 2.125 In. Above the Filter Face

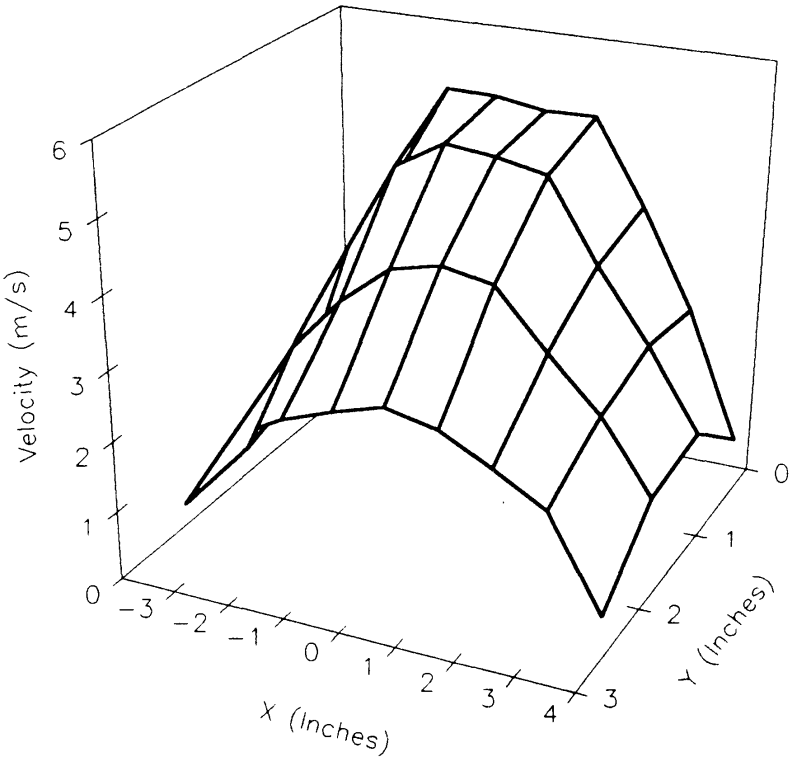

Figure 147. Three-Dimensional Plot of Velocity Profile for Test I, at a Plane 0.625 In. Above the Filter Face

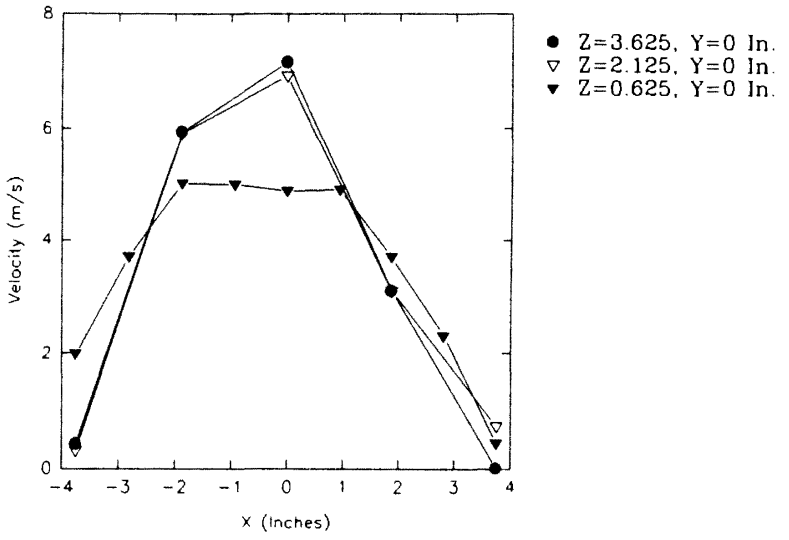

Figure 148. Comparison of Velocity Profiles for Tests K, J and I

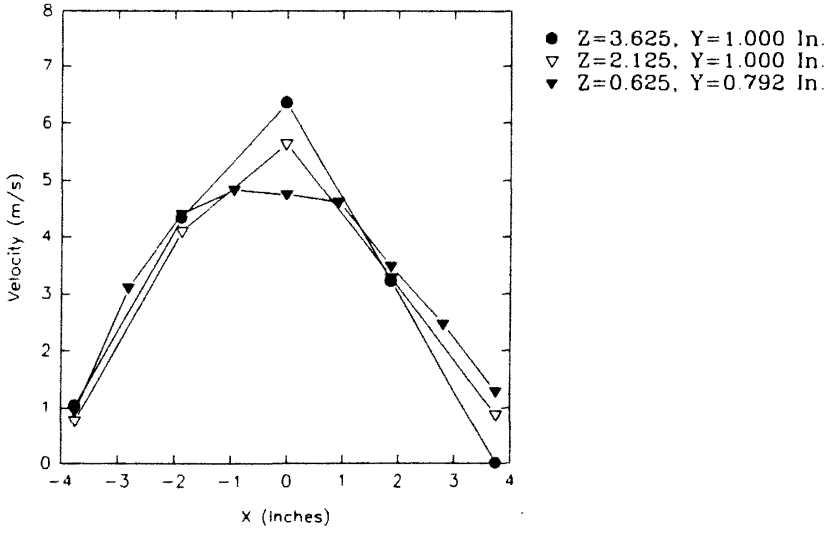

Figure 149. Comparison of Velocity Profiles for Tests K, J and I

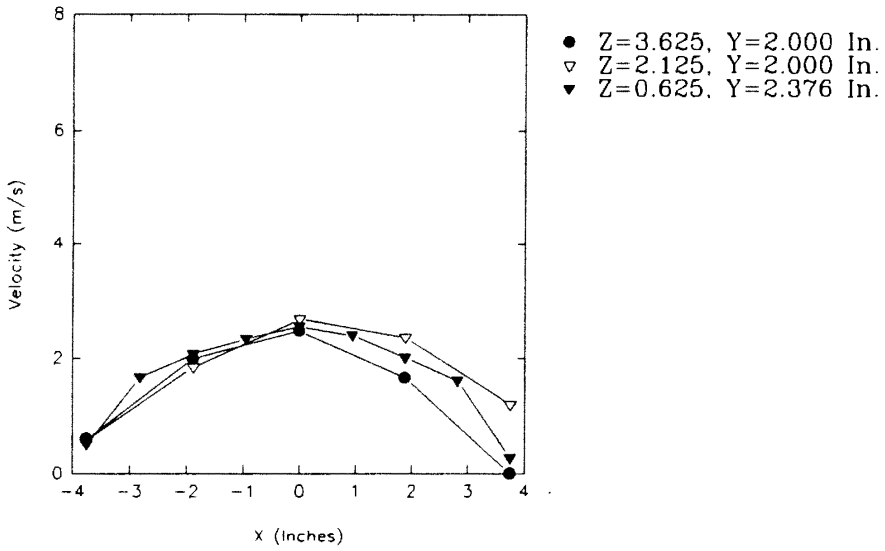

Figure 150. Comparison of Velocity Profiles for Tests K, J and I

and J and at y=2.375 in. for test I. As expected, the velocity profile decreases and tends to flatten as the flow progresses toward the filter face. For the grid planes y=0 in. and y=1 in., the velocity profiles for tests K and J are almost identical, showing that the velocity does not change much from 3.625 in. to 2.125 in.

It can therefore be deduced that, as the flow progresses toward the filter face, it expands and so does the number density distribution. Also a higher number density is observed close to the filter face which may be due to particles that bounce off of the filter face.

Time History Measurements

As mentioned before, the filter performance changes with time due to its constant usage. Therefore, the particle number density distribution would be different for different filters of different 'age'. The particle number density distribution would also be different for the same filter at different points in its 'life'. Three independent tests were conducted to study the time history effects on number density and velocity profiles over the filter face. These are identified as tests F, H and L. As observed from Table 4, each of these tests were conducted using a new filter. Tests F and H were performed under identical experimental conditions and at a plane closest to the filter face (0.625 in.) while test L was conducted at a plane 2.125 in. above the filter face. The study of time history involved repeated measurements at the grid points over an extended interval of time. Thus, the filter was mapped by taking measurements at the grid points, and those measurements constituted one set (or one cycle) of data. The process of mapping the filter was repeated to obtain five sets of data (or five cycles). The duration of the entire test varied for each test depending upon the grid employed for taking the measurements. Results of the first set of data (or first cycle) for these three tests have been presented and discussed before.

Figures 151 to 155 are three-dimensional plots of particle number density distributions for the five sets of data for test F. Figures 156 to 160 are the corresponding two-dimensional plots. It is important to note that measurements were taken only for the front half of the filter. 'Time' for a particular set indicates the relative time to the beginning of the measurements for that set with respect to a reference time of zero. Thus, the difference in the 'time' of a particular set and the 'time' of the set immediately following that set gives the actual time spent to take measurements for that particular set. The entire test lasted for about 180 minutes. It is observed from these figures that the number density gradually decreases with time for the entire filter. Also, the number density profile becomes more even and flat with the passage of time. This may be attributed to the supposition that when the filter is new, it repels the water particles, and when it gets older (and wetter), it starts attracting (or at least it decreases its repulsion for) the water particles. Therefore, at a plane close to the filter face, less and less particles are there which have been bounced off of the filter face, with the passage of time; and hence the number density steadily drops.

Figures 161 to 165 are three-dimensional plots of velocity profiles for the five sets of data for test F. Figures 166 to 170 are the corresponding two-dimensional plots. The velocity profiles does not show any significant variation with the passage of time. This, therefore, suggests that measurements pertaining to number density are indispensable; as velocity profiles alone does not reveal much (and accurate) information about number density distribution, especially if the filter is not new.

Figures 171 to 175 are three-dimensional plots of particle number density distributions for the five sets of data for test H. Figures 176 to 180 are the corresponding two-dimensional plots. For this test also, measurements were taken only for the front half of the filter. The entire test lasted for about 325 minutes. No significant trend or pattern is observed. However, an unusual peak is observed at the corner of the filter as observed in Fig. 178. Figures 181 to 185 are three-dimensional plots of velocity profiles for the five

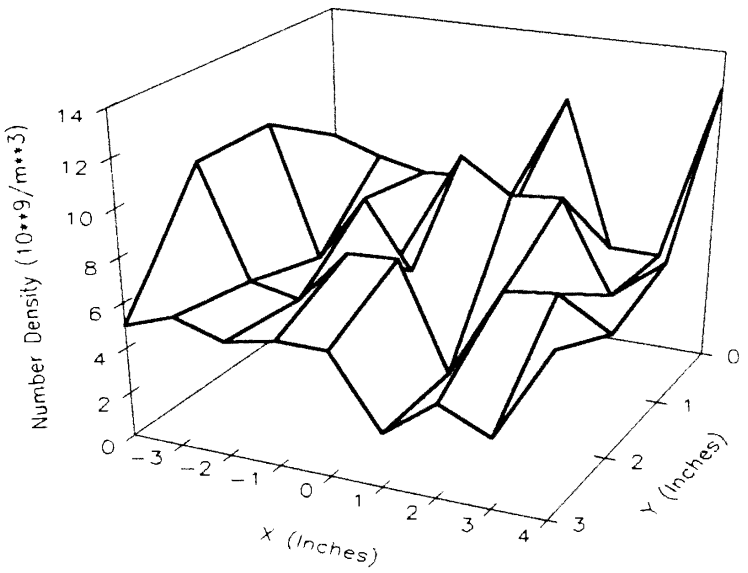

Figure 151. Three-Dimensional Plot of Number Density Distribution for Test F, at a Plane 0.625 In. Above the Filter Face (Time=0 min.)

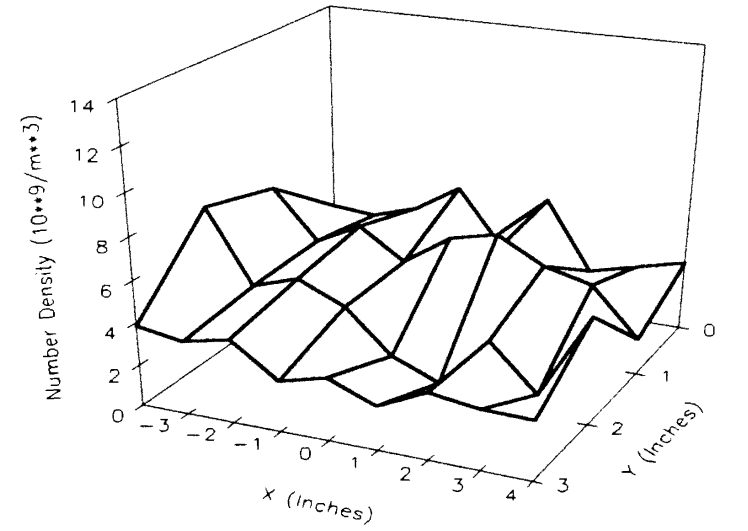

Figure 152. Three-Dimensional Plot of Number Density Distribution for Test F, at a Plane 0.625 In. Above the Filter Face (Time=30 min.)

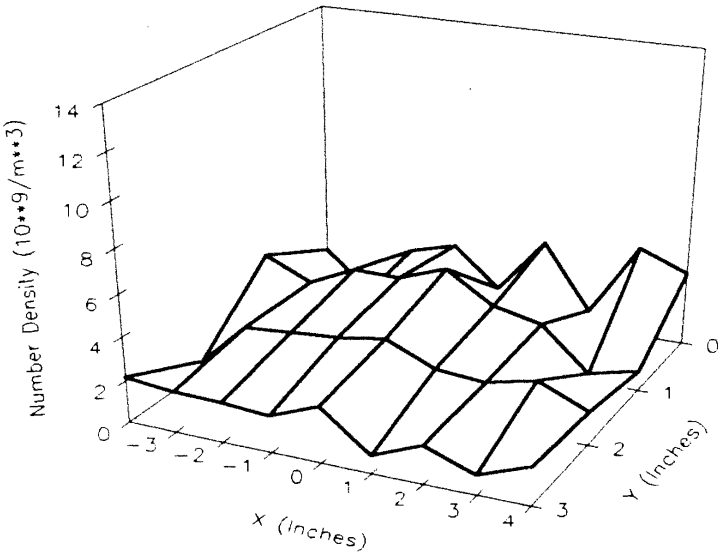

Figure 153. Three-Dimensional Plot of Number Density Distribution for Test F, at a Plane 0.625 In. Above the Filter Face (Time=60 min.)

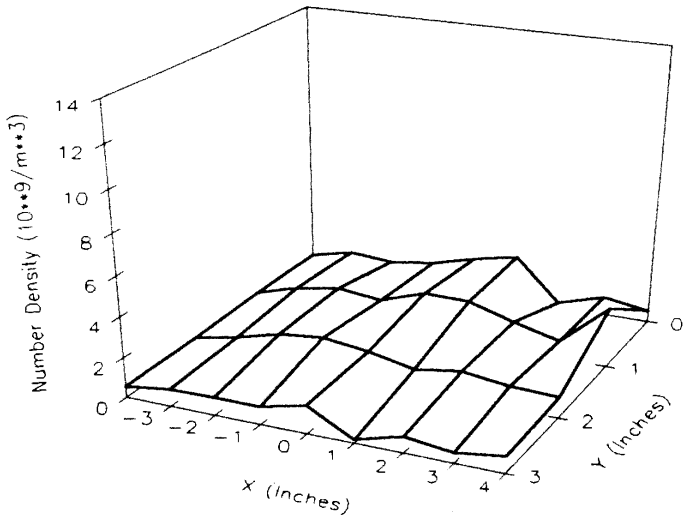

Figure 154. Three-Dimensional Plot of Number Density Distribution for Test F, at a Plane 0.625 In. Above the Filter Face (Time=90 min.)

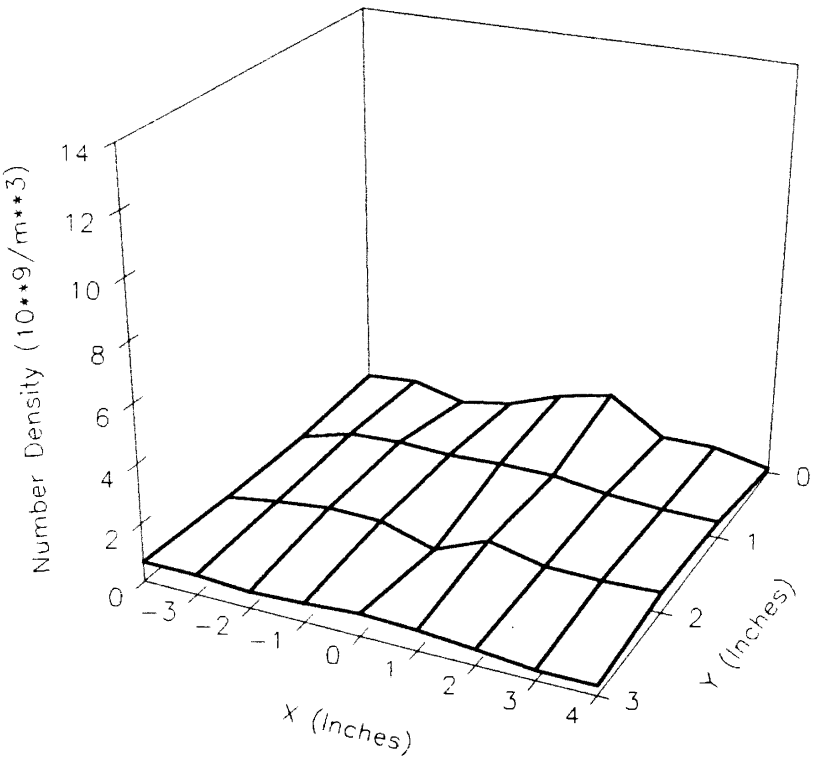

Figure 155. Three-Dimensional Plot of Number Density Distribution for Test F, at a Plane 0.625 In. Above the Filter Face (Time=150 min.)

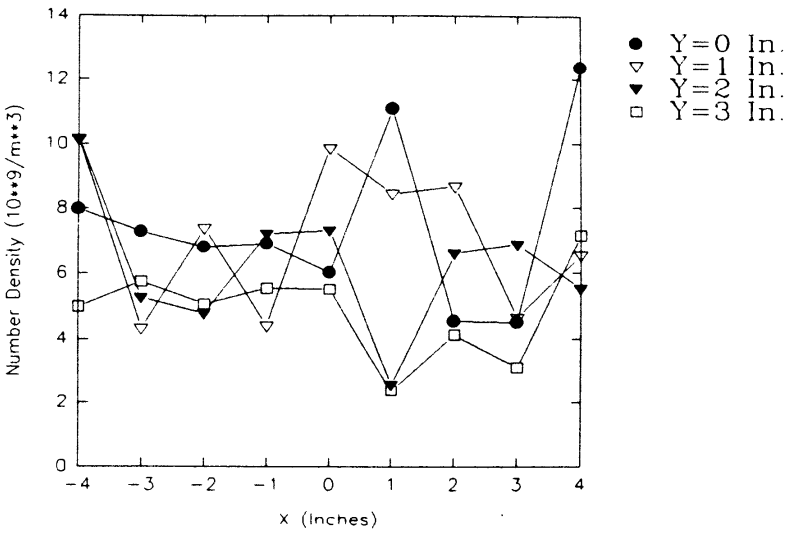

Figure 156. Two-Dimensional Plot of Number Density Distribution for Test F, at Different Grid Sections for a Plane 0.625 In. Above the Filter Face (Time=0 min.)

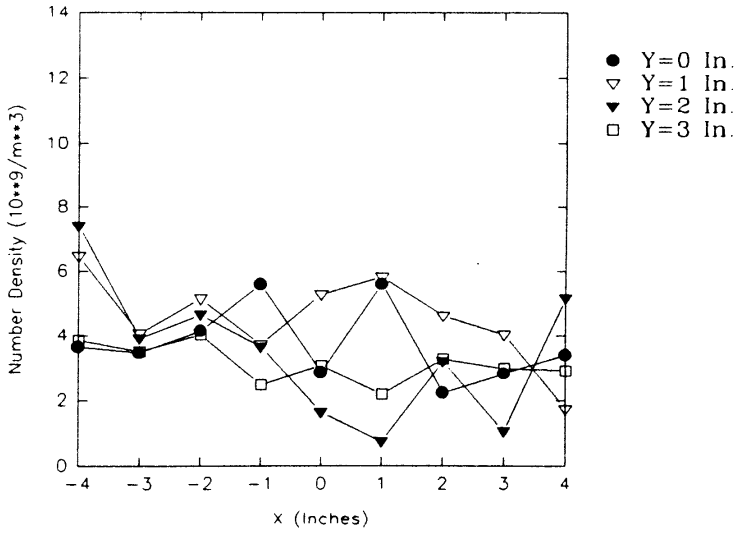

Figure 157. Two-Dimensional Plot of Number Density Distribution for Test F, at Different Grid Sections for a Plane 0.625 In. Above the Filter Face (Time=30 min.)

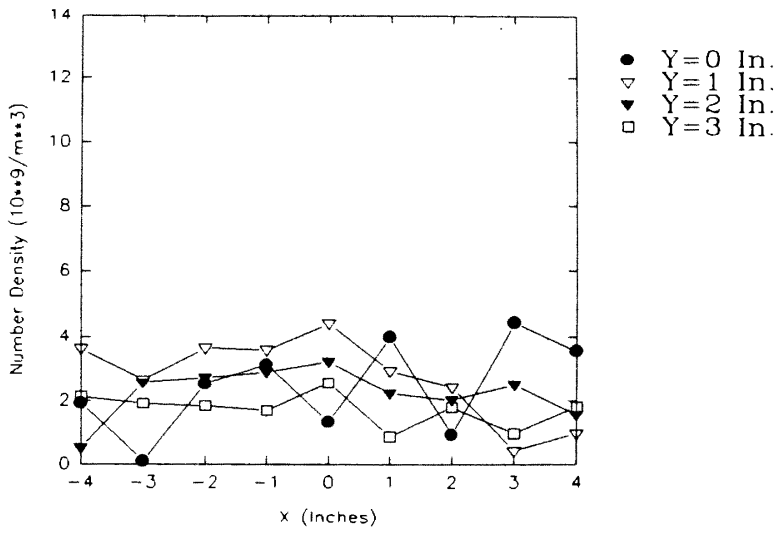

Figure 158. Two-Dimensional Plot of Number Density Distribution for Test F, at Different Grid Sections for a Plane 0.625 In. Above the Filter Face (Time=60 min.)

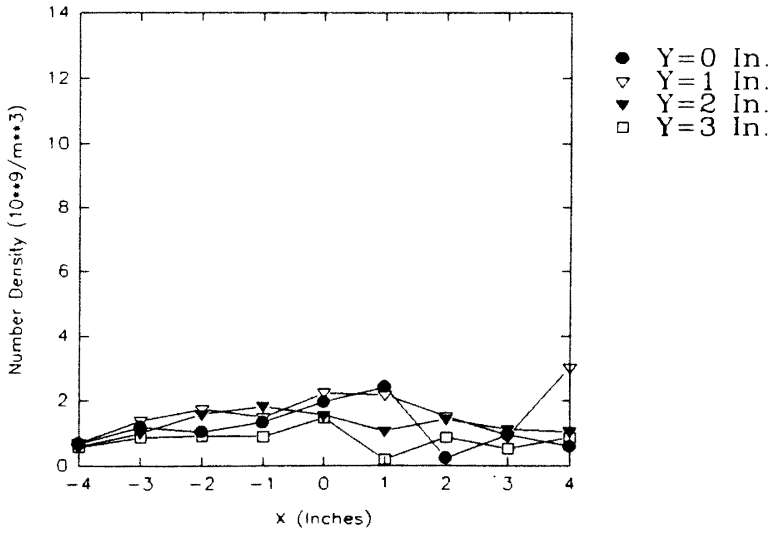

Figure 159. Two-Dimensional Plot of Number Density Distribution for Test F, at Different Grid Sections for a Plane 0.625 In. Above the Filter Face (Time=90 min.)

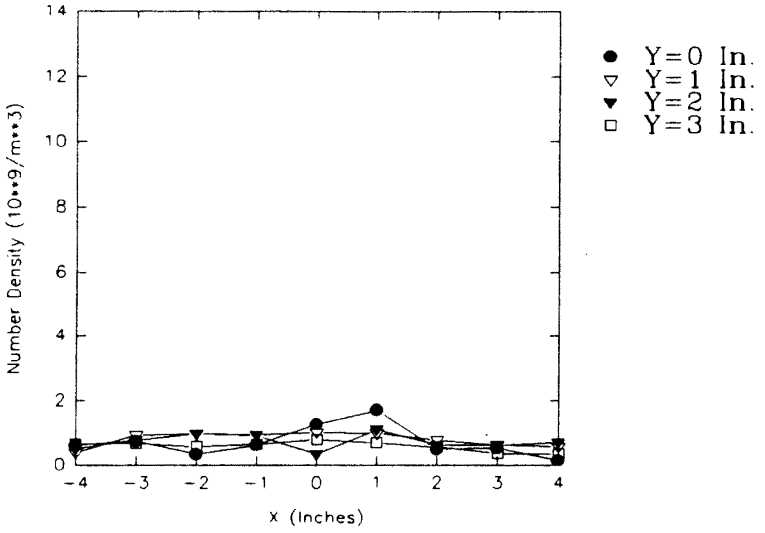

Figure 160. Two-Dimensional Plot of Number Density Distribution for Test F, at Different Grid Sections for a Plane 0.625 In. Above the Filter Face (Time=150 min.)

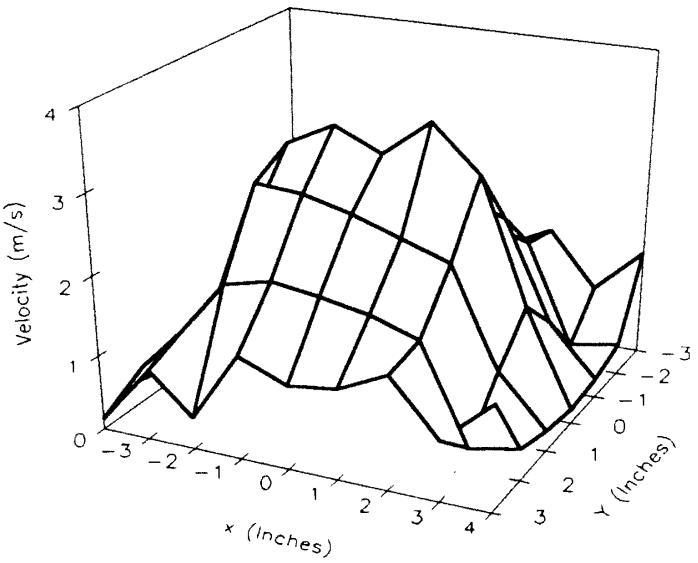

Figure 161. Three-Dimensional Plot of Velocity Profile for Test F, at a Plane 0.625 In. Above the Filter Face (Time=0 min.)

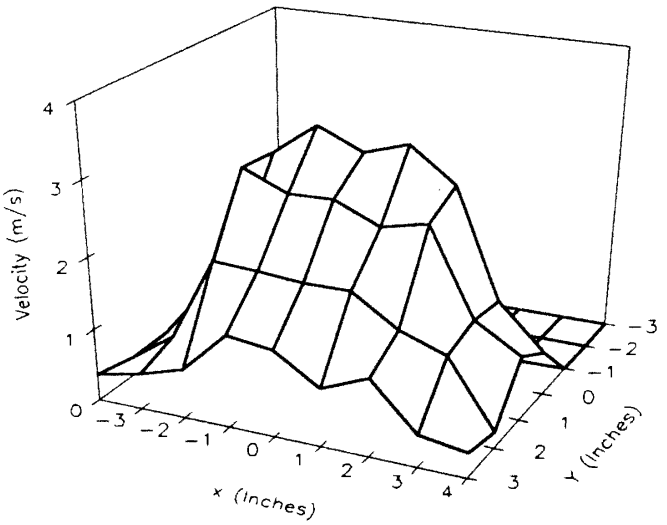

Figure 162. Three-Dimensional Plot of Velocity Profile for Test F, at a Plane 0.625 In. Above the Filter Face (Time=30 min.)

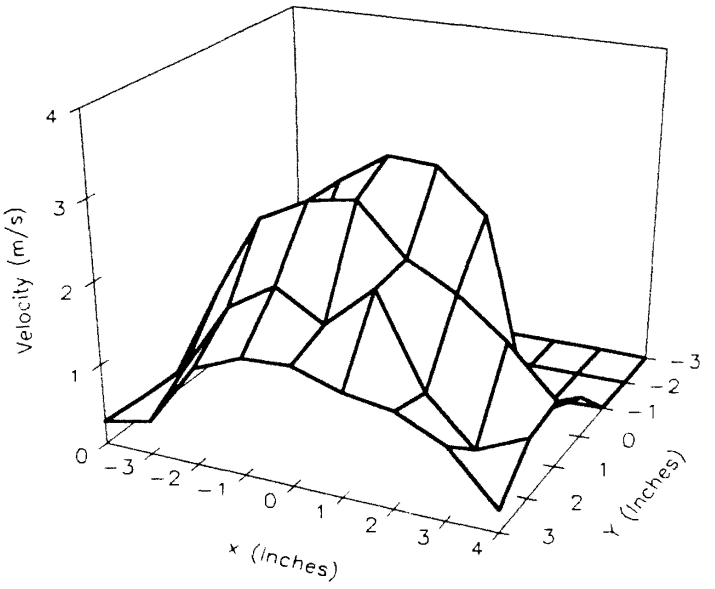

Figure 163. Three-Dimensional Plot of Velocity Profile for Test F, at a Plane 0.625 In. Above the Filter Face (Time=60 min.)

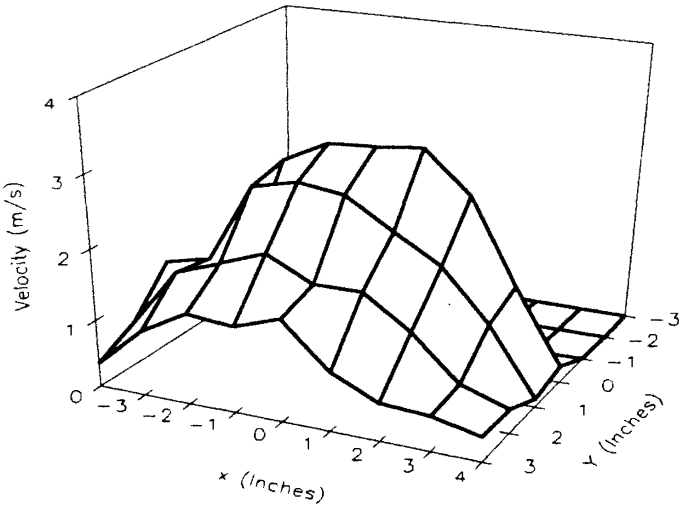

Figure 164. Three-Dimensional Plot of Velocity Profile for Test F, at a Plane 0.625 In. Above the Filter Face (Time=90 min.)

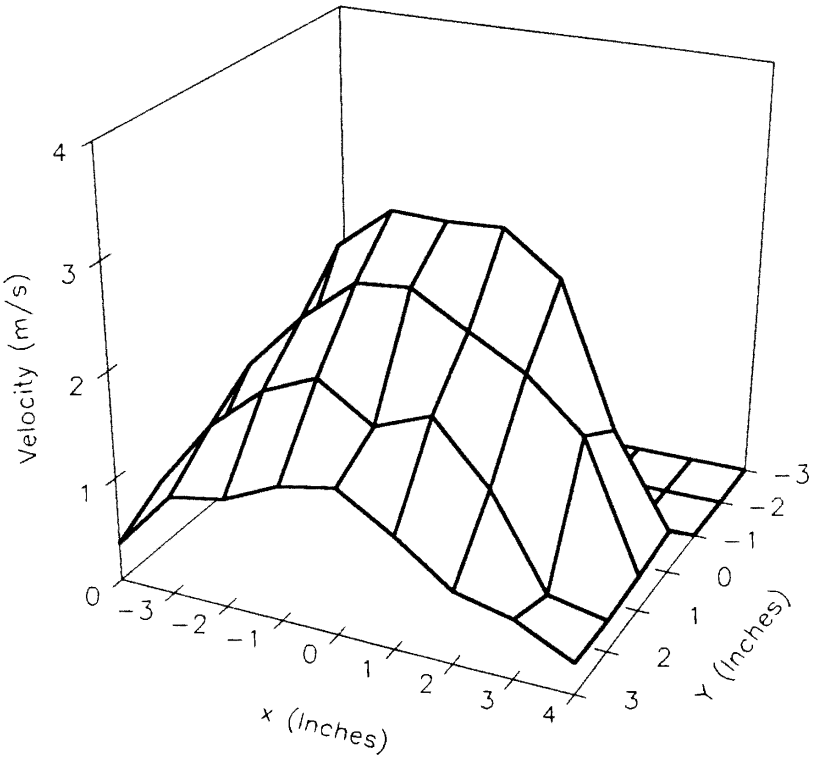

Figure 165. Three-Dimensional Plot of Velocity Profile for Test F, at a Plane 0.625 In. Above the Filter Face (Time=150 min.)

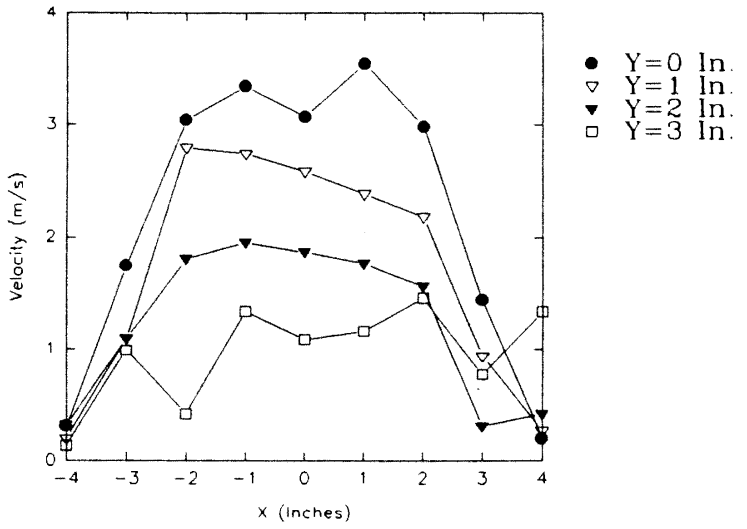

Figure 166. Two-Dimensional Plot of Velocity Profiles for Test F, at Different Grid Sections for a Plane 0.625 In. Above the Filter Face (Time=0 min.)

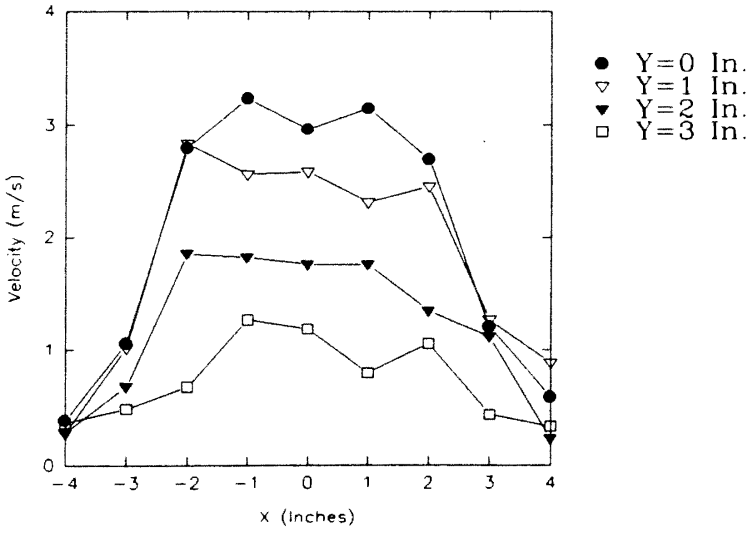

Figure 167. Two-Dimensional Plot of Velocity Profiles for Test F, at Different Grid Sections for a Plane 0.625 In. Above the Filter Face (Time=30 min.)

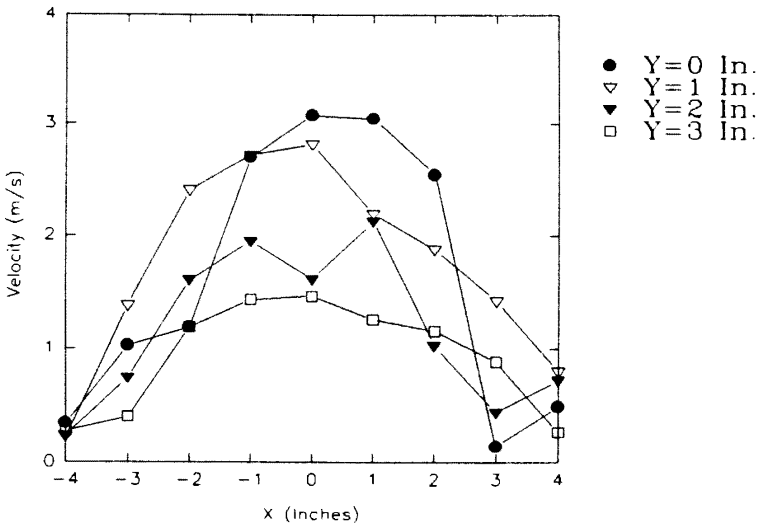

Figure 168. Two-Dimensional Plot of Velocity Profiles for Test F, at Different Grid Sections for a Plane 0.625 In. Above the Filter Face (Time=60 min.)

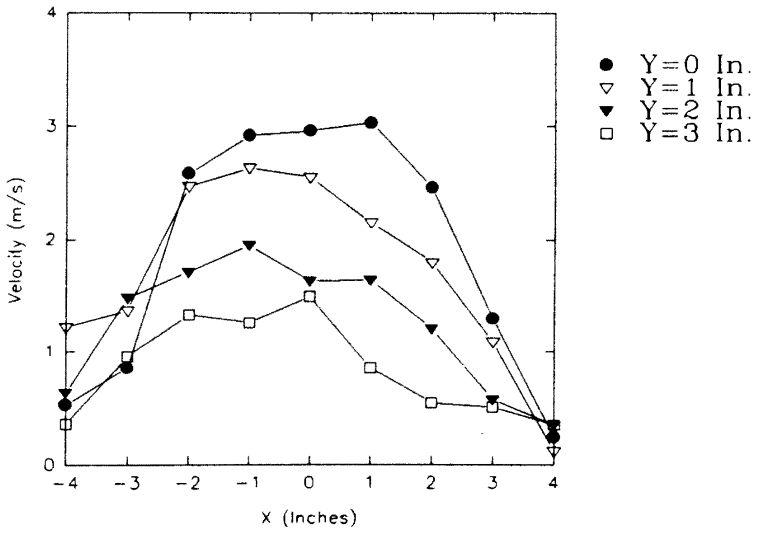

Figure 169. Two-Dimensional Plot of Velocity Profiles for Test F, at Different Grid Sections for a Plane 0.625 In. Above the Filter Face (Time=90 min.)

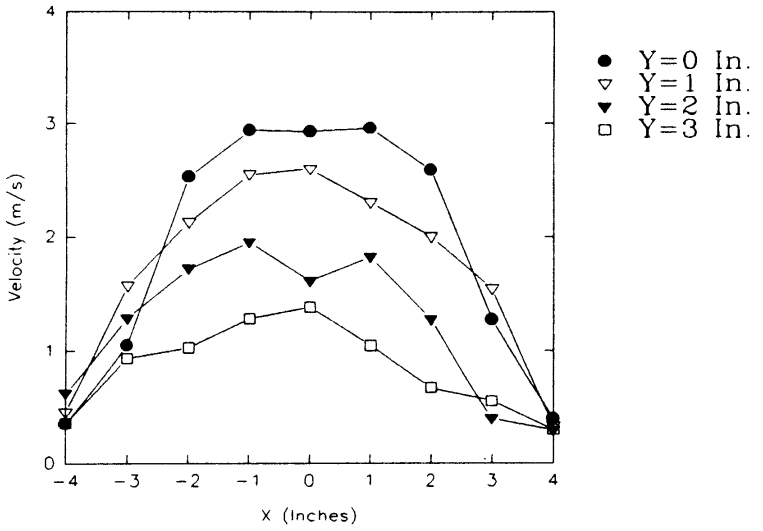

Figure 170. Two-Dimensional Plot of Velocity Profiles for Test F, at Different Grid Sections for a Plane 0.625 In. Above the Filter Face (Time=150 min.)

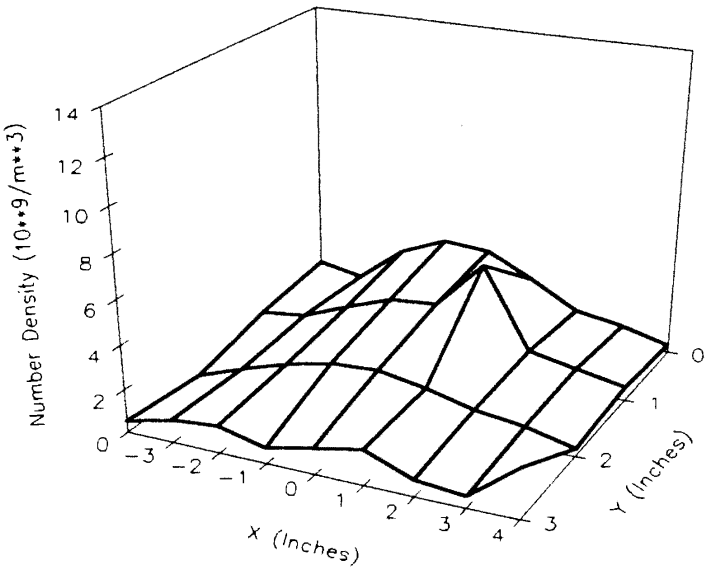

Figure 171. Three-Dimensional Plot of Number Density Distribution for Test H, at a Plane 0.625 In. Above the Filter Face (Time=0 min.)

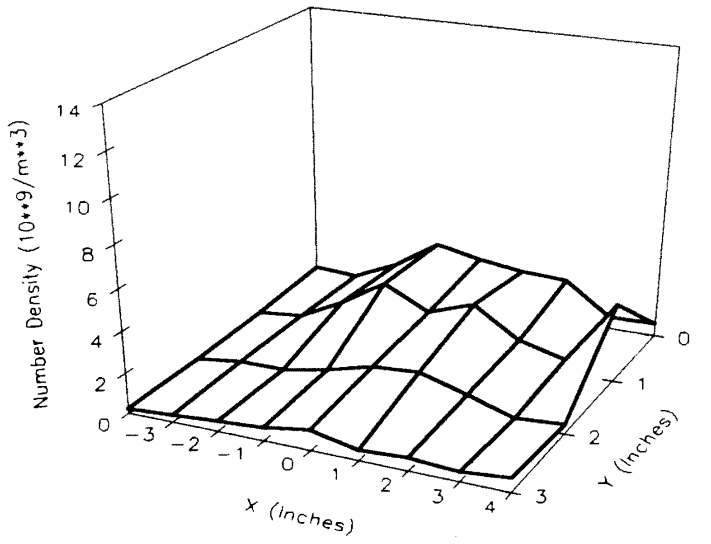

Figure 172. Three-Dimensional Plot of Number Density Distribution for Test H, at a Plane 0.625 In. Above the Filter Face (Time=45 min.)

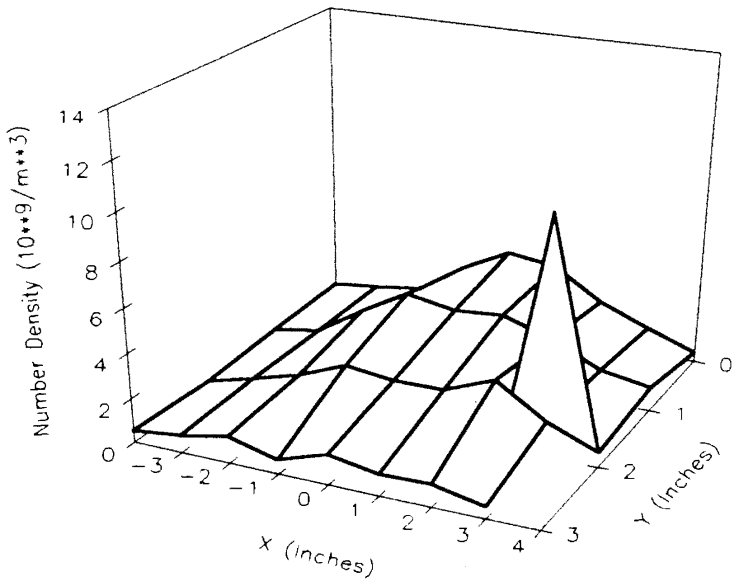

Figure 173. Three-Dimensional Plot of Number Density Distribution for Test H, at a Plane 0.625 In. Above the Filter Face (Time=90 min.)

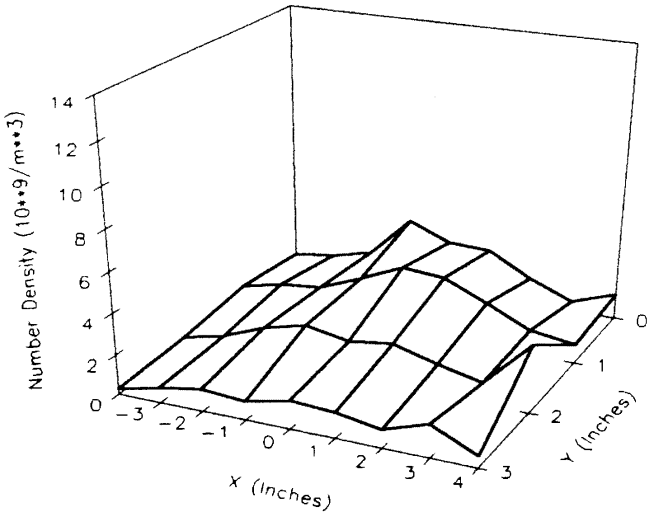

Figure 174. Three-Dimensional Plot of Number Density Distribution for Test H, at a Plane 0.625 In. Above the Filter Face (Time=135 min.)

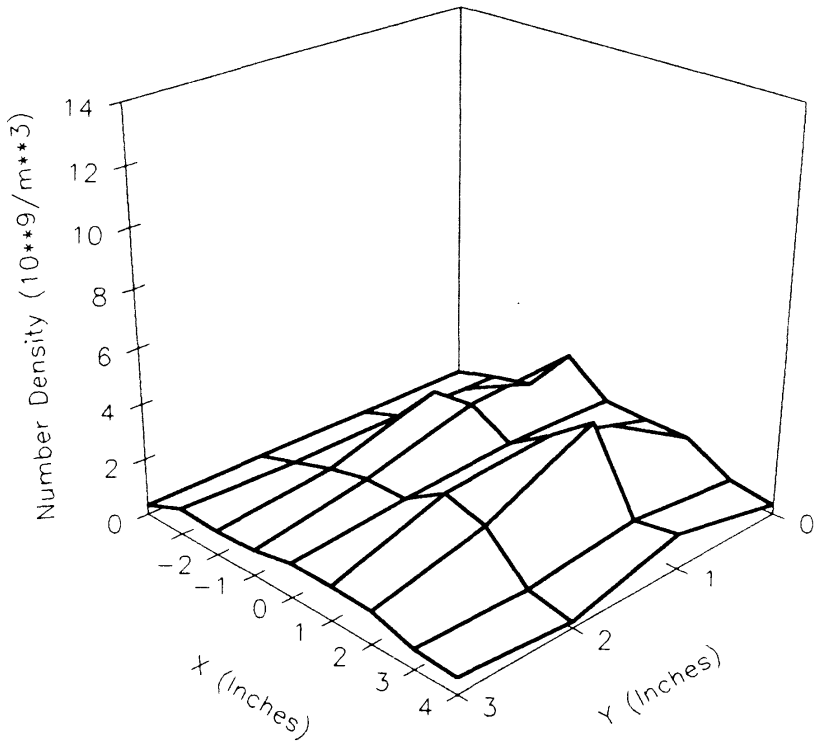

Figure 175. Three-Dimensional Plot of Number Density Distribution for Test H, at a Plane 0.625 In. Above the Filter Face (Time=280 min.)

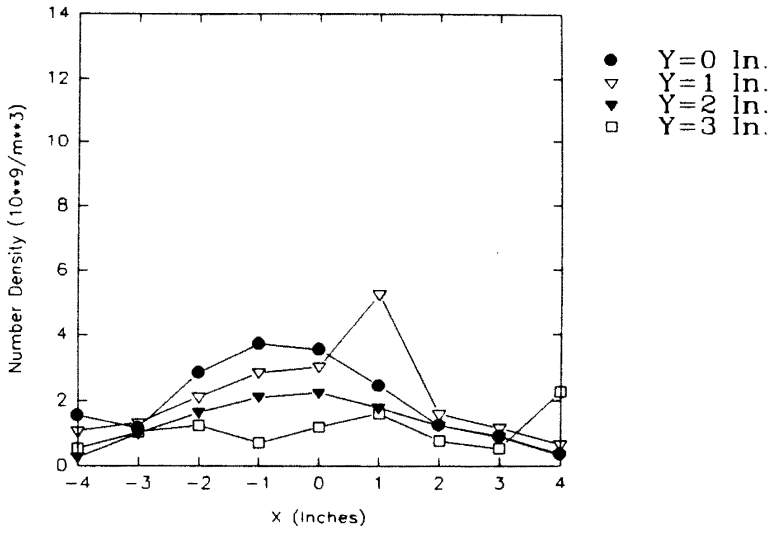

Figure 176. Two-Dimensional Plot of Number Density Distribution for Test H, at Different Grid Sections for a Plane 0.625 In. Above the Filter Face (Time=0 min.)

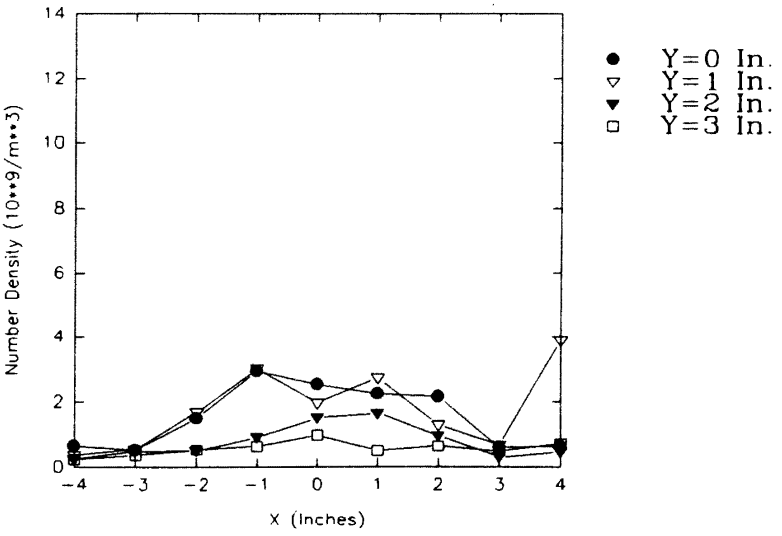

Figure 177. Two-Dimensional Plot of Number Density Distribution for Test H, at Different Grid Sections for a Plane 0.625 In. Above the Filter Face (Time=45 min.)

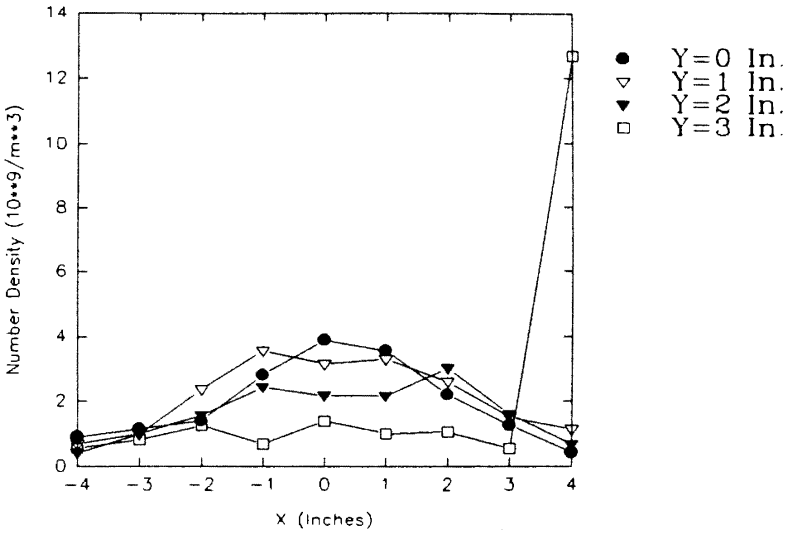

Figure 178. Two-Dimensional Plot of Number Density Distribution for Test H, at Different Grid Sections for a Plane 0.625 In. Above the Filter Face (Time=90 min.)

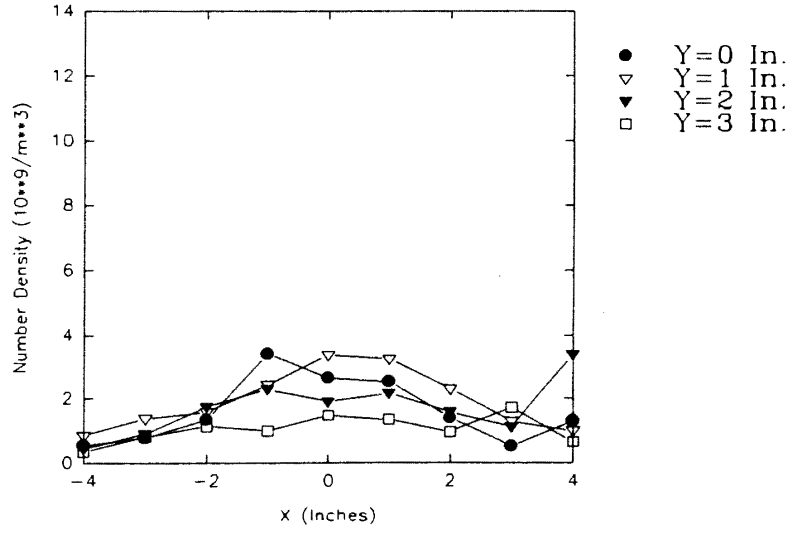

Figure 179. Two-Dimensional Plot of Number Density Distribution for Test H, at Different Grid Sections for a Plane 0.625 In. Above the Filter Face (Time=135 min.)

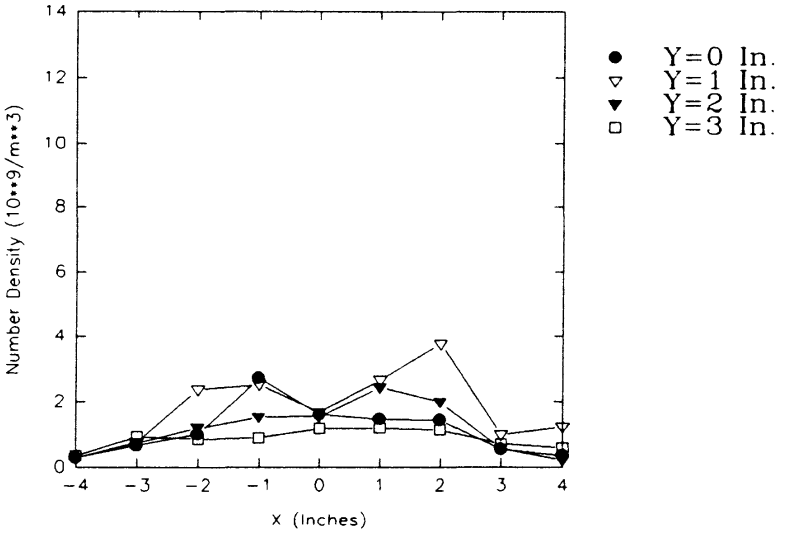

Figure 180. Two-Dimensional Plot of Number Density Distribution for Test H, at Different Grid Sections for a Plane 0.625 In. Above the Filter Face (Time=280 min.)

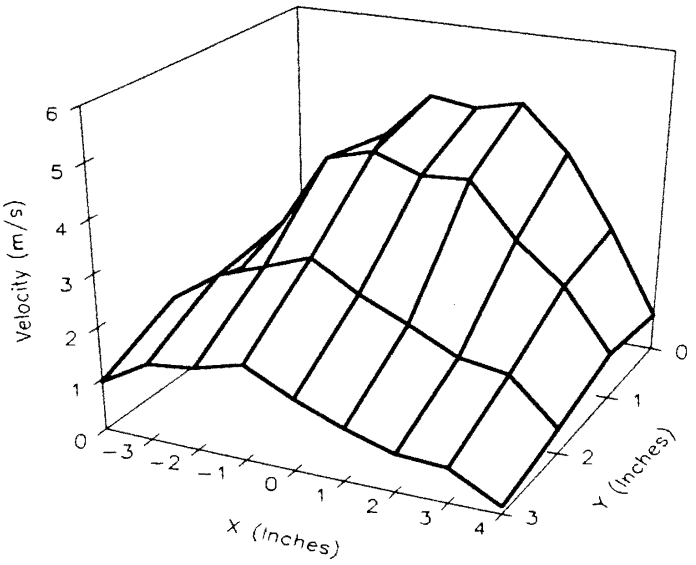

Figure 181. Three-Dimensional Plot of Velocity Profile for Test H, at a Plane 0.625 In. Above the Filter Face (Time=0 min.)

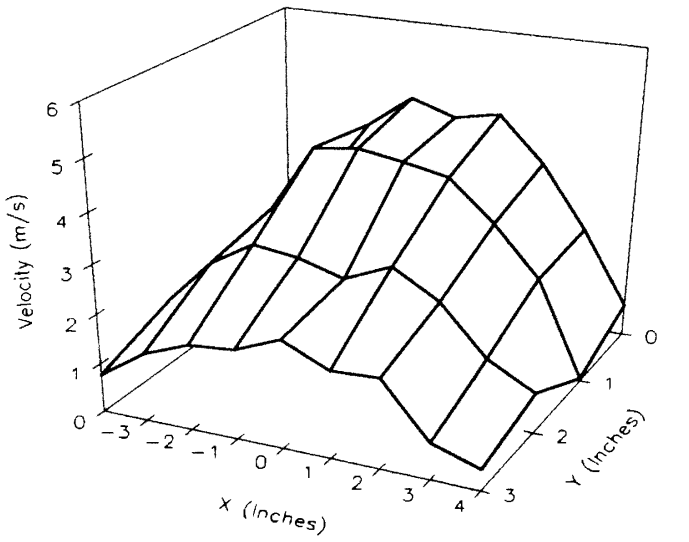

Figure 182. Three-Dimensional Plot of Velocity Profile for Test H, at a Plane 0.625 In. Above the Filter Face (Time=45 min.)

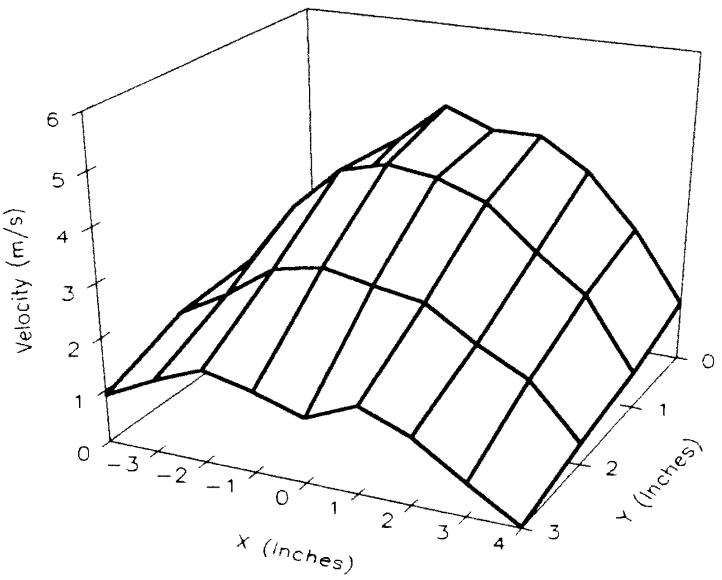

Figure 183. Three-Dimensional Plot of Velocity Profile for Test H, at a Plane 0.625 In. Above the Filter Face (Time=90 min.)

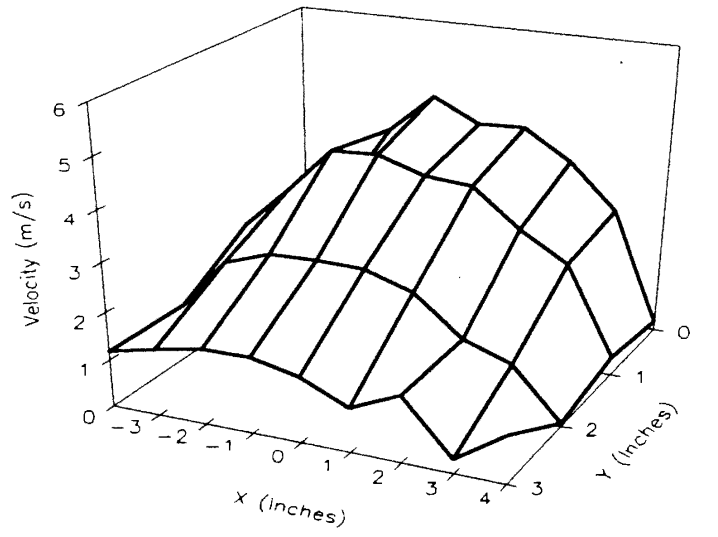

Figure 184. Three-Dimensional Plot of Velocity Profile for Test H, at a Plane 0.625 In. Above the Filter Face (Time=135 min.)

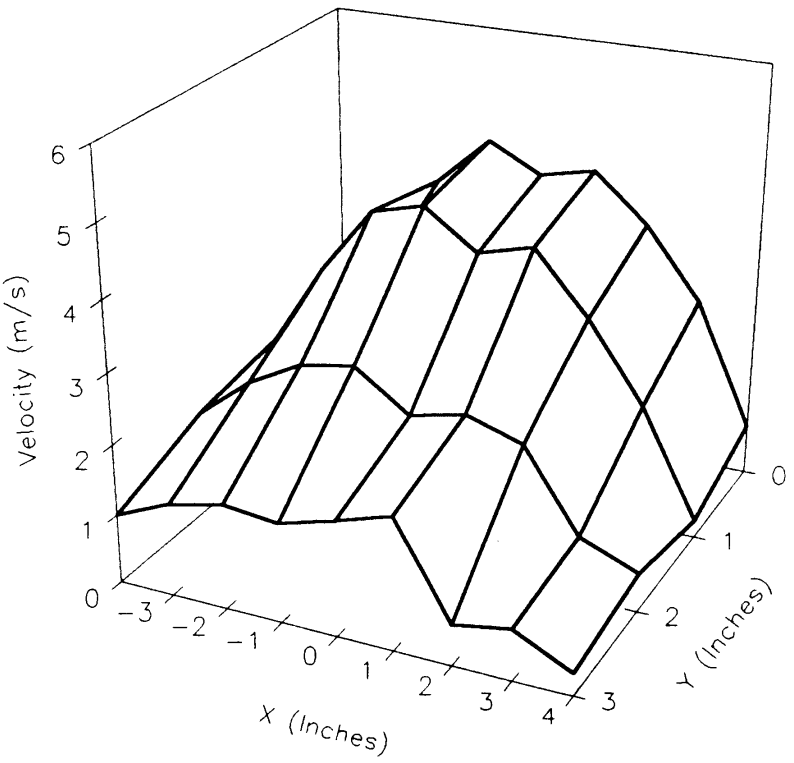

Figure 185. Three-Dimensional Plot of Velocity Profile for Test H, at a Plane 0.625 In. Above the Filter Face (Time=280 min.)

sets of data for test H. Figures 186 to 190 are the corresponding two-dimensional plots. As before, the velocity profiles does not show any significant variation with the passage of time.

Figures 191 to 195 are three-dimensional plots of particle number density distributions for the five sets of data for test L. Figures 196 to 200 are the corresponding two-dimensional plots. For this test, measurements were taken only for a quarter of the filter. The entire test lasted for about 350 minutes. No specific trend or pattern is observed. Figures 201 to 205 are three-dimensional plots of velocity profiles for the five sets of data for test L. Figures 206 to 210 are the corresponding two-dimensional plots. As for tests F and H, the velocity profiles for test L also do not show any significant variation with the passage of time.

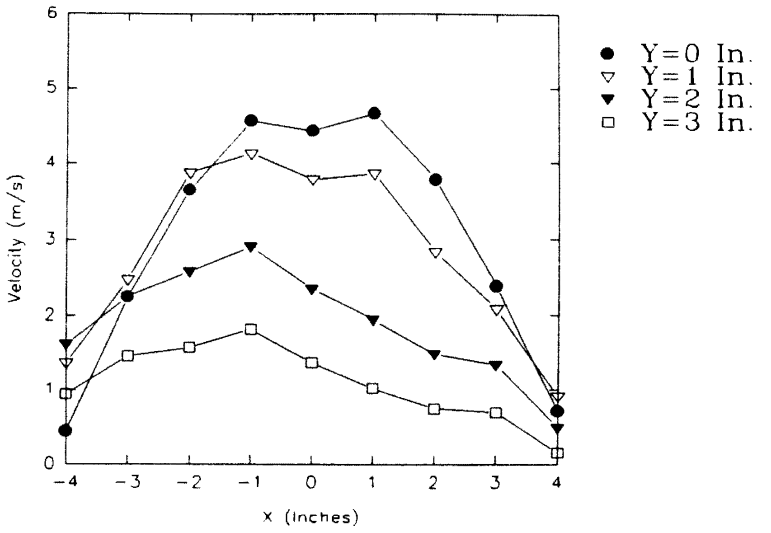

Figure 186. Two-Dimensional Plot of Velocity Profiles for Test H, at Different Grid Sections for a Plane 0.625 In. Above the Filter Face (Time=0 min.)

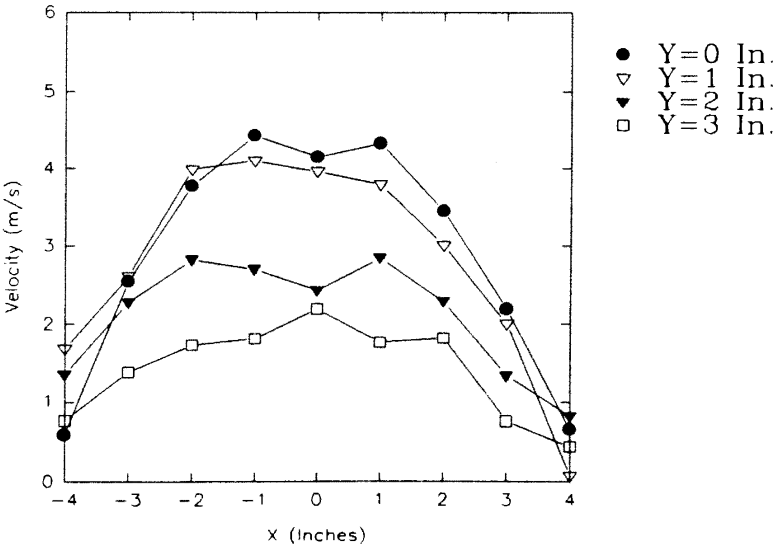

Figure 187. Two-Dimensional Plot of Velocity Profiles for Test H, at Different Grid Sections for a Plane 0.625 In. Above the Filter Face (Time=45 min.)

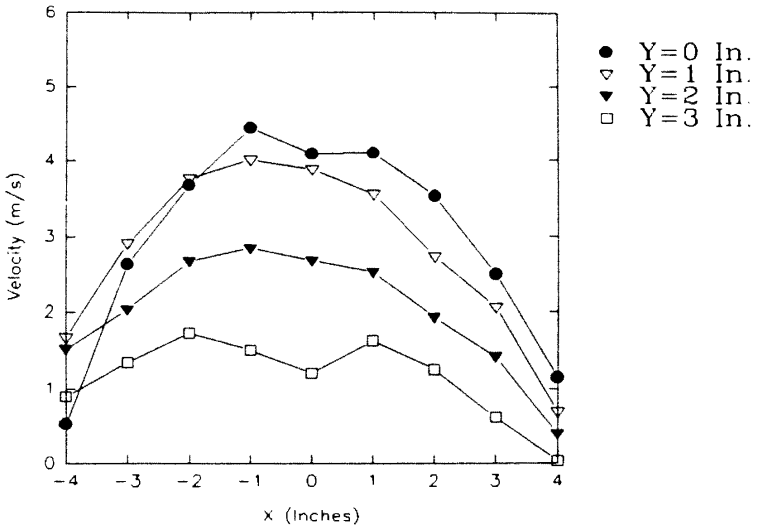

Figure 188. Two-Dimensional Plot of Velocity Profiles for Test H, at Different Grid Sections for a Plane 0.625 In. Above the Filter Face (Time=90 min.)

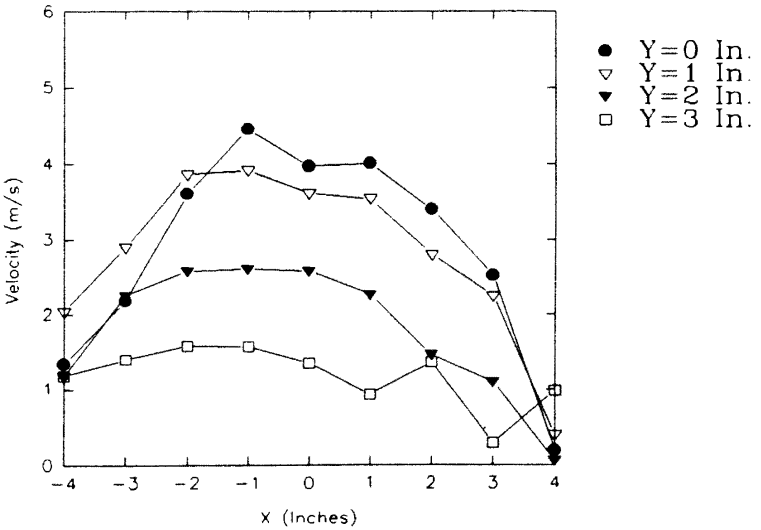

Figure 189. Two-Dimensional Plot of Velocity Profiles for Test H, at Different Grid Sections for a Plane 0.625 In. Above the Filter Face (Time=135 min.)

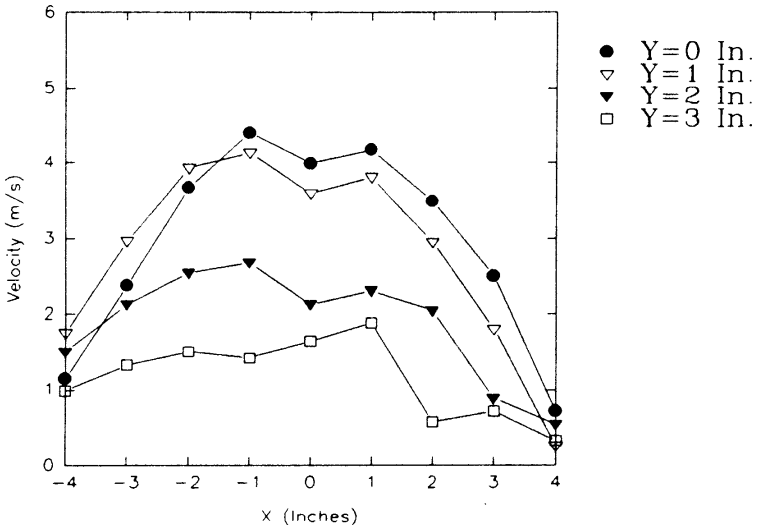

Figure 190. Two-Dimensional Plot of Velocity Profiles for Test H, at Different Grid Sections for a Plane 0.625 In. Above the Filter Face (Time=280 min.)

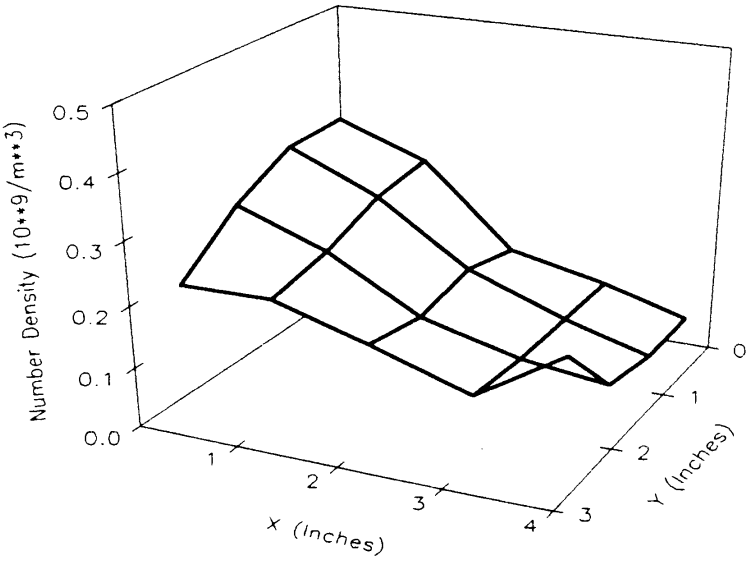

Figure 191. Three-Dimensional Plot of Number Density Distribution for Test L, at a Plane 0.625 In. Above the Filter Face (Time=0 min.)

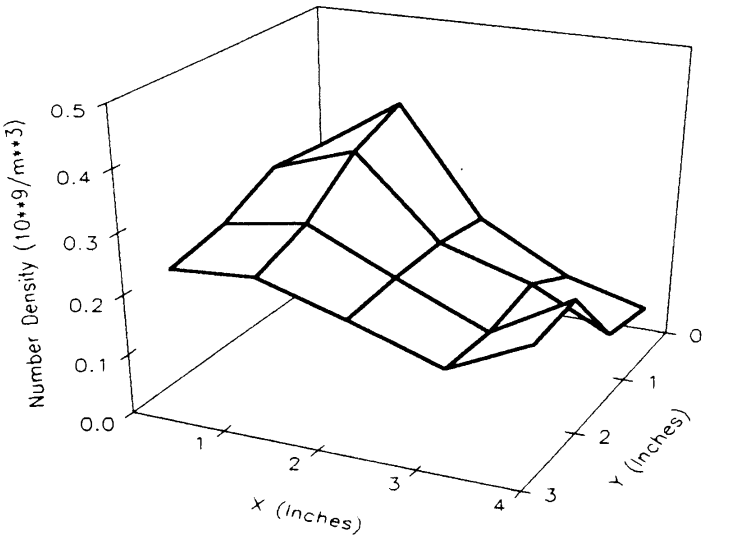

Figure 192. Three-Dimensional Plot of Number Density Distribution for Test L, at a Plane 0.625 In. Above the Filter Face (Time=50 min.)

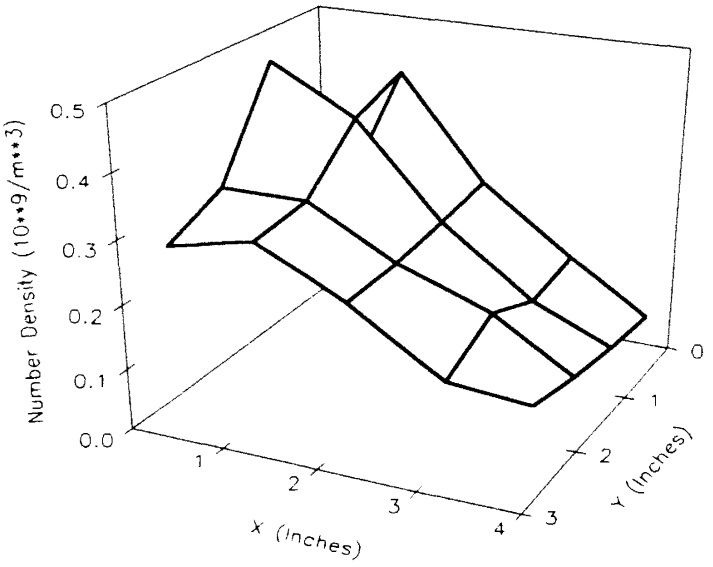

Figure 193. Three-Dimensional Plot of Number Density Distribution for Test L, at a Plane 0.625 In. Above the Filter Face (Time=100 min.)

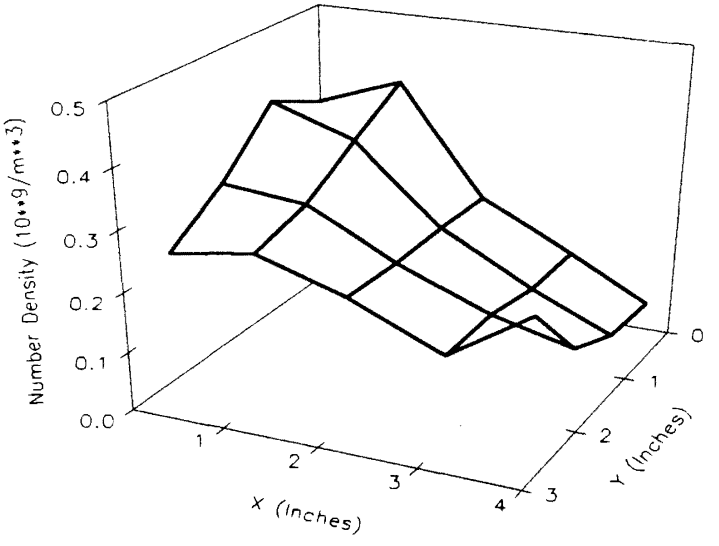

Figure 194. Three-Dimensional Plot of Number Density Distribution for Test L, at a Plane 0.625 In. Above the Filter Face (Time=150 min.)

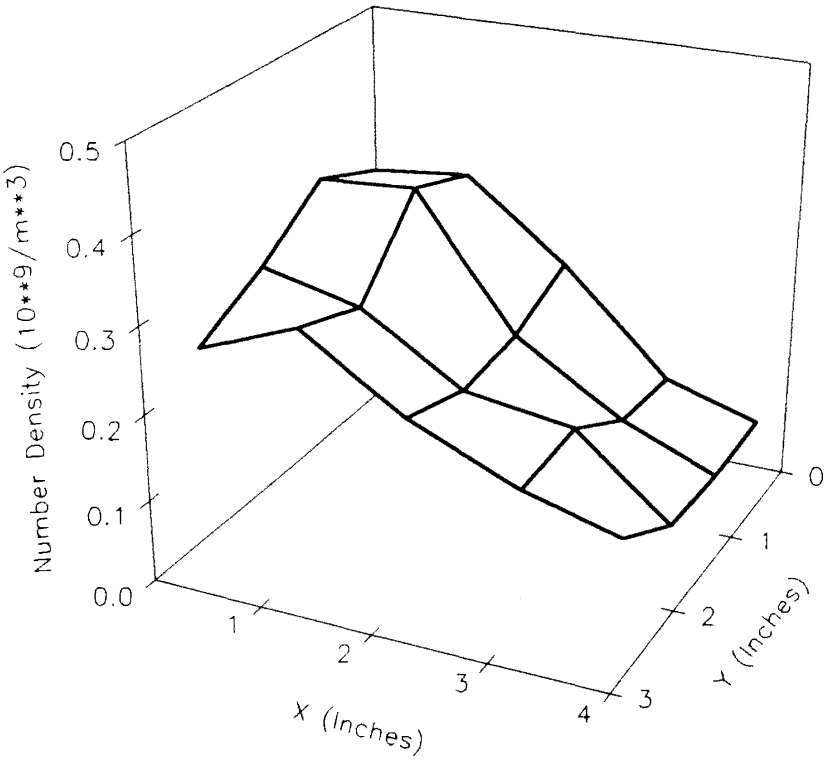

Figure 195. Three-Dimensional Plot of Number Density Distribution for Test L, at a Plane 0.625 In. Above the Filter Face (Time=300 min.)

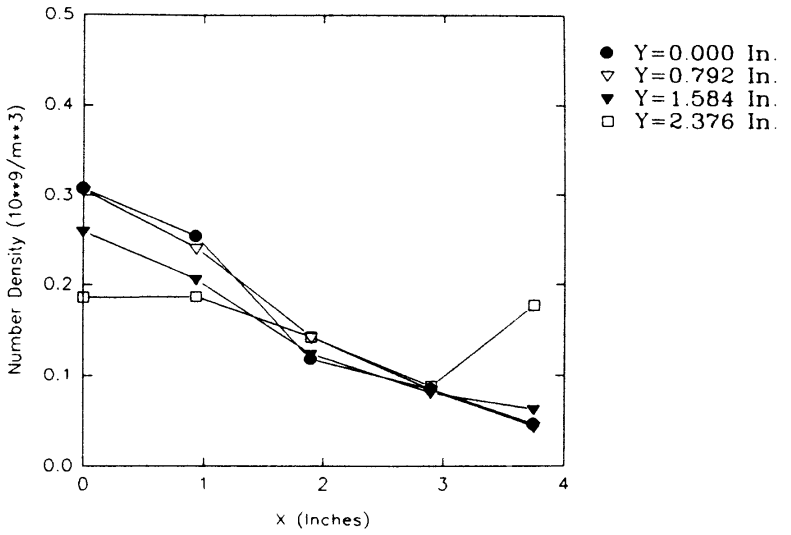

Figure 196. Two-Dimensional Plot of Number Density Distribution for Test L, at Different Grid Sections for a Plane 0.625 In. Above the Filter Face (Time=0 min.)

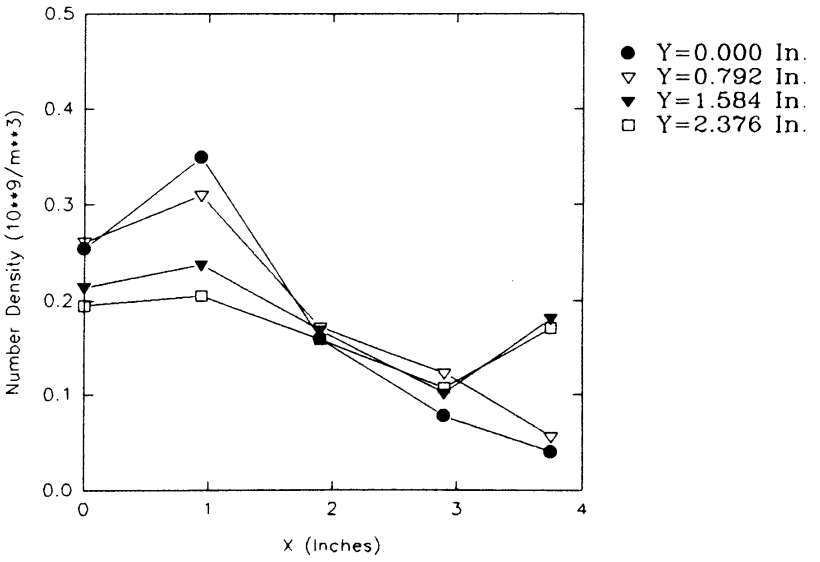

Figure 197. Two-Dimensional Plot of Number Density Distribution for Test L, at Different Grid Sections for a Plane 0.625 In. Above the Filter Face (Time=50 min.)

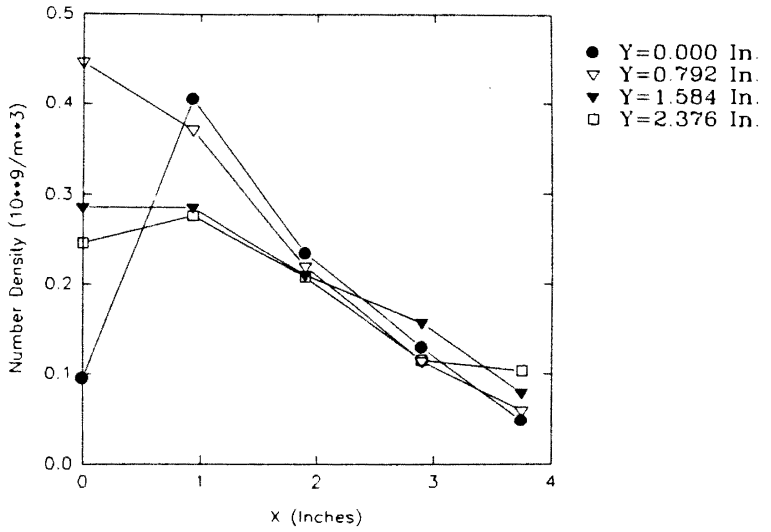

Figure 198. Two-Dimensional Plot of Number Density Distribution for Test L, at Different Grid Sections for a Plane 0.625 In. Above the Filter Face (Time=100 min.)

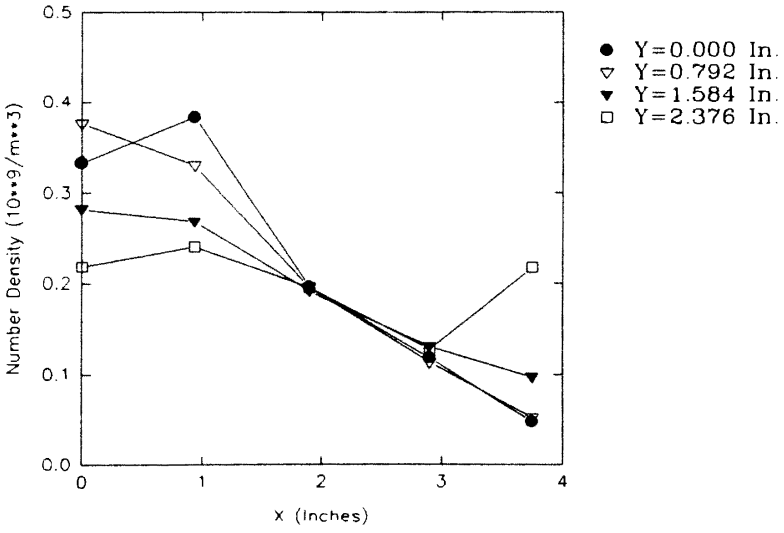

Figure 199. Two-Dimensional Plot of Number Density Distribution for Test L, at Different Grid Sections for a Plane 0.625 In. Above the Filter Face (Time=150 min.)

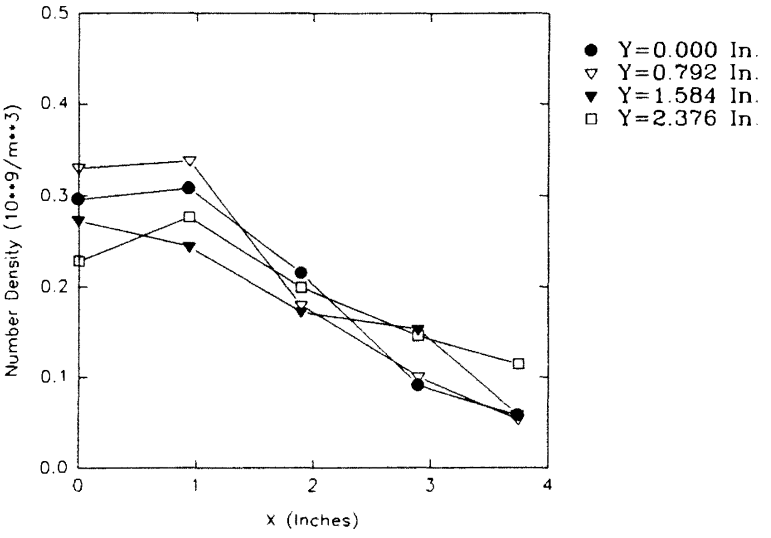

Figure 200. Two-Dimensional Plot of Number Density Distribution for Test L, at Different Grid Sections for a Plane 0.625 In. Above the Filter Face (Time=300 min.)

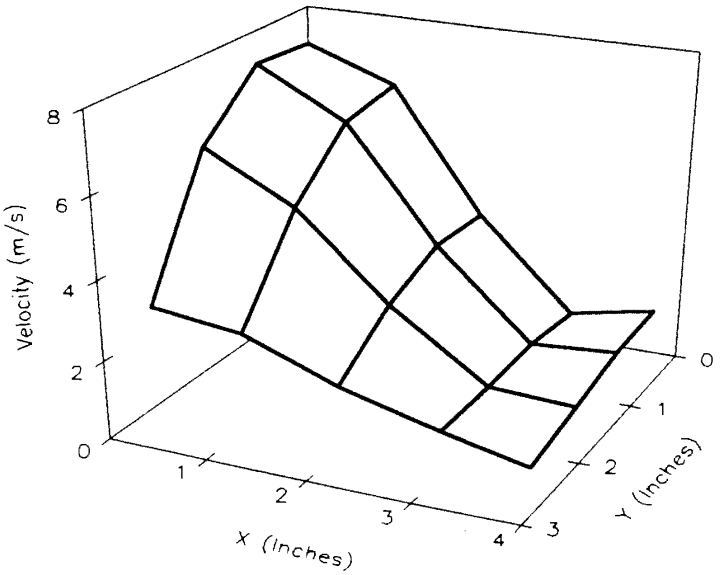

Figure 201. Three-Dimensional Plot of Velocity Profile for Test L, at a Plane 0.625 In. Above the Filter Face (Time=0 min.)

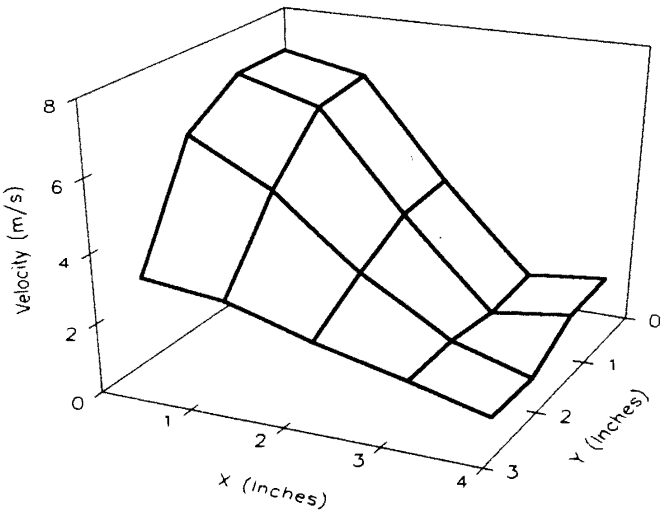

Figure 202. Three-Dimensional Plot of Velocity Profile for Test L, at a Plane 0.625 In. Above the Filter Face (Time=50 min.)

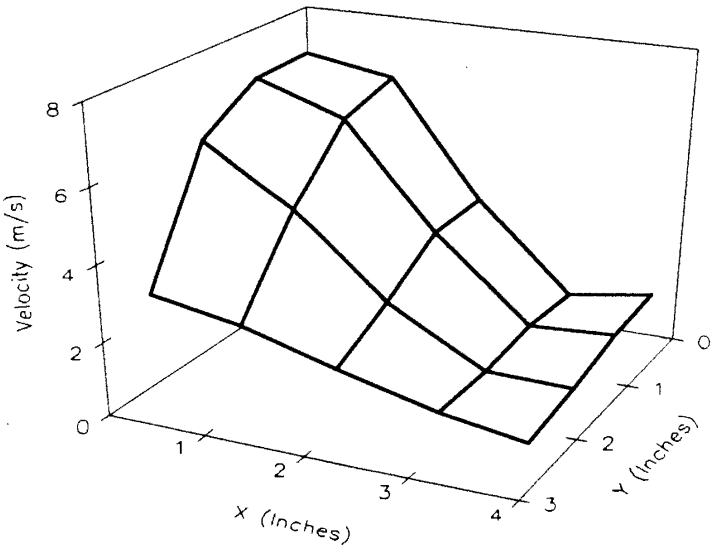

Figure 203. Three-Dimensional Plot of Velocity Profile for Test L, at a Plane 0.625 In. Above the Filter Face (Time=100 min.)

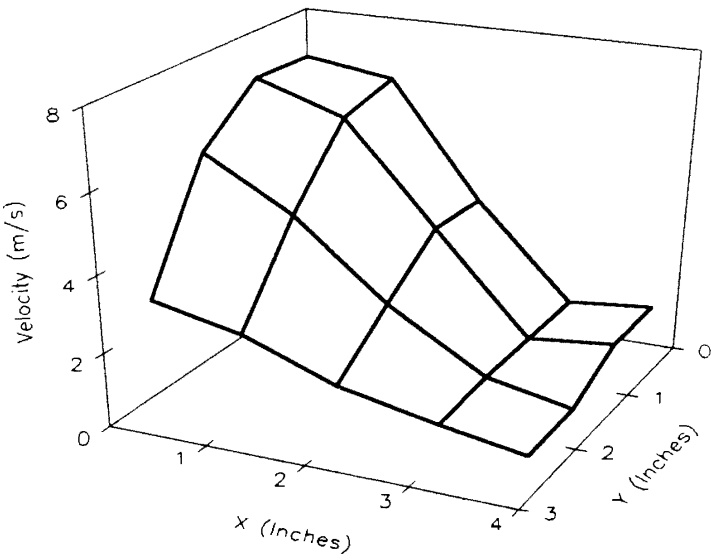

Figure 204. Three-Dimensional Plot of Velocity Profile for Test L, at a Plane 0.625 In. Above the Filter Face (Time=150 min.)

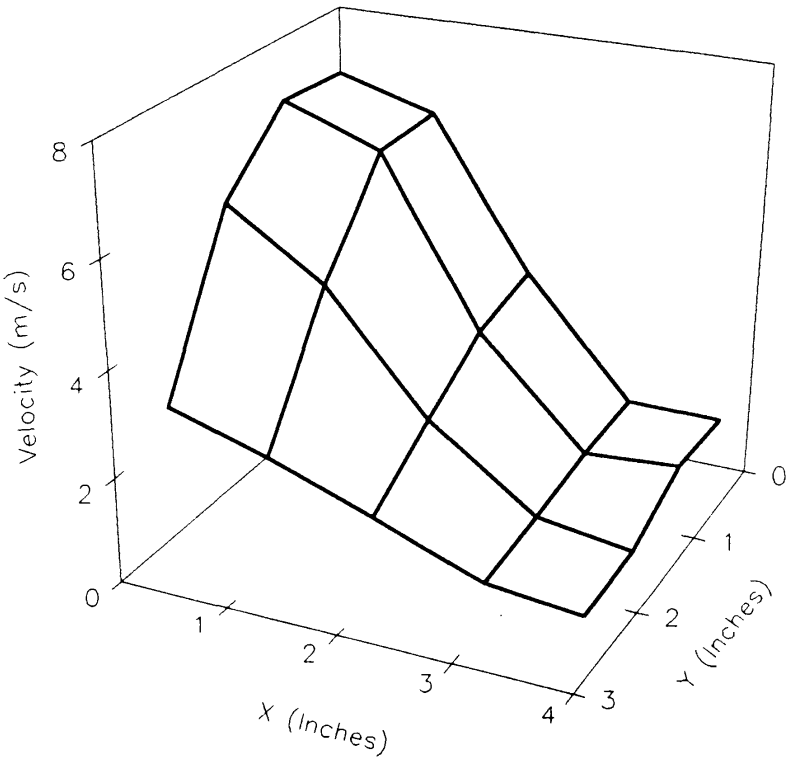

Figure 205. Three-Dimensional Plot of Velocity Profile for Test L, at a Plane 0.625 In. Above the Filter Face (Time=300 min.)

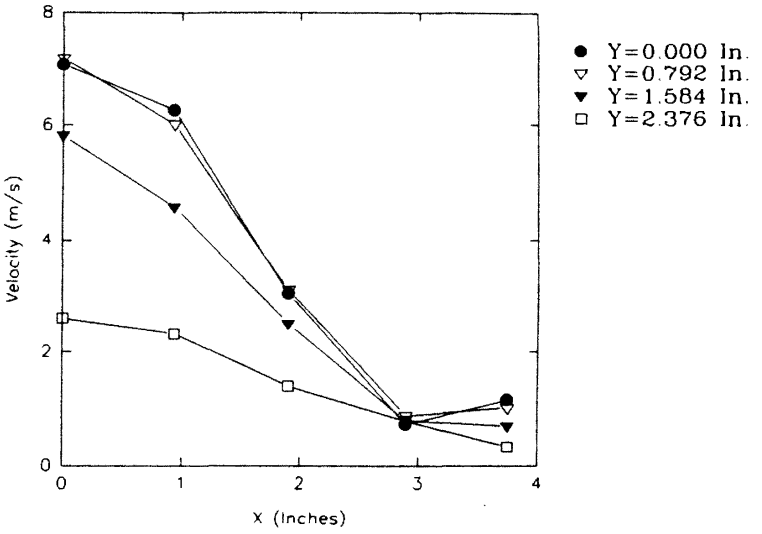

Figure 206. Two-Dimensional Plot of Velocity Profiles for Test L, at Different Grid Sections for a Plane 0.625 In. Above the Filter Face (Time=0 min.)

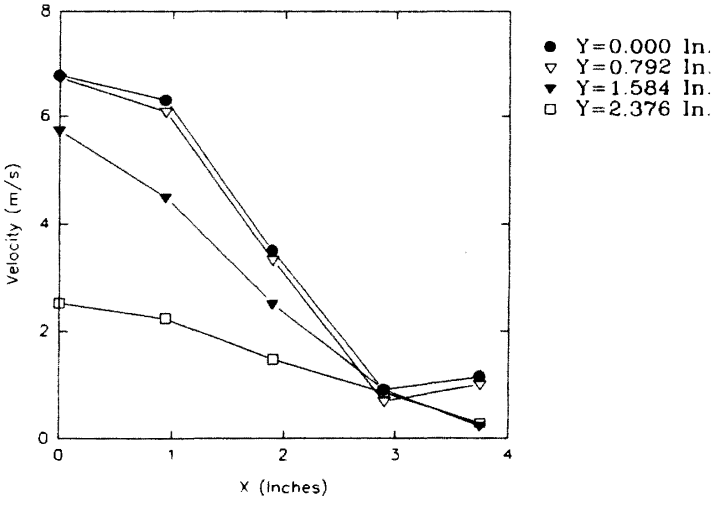

Figure 207. Two-Dimensional Plot of Velocity Profiles for Test L, at Different Grid Sections for a Plane 0.625 In. Above the Filter Face (Time=50 min.)

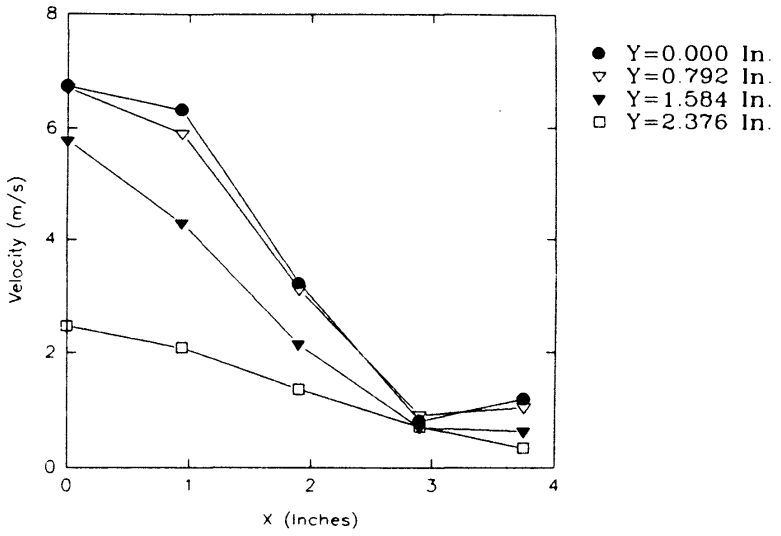

Figure 208. Two-Dimensional Plot of Velocity Profiles for Test L, at Different Grid Sections for a Plane 0.625 In. Above the Filter Face (Time=100 min.)

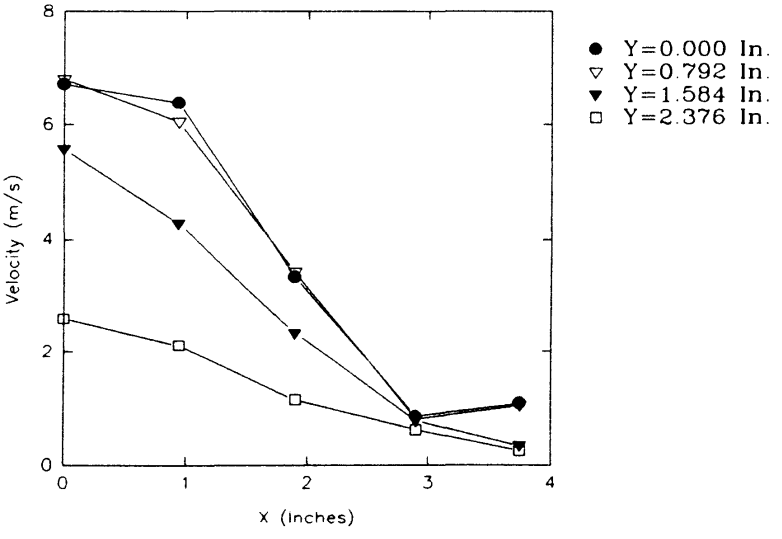

Figure 209. Two-Dimensional Plot of Velocity Profiles for Test L, at Different Grid Sections for a Plane 0.625 In. Above the Filter Face (Time=150 min.)

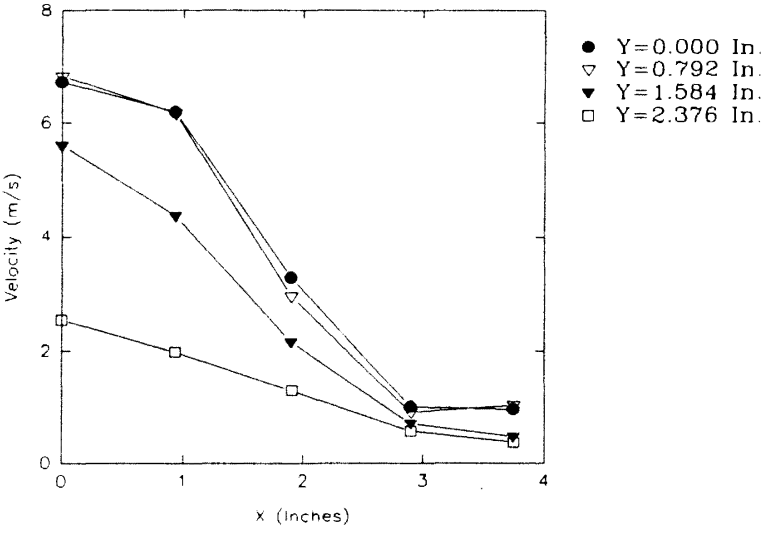

Figure 210. Two-Dimensional Plot of Velocity Profiles for Test L, at Different Grid Sections for a Plane 0.625 In. Above the Filter Face (Time=300 min.)

CHAPTER V

CONCLUSIONS AND RECOMMENDATIONS

It can be concluded that, in general, particle number density distribution seems to be similar to the velocity profile over the AF-3192 filter with a high number density around the center of the filter. The number density decreases toward the edges of the filter. The peak of the number density distribution is seldom at the exact geometrical center of the filter.

As discussed in Chapter IV, there were various uncertainties involved with the seeding of the flow. Water particles were generated by the humidifier at an unsteady rate. Also, there was no 'positive' connection between the humidifier outlet and the inlet (stabilizing) pipe of the housing. As a result, water particles were pulled into the housing in a nonuniform and random manner. Therefore, the differences in number density distributions (and number densities at a particular location) from filter to filter may have been due to the seeding problem (as discussed in Chapter IV, provided all other experimental conditions and parameters were the same). The same types of differences were also observed for velocities and velocity profiles, though velocity measurements were independent of the number of seeding particles (as long as seeding particle numbers did not go to very low values). Therefore, it can be concluded that the velocity profile may depend upon the specific filter under test.

It is recommended that a better method of providing seeding be used which is more steady and uniform. As an example, a 'six jet atomizer' (which is available in the lab; and can generate seeding particles from a wide variety of sources, such as water, polystyrene latex solution, oleic acid, etc. in the size range of 0.1 to 10 microns in

diameter) can be used to generate seeding water particles. In addition to uniformity and steadiness with regard to seeding, it also has a better control over the seeding particle concentration and over the total seeding particle output. Also a 'positive' connection should be established between the seeding source and the housing inlet pipe so as to ensure more complete (i.e., that all of the particles generated be pulled into the housing), uniform and constant seeding in the flow. Since air is pulled from the open end of the inlet pipe, it can not be directly connected to the seeding source or else the resistance against which the blower is working will increase until there is a leakage at some point in the system. Therefore, seeding should be 'injected' at some point in the inlet pipe and its length may need to be increased accordingly.

Number density distribution seems to maintain its shape as the flow progresses toward the filter face. Also the number densities show a steady increase as the flow approaches close to the filter. This, as discussed in Chapter IV, may have been due to the presence of water particles bouncing off of the filter face and staying close to the filter. However, as discussed in Chapter IV, a greater number of seeding particles getting into the housing due to the stabilizing pipe getting closer to the humidifier outlet as the test housing is raised, may have also been responsible for this. It is recommended that more tests be conducted keeping the relative positions of the humidifier outlet (or atomizer) and the housing inlet pipe the same. These tests should help determine the reason(s) behind the steady increase observed in the number densities as the flow approaches close to the filter. It is recommended that the humidifier (or atomizer) be mounted on a small platform which is clamped to the housing (inlet pipe) to ensure that the relative positions of the humidifier (or atomizer) outlet and the housing inlet pipe remain the same, even though the housing is raised or lowered. As recommended before, if the seeding is injected at some point in the inlet pipe, then this problem of varying relative positions of the humidifier and the inlet pipe is automatically eliminated.

The plane furthest from the filter face at which measurements were taken was 6.625 in. above the filter face. It is recommended that measurements be taken at other planes closer to the inlet (and further away from the filter face) to understand better the behavior of number density distribution and velocity profile as the flow progresses toward the filter face. Thus, by closely following the flow and its development (or change) with regard to the number density distribution and the velocity profile, from the point of its entrance into the housing to a plane close to the filter face, more confidence can be placed in a particular observed trend (as for example, number density seems to increase as the flow approaches close to the filter; or, at a particular location, an unusually high/low number density is observed due to some pleat disorder). Such measurements can also help determine the height above the filter face up to which the filter affects the number density distribution and the velocity profile.

It can be concluded that the velocity profile over the filter does not change much with the passage of time, while the number density distribution of water droplets may decrease uniformly and steadily, or may not change significantly with the passage of time. Since time history measurements are more involved and time consuming, only three of such tests were performed. More tests should be conducted so as to observe any repetitive trend and to investigate the complex and not yet adequately understood time history effects. As will be discussed later in this chapter, particles other than water should be used to study time history effects.

As discussed in Chapter II, the swept volume counting technique has a limitation on the size of particles that can be successfully counted using the current laser Doppler velocimeter. This limitation is due to the requirement that the particles should be sufficiently smaller than the probe volume, so that they are well within the probe volume and consequently generate good signals (unlike the particles which are at the boundaries of the probe volume i.e., are only partially within the probe volume, and fail to generate good signals). Further research is required to know the exact largest allowable particle

size (and still obtain accurate measurements). This allowable particle size can be experimentally determined by using 'standard sized' particles like those of polystyrene latex in conjunction with (say) a six jet atomizer. Measurements with regard to the number density can be taken with a 'size-series' of these particles, keeping the (arbitrary) concentration the same. As measurements are taken with monodisperse (single sized) particles in the ascending order of their sizes, the LDV will give erroneous measurements at some size and the allowable particle size can thus be determined. It is worth stressing that erroneous measurements will result with most of the particles being larger than the allowable particle size. However, if such large sized particles are only a small percentage of all the particles in the flow (in reality, the flow will have a size-range of particles, as for example seeding by dust may have particles from 1 to 200 microns in diameter), the measurements may not be affected much.

Due care should be taken so that the particles like those of polystyrene latex are not 'free' in the room atmosphere at any stage of the experiment (from their generation to their disposal). This is extremely important because such particles if inhaled, are deleterious to health. Therefore, the concept of 'complete' seeding becomes very critical while using such particles. Also, proper method(s) should be employed to trap such particles; if there are any left after the passage of the flow through the filter, before the flow is exhausted to the room atmosphere. A 'settling chamber' with extra filters exclusively meant to trap such particles may be incorporated in the current exhaust line.

Since the swept volume method does not allow the simultaneous presence of more than one particle in the probe volume, it has a limitation with regard to the highest particle concentration which it can successfully measure. Using the assumption that there is not more than a single particle in the probe volume at a given instant, this highest particle concentration is reciprocal of the probe volume. Using the dimensions of the probe volume as given in Chapter III, this highest particle concentration which can be successfully measured is calculated to be 0.593×10^{12} particles/m^3. All of the number

densities measured in this work were far less (of the order of 10^9) than this highest allowable particle concentration. This highest allowable particle concentration can be experimentally evaluated by injecting higher concentrations (say, by using two humidifiers together) in the flow and subsequently taking measurements. It is worth mentioning that, this number is not a 'fixed' number because the probe volume itself does not have specific and well determined boundaries (and dimensions). This is because the probe volume is the region of crossing of all the four laser beams (as explained in Chapter III) which do not have well determined precise boundaries (the beam intensities follow the Gaussian distribution). Further, with regard to the strength of the signal generated by particles of different sizes (as for example, a small particle contained well within the probe volume may not generate a good signal as opposed to a large sized particle outside the probe volume), there is a variation in the probe volume size.

Behavior of a filter may be different for different seeding particles. Also, solid particles may behave differently than the water particles in the flow with regard to their tendency to follow the flow and the manner in which they scatter light. The relationship (which is critical in the flow) between the actual and the aerodynamic size/shape may also be different for solid particles as opposed to water particles. Water particles may split into smaller particles. As discussed in Chapter IV, water particles do not seem to evaporate within the housing, but the use of solid particles totally eliminates this possibility. Also, the coalescing properties to produce larger sized particles should be different for water and solid particles. It is recommended to use particles other than those of water as seeding particles. This is especially important for time history measurements. The possibility of the filter getting dry (after it had already been wet) at some places with the passage of time is eliminated by using solid particles. 'Standard sized' particles like those of polystyrene latex may be used. That, as discussed above, may give relatively more realistic measurements (keeping dust particles in mind) as opposed to the water seeding particles.

As discussed in Chapter IV, the number of particle counts obtained by the system increased with an increase in the laser power till the saturation was obtained. That was because, at higher laser power, the system detected even the smaller particles. The saturation was an indication of all of the particles getting detected. By using 'monodisperse standard sized' particles (and gradually increasing the laser power, starting from the minimum), the saturation level, and hence the minimum allowable laser operating level (that should be used), can be determined for that specific size of the particles. Also, as discussed in Chapter IV, the number of particle counts obtained by the system decreased with an increase in the threshold setting for the system. That was because, at higher thresholds, only bursts due to large particles were analyzed. The use of 'monodisperse standard sized' particles (and gradually decreasing the threshold, starting from the maximum) should help determine the maximum allowable threshold setting (that should be used) for that specific size of the particles.

As discussed in Chapter IV, the velocity measurements were far more consistent than the number density measurements over a wide range of governing software parameters and variables. Further research is required to fully understand the effects of certain software parameter settings, such as the envelope filter setting and toggling of channel 1 or 2 off, on the number of counts obtained by the laser Doppler velocimeter. Also, further work should be done to confirm and firmly establish that the number of 'attempts' made by the system is actually the number of particles which the system detects. Experiments using a uniform and steady concentration of (say) polystyrene latex particles in a slug flow (where number density profile is fairly flat throughout the cross-section of the flow) may help to understand this.

As discussed in Chapter IV, laser power is an important parameter. It is recommended to ensure that, once adjusted, the laser beams do not change with regard to their individual intensities. Better alignment of the fiber couplers using better couplings/screws and the subsequent maintenance of that alignment should be helpful.

The laser and the fiber drive table should be supported on a more robust stand because the optical adjustments are susceptible even to the slightest vibration/movement of the supporting structure (which currently is a study table).

Automotive filters, in reality, are actually exposed to dust and other solid particles as opposed to water particles. The present work, which involved measurements using water particles, is nevertheless extremely critical and important. As mentioned before, it is one of its kind where time and location dependent effects on particle number density for a filter were researched. The measurements involved in this work are believed to be fairly representative (at least while the filter is not wet), with regard to the velocity and number density profiles (shapes), of the case where dust is the seeding material. However, the absolute (exact) number densities for dust measured by the LDV system may vary considerably from the measurements involved in this work (even if the same concentration of dust is injected). This, as mentioned before, may be due to the difference in the way light is scattered by the dust particles. The geometry of dust particles (sharp edges and corners) is significantly different than that of water particles (fairly spherical), and hence the light scattered by dust particles may be highly unpredictable with regard to the scattered direction. This will definitely influence the signal, and consequently the counts. As discussed before, even though other differences may exist between dust (solid) and water particle seeding, the trends of the velocity and number density profiles are believed to be the same as long as solid particles of a similar size range (most of the particles from 10 to 30 microns in diameter) and with the same injection densities (of the order of 10^{10}) as that of water particles are used. The comparison, as mentioned before, should be made while the filter is not wet.

However, before actually taking measurements using dust, a two stage test using 'standard sized' particles is strongly recommended. In the first stage, by using small sized particles (say, 1 micron in diameter) which are sure to follow the flow, measurements should be taken for the entire filter face with regard to the number density and velocity

profiles (and the similarity between the two with regard to the shape should be checked). In the second stage, similar measurements but with larger sized particles should be taken, and whether the particles still follow the flow should be checked. If they do not follow the flow, their distribution over the filter should be checked. This test should help determine the size range of particles which follow the flow. Also, for larger sized particles which do not follow the flow, this test should determine the difference(s) and the similarities (if any) in the behaviors of the particles and the flow. This two staged test will definitely result in a more smooth and comfortable transition from water particles to dust, and will facilitate understanding and analysis of the results obtained using dust (which might be more complex due to reasons explained before).

REFERENCES

Advantech Co., Ltd. (1990), PCL-818 High Performance Data Acquisition Card with Programmable Gain, User's Manual, Advantech Co., Ltd.

Aerometrics, Inc. (1991), Aerometrics Doppler Signal Analyzer for Phase Doppler Particle Sizing Applications, User's Manual, Aerometrics, Inc., Sunnyvale, CA.

Ahlers, K. D., and Alexander, D. R. (1985), "Microcomputer Based Digital Image Processing System Developed to Count and Size Laser-Generated Small Particle Images," Optical Engineering, Vol. 24(6), pp. 1060-1065.

Farmer, W. M. (1972), "Measurement of Particle Size, Number Density, and Velocity Using a Laser Interferometer," Applied Optics, Vol. 11(11), pp. 2603-2612.

Hack, R. L., Samuelsen, G. S., Poon, C. C., and Bachalo, W. D. (1981), "An Exploratory Study of Soot Sample Integrity and Probe Perturbation in a Swirl Stabilized Combustor,"ASME Journal of Engineering for Power, Vol 103(10), pp. 759-771.

Holve, D., Tichenor, D., Wang, J. C. F., and Hardesty, D. (1981), "Design Criteria and Recent Developments of Optical Single Particle Counters for Fossil Fuel Systems," Optical Engineering, Vol. 20, pp. 529-539.

Holve, D. J. (1982), "Transit Timing Velocimetry (TTV) for Two-Phase Reacting Flows," Combustion and Flame, Vol. 48(1), pp. 105-108.

Holve. J., and Annen, K. D. (1984), "Optical Particle Counting, Sizing, and Velocimetry Using Intensity Deconvolution," Optical Engineering, Vol. 23, pp. 591-603.

Liang, F., Haldhani, M., and Dougherty, R. (1993), "Particle Counting and Sizing by LDV for Automotive Air Filters: Part I. Particle Counting and Sizing Techniques," AIAA/ASME Oklahoma Symposium XIII, Session 5, Norman, OK, (Feb. 22, 1993).

Liu, B. Y. H., Szymanski, W. W., and Ahn, K. (1985), "On Aerosol Size Distribution Measurement by Laser and White Light Optical Particle Counters," The Journal of Environmental Sciences, Vol. 28, pp. 19-24.

Rudd, M. J. (1969), "A New Theoretical Model for Laser Dopplermeter," Journal of Physics E2, Vol. 2, pp. 55-58.

SAE J726 JUN87. (1987), Air Cleaner Test Code, SAE, Warrendale, PA.

Spears, K. G., and Robinson, T. J. (1988), "Particle Number Densities by Light-Scattering Fluctuation Analysis," The Journal of Physical Chemistry, Vol. 92(18), pp. 5302-5305.

Tedjojuwono, K., Asakura, T., and Kawase, Y. (1984), "Measurement of Particle Density Using the Variable-Fringe-Spacing Laser Doppler Velocimeter," Applied Optics, Vol. 23(15), pp. 2554-2558.

Wood, C. P., and Samuelsen, G. S. (1985), "Optical Measurements of Soot Size and Number Density in a Spray-Atomized, Swirl-Stabilized Combustor," Transactions of the ASME, Journal of Engineering for Gas Turbines and Power, Vol. 107, pp. 38-47.

Wu, J. W., Cooper, D. W., and Miller, R. J. (1989), "Improved Sequencing System for Sampling Clean Gases to Obtain Particle Size Distributions with a Diffusion Battery and a Condensation Nucleus Counter," Review of Scientific Instruments, Vol. 60, pp. 258-260.

APPENDIXES

APPENDIX A

EQUIPMENT LIST

1. A 4 Watt Argon ion laser: Coherent, Innova 70-A, P/S 92K-1758.
2. Remote control for the laser: Coherent, I-70, 92411171
3. Fiber drive: Aerometrics, Inc., FBD1240, 026
4. Bragg cell: IntraAction, Inc., ME-40H, 3247
5. Photomultiplier tubes: Aerometrics, Inc., RCM2200L, 029
6. Doppler signal analyzer: Aerometrics, Inc., DSA3220, 044
7. Oscilloscope: Hewlett Packard, 54501A
8. Computer and monitor: Gateway 2000, IBM compatible 80486
9. Computer for traverse system: Ager, Portable computer, LCD-386
10. Laser transceiver: Aerometrics, Inc., XRV1212, 001
11. Automated traverse system-

    Stepper motors: (Refer to Appendix B)

    Chopper modular drives: (Refer to Appendix B)

    Power supply: (Refer to Appendix B)

    Data acquisition board: (Refer to Appendix B)

    Daughter (or screw terminal) board: (Refer to Appendix B)
12. Plexiglas test housing: Full sized model of the SAE Panel Filter Universal Test Housing [SAE, 1987]
13. Test filter: Purolator, Inc., AF 3192
14. Ultrasonic humidifier: Pollenex, SH55R
15. Blower motor: Dayton Electric Mfg. Co., 5K242G

16. TSI mass flow sensor: TSI, 2018, 30644

APPENDIX B

TRAVERSE AUTOMATION

As mentioned in Chapter III, initially the traverse table on which the transceiver is mounted was manually controlled. As shown in Fig. 211, the traverse table consists of two rectangular frames one mounted on the other. The top frame has an aluminum table top with holes drilled in it. The transceiver is securely mounted on the table top using screw fasteners through the holes in the table top. Each frame is attached to a driving lead screw. These two driving lead screws are perpendicular to each other and are responsible for moving their respective frames. Thus, by moving each frame along one independent axis, the transceiver can be moved either parallel to or perpendicular to the length of the filter as shown in Fig. 212. Initially, the lead screws were operated using small handles attached to their ends. The counter on each lead screw allowed one to keep track of the exact position of the transceiver and hence the position of the probe volume. The manual control of the traverse had one drawback. It considerably impaired the speed and hence the efficiency of data collection. Especially when the filter was to be mapped with a fine grid, it would take a very long time to manually set the traverse at each specific location. In a number of instances, for example, the laser Doppler velocimeter system would take 10 or 15 seconds to collect data, and manually changing the coordinates of the traverse to the next location would take as long as 2 to 3 minutes. As described in Chapter IV, filter performance depends upon time; and for mapping number density for very wet filters, it is essential to take measurements speedily, during a short interval of time, to avoid biasing the data due to time dependence of filter performance. Also there was a high probability of human error involved in manipulating the traverse, as the job was monotonous and

strenuous. To overcome the above mentioned difficulties, I was assigned to automate the traverse. The automated traverse enabled the user to change traverse coordinates in about 30 to 60 seconds, as opposed to the manually controlled traverse which used to take about 2 to 3 minutes.

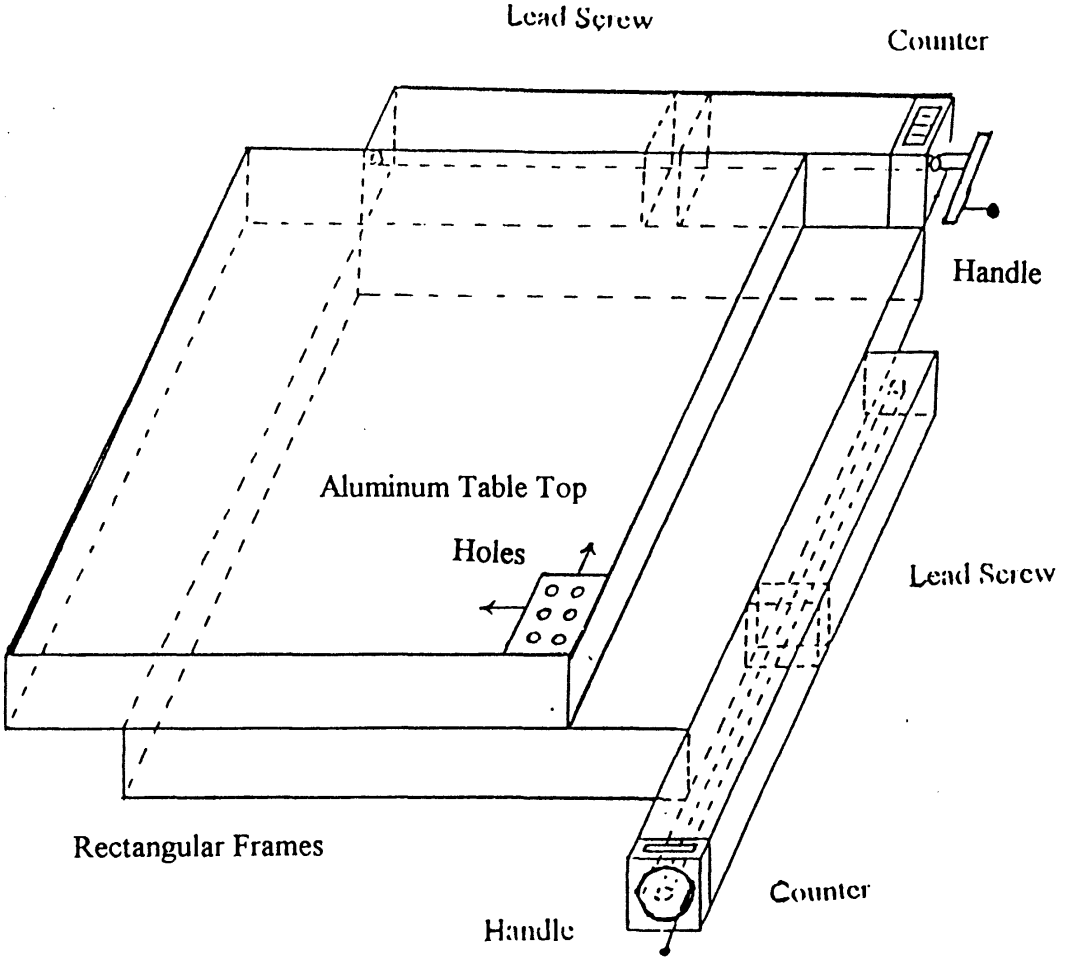

Figure 211. Three-Dimensional View of Traverse Table Before Automation

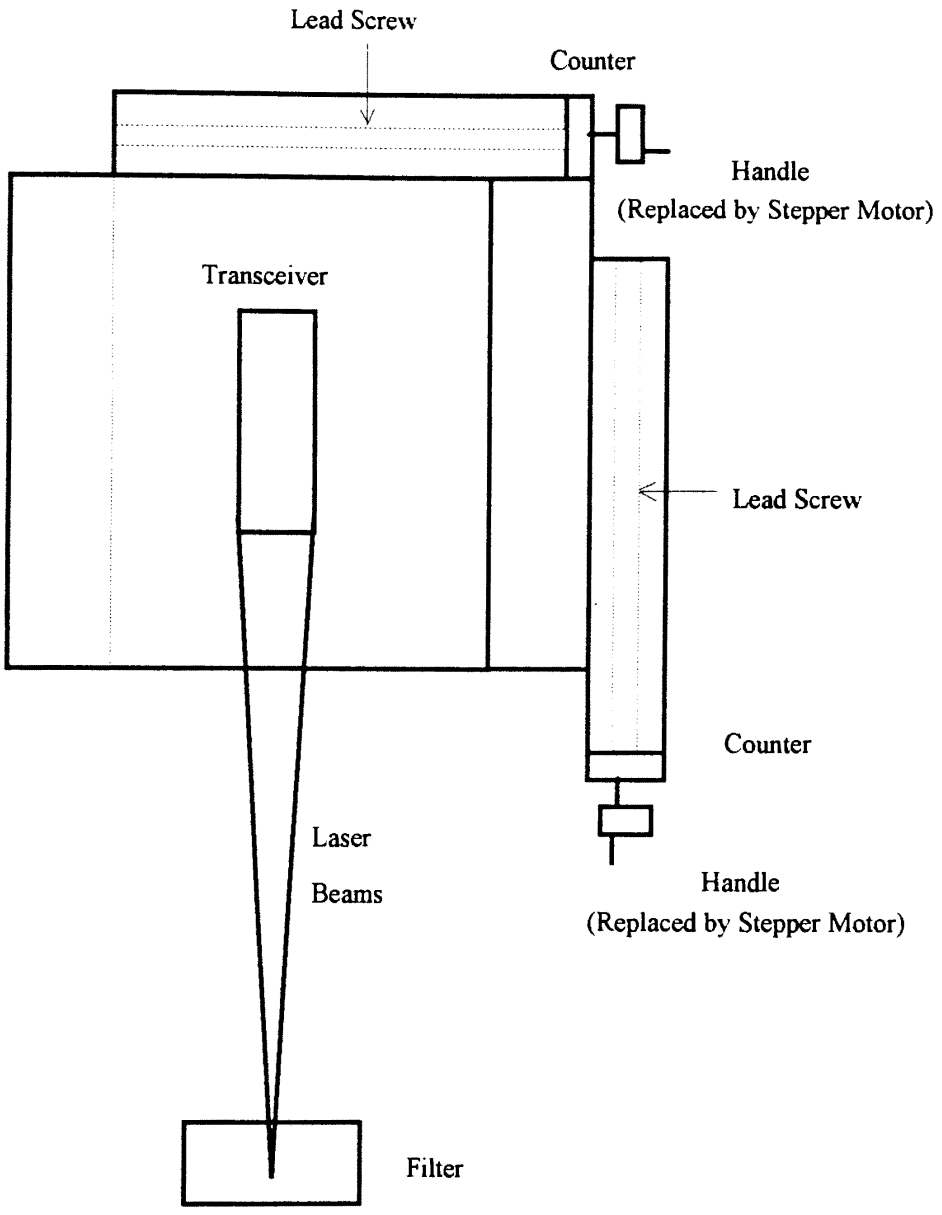

Figure 212. Top View of Traverse Table

Stepper motors were used to provide the required torque to turn lead screws and hence to move the frames. A stepper motor is a special kind of motor. Unlike other motors which provide continuous torque and hence the rotation, a stepper motor provides

torque in discrete steps or pulses. The least single discrete step or angular rotation which a motor can provide is known as least angular count of the motor. Also each motor, typically, is capable of providing a maximum of static and dynamic torque, and it should not be used for applications beyond its torque handling limits.

A piece of thread was wound on the lead screw's handle, and weights were hung on the end of the thread in steps. Thus, a rough estimate of the static torque required to operate the lead screws was made. Then, using a factor of safety of around 3, it was decided that a motor capable of providing around 100 oz.-in. of static torque would serve the purpose efficiently. For mapping the filter precisely, a very fine grid of the order of 0.005 in. was desired. The pitch of the lead screw was measured to be 0.1 in. A stepper motor with 1.8 degrees per step (with an accuracy of ± 5%) specification was selected that would provide, at least theoretically, a precision of 0.00025 in. using the half step mode as calculated below:

motor specification = 1.8 degrees/step

1 rotation = 360 degrees = 360/1.8 = 200 steps

1 rotation = 400 half steps

lead screw pitch = 0.1 in. per rotation

precision obtained (theoretically) = 0.1/400 in. = 0.00025 in. per half step

Half step operation reduces settling time and overshoot on the final step. It also reduces shock and acoustic noise on the system connected to the motor shaft. Hence, the operation is smoother. Thus, considering the torque and the accuracy requirements, two motors were selected, one for each lead screw. The following are the motor specifications:

Make:	Sanyo Denki
Voltage Rating:	3 Volts
Current Rating:	1.7 Amperes
Holding Torque:	110 oz.- in.

Pull out Torque: 75 oz.- in.

Body Dimensions: 3.25 in. diameter, 2.5 in. length with 3.25 square flange mount with 4 holes on 2.74 in. centers. Dual shaft. 0.375 in. diameter, 0.75 in. long at front and 0.687 long at rear.

The motor winding was two phase type and capable of bipolar operation, characterized by the need for current to flow in both directions in each coil of the motor. Bipolar motors require a dual polarity (+ and -) power supply as opposed to unipolar motors. Bipolar motors produce more torque at low speeds as compared to unipolar motors. This particular feature makes these motors ideal for the applications as stated above. Each motor selected had 8 leads wound in bifilar fashion, as shown in Fig. 213.

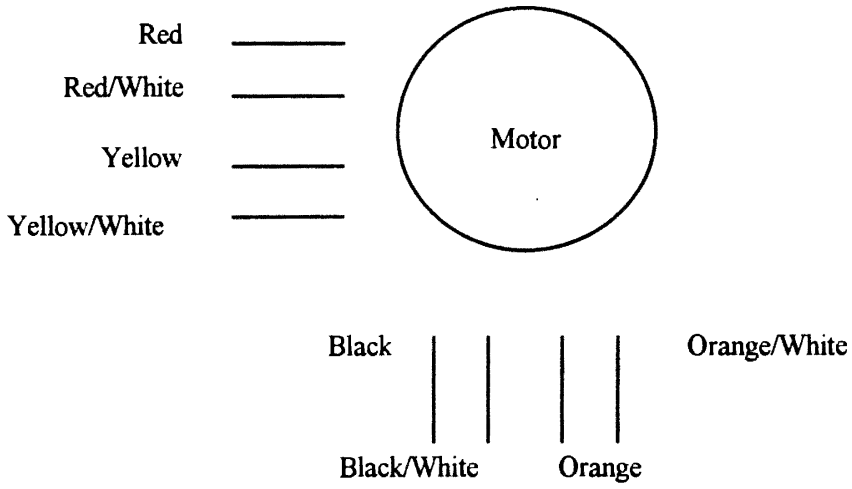

Figure 213. Eight Lead Bifilar Motor

The motors were mounted on the traverse using aluminum plates and blocks as shown in Fig. 214. That involved rigorous and careful design of the mounting parts with the constraint that minimum modification was to be done to the already existing traverse. Also the motor dimensions and its weight were to be carefully considered. The original handles over the lead screws were replaced by ingeniously designed 'adapters'. These are shown in Fig. 215. The adapter allows the lead screw to be connected to the stepper motor via itself, a hollow aluminum shaft, and 'Lovejoy couplings' as shown in Fig. 214. Hollow aluminum shafts were used to keep the stepper motors clear from the movement of the table tops. All of the components needed for mounting the motors were manufactured in the Mechanical and Aerospace Engineering North Laboratory workshop.

Figure 216 shows a block diagram of the traverse automation. A stepper motor requires a stepper motor drive in order to be driven, which in turn is controlled by a computer through a data acquisition card. A compatible power supply source is also needed for the stepper motor driver. Motor current increases when the motor is running at low speeds or when it is stopped, and this should be limited to its rated value. This can be accomplished by using the drives which vary the supply voltage with motor speed or by using chopper drives. The chopper drives apply a high voltage at the beginning of each step but prevent the current from exceeding its rated value by sensing and chopping it at a predetermined frequency. Two chopper modular drives (CMDs) were used to drive the two stepper motors independently of each other. These drives were selected after careful analysis of their compatibility with the already selected stepper motors. The following are the specifications of the chopper modular drives selected:

Make:	APIMCG, CMD-40
Type:	2 phase, bipolar, constant current
Chopping frequency:	Greater than 20 kHz.
Stepping modes:	Half / Full

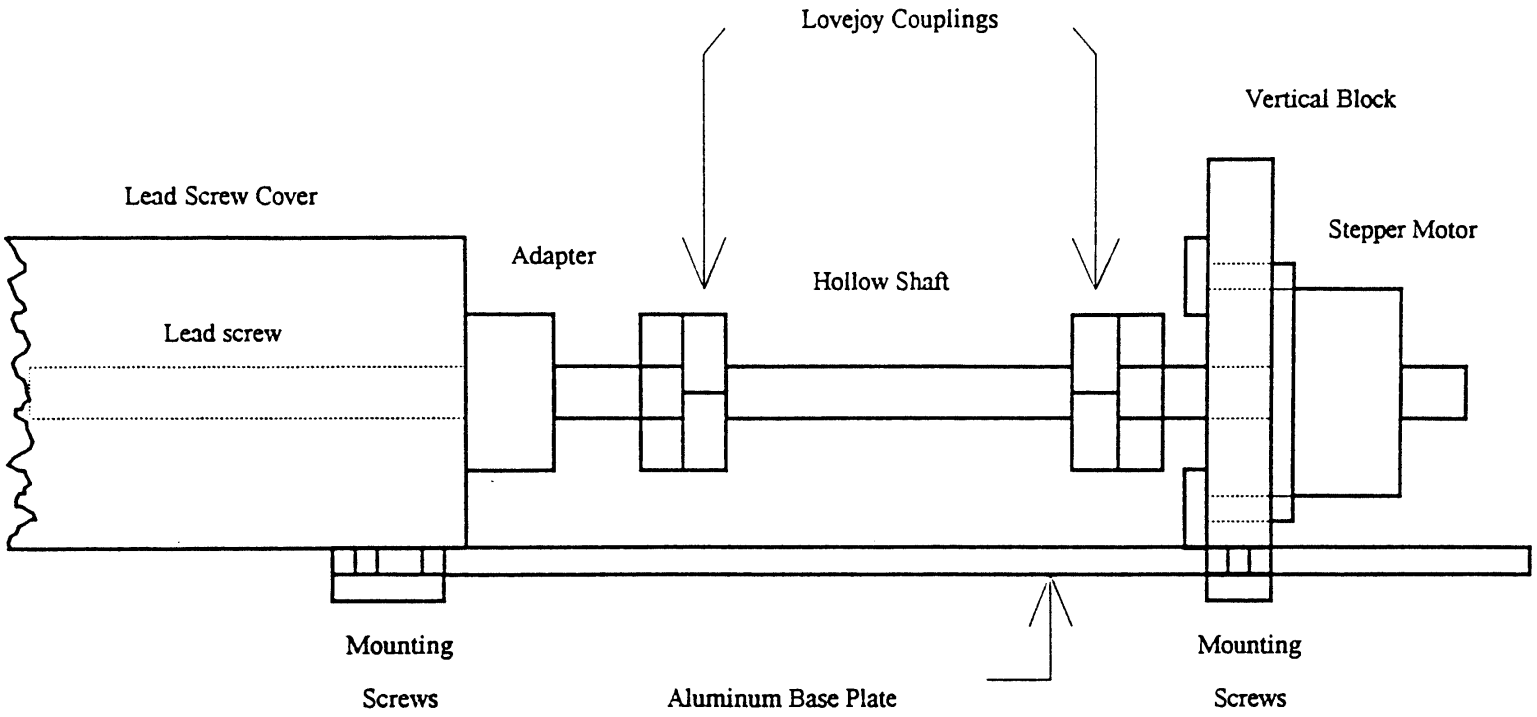

Figure 214. Stepper Motor Mounted on the Traverse Table

Motor/Logic Voltage:	15-40 Vdc unregulated with a 10% ripple
Optoisolation Voltage:	5 Vdc @ 100 ma. max.
Output rating for Bifilar motors:	0.3 to 2.8 amperes/phase

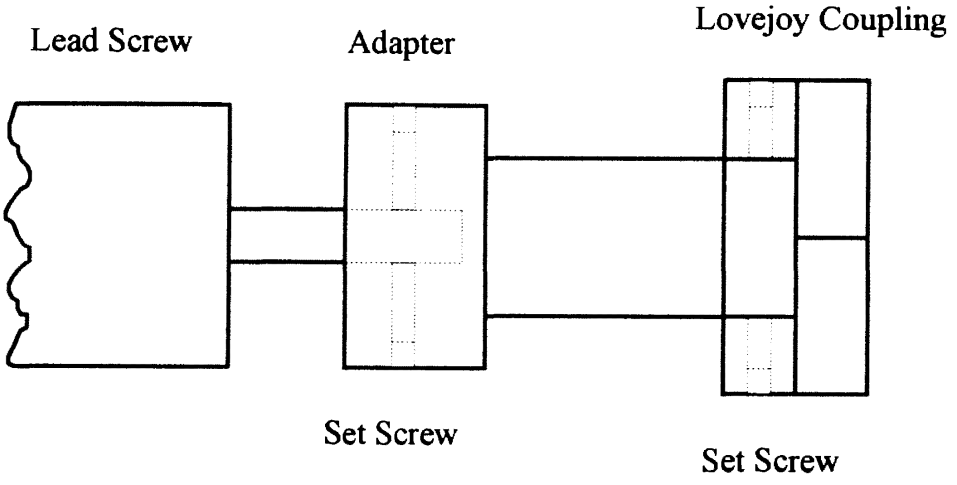

Figure 215. Adapter Connected to Lead Screw and Lovejoy Coupling

A 24 Vdc and 6 A power supply source from Acme Electronics was used for both CMD-40s. The basic installation steps for a CMD-40 included setting the current level, connecting the motor leads, and hooking up the required DC power needed for CMD-40 operation. As shown in Fig. 216, a CMD-40 is controlled by a computer through a data acquisition board. Therefore, logical control lines from the data acquisition board to the CMD-40 were also connected.

A CMD-40 contains two stages, the logical and the power switching stage, each having a specific function to operate the stepper motor efficiently. The logic section of the

drive acts to direct current in and out of the motor phases in a proper sequence in order to cause the desired rotation. The power switching stage controls the rate and amount of current flow into the motor windings as directed by the logic. In general, the faster the current is sent through a winding during each step, the greater the torque and the speed that is obtained. A CMD-40 uses a sophisticated bipolar chopping method of current control which yields the highest possible speed and torque. This technique involves overdriving the winding with high voltages (up to 40 Vdc) to decrease the current rise times, and then controlling the current level by a high frequency (20 kHz.) current chopping.

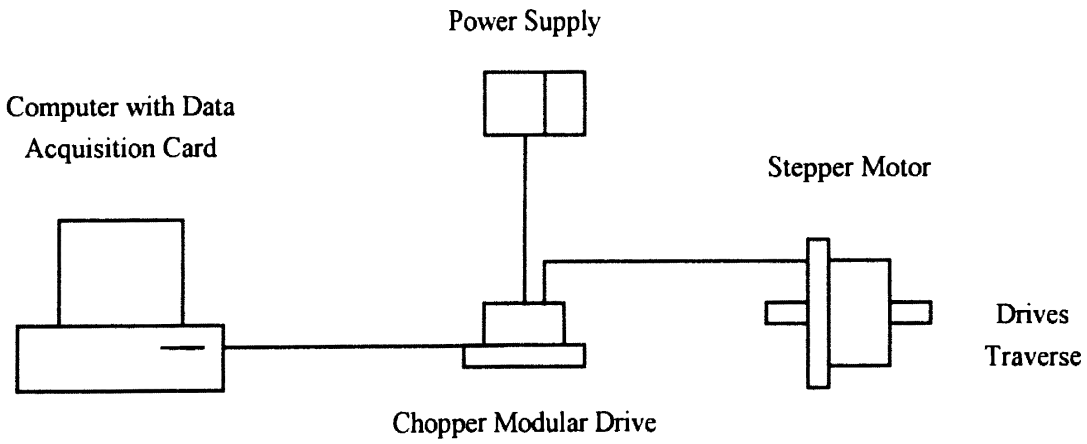

Figure 216. Block Diagram of Traverse Automation

Figure 217 shows the face of a CMD-40. There are two terminal strips over the face, Terminal Strip 1 (TS1) and Terminal Strip 2 (TS2). Power and motor terminal connections are made at TS2. Positive DC supply voltage, from the power supply was connected to terminal # 1 of TS2. The corresponding negative or ground of the power

supply was connected to TS1 terminal # 10. The DC power so obtained was used by both the logic section of the drive and the motor windings. Leads from the motor were connected to terminal #'s 2, 3, 4 and 5 of TS2 as shown in Fig. 218. Connecting the 8 lead motor in parallel optimizes the torque and speed of the motor due to 100% usage of the motor windings. This configuration results in best high speed performance with some loss of low speed performance. However, it may also cause some extra motor heating due to eddy current losses.

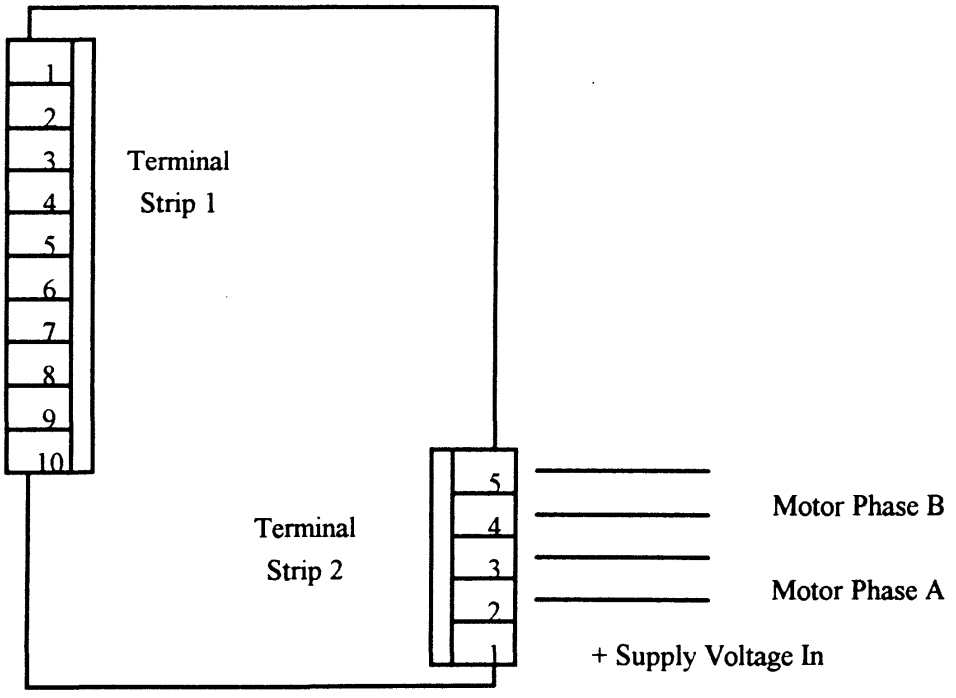

Figure 217. Face of a CMD-40 Showing Terminal Strips

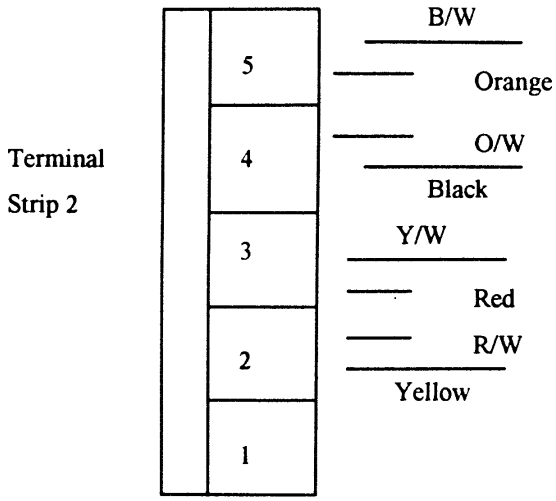

Figure 218. Eight Lead Motor Connected in Parallel

The logic inputs required by a CMD-40 were made at TS1 as shown in Fig. 219. All logical inputs have 2 possible input states, 'High' (open terminal) or 'Low'. Each of the logic inputs is clamped 'High' internally with a pull up resistor and requires a separate 5 Vdc supply and open collector outputs to pull it 'Low'. The 5 Vdc supply should be rated for at least 100 mA, and each open collector output used should be capable of sinking at least 15 mA. The optical isolation feature electrically isolates the motor and power stages of the drive in order to protect both circuits and eliminate electrical noise problems. The following logic inputs were given to the CMD-40 by a computer through a data acquisition board:

1. Step Input (Terminal # 3 on TS1): This instructs the motor to take a single step. The step is taken on the rising edge of each incoming pulse up to a rate of 50 kHz. The minimum input pulse width is 10 microseconds.

2. Direction (Terminal # 4 on TS1): This determines the direction of steps of the motor. A 'High' or open connection on this terminal would cause a clockwise (CW) rotation of the motor as viewed from the output shaft end. When taken 'Low', the direction would be counterclockwise (CCW).

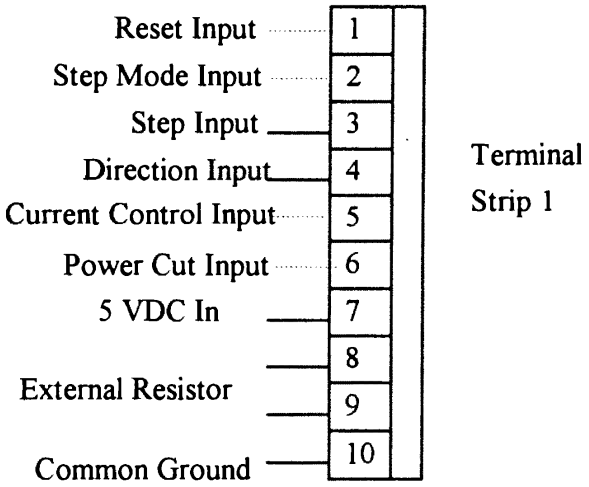

Figure 219. Connections on Terminal Strip 1

The 5 Vdc supply used by the optical isolation feature of logic inputs was connected to terminal # 7 on TS1. This 5 Vdc supply was also obtained from the same power supply source using an external voltage regulator with it. An external resistor of 33 kOhms was used between terminals # 8 and 9 of TS1 in order to set the current operating level for the motor. As mentioned before, the negative or ground of the power supply was connected to terminal # 10 of TS1.

Terminal #'s 1, 2, 5 and 6 on TS1 can be used for providing other logic inputs to the CMD-40. Terminal # 1 is for resetting the drive, terminal # 2 is for switching to 'full'

step mode instead of 'half' step mode, terminal # 5 is for controlling the current decay mode in the motor windings, and terminal # 6 is for cutting off power to the motor. However, these terminals were neither needed nor used in the present work.

As shown in Fig. 216, and mentioned before, the CMD-40s were controlled by a computer through a data acquisition board. A PCL-818, which is a data acquisition card capable of supporting programmable inputs, was suitably installed. The card is very versatile and can support a number of complex operations. However, in this setup, it was primarily used to generate digital output signals as dictated by the software and as discussed later in this chapter. The digital signals acted as logic inputs for the CMD-40s as explained before. Sixteen consecutive base address locations were required for an I/O base address. In conjunction to the PCL-818, a daughter board called the PCLD-780 was also used. The daughter board used was basically a screw terminal board for easy digital output connections. The following are the specifications of PCL-818 (pertaining to digital output) :

Channel:	16 bits.
Level:	TTL compatible
Output Voltage:	Low-Sink 8 mA at 0.5 V maximum.
	High-Source -0.4 mA at 2.4 V minimum.

Through the various switches on the card, selections were made with regard to base address, channel configuration and input range control mode. The card is equipped with five 20-pin insulation displacement (mass termination) connectors. Connector 3, as shown in Fig. 220, was used for the desired digital output. The card has 16 digital input channels and 16 digital output channels. These I/O channels use the input and output ports at address BASE +3 and BASE +11.

The PCL-818 was adequately supported by the principal operating software. Various driver routines written in assembly language and compiled into a machine language program called '818BAS.BIN' were provided with the card. The driver routines,

designed to work with BASIC language programming, could be accessed through the CALL statement of the interpreted or compiled BASIC language. A computer program in BASIC was developed to specifically provide complete computer control for the LDV traverse. This is discussed, and a copy of the computer program is given in Appendix C.

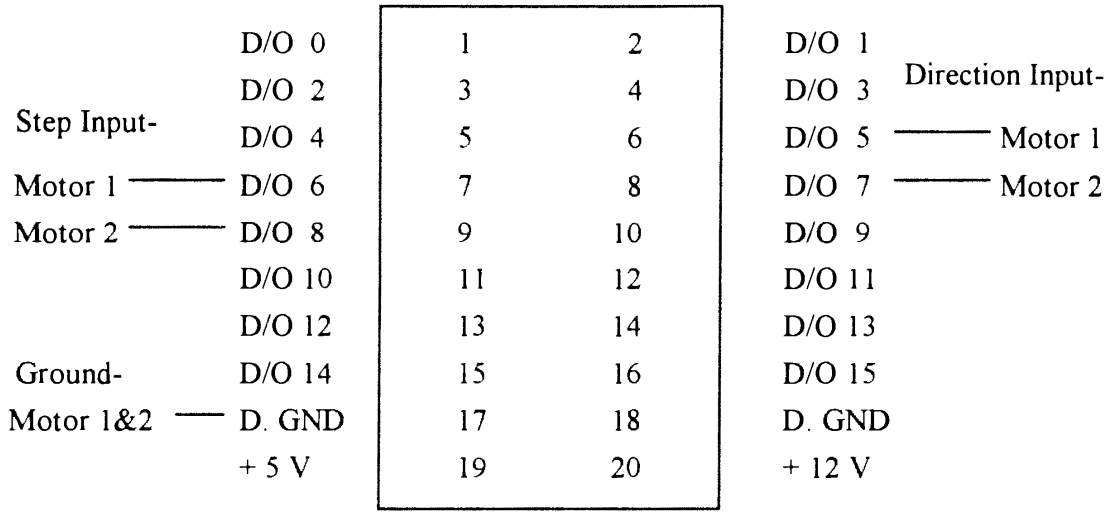

Figure 220. Connector 3 Used for Digital Output

Thus, in the above described manner, the traverse automation was successfully accomplished. This, as mentioned before, enabled movement of the probe volume conveniently, precisely and speedily to any desired location.

The present automated traverse can be further improved with regard to its reliability and efficiency by incorporating a 'feedback mechanism' in it. As for example, an 'encoder' can be installed which counts the steps taken by the lead screw and delivers this information to the user through the PCL-818 and the computer. The current computer

program should also be modified for this. The user can then compare the steps actually taken by the lead screw to the steps required to obtain the desired displacement. Currently, this confirmation with regard to the displacement is done by visually checking the reading on the counter. Thus, by 'close-looping' the traverse system, any error due to motor slippage or due to slippage at other connections can be detected. The program can also be modified to compare the 'actual' and the 'required' steps, and then to reinstruct the PCL-818 so that the desired displacement is achieved. Thus, the program and the lead screw can interact with each other till the required displacement is achieved.

As explained in Appendix C, though the present program warns the user if the requested displacement is not possible, it is still vulnerable to 'input errors' by the user. Therefore, it is recommended to add limit switches to the current traverse. That would ensure that the motors do not work beyond the allowable range of traverse movement.

APPENDIX C

LISTING AND EXPLANATION OF SOURCE CODE FOR TRAVERSE

As mentioned in Appendix B, a computer program in BASIC was developed to specifically provide complete computer control for the LDV traverse used for the present work. Out of the 27 driver functions available with the principal operating software of PCL-818, the following 2 functions were used in the program for our application:

1. Function 0: This initializes the PCL-818 routines by specifying the base address and other parameters.
2. Function 13: Writes data to digital output channels DO0 through DO3.

The following is the format of the CALL statement used in the program:

CALL PCL818(FUNC%, DAT%(0), ER%)

In this statement, PCL818 is a variable specifying the memory offset of the starting address of the PCL818 driver routine from the most recently defined current segment [Advantech Co., 1990]. FUNC% is a variable indicating the driver function to be executed, DAT%(0) is a variable specifying the starting location of the entire data array and ER% is a variable containing the return message code.

The program is highly user friendly. Though specially tailored for the current LDV traverse, it is generic enough to handle any two-dimensional traverse mechanism with a couple of simple and obvious changes as discussed later.

In the first part of the program (lines 110 to 190), the PCL818 machine language driver is loaded immediately after the normal BASIC work space area. Then, using function 0, initialization of the PCL-818 is done (lines 210 to 300).

Next, active interaction with the user follows (lines 320 to 520 and 860 to 1030). The user is asked to input information regarding the particular axis along which displacement is desired, absolute position, any reference position, the direction and magnitude of the desired displacement, etc. The program checks as to whether the requested displacement is possible or not, considering the current position of the traverse and the maximum movement available by the mechanism (lines 420 to 490 and 930 to 1000). If the requested displacement is not possible, it warns the user and asks for a different displacement value. If this program is to be used with a different traverse, then the built in maximum movement available limits have to be changed depending upon the specific traverse mechanism (lines 420 to 430 and 930 to 940).

Then using function 13 repeatedly and alternately, on two channels with a time delay in between, a digital output pulse is generated (lines 540 to 740 and 1050 to 1250). The number of repetitions depends upon the displacement desired. This pulse then drives the CMD-40 which in turn steps the motor, and the desired displacement is obtained.

The program updates the current position with each displacement and also calculates the relative position with respect to the initial reference position and gives this information as feedback to the user (lines 760 to 840 and 1270 to 1360). The user can actually compare and confirm the current position indicated by the program with that displayed on the counter. This variation is of the order of ±0.001 of an in. per 10 in. of displacement. This difference may be because the motion is not transferred very smoothly from motor to the lead screw. The inherent motor precision limitation may also be a contributing factor to the observed variation.

The following is a list of the variables and constants used in the program:

ABSX absolute position on x-axis as shown on counter (in.)

ABSY	absolute position on y-axis as shown on counter (in.)
DISX	required displacement on x-axis (in.)
DISY	required displacement on y-axis (in.)
IAXIS	axis along which displacement is desired
J	variable to provide the necessary 'delay' for pulse generation
KDIR	variable for selecting direction for the required movement
LMAXX	maximum movement available for negative x-axis (in.)
LMAXY	maximum movement available for positive y-axis (in.)
LX	lower limit of x-axis traverse (currently, 5.0 in.)
LY	lower limit of y-axis traverse (currently, 2.6 in.)
M	counter for motor steps accomplished
REFX	arbitrary reference position on x-axis (in.)
REFY	arbitrary reference position on y-axis (in.)
RELX	relative position on x-axis (in.)
RELY	relative position on y-axis (in.)
UMAXX	maximum movement available for positive x-axis (in.)
UMAXY	maximum movement available for negative y-axis (in.)
UX	upper limit of x-axis traverse (currently, 20.0 in.)
UY	upper limit of y-axis traverse (currently, 25.6 in.)
STEPSX	number of motor steps required for the desired displacement along x-axis
STEPSY	number of motor steps required for the desired displacement along y-axis

```
10  '*************************************************************************
20  'Program : MDUAL.BAS
30  'Prepared by : BALDHANI MANOJ KUMAR
40  'April 6, 1993.
50  '
60  'The following program provides complete computer control for the
70  'LDV-traverse. The program controls digital data output to PCL-818
80  'data acquisition card, which in turn controls the step motors through
90  'CMD-40s. PCL-818 driver functions 0 and 13 are used in the program.
100 '*************************************************************************
110 'Software loading
120 SCREEN 0, 0, 0: WIDTH 80: CLS : KEY OFF
130 CLEAR , 49152!
140 DEF SEG = 0
150 SG = 256 * PEEK(&H511) + PEEK(&H510)
160 SG = SG + 49152! / 16
170 DEF SEG = SG
180 BLOAD "818BAS.BIN", 0
190 PCL818 = 0              'DRIVER SEGMENT OFFSET
200 '*************************************************************************
210 'Initialization of driver using function 0
220 DIM DAT%(4)
230 PORT% = &H300           'SET I/O PORT ADDRESS
240 DAT%(0) = PORT%         'GET I/O PORT ADDRESS
250 DAT%(1) = 2             'SELECT INTERRUPT LEVEL 2
260 DAT%(2) = 3             'SELECT DMA 3
270 ER% = 0                 'ERROR RETURN CODE
280 FUN% = 0                'FUNCTION 0
290 CALL PCL818(FUN%, DAT%(0), ER%)
300 IF ER% <> 0 THEN PRINT "DRIVER INITIALIZATION FAILED!": STOP
310 '*************************************************************************
320 'Interaction with the user
330 ITNX=1
340 ITNY=1
350 PRINT"Select axis along which Displacement is required"
360 PRINT:INPUT"Enter 1 for X axis, 2 for Y axis:", IAXIS
370 IF IAXIS=2 GOTO 390
380 IF IAXIS=1 GOTO 900
390 IF ITNY>1 THEN GOTO 420
400 PRINT:INPUT"Enter ABSOLUTE POSITION on Y axis as on Counter(Inches):",ABSY
410 PRINT:INPUT"Enter Arbitrary REFERENCE POSITION on Y axis(in Inches):",REFY
420 LY=2.6              'LOWER LIMIT OF Y-AXIS TRAVERSE POSITION
430 UY=25.6             'UPPER LIMIT OF Y- AXIS TRAVERSE POSITION
440 UMAXY=ABSY-UY       'MAXIMUM MOVEMENT AVAILABLE FOR NEGATIVE Y-AXIS
450 LMAXY=ABSY-LY       'MAXIMUM MOVEMENT AVAILABLE FOR POSITIVE Y-AXIS
460 PRINT"Assuming that you are in front of tranceiver,use negative number for
    pulling the traverse towards you and positive number for pushing it away."
470 PRINT:INPUT"Enter req. Displacement on Y axis(in Inches):",DISY
480 IF DISY>LMAXY GOTO 510
490 IF DISY<UMAXY THEN GOTO 510
500 GOTO 550
510 PRINT"Requested Displacement is out of Range,Input again"
520 GOTO 470
530 '*************************************************************************
540 'Traversing along Y-axis using function 13
550 RELY=REFY+DISY      'CALCULATING RELATIVE POSITION
560 IF DISY>0! THEN KDIR=2    'SELECTING DIRECTION FOR REQ. MOVEMENT
570 IF DISY<0! THEN KDIR=1      'SELECTING DIRECTION FOR REQ. MOVEMENT
580 B=ABS(DISY)
590 STEPSY=4000*B       'NUMBER OF STEPS OF MOTOR REQUIRED
600 M=0
610 FUN%=13
620 DAT%(0)=1
630 CALL PCL818 (FUN%,DAT%(0),ER%)
640 M=M+1
```

```
650 J=1
660 J=J+1
670 IF J<=1 GOTO 660              'DELAYING FOR PULSE GENERATION
680 IF KDIR=1 THEN DAT%(0)=14     'SELECTING CHANNEL FOR THE REQ. DIRECTION
690 IF KDIR=2 THEN DAT%(0)=2      'SELECTING CHANNEL FOR THE REQ. DIRECTION
700 CALL PCL818 (FUN%,DAT%(0),ER%)
710 J=1
720 J=J+1
730 IF J<=1 THEN GOTO 720         'DELAYING FOR PULSE GENERATION
740 IF M<=STEPSY GOTO 620
750 '*************************************************************************
760 'Providing feedback to the user
770 IF KDIR=1 THEN ABSY=ABSY+B     'CALCULATING CURRENT ABSOLUTE POSITION
780 IF KDIR=2 THEN ABSY=ABSY-B     'CALCULATING CURRENT ABSOLUTE POSITION
790 PRINT "Current Absolute Position (Inches) is:",ABSY
800 PRINT "Check the Counter on Y axis, it should show this number."
810 PRINT "Current Relative Pstn. w.r.t. Initial Ref. Pstn(Inches):",RELY
820 REFY=RELY             'UPDATING REFERENCE POSITION
830 ITNY=ITNY+1
840 PRINT "##################"
850 '*************************************************************************
860 'Interaction with the user
870 PRINT:INPUT"Do you want to continue ? Enter 1 if yes, 2 if no.:",IN
880 IF IN=1 THEN GOTO 350
890 IF IN=2 THEN GOTO 1400
900 IF ITNX>1 THEN GOTO 930
910 PRINT:INPUT"Enter ABSOLUTE POSITION on X axis as on Counter(Inches):",ABSX
920 PRINT:INPUT"Enter Arbitrary REFERENCE POSITION on X axis(Inches):",REFX
930 LX=5!                 'LOWER LIMIT FOR TRAVERSE MOVEMENT, X-AXIS
940 UX=20!                'UPPER LIMIT FOR TRAVERSE MOVEMENT, X-AXIS
950 UMAXX=UX-ABSX          'MAXIMUM MOVEMENT AVAILABLE, POSITIVE X-AXIS
960 LMAXX=LX-ABSX          'MAXIMUM MOVEMENT AVAILABLE, NEGATIVE X-AXIS
970 PRINT"Assuming that you are in front of tranceiver, use negative number for
       the  movement in left and positive number for that in right direction
        respectively."
980 PRINT:INPUT"Enter req. Displacement on X axis (Inches):",DISX
990 IF DISX<LMAXX GOTO 1020
1000 IF DISX>UMAXX THEN GOTO 1020
1010 GOTO 1060
1020 PRINT"Requested Displacement is out of RANGE, Input again"
1030 GOTO 980
1040 '*************************************************************************
1050 'Traversing along X-axis using function 13
1060 RELX=REFX+DISX      'CALCULATING RELATIVE POSITION, X-AXIS
1070 B=ABS(DISX)
1080 IF DISX<0! THEN KDIR=1          'SELECTING DIRECTION FOR REQ. MOVEMENT
1090 IF DISX>0! THEN KDIR=2          'SELECTING DIRECTION FOR REQ. MOVEMENT
1100 STEPSX=4000*B      'CALCULATING MOTOR STEPS REQUIRED
1110 M=0
1120 FUN%=13
1130 DAT%(0)=3
1140 CALL PCL818 (FUN%,DAT%(0),ER%)
1150 M=M+1
1160 J=1
1170 J=J+1
1180 IF J<=1 GOTO 1170           'DELAYING FOR PULSE GENERATION
1190 IF KDIR=1 THEN DAT%(0)=14      'SELECTING CHANNEL FOR REQ. DIRECTION
1200 IF KDIR=2 THEN DAT%(0)=11      'SELECTING CHANEL FOR REQ. DIRECTION
1210 CALL PCL818(FUN%,DAT%(0),ER%)
1220 J=1
1230 J=J+1
1240 IF J<=1 THEN GOTO 1230      'DELAYING FOR PULSE GENERATION
1250 IF M<=STEPSX GOTO 1130
1260 '*************************************************************************
1270 'Providing feedback to the user
1280 IF KDIR=1 THEN ABSX=ABSX-B      'CALCULATING CURRENT ABSOLUTE POSITION
```

```
1290 IF KDIR=2 THEN ABSX=ABSX+B        'CALCULATING CURRENT ABSOLUTE POSITION.
1300 PRINT "Current Absolute Position is:",ABSX
1310 PRINT "Check the Counter on X axis, it should show this number."
1320 PRINT "Current Relative Pstn. w.r.t. Initial Ref. Pstn. is:",RELX
1330 ITNX=ITNX+1
1340 REFX=RELX                         'UPDATING REFERENCE POSITION
1350 ITNX=ITNX+1
1360 PRINT "################"
1370 PRINT:INPUT"Do you want to Continue? Enter 1 if yes,2 if no.:",IN
1380 IF IN=1 THEN GOTO 350
1390 IF IN=2 THEN GOTO 1400
1400 END
1410 '*************************************************************************
```

APPENDIX D

DSA CONFIGURATION AND VARIABLE SETUP PAGES

This appendix presents the various variable setup pages pertaining to the optical parameters of the LDV system, and the DSA hardware configuration. As mentioned in Chapter IV, the following pages show the factory settings of the variables and parameters. These variables and parameters were never changed after the successful installation of the system. It is worth mentioning that, during the course of progress of this work, several revised and improved versions of the DSA software from Aerometrics, Inc. were used. The following pages are from the latest version, 4.16 D of the DSA software. These pages can be accessed by going to the 'config' subdirectory in the 'dsa4' directory and executing 'dsacfg'. Then, keystroke F1 produces a 'help' menu. Table 6 shows the keystrokes that should be selected from the 'help' menu to access the various pages.

TABLE 6

CONFIGURATION PAGES AND THE ACCESSING KEYSTROKES

Page	Keystroke
Instrument Configuration	Ctrl F6
Configuration Menu # 1	Alt 1
Configuration Menu # 2	Alt 2
Factory Configuration # 1	Alt F
Factory Configuration # 2	Alt F then Alt 2
Factory Configuration # 3	Alt F then Alt 3
Factory Configuration # 4	Alt F then Alt 4
Factory Configuration # 5	Alt F then Alt 5

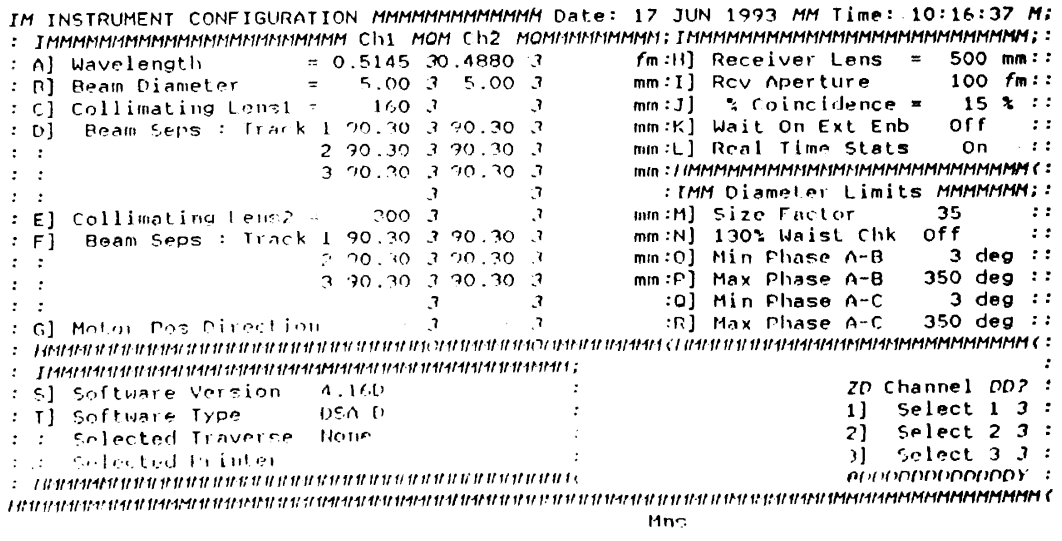

Figure 221. Instrument Configuration

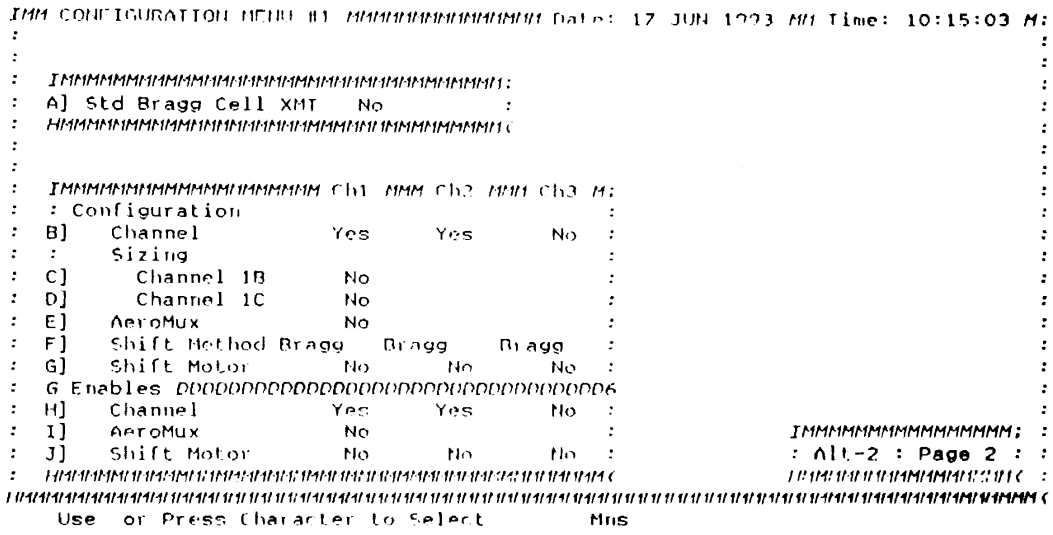

Figure 222. Configuration Menu # 1

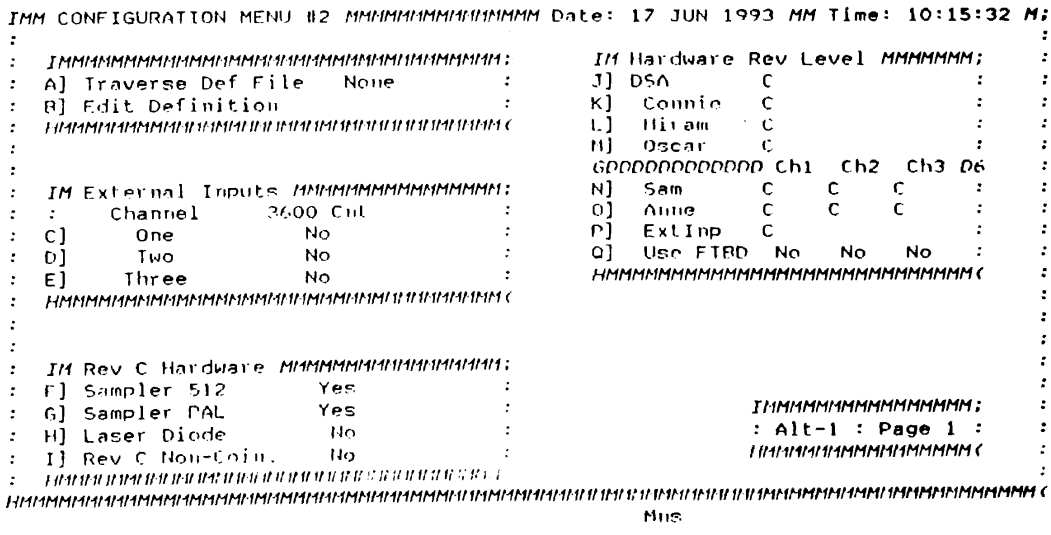

Figure 223. Configuration Menu # 2

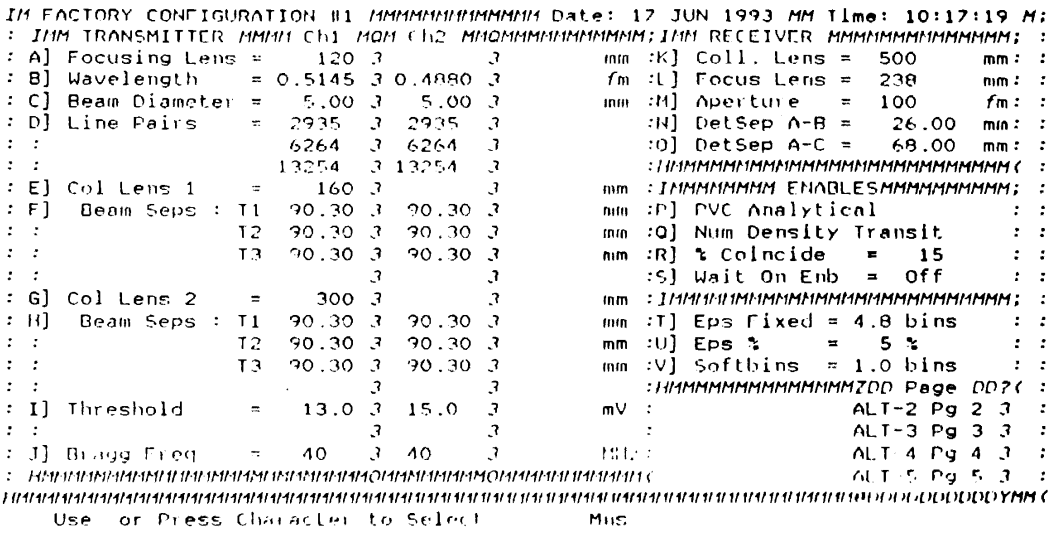

Figure 224. Factory Configuration # 1

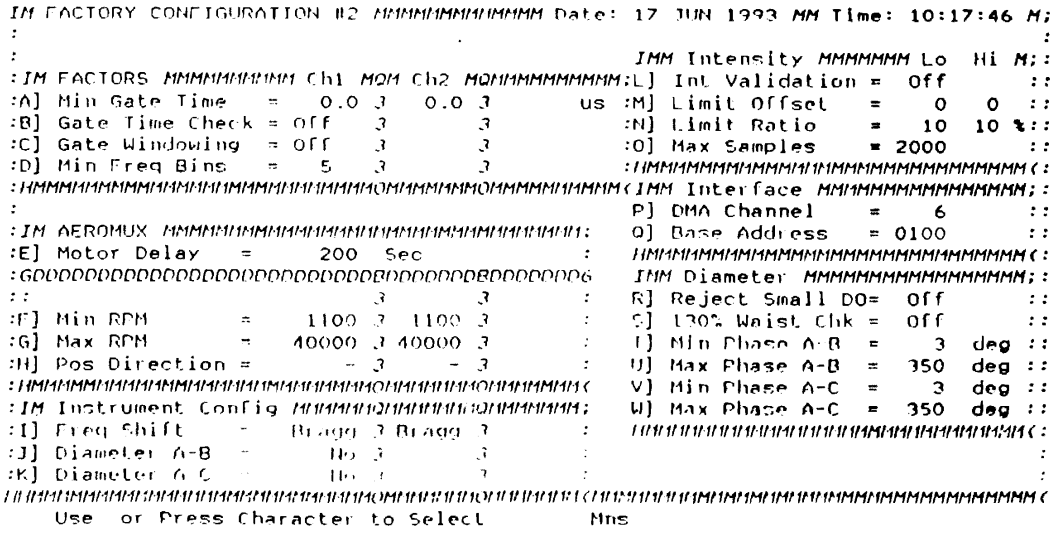

Figure 225. Factory Configuration # 2

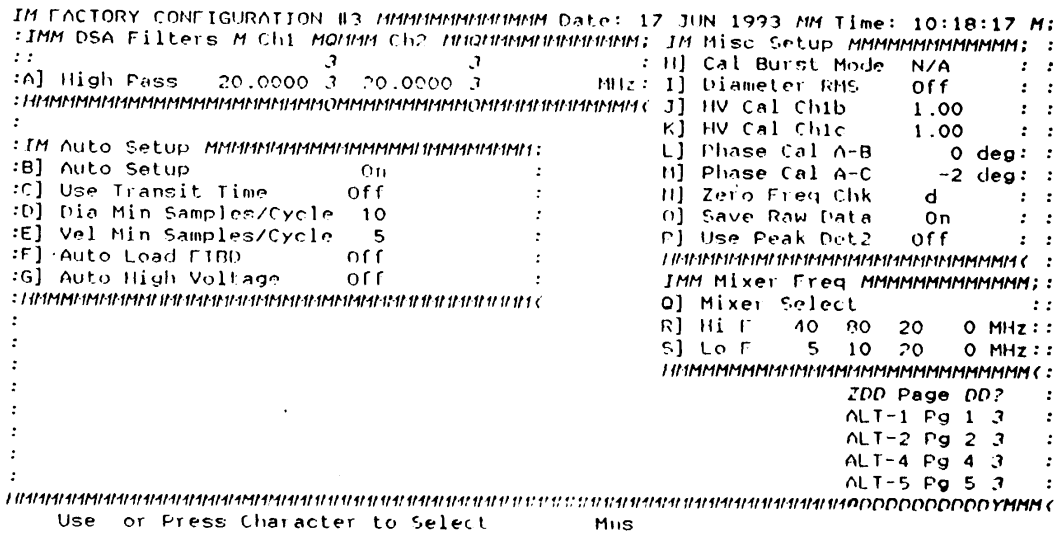

Figure 226. Factory Configuration # 3

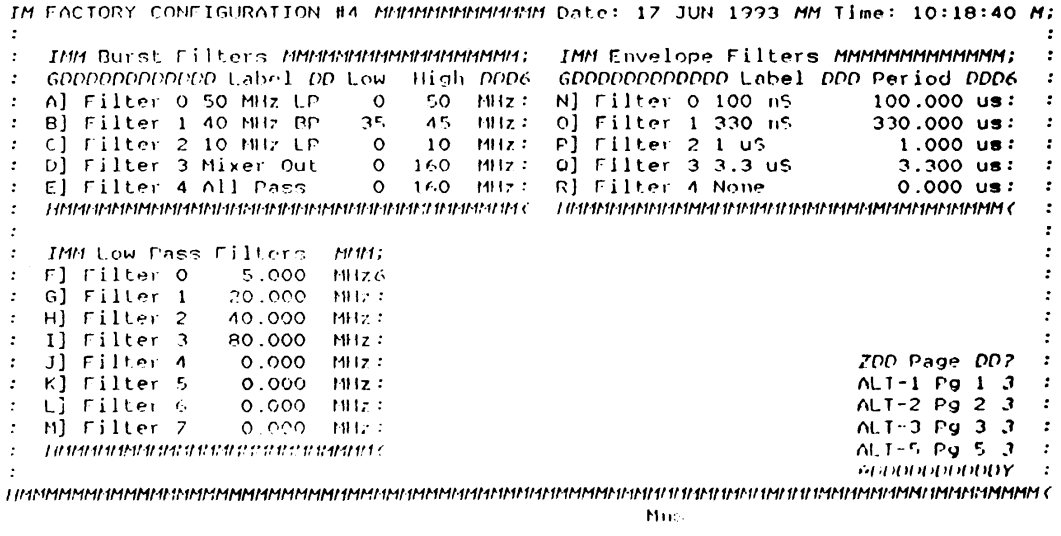

Figure 227. Factory Configuration # 4

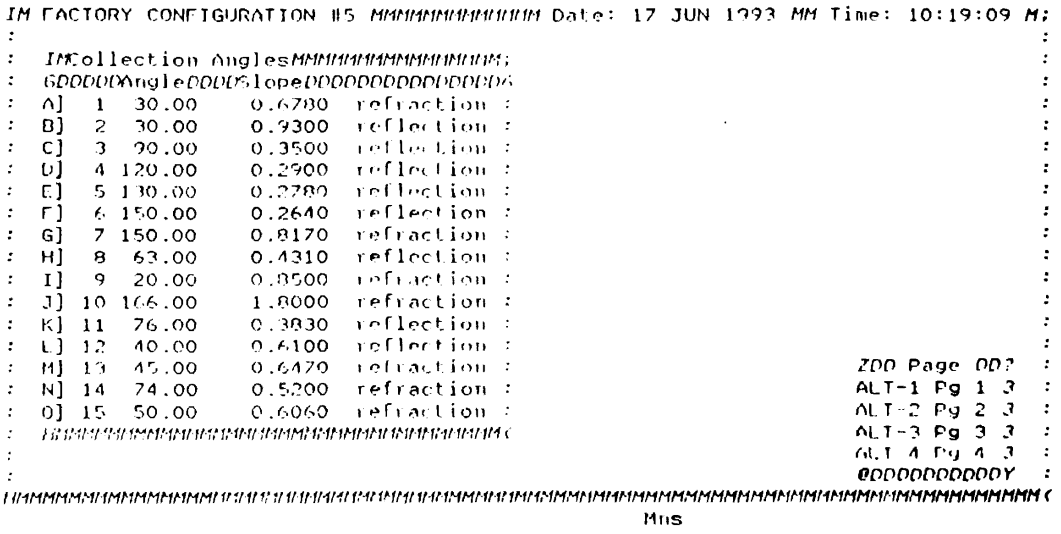

Figure 228. Factory Configuration # 5

APPENDIX E

PARAMETER SETUPS EMPLOYED

FOR MEASUREMENTS

As mentioned in Chapter IV, six different parameter setups were employed for taking the measurements involved in this work. This appendix presents those six different parameter setups.

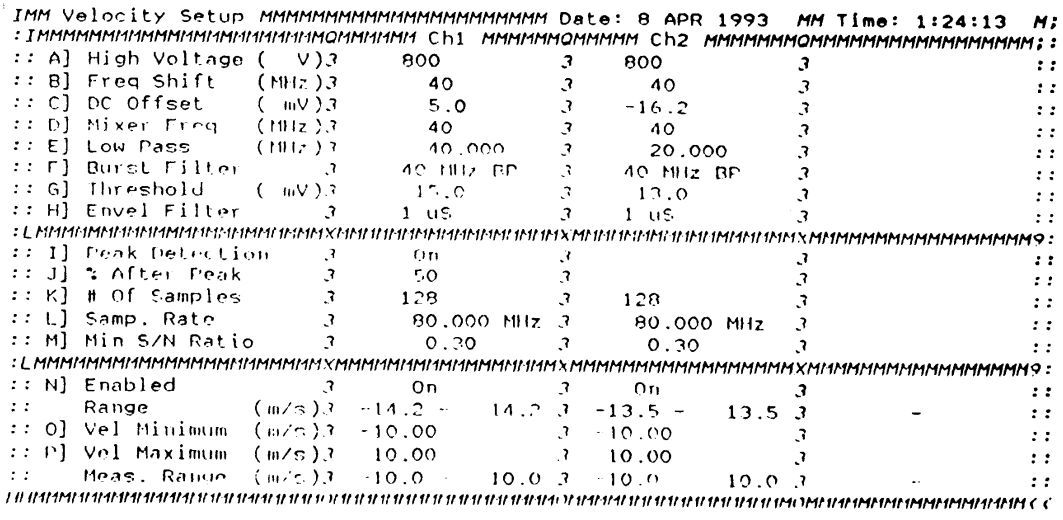

Figure 229. Parameter Setup I

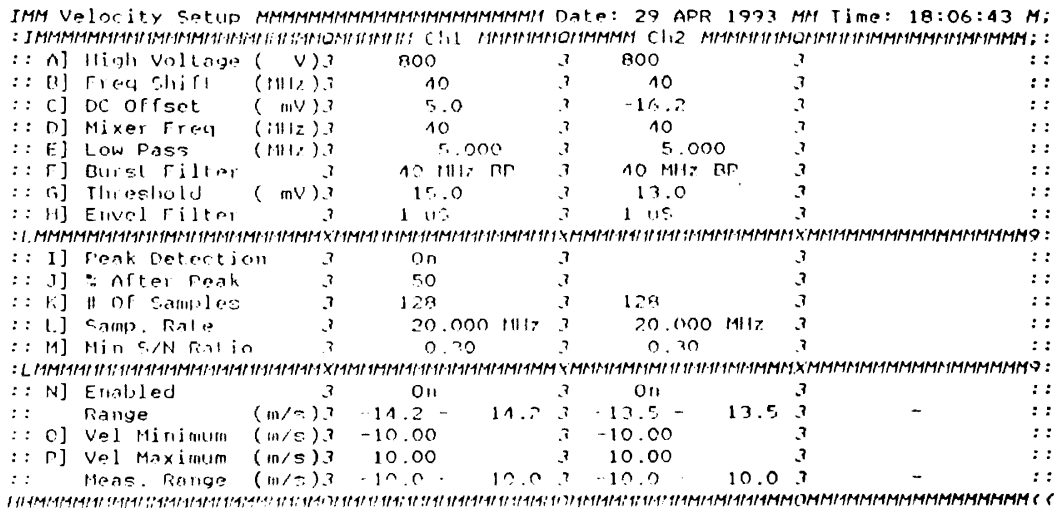

Figure 230. Parameter Setup II

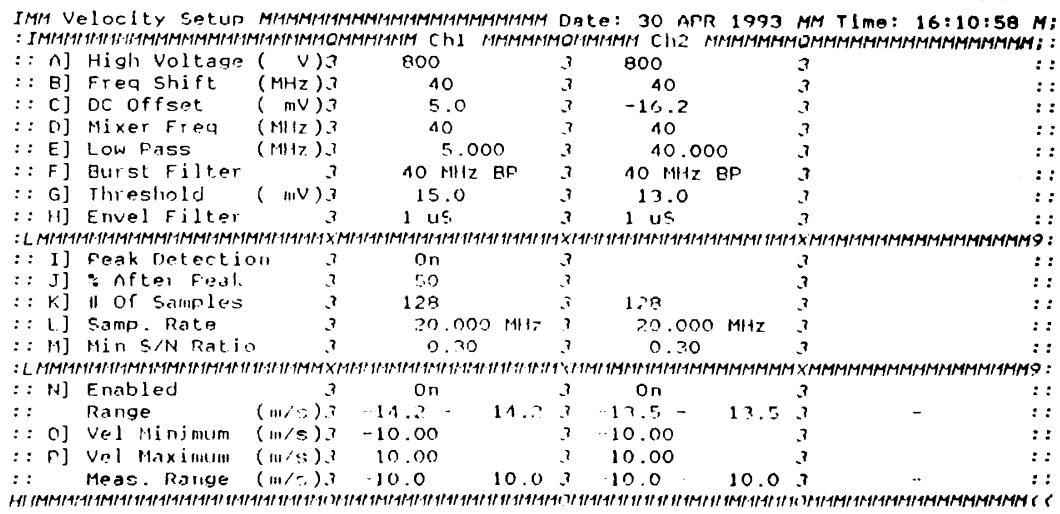

Figure 231. Parameter Setup III

```
Velocity Setup                    Date: 5 OCT 1992   Time: 1:36:33
                                  Ch1                Ch2
A] High Voltage (   V)      800                800
B] Freq Shift   (MHz)       40                 40
C] DC Offset    ( mV)       -0.3               -26.2
D] Mixer Freq   (MHz)       40                 40
E] Low Pass     (MHz)        5.000              5.000
F] Burst Filter             40 MHz BP          40 MHz BP
G] Threshold    ( mV)       4.0                8.0
H] Envel Filter             3.3 uS             100 nS
I] Peak Detection           On
J] % After Peak             50
K] # Of Samples             128                128
L] Samp. Rate               10.000 MHz         20.000 MHz
M] Min S/N Ratio            0.30               0.30
N] Enabled                  On                 On
   Range        (m/s)   -14.2 -   14.2    -13.5 -   13.5      -
O] Vel Minimum  (m/s)    -7.00              -5.00
P] Vel Maximum  (m/s)     7.00               13.50
   Meas. Range  (m/s)   -7.00 -   7.00    -5.00 -   13.5      -
```

Figure 232. Parameter Setup IV

```
Velocity Setup                    Date: 19 OCT 1992  Time: 3:15:46
                                  Ch1                Ch2
A] High Voltage (   V)      800                800
B] Freq Shift   (MHz)       40                 40
C] DC Offset    ( mV)       -2.6               -28.5
D] Mixer Freq   (MHz)       40                 40
E] Low Pass     (MHz)        5.000              5.000
F] Burst Filter             40 MHz BP          40 MHz BP
G] Threshold    ( mV)       4.0                8.0
H] Envel Filter             3.3 uS             100 nS
I] Peak Detection           On
J] % After Peak             50
K] # Of Samples             128                128
L] Samp. Rate               10.000 MHz         20.000 MHz
M] Min S/N Ratio            0.30               0.30
N] Enabled                  On                 On
   Range        (m/s)   -14.2 -   14.2    -13.5 -   13.5      -
O] Vel Minimum  (m/s)    -7.00              -5.00
P] Vel Maximum  (m/s)     7.00               13.50
   Meas. Range  (m/s)   -7.00 -   7.00    -5.00 -   13.5      -
```

Figure 233. Parameter Setup V

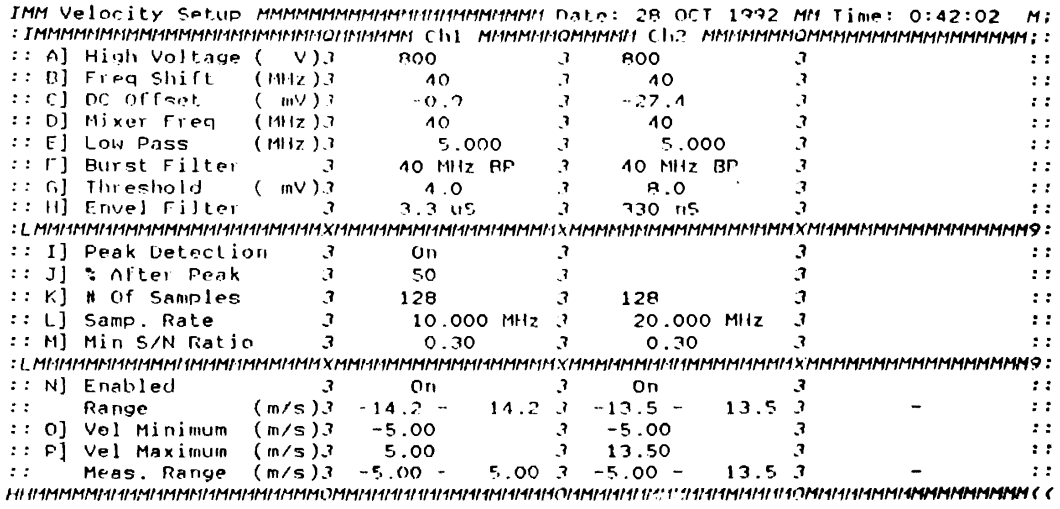

Figure 234. Parameter Setup VI

VITA

Manoj Kumar Haldhani

Candidate for the Degree of

Master of Science

Thesis: PARTICLE NUMBER DENSITY DISTRIBUTION AND ITS TIME HISTORY FOR AN AUTOMOTIVE AIR FILTER

Major Field: Mechanical Engineering

Biographical:

Personal Data: Born in Jodhpur, India, August 24, 1968, the son of Kamlesh K. and Usha K. Haldhani.

Education: Graduated from Maheshwari Public School, Jaipur, India, in May 1986 ; received Bachelor of Engineering Degree in Mechanical engineering from University of Rajasthan, Jaipur, India in July, 1991; completed requirements for the Master of Science degree at Oklahoma State University in December, 1993.

Professional Experience: Research Assistant, Department of Mechanical Engineering, Oklahoma State University, March, 1992 to July, 1993.